N° D'ordre : 107

Ecole Doctorale ''Sciences pour l'Ingénieur Microtechnique''

Université de Franche-Comté

Université de Technologie de Belfort-Montbéliard

THESE

Présentée pour obtenir le grade de

Docteur de l'Université de Technologie de Belfort-Montbéliard et de l'Université de Technologie de Dalian en Sciences pour l'Ingénieur

Par

Zhiguo ZHANG

Élaboration de dépôts nano-composés par pulvérisation cathodique magnétron pour la substitution du chrome électrolytique (thèse en anglais)

Soutenue le 12 Décembre 2008 devant le jury composé de :

Rapporteurs

Monsieur **Alain JACQUES, Directeur de Recherche HDR**
Ecole Nationale Supérieure des Mines de Nancy (INPL)
Monsieur **Laurent LE BRIZOUAL, Maître de Conférences HDR**
Institut des Matériaux Jean Rouxel de Nantes

Examinateurs

Monsieur **Christian CODDET**, **Professeur des Universités**
Université de Technologie de Belfort-Montbéliard
Monsieur **Chuang DONG**, **Professeur des Universités**
Université de Technologie de Dalian
Madame **Nathalie ALLAIN**, **Maître de Conférences**
Université de Metz
Monsieur **Olivier RAPAUD**, **Enseignant-chercheur**
Université de Technologie de Belfort-Montbéliard

Acknowledgments

Foremost, I would like to thank my adviser Prof. Christian Coddet and the co-supervisors Nathalie Allain, Olivier Rapaud for giving me the chance to work with them for my graduate degree. I am grateful for their guidance and support during my thesis. I would also like to thank my adviser Prof. Chuang Dong in the faraway China. Thank you for giving me a chance to go abroad and teaching me many things in scientific work.

I would like to acknowledge Mr. Laurent Le Brizoual and Mr. Alain Jacques for their serving in my thesis committee and for their numerous insightful suggestions.

I am grateful to Prof. Hanlin Liao, who provides me the opportunity to work in the lab of LERMPS and helps me a lot in my daily life and research work.

I would like to express my deepest and special thanks to my wife, my parents and my great family, whose support and encouragement made the research work become enjoyable. Especially for my wife, I am deeply grateful to you for accompanying me in France. I would also like to thank my parent for being exceedingly proud of their son. Nothing would have been possible without them.

I would like to express my heartfelt gratitude to my colleagues in the same office during the last three years. Mira, Rafik and Mohammad, thank you for your helps since I came to Montbéliard. I would like to say, without you, the beginning of my life in France would become almost impossible. Thank you also for your encouragement in my learning French and for the past three happy years.

I am also grateful to all my lab mates and for all their helps, support and friendship. I would especially like to thank Sophie Larmy and Odile Ribet for their helps in my experimental works. Many thanks to Alain Billard and David Mercs for their kind suggestions in my articles. Thank Salim Lamri for his help in my French.

I would like to thank Madam Valerie Demange and Valeri Brien in Nancy for their kind helps in TEM analysis.

I would like to thank my friends in Université de Technologie de

Belfort–Montbéliard (UTBM): Wei Gao, Chao Zhang, Ga Zhang, Xueping Guo, Hui Li, Sihao Deng, Sibo Yang, zhiming Zhang, Nannan Zhang and others. Thank you very much for the friendship and the good time that I have enjoyed with you.

I could not have lasted all these years without the friendship and company of my friends in the faraway east. They have been a source of entertainment and support. I would like to thank Yong Ye, my best friend for his always support in my research work. Chenglong, Liu, Haiwei Chang, Shoumou, Miao, my pre-roommates, thanks for helping me to look for the electronic source and the discussion in my dissertation.

This thesis was made possible by the support of the Laboratoire d'Etudes et de Recherches sur les Matériaux, les Procédés et les Surfaces Université de Technologie de Belfort–Montbéliard (LERMPS) and State Key Laboratory of Materials Modification Dalian University of Technology. Special thanks to them. This thesis work was financially supported by the "Communauté d'Agglomération du Pays de Montbéliard (CAPM)" which is gratefully acknowledged.

Abstract

Elaboration of Nano-composite Coatings using Sputtering Processes with Application to the Substitution of Electrolytic Cr Coating

Zhiguo ZHANG

This research focuses on the synthesis and characterization of CrN based multilayer coatings for the replacement of electrolytic chrome. The studied materials include chromium nitrides coatings, Cr-Zr-N ternary multiple phase and multilayer coatings and Si added CrN/ZrN multilayer coatings. The main objective of this thesis is to deposit the controllable coating structure and properties based on a magnetron sputtering technology so that the coating performance can be optimized to satisfy the replacement of Cr in industry scale. Coating structures are characterized by various techniques such as glow discharge optical spectrometer (GDOS), X-ray diffraction (XRD), scanning electron microscope (SEM), transmission electron microscope (TEM). The mechanical, tribological and corrosion properties of the deposited coatings are evaluated using nanoindentation, scratch test, pin-on-disk, dynamic polarization techniques respectively.

The first study is related to chromium nitride coatings with controllable structure. The hysteresis curve and target voltage versus nitrogen flow rate curve are used to predict the phase evolution of chromium nitride. Optical emission spectroscopy (OES) analysis for various RF biases reveals that the increased substrate bias leads the nitrogen content to decrease. The second study is concentrated on Cr-Zr-N system. Solid solution CrN(Zr) coatings and nanoscale multilayer CrN/ZrN coatings with bilayer thickness (Λ) ranging from 11.7 to 66.7 nm are prepared. CrN(Zr) coatings show a maximum hardness value of approximately 24 GPa while CrN/ZrN multilayers present constant hardness of 29 GPa. In corrosion tests, these coatings show good chemical inert and very low corrosion current densities. To enhance the performance of CrN/ZrN multilayers, a further effort to add Si into CrN/ZrN multilayer is carried out. The deposited CrSiN/ZrN multilayer coatings with Λ from 13.4 nm to 86.9 nm have nanocrystalline/amorphous structure (nc-CrSiN/a-ZrN). They demonstrate elevated corrosion potentials in comparison with the single layers. On the other hand, CrN/ZrSiN multilayers with Λ from 11 nm to 153 nm form nanocrystalline/amorphous period structure (nc-CrN/a-ZrSiN). This multilayer structure shows a good combination of high hardness from ZrSiN and good toughness from CrN. The addition of Si into ZrN individual layer has been shown to be an efficient way to inhibit pitting corrosion.

Key words: Magnetron sputtering; Multilayer; Mechanical, tribological and corrosion properties; CrN; Cr-Zr-N; CrSiN/ZrN; CrN/ZrSiN

Résumé

Élaboration de dépôts nano-composés par pulvérisation cathodique magnétron pour la substitution du chrome électrolytique

Zhiguo ZHANG

Cette thèse concerne l'élaboration et la caractérisation de multicouches à base de CrN pour le remplacement du chrome électrolytique. L'objectif principal est d'élaborer des revêtements, dont les propriétés (structurales, mécaniques, tribologiques etc.) sont contrôlables par pulvérisation cathodique magnétron. Les structures des dépôts sont caractérisées par diverses techniques telles que la Spectroscopie à Décharge Luminescente (SDL), la Diffraction de Rayons X (DRX), la Microscopie Electronique à Balayage (MEB), la Microscopie Electronique à Transmission (MET). Les propriétés mécaniques, tribologiques et de corrosion des dépôts sont évaluées en utilisant respectivement un nano-indentateur, des tests de rayure et de pion-disque et des mesures de polarisation dynamique.

La première étude concerne la synthèse du nitrure de chrome. Les courbes de la tension de la décharge et de la pression totale en fonction du débit d'azote injecté sont utilisées pour prévoir la phase d'obtention du nitrure de chrome. L'analyse optique par spectroscopie d'émission (OES) a permis de corréler le taux d'azote dans les revêtements avec la tension de polarisation du substrat.

La deuxième étude concerne le système Cr-Zr-N. Dans un premier temps, le zirconium est introduit en solution solide dans CrN pour former CrN(Zr). Des multicouches CrN/ZrN à l'échelle nanométrique sont ensuite élaborés avec des périodicités comprises entre 11.7 et 66.7 nm. Concernant la dureté des revêtements, on a montré que CrN(Zr) présente un maximum de dureté de 240 GPa à 1,5 at.% de Zr. Par ailleurs, les multicouches CrN/ZrN présentent une valeur de dureté constante de 29 GPa. Les essais de corrosion réalisés sur ses dépôts ont montré une bonne stabilité chimique des revêtements et de faibles densités de courant.

Du silicium est ensuite ajouté au système multicouche CrN/ZrN. Les revêtements multicouche CrSiN/ZrN et CrN/ZrSiN avec des périodicités différentes sont synthétisés et forment des structures nanocristalline/amorphe. Une amélioration de la tenue à la corrosion pour le système CrSiN/ZrN est observée comparée aux monocouches CrN et ZrSiN De même, la structure CrN/ZrSiN permet une bonne combinaison de la dureté élevée de ZrSiN et de l'excellente résilience de CrN. De plus, on constate que l'addition du silicium dans ZrN empêche de manière efficace la corrosion de type piquration.

Mots clés : Pulvérisation cathodique magnétron ; Multicouche ; Propriétés mécanique, tribologique et de corrosion ; CrN ; Cr-Zr-N ; CrSiN/ZrN ; CrN/ZrSiN

Table of Contents

ACKNMMOWLEDGMENTS ..... **I**

ABSTRACT ..... **III**

RÉSUMÉ ..... **IV**

TABLE OF CONTENTS ..... **V**

LISTS OF TABLES ..... **IX**

LISTS OF FIGURES ..... **X**

CHAPTER 1 . INTRODUCTION **1**

1.1. ELECTROPLATED CHROMIUM 1
1.2. ELECTROPLATED CHROME APPLICATIONS 2
1.3. THE DRIVING FORCES OF CHROMIUM REPLACEMENT 4
1.3.1 General environmental impacts *4*
1.3.2 Regulations *5*
1.3.3 Industrial today *6*
1.4. ALTERNATIVE TECHNIQUES 7
1.4.1 Options of alternatives *7*
1.4.2 PVD coatings as replacements of electroplated chrome *9*
1.4.3 PVD coating applications for replacing electroplated chrome *12*
1.5. MAGNETRON SPUTTERED NANOCOMPOSITE AND MULTILAYER COATINGS 15
1.5.1 Magnetron sputtering techniques *15*
1.5.2 Multilayer configuration *15*
1.5.3 Multilayer conceptual design *17*
1.5.4 Design nanoscale multilayer coatings *18*
1.6. OBJECTIVE OF THIS THESIS 22
1.7. ORGANIZATION OF THIS THESIS 23

CHAPTER 2 . EXPERIMENTAL DETAILS **25**

2.1. THIN FILM SYNTHESIS 25
2.1.1 Magnetron sputtering *25*
2.1.2 Coating deposition system *27*
2.1.3 Magnetron sputtering deposition parameters *29*
2.2. DETERMINATION OF THE BASIC DEPOSITION PARAMETERS 31
2.3. CHARACTERIZATION 33
2.3.1 Coating chemical composition *33*
2.3.2 X-ray diffraction for structure analysis *34*
2.3.3 Scanning Electron Microscopy *35*
2.3.4 Transmission electron microscopy *36*
2.3.5 Nanoindentation hardness and modulus *36*
2.3.6 Scratch adhesion testing *39*

2.3.7 Tribology test *41*
2.3.8 Potentiodynamic polarization *43*

CHAPTER 3 . DEPOSITION AND OPTIMIZATION OF MONOLAYER CRN COATINGS ..45

3.1 INTRODUCTION 45
3.2 COATING PREPARATIONS 47
3.3 INFLUENCE OF N_2 FLOW RATES ON STRUCTURES AND PROPERTIES OF CHROMIUM NITRIDE COATINGS 48
3.3.1 The hysteresis effects and deposition parameter selection *48*
3.3.2 Coating compositions and microstructures *51*
3.3.3 Mechanical properties *55*
3.3.4 Tribological properties *58*
3.3.5 Corrosion properties *61*
3.4 INFLUENCE OF RF BIAS ON STRUCTURES AND PROPERTIES OF CRN COATINGS 64
3.4.1 Plasma characteristics by OES on film synthesis *64*
3.4.2 Correlations between OES signals and coating compositions and structures *70*
3.4.3 Coating morphologies *74*
3.4.4 Coating mechanical properties *77*
3.4.5 Coating tribological properties *79*
3.4.6 Coating corrosion properties *81*
3.5 SUMMARY 84

CHAPTER 4 . STRUCTURE AND PROPERTIES OF MONOLAYER AND MULTILAYER COATINGS OF CR-ZR-N 85

4.1 INTRODUCTION 85
4.2 COATING PREPARATIONS 87
4.3 ZR MODIFIED CRN COATINGS 89
4.3.1 Coating compositions and structure characteristics *89*
4.3.2 Coating mechanical properties *94*
4.3.3 Coating tribological properties *97*
4.3.4 Coating corrosion properties *100*
4.4 CRN/ZRN MULTILAYER COATINGS 105
4.4.1 Coating microstructure characteristics *105*
4.4.2 Coating mechanical properties *111*
4.4.3 Coating tribological properties *114*
4.4.4 Coating corrosion properties *117*
4.5 SUMMARY 122

CHAPTER 5 . INFLUENCE OF SI ADDITIONS ON MICROSTRUCTURES AND PROPERTIES OF CRN/ZRN COATINGS 125

5.1 INTRODUCTION 125
5.2 COATING PREPARATIONS 126
5.3 CRSIN/ZRN MULTILAYER COATINGS 128
5.3.1 Coating structure characteristics *128*
5.3.2 CrSiN/ZrN mechanical properties *132*

5.3.3 CrSiN/ZrN tribological properties *135*
5.3.4 CrSiN/ZrN coating corrosion properties *138*
5.4 CRN/ZRSIN MULTILAYER COATINGS 141
5.4.1 Structures of ZrSiN and CrN/ZrSiN multilayer coatings *141*
5.4.2 Mechanical properties of CrN/ZrSiN coatings *148*
5.4.3 CrN/ZrSiN tribological properties *154*
5.4.4 CrN/ZrSiN corrosion properties *156*
5.5 SUMMARY 159

CONCLUSION AND PERSPECTIVE 161

CONCLUSION 161
PERSPECTIVES 163

REFERENCE 167

Lists of Tables

Table 1.1. Desirable characteristics of electroplated chrome. 1

Table 1.2. General chrome coating requirements in aerocraft industry [7]. 4

Table 1.3. Industrially applied PVD coatings for wear resistance to replace hard chrome [17]. 10

Table 1.4. An overview of present and future PVD applications [27, 28]. 13

Table 1.5. Nanoscale multilayer PVD coatings for various applications [47, 50-57]. 20

Table 3.1.Deposition parameters under a constant argon flow rate of 10 sccm and the main characteristics of the Cr-N coatings. 50

Table 3.2. Selected optical emission spectroscopy lines. The data was referenced to National Institute of Standards and Technology (NIST) atomic spectra database and Ref [9,11]. 66

Table 3.3. Effects of RF substrate bias voltage on the discharge characteristics. The corresponding target current I = 1.5 A, Jdc = 17.7 mA/cm2, and the total pressure p = 0.27 Pa. 67

Table 4.1. Element content and nitrogen to metal ratios of x=N/(Cr+Zr) in the Cr-Zr-N coatings as a function of the numbers of Zr coupons. 89

Table 4.2. The corrosion current (Icorr), and corrosion potentials (Ecorr) determined from the polarization curves in a 3.5 % NaCl solution for the CrN(Zr) coatings with different Zr contents. 102

Table 4.3. Main parameters of deposited CrN/ZrN coatings. 105

Table 4.4. Interplanar distances for CrN, ZrN and the CrN/ZrN multilayer with Λ=11.7 nm. 109

Table 5.1. Main parameters of deposited CrSiN/ZrN coatings. 128

Table 5.2. Main parameters of deposited coatings 144

Lists of Figures

Fig. 1.1 Worldwide Chrome Plating Demand, Functional vs. Decorative, 2003 [5]. 2

Fig. 1.2. Chrome plating process and its problems [8]. 4

Fig. 1.3. Hard chrome plating alternatives, shown by major process types [12]. 8

Fig. 1.4 Estimated global use of PVD coatings in friction applications [17]. 10

Fig. 1.5 Hard materials for nanocomposite coatings in the bond triangle and changes in properties with the change in chemical bonding superlattice PVD coatings for various applications [49]. 18

Fig. 1.6 Designed superlattice PVD coatings for various applications [47, 50-57]. 19

Fig. 1.7 Coated mild steel samples after salt spray tests: (a) CrN/NbN directly on substrate after 24h; (b) chromium electroplated after 200h; (c) sample with CrN/NbN coating containing Nb barrier layer after 300h [58]. 21

Fig. 2.1 The principle of magnetron sputtering. 26

Fig. 2.2 Photographs of the reactive magnetron sputtering system (a) sputtering system; (b) inside the deposition chamber. 28

Fig. 2.3 The characteristics of sputtering discharge with different Ar flow rates. 32

Fig. 2.4 Scanning electron fracture micrograph of Cr deposited with various deposition parameters 33

(a) Target current: 1.25 A and Ar flow: 15 sccm; (b) Target current: 1.5 A and Ar flow: 15 sccm; (c) Target current: 1.25 A and Ar flow: 10 sccm; (d) Target current: 1.5 A and Ar flow: 10 sccm. 33

Fig. 2.5 A diagram of inside components in the MTS-XP nano-indentation tester [79].....37

Fig. 2.6 The diagram of Oliver and Pharr method to determine nano-hardness [80, 81].....37

Fig. 2.7 Schematic of the scratch test method [83]. 40

Fig. 2.8 Schematic of pin-on-disk setup where F is the normal force applied on the ball, r is the ball diameter, R is the radius of the wear track and w is the rotational speed of the disk.....41

Fig. 2.9 Three possible situations for different wear resistance of ball and flat disk specimens; (a) only the ball wears, (b) only the disk wears, and (c) both ball and disk wears 42

Fig. 3.1. Cr-N binary phase diagram [91]. 46

Fig. 3.2 Evolution of the total deposition pressure and sputtering voltage as a function of the introduced nitrogen flow rates. 49

Fig. 3.3 GDOES quantitative elemental depth profile of chromium nitride coatings deposited at Ar flow rate of 10 sccm and N2 flow of 5 sccm. 52

Fig. 3.4 XRD spectra of chromium nitride thin films deposited with different nitrogen flow rates. 53

Fig. 3.5 Scanning electron micrographs of fracture cross-sections.....54

Fig. 3.6 Hardness and elastic modulus at various nitrogen flow rates. 56

Fig. 3.7 Optical micrographs of the scratch tracks (a) Cr at the end of the track; (b) Conformal cracks for chromium nitride deposited at 12 sccm N_2 with L_{c1}=2.6 N; (c) Chipping failure for chromium nitride deposited at 12 sccm $N_2$with L_{c2}=15.1 N. 57

Fig. 3.8 Two typical curves of friction coefficients vs. sliding distance.....59

Fig. 3.9 Friction coefficients at different nitrogen flow rates. 60

Fig. 3.10 Optical, 3D photographs and profiles of the wear track after the pin-on-disc tests (a) Cr; (b) Cr_2N; (c) CrN coatings; (d) typical ball wear scar. 61

Fig. 3.11 Polarization curves for different chromium nitride coatings and AISI 304 substrates (N_i corresponds to the nitrogen flow rate; i.e. N2: 2 sccm N_2). 62

Fig. 3.12 E_{corr} and I_{corr} of chrome nitrides as a function of nitrogen flow rate. 63

Fig. 3.13 coating surface morphologies after corrosion test. 64

Fig. 3.14 Typical OES spectrum at near-target-zone. 66

Fig. 3.15 Various OES signals as functions of the substrate bias at “near-target-zone”. 69

Fig. 3.16 Various OES signals as functions of the substrate bias at “near-substrate-zone”. 69

Fig. 3.17 Evolution of coating compositions vs. substrate bias |Ub|. 70

Fig. 3.18 A good agreement between OES signal intensity ratio I(N2)/I(Cr) and composition ratio C(N)/C(Cr). 72

Fig. 3.19 Evolution of CrN coating structures vs. substrate bias $|U_b|$ in XRD patterns. 73

Fig. 3.20 Evolution of CrN cross-section morphology vs. substrate bias $|U_b|$. 74

Fig. 3.21 The top-view AFM images of CrN coatings deposited at different substrate bias $|U_b|$: ..75
0 V; (b) 20 V; (c) 60 V; (d) 100 V; (e) 150 V; (f) 200 V. 75

Fig. 3.22 Nano hardness and elastic modulus as functions of the substrate bias $|U_b|$. 78

Fig. 3.23 Optical images of scratch test results of chromium nitride coatings and their critical load with different substrate bias. 79

Fig. 3.24 Friction coefficients and wear rates during the sliding wear for chromium nitride coatings with different substrate biases. 80

Fig. 3.25 wear track after the pin-on-disk tests for the coating deposited with a substrate bias – 100 V. (a) wear track on the coating; (b) wear track on the counter ball. 81

Fig. 3.26 Dynamic polarization curves for chromium nitride coatings with different substrate bias (i.e. B20: $|U_b|$=20 V). 82

Fig. 3.27 Corrosion potential (E_{corr}) and corrosion current density (I_{corr}) as a function of substrate bias. 82

Fig. 3.28 SEM surface images of chromium nitride after dynamic polarization tests; (a) 0 V; (b) -20 V; (c) -60 V; (d) -100 V; (e) -150 V; (f) -200 V. 83

Fig. 4.1. Schema of a simple alloying method to add Zr into CrN. 88

Fig. 4.2. Typical GDOES elemental depth profile of CrN(Zr) coatings deposited with Zr content of 3.2 at. %. 90

Fig. 4.3 X-ray diffraction patterns of Zr modified CrN coatings with different Zr contents ..... 92 (S: substrate). 92

Fig. 4.4 SEM showing fracture cross-section from Si substrate and surface morphologies from AISI304 substrate (a) CrN coating; (b) CrN(Zr) coating with Zr content of 2.1 at. %; (c) Surface defects of CrN(Zr) coatings; (d) magnification image of typical defects. 93

Fig. 4.5. Nanohardness (H) and Young's modulus (E) of CrN(Zr) coatings as a function of the atomic percentage of Zr in the coatings. 95

Fig. 4.6. Determine adhesive critical load (L_{c2}) and coating spalling out critical load (L_{c3}) using a combination of friction force, acoustic emission signal and optical image. 96

Fig. 4.7. Adhesive critical load (L_{c2}) and critical load (L_{c3}) as a function of Zr content in Zr modified CrN coatings. 97

Fig. 4.8. Evolution of the friction coefficient during 500 m against a 100Cr6 ball 6 mm in diameter and a 2 N applied load for: 1.5 at. % CrN(Zr) coating. 98

Fig. 4.9. Friction coefficients and wear rates during the sliding wear for CrN(Zr) coatings with different Zr content. 99

Fig. 4.10. Wear track of CrN(Zr) coatings: (a) 1.5 at.% Zr coating with complete adhesive wear, coating surface did not damage; (b) 3.2 at.% Zr coating has a combination of abrasive and adhesive wear, a few damages of coating surface can be observed. 100

Fig. 4.11. Potentiodynamic polarization curve for CrN(Zr) coatings with different Zr contents and the substrate. 101

Fig. 4.12. SEM micrographs of corroded spots on Zr modified CrN coatings (a) corrosion on the points of small pores and defects, (b) magnification of corrosion on the defect point. 103

Fig. 4.13. Schematic diagram outlining the corrosion mechanisms of macroparticles and growth defects (reaction 2 and 3) and the galvanic corrosion of the substrate associated with these (reaction 4) and other defects such as droplet shrinkage pinholes (reaction 1) [145]. 104

Fig. 4.14. Low angle XRD diffraction spectra of CrN/ZrN with 180 layers. The calculated bilayer thickness from the ratio of thickness vs. layer is about 11.7 nm. 106

Fig. 4.15. X-ray diffraction patterns of CrN, ZrN and CrN/ZrN multilayer (S: substrate). 107

Fig. 4.16. Cross-sectional TEM bright field image and corresponding electron diffraction pattern for the CrN/ZrN multilayer with Λ=11.7 nm. 108

Fig. 4.17. SEM cross-sectional images on Si substrates (a) CrN; (b) ZrN; (c) CrN/ZrN Λ=66.7 nm; (d) CrN/ZrN Λ=35.0 nm; (e) CrN/ZrN Λ=11.7 nm (180 layers). 110

Fig. 4.18. Nanohardness (H) and Elastic Modulus (E) of CrN/ZrN multilayer coatings as a function of bilayer thickness. 112

Fig. 4.19. Cohesive critical load (L_{c1}) and adhesive critical load (L_{c2}) of CrN/ZrN as a function of bilayer thickness. 113

Fig. 4.20. The friction coefficients of CrN, ZrN and CrN/ZrN multilayer coatings with bilayer thickness of 66.7 nm and 11.7 nm as a function of sliding times. 115

Fig. 4.21. Friction coefficients and wear rates of the as-deposited CrN/ZrN multilayer coatings. 115

Fig. 4.22. Surface and 3D morphologies after pin-on-disk tests for CrN/ZrN multilayer coatings: (a),(c) Λ=66.7 nm ; (b),(d) Λ=11.7 nm. 117

Fig. 4.23. Potentiodynamic polarization curve for CrN, ZrN and CrN/ZrN multilayer coatings with different bilayer thicknesses. 118

Fig. 4.24. Variations of I_{corr} and E_{corr} of single CrN, ZrN and CrN/ZrN multilayers with different bilayer thickness in 3.5% NaCl solution. 120

Fig. 4.25. SEM micrographs of corroded spots on CrN/ZrN multilayer coatings 121

(a) Λ =66.7 nm ,(b) Λ =11.7 nm. 121

Fig. 5.1. X-ray diffraction patterns of CrSiN, ZrN and CrSiN/ZrN multilayers. 129

Fig. 5.2. Cross-sectional TEM images for CrSiN/ZrN coating with bilayer thickness of 13.4 nm. (a) bright field image; (b) electron diffraction image. 131

Fig. 5.3. SEM cross-sectional images on Si substrates (a) CrSiN; (b) CrSiN/ZrN Λ=86.9 nm; (c) CrSiN/ZrN Λ=44.4 nm; (e) CrSiN/ZrN Λ=13.4 nm. 132

Fig. 5.4. Nanohardness (H) and Elastic Modulus (E) of CrSiN/ZrN multilayer coatings as a function of bilayer thickness. 133

Fig. 5.5. Cohesive critical load (L_{c1}) and adhesive critical load (L_{c2}) as a function of CrSiN/ZrN multilayer coating bilayer thickness..... 134

Fig. 5.6. The friction coefficients of CrSiN, ZrN and CrSiN/ZrN multilayer coatings with bilayer thickness of 86.9 nm and 13.4 nm as a function of sliding distance. 136

Fig. 5.7. Friction coefficients and wear rates of as-deposited coatings..... 137

Fig. 5.8. Coating surface 3D morphologies and counter ball optical images after pin-on-disk tests for CrSiN/ZrN multilayer coatings: (a) Λ=86.9 nm ; (b) Λ=13.4 nm 137

Fig. 5.9. Potentiodynamic polarization curve for CrSiN, ZrN and CrSiN/ZrN multilayer coatings with different bilayer thicknesses..... 139

Fig. 5.10. Variations of I_{corr} and E_{corr} of single CrSiN, ZrN and CrSiN/ZrN multilayers with different bilayer thickness in 3.5% NaCl solution. 140

Fig. 5.11. SEM micrographs of corroded spots after corrosion test (a) CrSiN single layer; (b) CrSiN/ZrN with Λ =13.4 nm. 141

Fig. 5.12. X-ray diffraction patterns of single layer CrN and ZrSiN coatings. 142

Fig. 5.13. FTIR absorption spectra for different bilayer thickness CrN/ZrSiN coatings. 143

Fig. 5.14. X-ray diffraction patterns of multilayer CrN/ZrSiN coatings with bilayer thickness from 11- 153 nm. 145

Fig. 5.15. Cross-sectional TEM images for CrN/ZrSiN coating with bilayer thickness of 11 nm. (a) bright field image; (b) electron diffraction; (c)dark field image. 146

Fig. 5.16. SEM cross-sectional images of as-deposited coatings: (a) CrN; (b) ZrSiN; (c) CrN/ZrSiN, Λ=153 nm; (d) CrN/ZrSiN, Λ=83 nm; (e) CrN/ZrSiN, Λ=42 nm; (f) CrN/ZrSiN, Λ=11 nm. 147

Fig. 5.17. Hardness as a function of displacement of indentation.....148

Fig. 5.18. Nano-indentation Hardness (H) and Elastic Modulus (E) of CrN/ZrSiN multilayer coatings as a function of bilayer thickness.....149

Fig. 5.19. Typical load-displacement curve of CrN, ZrSiN and CrN/ZrSiN multilayer coatings. 150

Fig. 5.20. SEM micrographs at a high load of 10 N Vickers indentation for (a) CrN; (b) ZrSiN; (c) CrN/ZrSiN Λ = 153 nm.....151

Fig. 5.21. Cohesive critical load (Lc1) and adhesive critical load (Lc2) as a function of CrN/ZrSiN bilayer thickness.....154

Fig. 5.22. Friction coefficients and wear rates of as-deposited CrN/ZrSiN multilayer coatings. .156

Fig. 5.23. Potentiodynamic polarization curve for CrN, ZrSiN and CrN/ZrSiN multilayer coatings with different bilayer thicknesses.....157

Fig. 5.24. Variations of Icorr and Ecorr of single CrN, ZrSiN and CrN/ZrSiN multilayers with different bilayer thickness in 3.5% NaCl solution. 158

Fig. 5.25. SEM micrographs of corroded spots on CrN/ZrSiN multilayer coatings (a) ZrSiN; (b) CrN/ZrSiN Λ =11 nm. 159

Chapter 1. Introduction

1.1. Electroplated chromium

In the last century, electroplated chrome has become a commercially available product, and the related industries have developed into a huge, well organized, sophisticated and financial business [1]. Chrome plating is actually an electrolytic process, which utilizes a chromic acid-based electrolyte to deposit metal on compounds. Because of the intrinsic property of chromium and the mature technology, electroplated chromium coatings exhibit a number of desirable characteristics, which are shown in Table 1.1.

Table 1.1. Desirable characteristics of electroplated chrome.

➢ Lubricious	➢ Inexpensive
➢ Easily applied	➢ Various thickness
➢ Not flammable	➢ Provides versatile colors
➢ Stable for weeks or months	➢ Conductive
➢ Resilient (repairs itself)	➢ Flexible
➢ Re-hydrated after baking	➢ Easy to strip
➢ Coats in recesses	➢ Single tank
➢ Inexpensive equipments	➢ Durable
➢ Prevents oxyde formation	➢ Provides adhesion for organics
➢ Slow corrosion in prototypic tests (e.g. salt spray, roof top, etc.)	➢ Help prevent corrosion of painted surfaces (e.g. creep)

In addition to an excellent hardness, electroplating chrome products generally provide good adhesion to most substrates, bright appearance with no discoloration, low friction coefficient and high service temperature capability as well as high resistance to corrosive environments. Electroplated chromium has a unique “self-healing” property in most cases [2]. When they are damaged, the chromium compounds would repassivate the exposed areas. Moreover, chrome plating is low-cost, easily applied technique. The combinations of performance and economy make it one of the greatest competing products for aerospace, oil and gas industry,

heavy equipments and a wide range of general applications in industry as well as decorative metallic coatings. However, traditional hexavalent chromium plating technology suffers from some quality and process problems [3]. The low cathode efficiency in hexavalent chrome plating results in a major issue: poor coverage in low current density areas and excessive build-up in high current density areas. The abilities of such coatings to cover the part uniformly are very small. In some cases, the part is over-plated and even it affects the final dimensions. In order to reduce this effect, auxiliary anodes are usually used to provide more uniform coatings of the part. The other drawbacks of chrome plating technique are that it is easy for embrittlement and very difficult to be used in barrel plating. The most important drawbacks is that it is a unfriendly process to worker and environment due to the toxic hexavalent chromium ion source [4].

1.2. Electroplated chrome applications

The most common hexavalent chrome solutions can be roughly divided into two parts: decoration and function, which is based more upon their applications than the chemistry of the processes [5]. However, in the overall hexavalent chrome plating market, the hard or functional chrome plating possesses much less percentage, only less than a quarter of the overall hexavalent chrome plating (See Fig. 1.1).

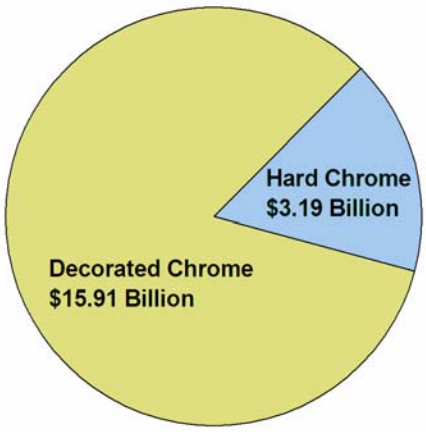

Fig. 1.1 Worldwide Chrome Plating Demand, Functional vs. Decorative, 2003 [5].

Decorative electroplated chrome provides a durable coating with a substantial amount of abrasive wear and chemical corrosion resistance as well as visual appearance. It is usually deposited on substrates such as steel, aluminum, plastic, copper alloys and zinc-die castings with a thickness range of 0.5-30 μm. Thinner deposits are very porous and only offer the minimal physical property whereas thicker deposits tend to be dull and form visible cracks. However, the final performance of these deposits depends upon the chromium deposit interacting in synergy with their underlying deposit, typically nickel. Their functions, besides aesthetic appearance, include thermal control and energy saving in buildings and applications to surfaces, which are subjected to abrasive wear and high temperature. Common items of decorative chromium include appliances, jewelry, plastic knobs, hardware hand tools, office furniture and automotive trims.

Functional chromium plating (or hard chromium) often offers protective electroplated layers against wear, abrasive and corrosion to machinery, components and tools. Substrates on which chromium is plated include both hardened and unhardened steels, tool steels, stainless steels, cast irons and aluminum. Common applications of functional chromium plating are aerocraft land gear, hydraulic cylinders and rods, crankshafts, printing plates/rolls, pistons for internal combustion engines, molds for plastic and fiberglass part manufacturing, and cutting tools. Specially, it is also used to rebuild worn parts such as rolls, molding dies, cylinder liners, and crankshafts. A general property requirement in aerocraft industry is shown in Table 1.2 [6]. In this case, the coating is mainly built as a wear resistant layer. However, because the types of components and applications for which hard chrome is currently used are various, the requirements are versatile. In some cases, the chrome plating process has to be designed together with the other manufacture process. For example, during engineering practice, chrome plating has been integrated with today's diesel-engine design and manufacturing. Through combining its low cost, high performance and ease of manufacturing, functional chrome plating has been approved to be a relatively cost-efficient and effective solution [7].

Table 1.2. General chrome coating requirements in aerocraft industry [7].

Properties	Requirements	Comments
Thickness	3μm to 150μm	Thin dense, Rebuilding
Hardness	600-1000HV	Wear/corrosion resistance
Porosity	< 2%	Prevent gas/fluid leakage
Fatigue	Low	Add life time
Embrittlement	Low	Increase strength
Finish capability	Fine	Minimize seal wear
Process control	Good	Decrease costs
Fit with depot and field repair	Yes	Decrease costs

1.3. The driving forces of chromium replacement

1.3.1 General environmental impacts

Health and environment are the initial impetus for considering alternatives to electroplated chrome [8]. It should be noted that for electroplated chromium coatings, the problem is not with the chromium itself because it is almost inert, but with the hexavalent chrome plating process, which uses a chromic acid solution, releasing into the air in the form of a fine mist and producing a large volume of chrome contaminated toxic waste. Moreover, it has been long known that hexavalent chrome is carcinogenic and causes a wide array of medical problems such as deviated septa and skin and lung irritation [5, 8]. Fig. 1.2 presents the general plating chrome process and its deduced health and environmental problems.

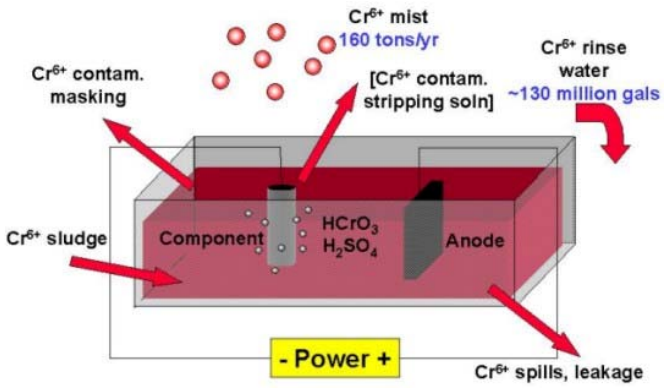

Fig. 1.2. Chrome plating process and its problems [8].

The main problems encountered with its use are listed as follows:

- The plating process liberates high volumes of Cr^{6+} mist, which must be ducted away from the plating tank in order to prevent its emission into the air.
- Chrome tank wastes are toxic, as are Cr^{6+} -contaminated maskants.
- The process produces high volumes of Cr^{6+} -contaminated rinse water.
- Personnel are exposed to Cr^{6+} mist in the plating facility, but it has been found that uncontrolled exposures also occur during demasking.

1.3.2 Regulations

In order to reduce the threat of the deteriorative environment, many efforts have been made worldwide to restrict the industrial pollutions. As quoted in the Environmental Safety and Occupational Health (ESOH) issues of the USA, the regulations of industrial processes and products associated with chemical and heavy metals are tightening globally. In response to growing health concerns, in the USA, the Environmental Protection Agency (EPA) began to regulate chromium emissions into the air. The permissible exposure limit (PEL) for hexavalent chromium in the workplace is now 0.1 mg/m^3. A proposal for change made by the Occupational Safety and Health Administration (OSHA) to 5 $\mu g/m^3$ exists, with the ultimate goal of being a total ban [9]. EPA is now advancing a new round of pending air emission controls for small and medium-sized plating operations. Their final regulation was published in 2008. The implication of current hazard classification trend is that even metals traditionally viewed by the commercial community as “green” alternatives to chromates or electrolytic hard chrome (EHC) are now being targeted as potential carcinogens and candidates for further regulations or eliminations.

In the European Union (EU), ELV (End-of-life Vehicle), WEEE (Waste Electrical and Electronic Equipment) & RoHS (Restriction of Hazardous Substances) directives regulate the management of waste from a wide range of electrical and electronic consumer appliances as well as professional equipments [10]. ELV directive restricts the use of lead, mercury, cadmium and hexavalent chromium on

new vehicles. WEEE directive requires that producer should be responsible for taking back and recycling electrical and electronic equipment while RoHS directive regulates the substitution of various heavy metals (lead, mercury, cadmium, and hexavalent chromium) and brominated flame-retardants in new electrical and electronic equipment put on the market after 1 July 2006. There are also other EU and international agreements and initiatives relevant for metal finishing as well, which include the Stockolm Convention on Persistent Organic Pollutants (POPS), the Convention on Long Range Transboundary Air pollution (LRTAP) and Heavy Metal protocols. Actions under these agreements restrict materials such as perfluoro-alkalis as key ingredients in chemical fume suppressants used to control Cr^{6+} emission in the workplace and ambient air [11]. In Asia, Japan and some other countries have comprehensive bans on hexavalent chromium under considerations. And there appears to be no near-term legislative initiatives. It is worthwhile to note that as more products are produced and sold globally, the location regulation is becoming global effects on the chrome plating industry. Their cost is expected to be high, which pushes the chrome plating economic viability to the limits.

1.3.3 Industrial today

Although the continuous increasing costs in chrome plating industry associated with waste treatments, air pollution controls, operator personal protections and immigrations of plating shop are bringing the alternatives into a much more economically competitive situation. The situation that a sudden changeover is expected from chrome plating to one of those alternatives has failed to happen. On the contrary, the chrome plating industry has largely stabilized in the past few years. The plating shops did quite well and some even were thriving in many cases. Many customers have little or no interest in giving up chrome. In Europe and North America, it is ambivalent while Asia is largely unconcerned with regulating chrome plating.

1.4. Alternative techniques

The replacement of chromium by other coating technologies has been under way during the last decades. However, either in business or in engineering, replacing a widely used coating technology such as hard chrome is not a single replacement in technology but rather several alternatives suited for different applications. In practical operations, it depends upon many factors but ultimately comes down to individual decisions based on economics. Only when electroplated chrome fails to provide adequate performance but has to afford the very high waste-disposal costs will the arguments of replacements increase. This is the case especially when the alternatives can provide more stringent customer performance requirements.

1.4.1 Options of alternatives

Many industrial initiatives and efforts have been undertaken to find suitable alternatives and eliminate hexavalent plate chrome from the coating market. A number of coating techniques have emerged that may pose the competitors to hexavalent plate chrome (in case of hard chrome, see Fig. 1.3). While some remain still in the developing stage, the others have already begun to take market share away from chrome plating. However, as the chrome plating industry has been developed for almost 70 years and the wide range of applications corresponds to different requirements, it is quiet difficult to replace it by any single technology or coating. From the view-point of environmental, performance and costs, three major groups of technologies can be thought to be perspective replacements for electroplated chrome [12]. These alternatives include the bath technologies in terms of trivalent chrome and the dry, clean coating methods: thermal spraying and Physical Vapor Deposition (PVD).

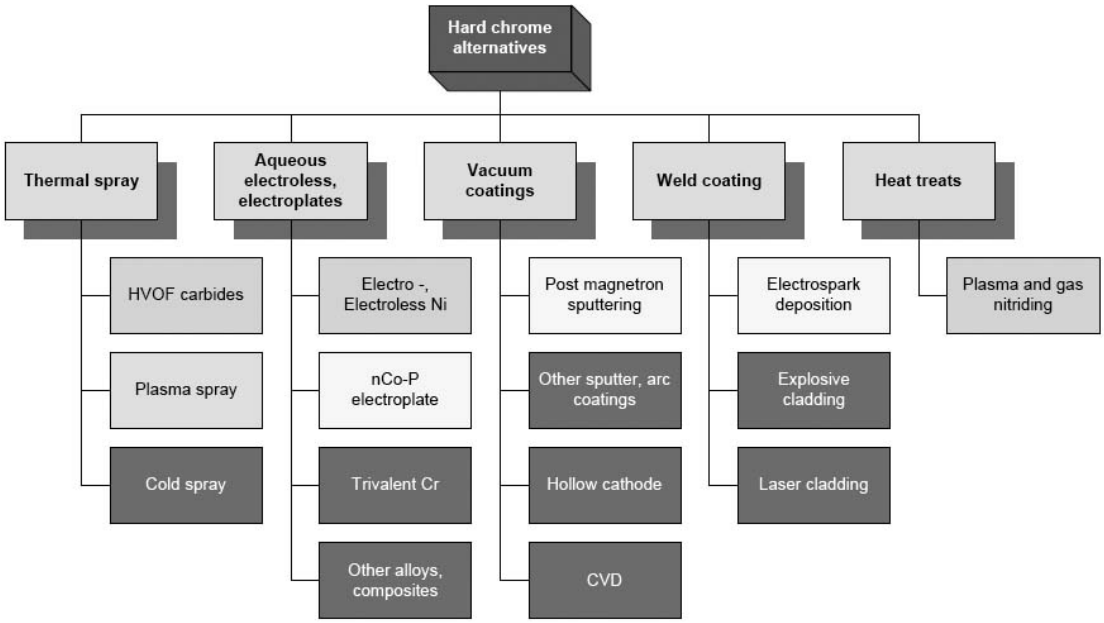

Fig. 1.3. Hard chrome plating alternatives, shown by major process types [12].

Among the various electroplated chrome techniques, trivalent chrome is a new electroplating technique, which uses a similar processing method to hexavalent chrome but reduces most of the hazards. Such a technique has already made serious inroads in decorative chrome market [13]. The prospects of trivalent chrome are becoming viable due to the recent improvements. In the long run, a hard trivalent chrome coating may provide an alternative to hexavalent chrome that would allow chrome platers to maintain their client set in critical wear coating market. To date, however, there is no satisfactory hard trivalent chrome process, but a number of companies and consortia have initiated development efforts. The detailed examples of using trivalent chromium technology to replace electroplated hexavalent chrome can be found in Ref. [2, 14].

The form of thermal spraying that represents the greatest commercial threat to hard chrome is HVOF (High Velocity Oxygen Fuel) thermal spray technology, which is a dry process that can use a wide range of coating materials, allowing coating customized for individual tasks. HVOF sprays are used in aerospace applications on landing gears, flap actuators, shafts and hydraulic parts. These coatings can be made

very thick, so that they can be applied for rebuild. HVOF coatings applied in wear applications provide superior performance in most situations when compared to electroplated chrome [3, 6, 15, 16]. The weakness of thermal spraying is generally considered to be the cost. Another important limitation of all forms of thermal spraying is that they are “line-of-sight” technologies.

PVD, another dry and clean technology, is technically competitive and environmentally friendly to replace electroplated chrome [1, 5, 12, 17, 18]. In the last decades PVD technology has developed rapidly into a mature, profitable and increasingly important sector of the surface engineering industry. The advanced PVD coating system can be used to deposit compound coatings with composition so far that can not obtained by any other conventional plating process. They produce high quality coating material savings and environmental benefits in numerous applications, e.g. through increasing service life, reducing emissions and energy consumption, improving recycle abilities. In PVD coating fields, different deposition technologies are available, but when it comes to replace chrome plating, only two of them are commonly considered to be the potential alternatives [12]. These are magnetron sputtering process and electron beam PVD (EBPVD). However, in comparison with EBPVD, the coating quality deposited by magnetron sputtering is more convenient to be controlled so that most of the developed coating systems are based on magnetron sputtering technology.

1.4.2 PVD coatings as replacements of electroplated chrome

A number of PVD coatings have been developed during the last decades. However, only very special coatings have been engineered for specific applications at present. Fig. 1.4 shows an overview of the most frequently used PVD coatings in friction applications [17]. These coatings are considered to be the potential replacements of hard chrome. The main coating properties can be found in Table 1.3.

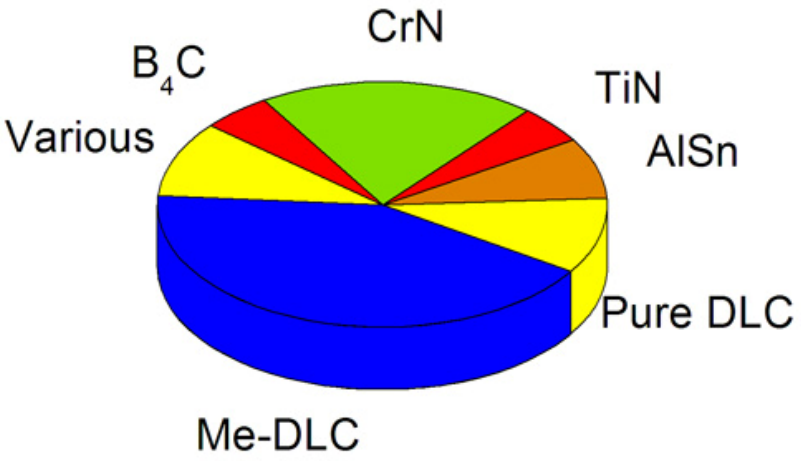

Fig. 1.4 Estimated global use of PVD coatings in friction applications [17].

Table 1.3. Industrially applied PVD coatings for wear resistance to replace hard chrome [17].

	CrN	**Me-C:H**	**a-C (pure DLC)**	**MoS_2**	**TiN**
Deposition temperature (°C)	150 -300	150 -250	150 -500	150 -250	150 -450
Hardness (HV 0.05)	1200-2200	800-2200	3000-7000	300-600	2000-2500
Internal stress (GPa/μm)	0.1 -1	0.1 -1.5	2 -6	0.1 -1	1 -2
Thickness (μm)	1 -50	1 -5	1 -2	1 -10	1 -6
Friction coefficient	0.4 -0.6	0.1 -0.2	0.02 -0.1	0.1 -0.2	0.5 -0.7
Maximum temperature (°C)	750	350	450	400	450
Abrasive wear	-	+	+++	++	-
Adhesive wear	-	+++	+++	-	-
Corrosion	+++	+	+++	+	+
Practical problems	low	low	adhesive flaking	low shear	
Industrial experience	++++	++++	-	+	++++

TiN

TiN is the most well-known PVD coating. It has been used extensively in the fields of cutting tools. Due to its long term experience and availability, it is sometimes used as a replacement for hard chrome. However, the properties of TiN need to be optimized in order to satisfy the specific applications.

MoS_2

Molybdenum Disulfide shows excellent tribological properties, especially their very low friction coefficients. A major drawback of pure MoS_2 is that the resistance to shear stress is relatively low. Therefore, coatings of pure MoS_2 are used in combination with other hard coatings like TiAlN in order to produce specific sliding wear properties [19, 20].

DLC and Me-DLC

Due to intense research and development efforts, DLC (Diamond-Like Carbon) coatings are suitable for many industrial applications and at present they are widely commercially available. The increasing interest for DLC coatings is that it is substantially harder than any other conventional hard coating. Moreover, it can provide excellent tribological characteristics similarly to those of graphite. It is therefore the best surface material currently available for high-precision, high-stressed mechanical compounds. They are also considered the most potential replacements for electroplated chrome.

To improve the quality of DLC and especially to satisfy specific applications, other chemical elements can be incorporated into the pure DLC coatings to tailor their chemical compositions and vary their properties. The addition of the other elements can improve the elasticity, toughness, adhesion and conductivity. The doped elements including Ti, Cr, W, and Si have been proposed as an alternative way to reduce the residual stress while maintaining fairly constant hardness values of DLC [21]. For example, a 1% to 2% of Si doping DLC coating is very suitable for improving the adhesion of DLC film to substrates, which can reduce the internal stress while

maintaining the surface hardness of DLC films [22]. The Cr doped DLC coatings deposited by unbalanced dual-magnetron sputtering in pulsed DC mode, present some admirable properties, for example, very smooth surface, high hardness of nearly 27 GPa, good adhesion and low average friction coefficient of 0.08 [23]. In short, these kinds of Me-DLC coatings provide great flexibilities to tailor the pure DLC coating properties.

Another important development in DLC thin film field is that DLC coatings have been successfully deposited on flexible polymers and rubber-like flexible substrates. These new coatings possess a compositionally graded microstructure and thus have a gradient of mechanical properties. In addition to these coatings that hold promise for application on flexible or polymeric substrates, new forms of carbon films with structure and properties close to those of DLC are now being concerned. They show excellent mechanical and tribological properties. For instance, the coatings produced under magnetron sputtering with a fullerene like microstructure present very hard and resilient as well as exceptional ability of elastic recovery [24].

CrN

Chromium nitride has been widely used as an anti-wear coating [25, 26]. Though having generally a higher friction coefficient than hard chromium, a great advantage of CrN is that the internal stresses are very low. Coatings with thicknesses over 40 μm are routinely used in automotive applications. They are the initial replacements for electroplated chrome.

1.4.3 PVD coating applications for replacing electroplated chrome

A number of PVD coating applications have been introduced in the last ten years. The range of PVD coatings has been extended from the initial cutting tool fields to various industries, such as aviation, astronavigation and automobile products. A simple overview is given in Table 1.4 [27, 28].

Table 1.4. An overview of present and future PVD applications [27, 28].

Segment	Substrate	PVD Coating	Thickness	Remark
Present applications				
	Automotive Piston ring	CrN	40 µm	Routinely used by one of the largest Japanese piston ring supplier
	Drive rods	CrN	3 µm	Used for highly loaded race engines (Formula 1)
	Turbo shafts	Cr/W -C:H	3 µm	For passenger car turbo engines
	Fuel injection	Cr/W -C:H DLC	3 µm	Diesel fuel pumps Fuel injectors Applied already on over 50% of the world production
	Valve train	Cr/W -C:H	3 µm	Tappet, Camshaft Starting to be applied on large scale
	Drive train	B_4C Cr/W -C:H		sun gears
Various	Forming tools	CrN, CrCN	2 µm	
	Moulds, dies	CrN, CrCN and Cr-C:H	2 µm	
Future applications				
Hydraulics	Pistons	CrN based multilayers	up to 20 µm	Improved field life expectancy
Cutlery	Cutting tools	CrN based multilayers	up to 3 µm	Use expected in cutting, slitting, medical fields
Aeronautical	various	various		
Textile	various	CrN based multilayers	up to 10 µm	replacement of Ni/Cr

The main applications of PVD coatings at present are in the automotive segments. The important applications can be found in the fuel injection train in the near future. The new generation train with very high pressure fuel injection systems has become economically feasible by using PVD coatings. This is due to the considerable advantages of PVD coatings that the coating can be made relatively thin. PVD coating thickness requirements are only a few µm, allowance for coating thickness is not required, and the part to be coated can be remained at a final dimension. The other examples of PVD coating application are shafts of the turbo

compressor. In the other way, considerable growth for PVD is expected in the automotive industry. Applications at present are mainly for high performance car parts. This will certainly have spin-offs for the normal car productions. The continuous driving force for improved energy efficiency, weight reduction, noise reduction, and volume reduction are all favorable conditions to increase the use of low friction PVD coatings.

The applications which are growing rapidly rely on the fields of punching and forming tools. In these cases, the goals are to increase the lifetime of the forming tool and to improve the surface quality of the final formed part. Coatings that provide high hardness and reduce mechanical forces by adding a lubricative coating during elaborations are possible by PVD techniques. In this case, combinations of hard and soft coatings are often proposed, mainly CrN, Cr-C-N and Me-C:H. The other important applications are in moulds, dies and extrusion forms. Initially, CrN coating was widely used in these areas, but the use is now shifting to combinations of hard and soft coatings.

In addition to the above applications for PVD coatings, a number of research reports has shown the possibilities of using PVD coatings to replace electroplated chrome [2, 4, 17, 29-31]. However, like any new technique under development, the weakness of PVD coatings is its high cost. However, this problem is progressively solved because of the development of PVD coating equipments and technologies. It has been reported that the average cost price reduction of around 7% per year on top of normal inflation has been achieved in the last decennium. It is also expected that the price reduction corrected for inflation will remain at a level of 10 % per year for the near future by further technological development [17]. Also, the superior properties provided by PVD coatings are attracting a great attention.

1.5. Magnetron sputtered nanocomposite and multilayer coatings

1.5.1 Magnetron sputtering techniques

As mentioned above, magnetron sputtering technology is one of the most available PVD techniques. The process relies on a suitable ion bombardment of a target material by noble gas ions (normally Ar^+) in glow discharge plasma [32-38]. As well as being considered a dry and clean technology among the various coating techniques, magnetron sputtering provides a combination of advantages like no others. Firstly, it is a method of production which is economically efficient generating the thinnest and most uniform coating possible. The second is that it is a dry process at low temperature and low pressure, which forms an indestructible bond between coating and substrate so that a good adhesion is available. Moreover, it offers great versatilities as compared to the other coatings. Since being a cold transfer, it can be used for the deposition of a wide range of materials on any type of substrates, including metals, ceramics and temperature sensitive plastic materials. In addition, the process is a controllable deposition that can be repeated in a automatic mode. In summary, this solution is adopted to create more resistant, higher, cleaner and more economical materials not only affecting the current industry but everyday life. Magnetron sputtering techniques is also considered to be the best choice to deposit multilayer coatings. Due to its advantages, magnetron sputtering can be thought as a perspective technology to replace chromium plating technique in industrial scale.

1.5.2 Multilayer configuration

The concept of multilayer coatings comes from the composite coating. A composite coating usually consists of two or more phases combined either as different layers (multilayer) or as a homogeneous isotropic mixture of different phases (multiphase). The aims of such coatings are to combine the desired properties from different components as well as the creation of new properties generated by the combination of suitable materials. Since the thin, high quality coatings are usually

deposited by PVD processes, multilayer coatings can easily be obtained by the alternate use of different material sources (magnetron, evaporator, etc.) in PVD deposition processes [39]. However, comparably, as described above, magnetron sputtering is the most suitable technology for the deposits of multilayer coatings due to the facts that they are easily controllable.

When dealing with multilayer coatings two cases have to be distinguished. Classical multiple layer coatings and nanoscale multilayer coatings. Classical multilayer or multiple layer coatings consist of a few (usually 3 to 20) different layers with a total thickness of 1-8 μm. These types of multilayer coatings are commercially available since the early 1970s. They usually consist of one or more Al_2O_3 or TiAlN layers between the layers of TiN, TiC, and TiCN [40]. The Al_2O_3 or TiAlN layers are introduced to obtain a better high temperature oxidation resistance. Additionally, multilayer coatings consisting of materials with different mechanical properties may show a better performance since crack propagation may be deflected or stopped at the interfaces or in the more ductile material [41]. The tribological behavior of the classical single layer coatings TiN and TiC can be improved by building multilayer structures. The classical examples of TiN/TiC, TiN/TiC/BN, TiN/TiC/B_4C, TiN/TiVC/AlN, and TiN/TiC/SiC multilayers with structures composed of 3-150 layers have exhibited a lower coefficient of friction as well as a longer edge life when they are applied on cutting tools in comparison with the single layer TiN and TiC coatings [42].

Multilayer coatings with layer thickness in the nanometer range have shown extremely high hardness, which makes them very attractive for tribological applications. They are so called nanoscale multilayers. For PVD single layered coatings applied in practice, they are relatively thin when compared to electroplated coatings and normally have a columnar structure. Failure of these coatings may occur owing to coating porosity, micro-cracking, residual stress and thermal expansion mismatch. These disadvantages can be overcome by growing a multilayer with relatively short period. As a result, the obtained high hardness and toughness enhance the resistance to fatigue owing to crack deflection at the multiple interfaces within the

coatings. The bilayer in the nanoscale results in the significant reduction of residual stress. Furthermore, the multilayer structure provides an additional capability to perform an increased corrosion resistance. Multilayer coating usually uses a graded interlayer to enhance adhesion, which can be attributed to the formation of diffused interfaces to ensure good bond to the substrate. Another advantage of multilayer coating is that the composite coating principle applied in multilayer designs can provide a convenient way to predict coating property, which means that the combination properties such as high hardness, high toughness and low friction can be obtained simultaneously to satisfy various applications through selecting different coating partner systems [43-47]. In these cases, the multilayer deposition process is usually carried out by magnetron sputtering or reactive magnetron sputtering technology. The multilayer structure can be controlled by switching on and off the different sources, shuttering the different sources or a suitable sample movement in front of different sources. Appropriate multi-target geometry and controlled target poisoning conditions by optimized pumping conditions can lead the deposition conditions to be similar in their economy to the deposition of typical monolithically grown binary hard coatings. In this way, the deposit coating offers one of the best categories, in particular high hardness, wear and corrosion resistance and low friction as well as high temperature performance.

1.5.3 Multilayer conceptual design

Multilayer conceptions provide the flexibilities to design coating for specified applications. In designing the proper multilayer system, the task can generally be divided into two areas: structure design and functional design. Multilayer structure can be tailored by changing the geometry and morphology of the grains, grain size, growth orientations, thickness of the individual layer and the constitution and size of the interfacial boundary layer. In this way, the changed structural components ensure the coating to enhance toughness and hardness so as to produce more wear resistant coatings [45, 48]. On the other hand, the functional design aspect includes the

selection of the material which depends on the type of bonding (i.e., metallic, ionic, and covalent), the thermal, physical and mechanical properties of the material. Fig. 1.5 presents the bonding triangle and property changes with the differences in chemical bonding [49]. The hardness of a material is often dictated by its intrinsic properties. Materials with a high degree of covalent bonding are generally harder than those with metallic or ionic bonding because of their generally shorter bond lengths. However, chemical stability and inertness usually occurred as a result of ionic bonding whereas metallic bonds yield better adhesion and toughness. Unfortunately, few materials consist of entirely one type of bonding. Mixed bonding can be tailored to create a film that exhibits properties indicative of each type of bonding. For example: with the increasing demands on material systems, high hardness and good toughness are required. This can be realized by a combination of covalent bonding and metallic bonding. It is important to mention that chemical inertness between the coating and the machined material in various environments is also required and should not be ignored.

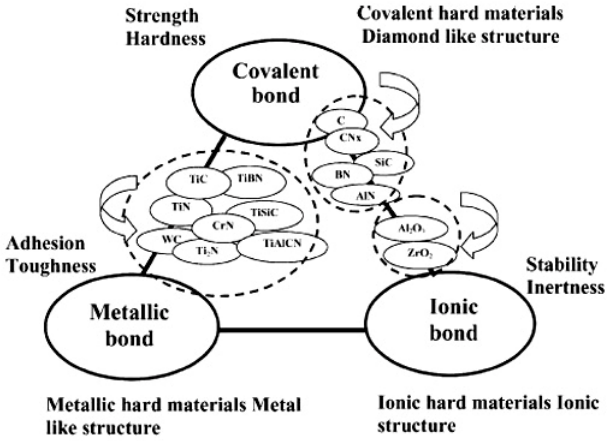

Fig. 1.5 Hard materials for nanocomposite coatings in the bond triangle and changes in properties with the change in chemical bonding PVD coatings for various applications [49].

1.5.4 Design nanoscale multilayer coatings

Fig. 1.6 presents the various designed nanoscale PVD coatings dedicated to high temperature performance: TiAlCrN/TiAlYN, to tribological applications: TiAlN/VN,

Cr/C and to combination of wear and corrosion resistance: CrN/NbN, respectively. These coatings present a bright future as shown in Table 1.5. The works have been done by Materials Analysis & Research Services of Sheffield Hallam University, UK. The figures and the related properties data are from their website and their recent publications [47, 50-57].

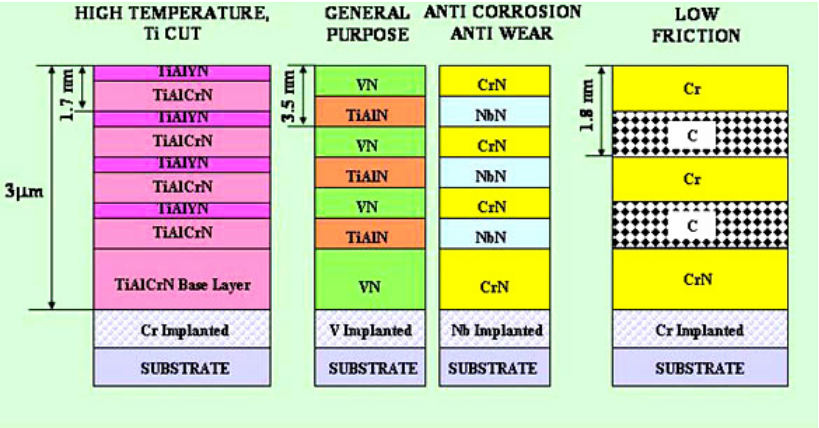

Fig. 1.6 Designed superlattice PVD coatings for various applications [47, 50-57].

The abrasion resistant TiAlN is combined with VN to achieve a wear resistant low friction coefficient superlattice coating. The lower friction coefficient is expected to result from the formation of V_2O_5 at asperity contacts during sliding wear, a lubricious oxide due to its low melting point [47]. TiAlN/VN is characterized with exceptionally low friction coefficient, μ=0.4 and exceptionally high wear resistance in dry sliding conditions. This kind of coating is generally the purposed coating for high speed steels, cutting tools and high alloy steels.

Another typical example for reducing wear is Cr/C superlattice coating. The idea to design Cr/C coatings is originated from the excellent tribological properties of carbon and carbon based materials, particularly their low friction coefficients. The lower value of 0.11 is achieved when the coating is deposited on mirror polished high speed steel (HSS) sample and is retained during sliding in dry air, oil and in water environment. The coefficient of friction increases to 0.2 when the C/Cr is deposited on the PVD coated HSS substrates. When this coating is deposited on top of PVD hard coatings (TiAlCrYN), it reduces the wear coefficient by almost a factor of 3 and

shows exceptionally low wear rate in the range of 10^{-17} m^2N^{-1} when deposited on polished steel substrate.

Table 1.5. Nanoscale multilayer PVD coatings for various applications [47, 50-57].

Coating	Application
TiAlCrYN Pseudo/Superlattice Coating	• Dry High Speed Cutting of Die Steels • Dry Cutting of Aluminum and Titanium alloys • Aluminum injection moulding and forging • Machining of Inconel. Tools for hot forming operations. • Injection mould coating in abrasive applications. • Protection of aerospace Ti alloys
TiAlN/VN Superlattice Coating	• Low friction wear resistant general purpose coating for high speed steels • Cutting tools for Inconel, Hastelloy and High Alloy Steels
CrN/NbN Superlattice Coating	• Corrosion and Wear Resistant applications • Textile Parts, Petrochemical Applications • Moulds for plastic manufacturing • Hydraulic applications • Wood cutting and paper industries • Protection of steam turbine blades • Cutting knives, surgical blades • Protection of machine parts in food processing machines • Low temperature, (< 250 ^{0}C) process available • Potential replacement of electroplated hard chrome
C/Cr Multilayer/ Superlattice Coating	• Low friction (μ= 0.15-0.2) solid lubricant coating • Automotive components • Precision Parts, Bearings. • Topcoat on all the above mentioned coatings to further reduce the friction • Cutting of special high Co containing Ni based aerospace alloys • Food industry, Surgical instruments, implants. • Low temperature (< 250 ^{0}C) process available

In the case of the designed multilayer coatings, TiAlYN/TiAlCrN multilayer coatings are designed to achieve good high temperature performance. The role of Y on the tribological properties at elevated temperatures as well as on the oxidation resistance has been extensively studied and reported [58]. High-temperature

pin-on-disc tests show that in contrast to other PVD coatings, the Y containing "superlattice" shows a decrease of friction coefficient from 0.95 to 0.56 and wear depth values from 2.8 to 0.9 mm when the environment temperature increases from room temperature to 900 ℃. Due to its exceptional thermal stability, the TiAlCrN/TiAlYN coating find successful applications in protecting moulds for glass industry, extrusion dies and forging dies for production of turbine blades.

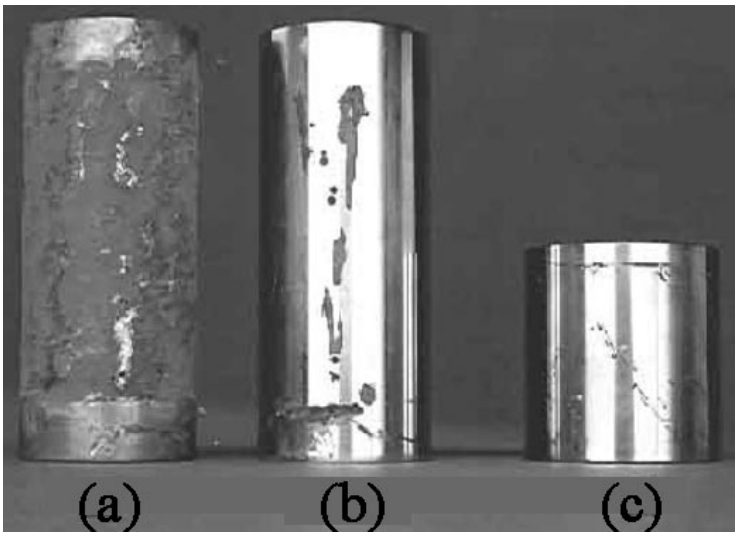

Fig. 1.7 Coated mild steel samples after salt spray tests: (a) CrN/NbN directly on substrate after 24h; (b) chromium electroplated after 200h; (c) sample with CrN/NbN coating containing Nb barrier layer after 300h [58].

For the applications of corrosion resistance, the efforts on CrN/NbN superlattice coatings have been carried out. The purpose of these efforts is to find a replacement of electroplated hard Cr [52, 54, 56, 59]. This particular combination utilizes superhardness with the exceptional chemical stability; therefore a superior corrosion resistance has been achieved due to the presence of Nb. The potentiodynamic polarization tests in acetic acid/sodium acetate buffer solution show their outstanding corrosion current densities in the range of 10^{-9} Acm^{-2} and no pitting up to potentials of +800 mV is demonstrated by the smooth CrN/NbN coating deposited on Nb^{+} ion etched substrate [56]. Fig. 1.7 shows a corrosion resistance comparison among hard Cr, CrN/NbN directly deposited on mild steel and CrN/NbN with a Nb barrier layer

during salt spray tests [47]. The results clearly show that the CrN/NbN coating with a Nb barrier layer has the best corrosion resistance. This combination of tenfold improves wear resistance with excellent corrosion performance of the CrN/NbN superlattice coating, which allows hard Cr to be successfully replaced in case of hydraulic ball valves, wood cutting tools, and various wear parts in petrochemical, automotive and textile industries [60].

1.6. Objective of this thesis

As it has been introduced above, there has been increasing pressure on electroplated chrome industry and considerable progress in the areas of nanoscale multilayer PVD coatings. Thanks to their advantages, the PVD coating has become an attractive electrolytic chrome replacement. However, as to the PVD multilayer coatings themselves, there are still numbers of open questions associated with the concept of coating design, coating synthesis, and the interpretation of material characterizations. Nowadays, the new nanocomposite coatings have attracted much attention [39, 45, 46, 61-65]. How to benefit from the advanced nanocomposite concept for designing the multilayer coating structure and properties is one of the emphases of this thesis.

In the past, our laboratory has developed a series of experiments in the fabrication and characterization of hard coating such as CrN, CrSiN [66-70]. The subject of this thesis is also expected to extend these works to novel approaches, such as the fabrication of new nano-structured multilayer materials.

This thesis is one of the sub-projects included in the large project <Substitution au Chromage Electrolytique>, which aims at finding the good solutions to substitute electroplated chrome using an environment friendly technique in industrial scale. In this thesis, the aim is to find the reliable coating systems based on the magnetron technology so that the coating performance can satisfy the replacements of versatile electroplated chrome applications. The following aspects are important for advancement in the field of multilayer coatings for the purpose of replacing

electroplated chrome and they also represent the objectives of this work.

- Developing a reliable PVD process control technique to ensure coating final performance.
- Optimizing CrN coating deposition parameters for a specified coating deposition system.
- Looking for a good multilayer partner with CrN to ensure the enhanced performance in comparison with CrN.
- Designing a novel multilayer coating system with good performance and investigating the evolution of coating properties as a function of the key deposition parameters.
- Investigating the influence of an additional element on multilayer coating structure and properties. It is preferred to combine the advantages of nanocomposite and multilayer designing concept so that further improvement of multilayer coating performance can be expected.

1.7. Organization of this thesis

This thesis is divided into 6 chapters: Chapter 2 describes the experimental equipments and characterized techniques. Chapter 3 presents the process of synthesizing and optimizing CrN coatings. The aim of this chapter is to control the deposition parameters for the stoichiometric Cr, Cr_2N and CrN coatings. To reach this purpose, the hysteresis effects of nitrogen partial are studied and an optical emission spectra (OES) technique is applied to investigate the detailed reactive process. Chapter 4 shows the investigations in Cr-Zr-N system. The selection of ZrN as a partner of CrN is based on a previous work. The ternary CrN(Zr) coating and CrN/ZrN multilayer coating are produced. The influence of the main deposition parameter: bilayer thickness or (deposition period) on coating structure and properties is studied. Chapter 5 studies the influence of Si additions into multilayer coatings on coating final performance. Two kinds of multilayer systems: nc-CrSiN/a-ZrN and nc-CrN/a-ZrSiN are developed.

Chapter 2． Experimental details

The intent of this chapter is to describe the main experimental details of this research work. Much of this chapter is devoted to the description of the magnetron sputtering system and the details of the reactive sputtering process. Additionally, various other techniques and equipments utilized for the characterization of the coatings are also presented.

2.1. Thin film synthesis

2.1.1 Magnetron sputtering

As one of the most important forms of physical vapor deposition (PVD) techniques,, magnetron sputtering is commonly used in areas such as microelectronics, magnetic films and solar control, machine tools and mechanical components. In comparison with the other techniques, magnetron sputtering offers many attractive advantages: (1) the high adhesive strength between coating and substrate; (2) the well defined microstructural and compositional control of the layers; and (3) the low deposition temperature, which is compatible with either the microstructure of tempering and annealing metallic substrates, or the use of sensitive materials like glasses and plastics. In addition, sputtering coatings usually have compressive stress, which may reduce cracking although low stress is favorable to adhesion [35-37, 71].

In a conventional sputtering system, the coating material is inserted into the vacuum chamber as a sputtering cathode under the form of a metal plate. After the chamber has been emptied, the gasses usually argon or its mixtures are introduced with a pressure range of 1-10 mTorr. Under this pressure, a negative potential U is applied to the sputtering target, which firstly repels the stray electrons inside the system. These free electrons collide with Ar atoms and ionize them into ion state, meanwhile they produce more electrons. It is the initial stage of sputtering target discharge. The visual glow near the target is due to the de-excitation of the atoms and

ions. This collection of ions, electron and neutrals is so called plasma. As more collisions occur and more ions and electron are generated, the plasma becomes self-sustaining. When the ions strike the target through the accelerating electron fields exerted on the cathode, the target material is sputtered as a result of momentum transfer. On the other hand, they also generate secondary electrons. The sputtered materials then moved toward the opposed substrate surfaces and were finally deposited on the substrate. In the cases of magnetron sputtering, a magnet is located behind the sputtering target. It is designed to trap the emitted secondary electrons in cycloids and circulate movement in the vicinity of the target, hence increasing the ionization efficiency, which can be up to one hundred times smaller than for a conventional sputtering. This advantage allows the high deposition rates and a higher kinetic energy at the impact on the substrate to be realized because of the lower pressure. Unlike many other vacuum deposition techniques, there is no fusion of material, therefore all the metals and alloys can be deposited with efficiency and high control abilities [33]. If a reactive gas such as nitrogen, oxygen or acetylene is introduced into the chamber additionally to the process gas, the nitride or oxide coatings are deposited on the substrates. Different cathodes made of different materials can be inserted in a vacuum coating system to produce multilayer systems. A simple diagram of the principle of magnetron sputtering is presented in Fig. 2.1.

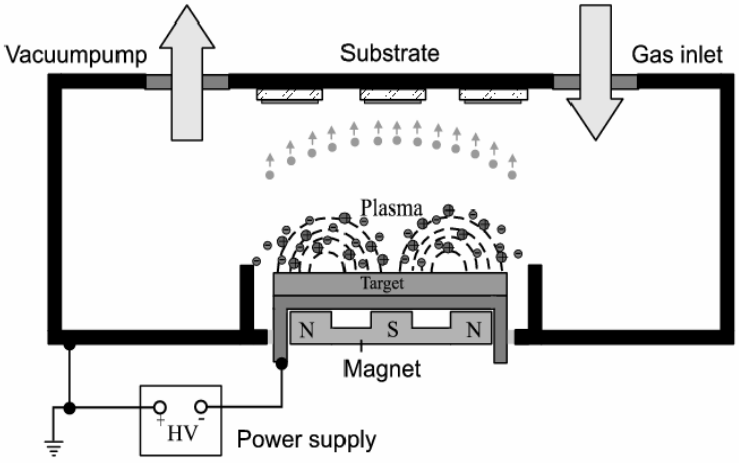

Fig. 2.1 The principle of magnetron sputtering.

The basic task in magnetron sputtering depositing thin films is to produce coatings with the prescribed physical functional properties and in a fully reproducible way. Therefore, different operating conditions are developed to enable he microstructure, phase and chemical composition of the growing films to be controllable. Among all cases, non-reactive DC or RF sputtering, reactive sputtering, argon ions-assisted sputtering, coating material ions-assisted sputtering and pulsed DC sputtering are well-developed and are now currently used in the industrial production of coatings [37]. Such techniques extend the applications of magnetron sputtering into a wider range including dielectric films and insulated coatings.

2.1.2 Coating deposition system

In this thesis, the coatings are deposited by a conventional magnetron sputtering technique using a modified Alcatel SCM 450 sputtering unit (see Fig. 2.2). As can be seen, in such system, up to three planar magnetron cathodes (Φ = 16 cm) with water-cooling system can be equipped on the base plate of the cylindrical vacuum chamber (Φ = 68 cm H = 30 cm). The cathode sputtering materials could be different so that various gradient and multilayer coatings can be synthesized. The sputtering materials are bonded to a water-cooled copper carrier, ensuring good electrical and thermal contact. A mask is used to guarantee that only one target at a time is used for deposition, which prevents the other targets from being polluted. The rotational substrate holder with water-cooling system is attached to the top cover opposite to the targets. The maximum distance between the target and the substrate is limited to 85 mm by the dimensions of the chamber while the minimum separation is approximately 30 mm where the plasma process is disrupted for a lower distance. During the deposition of multilayer coatings, the substrate holder is rotated until a position directly above the target is reached. Then it remains stationary until the desired films thickness designed by the deposition rate and time.

Various generators such as Direct current (DC), Radio Frequency (RF) and DC pulse can be connected to both targets and substrate. For DC and DC pulse, constant

current mode, constant power and constant voltage mode are available, whereas for RF, controlling the output power is more conventional. In order to keep the base pressure below 5 x 10^{-6} mbar, a turbo molecular pump system with speed of 27000 r/min is equipped. The pump speed at the pressure ranging from 10^{-4} –10^{-1} Pa is about 380 l/s. Argon, nitrogen and oxygen gases are mixed before being introduced into the reactor close to the target. They have the purity of 99.999% and are regulated with brooks and EIC mass flow controllers. The dynamic ranges are 0-50 sccm for both N_2 and O_2 and 0-100 sccm for Ar. The total pressure is monitored with EDWARD active gauge controller while a more accurate MKS gauge is also equipped to monitor the small changes of gas pressure in reactive sputtering process. In addition, a convenient computer program is applied to control the vacuum system, gas flux and water-cooling system.

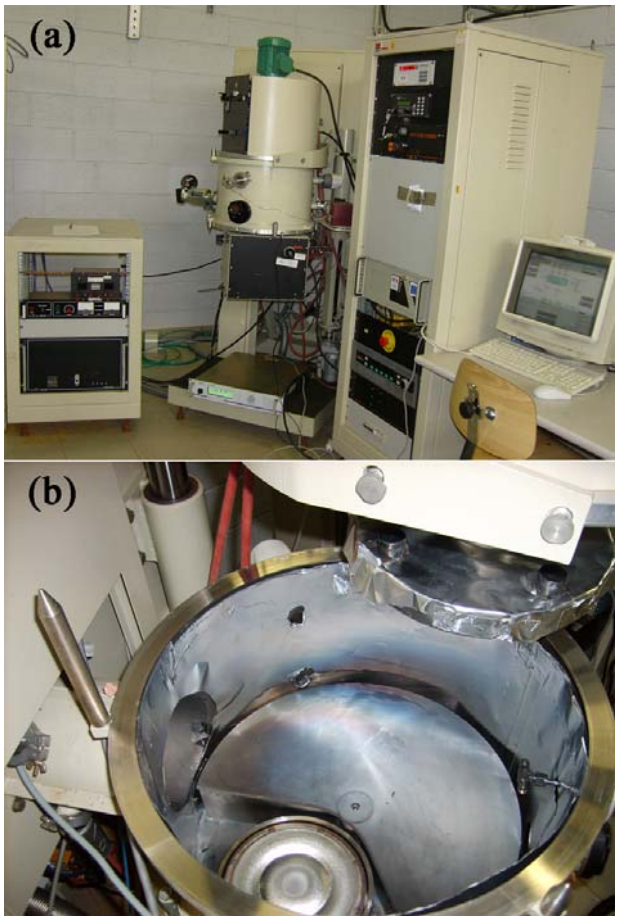

Fig. 2.2 Photographs of the reactive magnetron sputtering system (a) sputtering system; (b) inside the deposition chamber.

2.1.3 Magnetron sputtering deposition parameters

The synthesized coating properties by means of magnetron sputtering system can be controlled by adjusting the sputtering parameters. The main parameters include the total pressure, volume fraction of reactive gases, substrate bias, target power density, substrate-to-target distance, and the substrate temperature.

The sputtering current (I) determines mainly the rate of the deposition process and hence the time which remains for the arriving particles during the growth process for either surface diffusion and agglomeration on existing growth centers or nucleation with other adatoms. The applied voltage (U), however, limits the maximum energy, with which sputtered particles can escape from the target (reduced by the binding energy). Usually, the energy of the sputtered particles shows a broad distribution with a maximum between 1 eV and 10 eV. The applied voltage determines also the sputter yield, which is defined as the number of sputtered particles per incoming ion.

The total pressure (p) in the deposition chamber affects the mean free path (λ) for the sputtered material, which is proportional to 1/p. Combining with the target-substrate distance (TS) the pressure controls how many collisions occur between the particles on their way from the target to the substrate. This can influence not only the porosity and the deposition rate of the films but also the crystalline and the texture. Moreover, the ability of magnetron sputtering enables it to work on a low pressure. The low pressure in the deposition chamber enables to create a cleaner thin film. The typical working pressure range for magnetron sputtering is 0.1-1 Pa.

The substrate temperature has a strong impact on the growth behavior with respect to the crystallinity or the density of the samples. It can be adjusted between room temperature and 700 ^{o}C according to the substrate materials. However, even during sputtering without external heating the substrate temperature may rise considerably due to sputtered ion bombardment, especially during a long sputtering time for the deposition of thick films. For instance, a one-hour deposition of CrN coatings with a RF bias of 50 V in the current magnetron sputtering unit can raise the

substrate temperature nearly to 150 ^{o}C. Since the setup is only equipped with a water cooling system, the substrate temperature can keep a constant value of about 15 ^{o}C. However, in all the depositions of this thesis, the water cooling system wasn't used in order to increase the coating density. The higher deposition temperature i. e. 500 ^{o}C is impossible in the present setup due to the absence of the substrate heating equipment.

Usually substrate and target surfaces are parallel to each other during the deposition. A variation of the deposition angle (or sputtering incidence angle) can be achieved by tilting the substrate. Thereby a new preferential direction for the film growth and the potentially anisotropic films can be produced [72]. In this thesis, the substrate and target surfaces are always parallel and their distance is regulated at a constant value of 80 mm.

Via the gas mixture one can control the coating stoichiometry. For the deposition of nitride ceramic coatings, the nitrogen flux (F_{N2}) is usually the parameter that varies whereas the desired total pressure is kept constant by the regulation of the Ar flow rate or a simple method is applied to keep the Ar flow rate as constant.

The low energy (< 200 eV) ion bombardment method during deposition is often used to affect the nucleation and growth kinetics of growing films, which eventually can alter the microstructure, texture, surface morphology, internal stress, adhesion, hardness, mechanical, physical and chemical properties of the coatings. An optimum level of low energy ion bombardment can result in an increase in the mobility of surface species that may improve surface roughness, increase film density and reduce the number of pinhole defects. The ion bombardment is essential especially when deposition is carried out at low temperature when there is little or no surface and bulk diffusion. If the ion bombardment energy is too low or too high, the advantage of ion bombardment can not be demonstrated evidently. Usually, bombardment by high-energy ion beyond a critical threshold results in irradiation induced defects and the damage of the film. Obviously, if the energy is too low, little effect is observed. In addition to the ion energy, the ion flux can also play an important role in the influence of film properties. One can obtain the beneficial effects without ion bombardment induced defects by reducing the ion energy while increasing the ion flux. The

energetic particles can come from the self-energy of the depositing atoms, from the flux of energetic neutrals that result when using heavy target material, and most importantly, from the flux of gas ions that were accelerated by a substrate bias. Furthermore, the bias form and voltage have an important influence on the ultimate coating properties [35, 73-75].

2.2. Determination of the basic deposition parameters

As discussed above, there are many deposition parameters that affect the final coating performance. For a specified coating system, all these parameters need to be optimized in order to get the best coating performance. The amount of work is huge as there are complex interactions between these parameters. And for different coating systems, the optimized deposition parameters are different. Therefore, in this thesis, only the widely investigated parameters are concerned in detail, e.g. the nitrogen partial, the substrate bias in the single coating system and the bilayer period for multilayer coatings. As to the other deposition parameters, a simple method based on Cr coating deposition is used to determine their values. The goal is fixed to obtain a maximum deposition rate with high efficiency and a fine coating structure for the deposition of Cr. To avoid the damage of the cathode sputtered particles on substrate, the target-to-substrate distance was regulated at the nearly maximum value of 80 mm. The substrate temperature, however, was maintained at room temperature at the beginning of the deposition due to the limitations of this setup. In all cases, the cooling system was not used in order to increase the substrate surface atomic diffusion. The maximum deposition temperature is about 150 ℃ as discussed above. The power of sputtering target was regulated as a constant current mode. Hence, the discharge characteristics of magnetron target (Cr) vs. the deposition pressure can be obtained and the results are shown in Fig. 2.3. In this case, no substrate bias was applied.

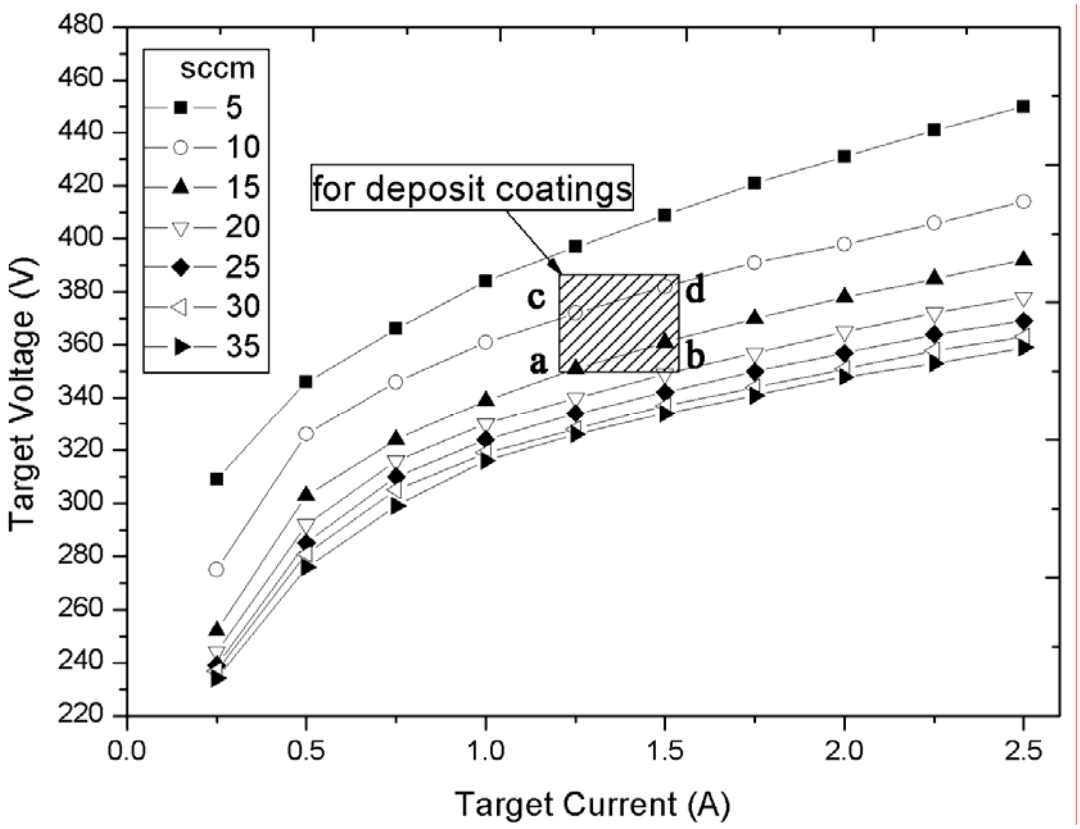

Fig. 2.3 The characteristics of sputtering discharge with different Ar flow rates.

From this figure, it can be seen that at different Ar flow rates, increasing the target current I, the target voltage U initially increases dramatically, then changes into a slight increment. The current range between 1.25 A and 1.5 A is considered to be a transition zone. Below this range, the target current is insufficient to support sputtered particle energy. Above this range, the increase of target current show little effect on improving sputtered particle energy. On the other hand, with increasing Ar gas flow rates, the target voltage vs. current curves firstly decrease rapidly, and then show a very small change. The transition point corresponds to the Ar flow rate ranging from 10 to 15 sccm. Therefore, the shadow zone as shown in Figure. 2.3 can be considered a zone to obtain the high efficiency for depositing Cr coating. These four points are then chosen to deposit pure Cr coatings on glass substrate. The cross-sectional images of the obtained Cr coatings are shown in Fig. 2.4.

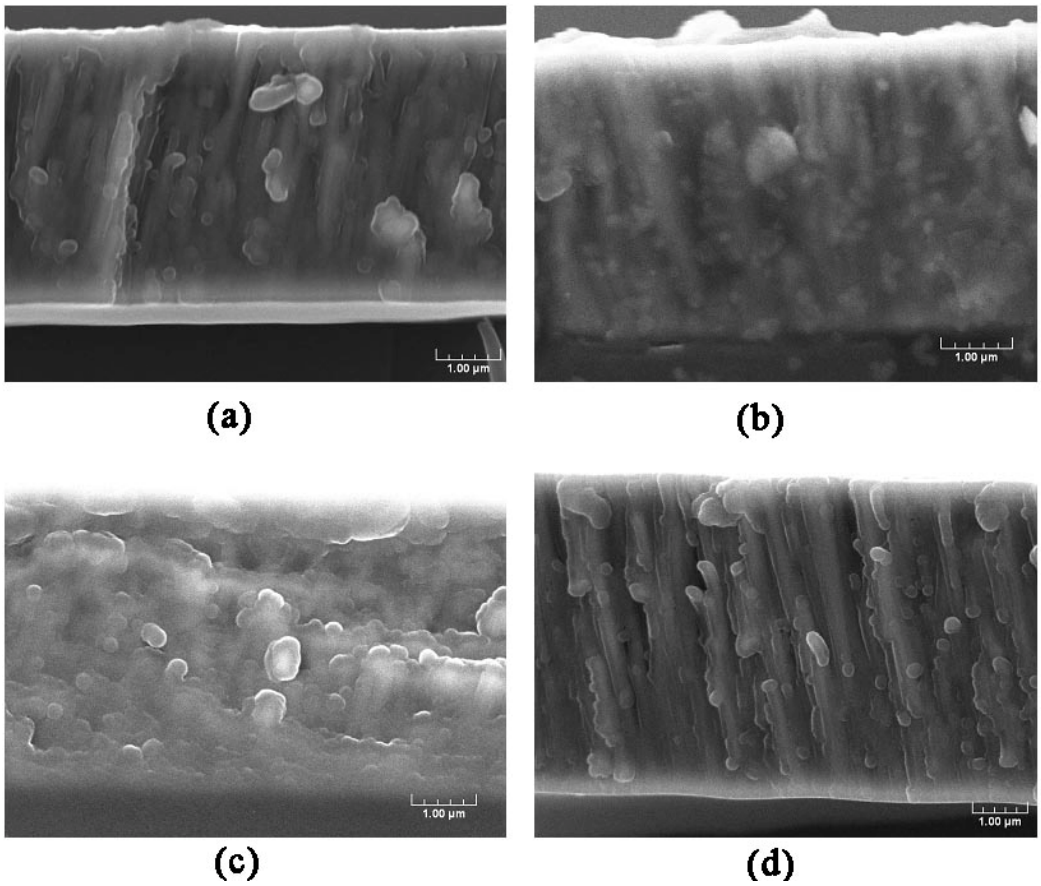

Fig. 2.4 Scanning electron fracture micrograph of Cr deposited with various deposition parameters (a) Target current: 1.25 A and Ar flow: 15 sccm; (b) Target current: 1.5 A and Ar flow: 15 sccm; (c) Target current: 1.25 A and Ar flow: 10 sccm; (d) Target current: 1.5 A and Ar flow: 10 sccm.

It can be observed that the obtained Cr coating under a target current of 1.5 A and a Ar flow rate of 10 sccm has a typical columnar structure and the highest thickness. As all the samples are prepared using the same deposition time, this coating thus has the highest deposition rate. Therefore, in this thesis, without special issues, the Cr target current will be regulated at a value of 1.5 A while Ar flow rate maintained at 10 sccm.

2.3. Characterization

2.3.1 Coating chemical composition

Coating chemical compositions are generally evaluated by a Leco DS-750 Glow discharge-optical emission spectroscopy (GD-OES) technique. It is a fast, easy-to-use

analytical procedure, which can produce detailed information on both conductive and non-conductive coatings. By the spectroscopy, sample analysis can be performed in less than one minute and there is the added capability of direct depth profiling of the solid sample without the need for any prior sample preparation [76-78].

Glow discharge utilizes a low-pressure, non-thermal process in which material is uniformly sputtered from the sample surface by a stream of argon ions. The sputtered material is then atomized and excited in a low-pressure plasma discharge, away from the sample surface. The cathodic sputtering of the sample surface removes material layer by layer, without any change in sample chemical compositions caused by melting, selective volatilization, oxidation or re-solidification. The light emitted from this excitation is analyzed using an optical emission spectrometer. The composition and intensity of the light allows the quantification of the elemental components. The excitation of the atoms occurs in the glow discharge plasma discretely away from the sample surface, thus reducing the metallurgical and chemical history inherent in all samples. Calibration curves are essentially linear and permit a good estimation of concentrations by extrapolation beyond the calibration range. This process characteristic makes the glow discharge an ideal source for very precise bulk content analysis and an ideal analytical tool for the depth concentration profile analysis. The design of the excitation source results in very little sample-to-sample carryover, allowing quick matrix changes. In this thesis, GDOES depth profile is used to estimate coating compositions. The operations were in agreement with ISO 14707:2000 standards.

2.3.2 X-ray diffraction for structure analysis

X-ray diffraction is a common technique to perform the structure characterization of a solid material. The wavelength of the X radiation is of the order of the interaction distances of the crystals, which acts as diffraction arrays. Indeed, X-rays are diffracted in determined intensities and directions. Thus, the diffractogram of a solid is a representation of its crystalline structure. Diffraction maxima are

produced when the subtended angle is formed between the emergent and incident X-ray beams. Their principles follow by Bragg's Law. In this research, the coating structure is mainly examined by a X' Pert Pro diffractometer using the Cu Kα radiation (wavelength λ = 1.541 Å), at a tube voltage of 40 KV and current of 30 mA. High-angle (θ-2θ) scan is used to obtain information such as crystallinity, phase, and crystallographic orientation when compared to the tabulated references obtained from the Joint Committee for Power Diffraction Studies (JCPDS). In multilayer structure characterization, small angle X-ray diffraction (SMXRD) or X-ray reflectivity (XRR) is used to determine the individual layer thickness and the interface quality. Reflectometry is effective for the study of films with poor crystallinity as for instance, amorphous materials with embedded nanocrystals. In this way, low angle incidence provides more fraction of the X-ray beam to be diffracted which increases the signal to noise ratio. Many film characteristics may be achieved by a simulation process of XRR diffractograms. In this thesis, for the characterizations of multilayer, the SMXRD scans are performed with a Bruker D8 advanced diffractometer.

2.3.3 Scanning Electron Microscopy

The scanning electron microscopy is a valuable tool for imaging coating morphology. In this study, the morphological information of the as-deposited coating specimens are obtained by using a JEOL JSM 5800 LV scanning electron microscopy (SEM). Generally, the fractured cross-sectional images on silicon substrate are achieved for a straight-forward observation of the film thickness and the identification of the coating growth style. The surface morphological photographs after the electrochemical tests also are obtained in order to investigate the corrosion mechanism. This setup is equipped with a Princeton Gamma-Tech EDX system, which makes it possible to determine the topography and the composition of the corrosion products.

2.3.4 Transmission electron microscopy

The structures of certain as-deposited coatings are studied by means of transmission electron microscopy (TEM). It is a powerful analysis tool to observe the microstructure directly by means of a focus beam of electron passing through a thin foil specimen. By changing the focal length of the electron beam, TEM can be used in either imaging mode or diffraction mode. In the former, the electron beam transmits an image of the specimen onto the phosphorous screen. However, in the diffraction mode the electron beam transmits diffraction contains information regarding the crystal structure and orientation of the specimen onto the phosphorous screen. In this thesis, TEM observation is performed on a Philips CM20 microscope operating at an accelerating voltage of 200 kV. The samples are typically obtained on silicon substrates thanks to their easy preparation. For multilayer coating specimens, the cross-sectional images are preferred in order to get the detailed information about the bilayer period directly and the thickness of different coating layers.

2.3.5 Nanoindentation hardness and modulus

The nanohardness and the elastic modulus are characterized by means of a B2120 nano-indenter (Berkovich) on a MTS-XP Nanoindentation tester configured on a continuous stiffness measurement (CSM) mode [79]. The major components inside the MTS Nano Indenter XP are shown below. This indenter sits on a mechanical vibration isolation table and its container has sound dampening materials inside. The load frame is essentially the gantry of the indenter and should be as stiff as possible, so not to contribute significantly to the displacement of the load train. The load frame stiffness can be calibrated by an iterative procedure in which a number of deep indentations are made in a standard material (i.e. fused silica).

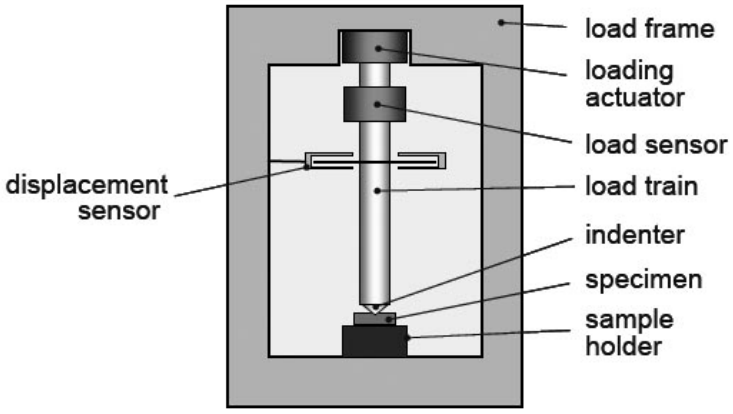

Fig. 2.5 A diagram of inside components in the MTS-XP nano-indentation tester [79].

Currently, the most common method for extracting the hardness and modulus values from an indentation curve is known as the "Oliver and Pharr" method [80, 81]. This is also the method that the MTS-XP Testworks software uses to determine hardness and modulus. Their method is based on the contact mechanics solutions developed for a solid of revolution indenting a half-space. This method applies to both sharp and spherical indentation. The Oliver and Pharr method begins by assuming a flat, smooth, isotropic and orthogonal contact between the tool and the material. Elastic deflections of the material are taken into account, as shown below. This consideration allows more precise measurements of hardness and modulus properties, as well as a more accurate determination of phase transformation pressures when combined with other contact mechanics relations.

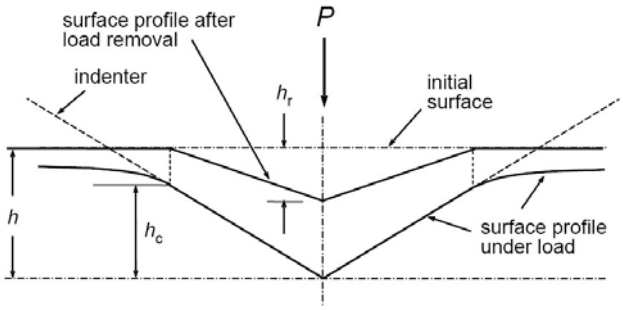

Fig. 2.6 The diagram of Oliver and Pharr method to determine nano-hardness [80, 81].

From the generated curve, the three most important pieces of information that are used to calculate hardness and modulus are the maximum applied load, P_{max}, the displacement into the surface at maximum load, h_{max}, and the slope at the beginning of the unloading curve which is unloading contact stiffness, S. As described by Oliver and Pharr, this unloading curve is fit to the function:

$$P = C(h - h_r)^m,$$

Where P is the applied load at a point in the unloading curve, C, m, and residual depth h_r are empirically fit constants, and h is depth into the surface corresponding to a load P. The value of m will be between about 1 and 2. This fit equation is then differentiated, and the stiffness is found by evaluating:

$$S = \left(\frac{dP}{dh}\right)_{h=h_{max}},$$

While h_r can be found experimentally for complete unloading, for this analysis it remains a fit constant. To find material hardness, the relation:

$$H = \frac{P}{A}$$

is used, where A is the area of contact between the indenter and the material at load P. Different hardness definitions exist, but this is the definition used in depth-sensing indentation. This is similar to the way hardness is found for Brinell, Vickers, and Knoop methods, except that in this case the elastic deflection of the surrounding material is taken into consideration. Hardness is typically evaluated at P_{max}, but this relation can be used to describe contact pressure at any point in the loading curve as well, provided the tip geometry is known.

To calculate modulus, one firstly finds the reduced modulus derived as:

$$E_r = \frac{S\sqrt{\pi}}{2\beta\sqrt{A}},$$

Where β is a constant close to 1 that varies depending on indenter geometry (β= 1.034 for a Berkovich indenter). This relation was originally derived from purely elastic theory for unloading between a conical indenter and a surface, but also holds true for Berkovich and spherical indenters. The reduced modulus is related to material

modulus E by the relation:

$$\frac{1}{E_r} = \frac{(1-\nu^2)}{E} + \frac{(1-\nu_i^2)}{E_i},$$

Where ν is the Poisson's ratio and the subscript i refers to the properties of the indenter. For diamond indenter, E_i =1141 GPa and ν_i = 0.07 [79]. An inherent weakness of this method is that ν of the tested material must be known or closely estimated beforehand. In this entire thesis, the Poisson's ration was assumed as 0.25. Although this assumption is not in the fact, it is shown that there are little uncertainties to estimate the results [82]. For this work, the typical continuous stiffness measurement (CSM) mode was operated with a constant strain rate of 0.05 s^{-1} and the penetration depth was generally fixed at 500 nm. Without any special issues, the nanohardness tests were performed on the AISI304 stainless steels.

2.3.6 Scratch adhesion testing

In scratch testing, a diamond stylus of defined geometry is drawn across the surface of a coated sample at a constant speed with a defined normal force over a defined distance. The normal force that can be constant, may progressively increase, or may incrementally increase. The diamond stylus typically has a Rockwell C geometry with an angle of 120 degrees and a spherical tip radius of 200 μm. Different tip radii can serve to change the contact pressure.

In a scratch testing, the tangential force, the penetration depth, and the acoustic emission signals are recorded as secondary test data, along with the normal force. After the completion of the test, the scratch track is microscopically analyzed for specific, well-defined damage such as cracking, deformation, buckling, spallation, or delamination of the coating. The critical load L_c is defined as the load that corresponds to the different failure events. This load is related to the practical adhesion strength and the damage resistance of the coating/substrate system. The critical load depends strongly on the test parameters (stylus parameters and geometry, loading rate, scratch speed) as well as on the properties of the coated sample (coating

thickness, surface roughness and microstructure, damage mechanism, hardness, modulus of elasticity, fracture strength) [83].

Fig. 2.7 illustrates the scratch test method. Three load modes can be used to determine the adhesion: constant-load, progressive-load, and incremental-load. The widely used test method for PVD coatings is the progressive-load mode. In such a mode, the stylus is drawn along the sample while the normal force is linearly increased to a maximum predetermined value. The critical load is recorded as the normal force at which the damage is first observed.

The tangential force F_t is defined as the force that opposes the relative motion between the stylus and the sample. During the scratch test, the tangential force (or frictional force) may change in amplitude as different types of damage develop with increasing load. The acoustic emission sensor can detect any high-frequency elastic waves generated in the coating/substrate system by brittle damage events such as cracking, delamination, chipping, or buckling. However, it is much preferred to use the optical observations to determine the real damage events.

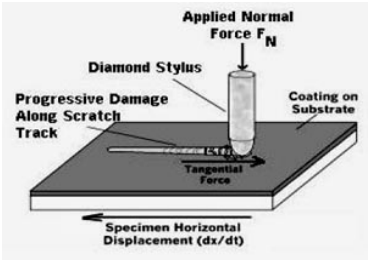

Fig. 2.7 Schematic of the scratch test method [83].

In this work, the apparatus used for this testing is a Teer ST3001 test machine. The typical tests are carried out using a Rockwell diamond tip (200 um diameter) on M2 high speed steel ($HV_{0.1}$ =230) and work with a constantly increasing load rate of 100 N/min at a horizontal speed of the sample of 10 mm/min. After the tests, the samples are observed by an optical microscopy but the critical load is derived from the friction coefficients vs. displacement curve. The different damage events depending on the coating system are defined and can be found in the next chapters.

2.3.7 Tribology test

In tribological test, a flat, a pin or a sphere is loaded onto the test sample surface with a precisely known force. The pin is mounted on a stiff lever, designed as a frictionless force transducer. The friction coefficient is determined during the test by measuring the deflection of the elastic arm. Wear coefficient for the pin and disk materials are calculated from the volume (or mass) of material lost during the test. This simple method facilitates the study of friction and wear behavior of almost every solid state material combination with or without lubricant. Furthermore, the control of the test parameters such as speed, frequency, contact pressure, time and the environmental parameters (temperature, humidity and lubricant) allows to simulate the real life conditions of a practical wear situation.

In this thesis, a CSM pin-on-disk tribometer is applied to evaluate the coating tribological properties. Following a ASTM standard (ASTM G99-95 a), the amount of wear were determined by measuring appropriate linear dimensions of both specimens (ball and disk) before and after the test, or by weighing both specimens before and after the test. In practice, linear measures are often preferred since the mass loss is often too small to be measured precisely. The standard pin-on-disk setup is shown in Fig. 2.8 with the parameters required to calculate wear.

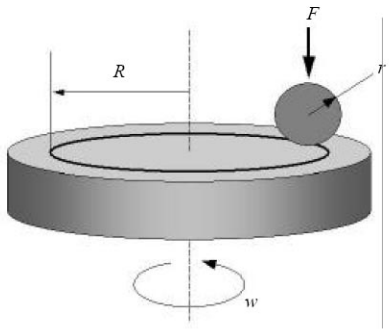

Fig. 2.8 Schematic of pin-on-disk setup where F is the normal force applied on the ball, r is the ball diameter, R is the radius of the wear track and w is the rotational speed of the disk.

To calculate the wear rate, one should estimate the wear mechanism firstly after a test. If the main wear form is abrasive wear, the test material pair will dictate whether the ball, the disk or both, will become significantly worn. An example of

each case is summarized in Fig. 2.9. Assuming that there is no significant disk wear, the volume loss of the spherical ball (or spherical-ended pin) is given by:

$$\text{Pin volume loss} = (ph/6)[3d^2/4 + h^2]$$

where $h = r - [r^2 - d^2/4]^{1/2}$ (height of material removed)

d = wear scar diameter

r = ball radius

Assuming that there is no significant pin wear, the volume loss of the disk is given by:

$$\text{Disk volume loss} = 2pR[r^2 \sin^{-1}(d/2r) - (d/4)(4r^2 - d^2)^{1/2}]$$

where R = wear track radius

d = wear track width

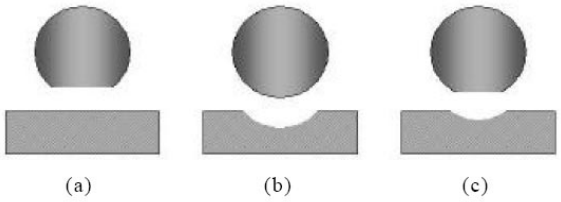

Fig. 2.9 Three possible situations for different wear resistance of ball and flat disk specimens; (a) only the ball wears, (b) only the disk wears, and (c) both ball and disk wears .

It should be noted that the disk volume loss calculated in this manner may have certain error due to variations around the wear track, accumulations of debris and plastic deformation. A stylus profilometer is often used to measure the cross-sectional area of the wear track in several places around the track. This provides a more accurate measure of the disk volume lost when multiplied by the track length. However, if the wear mechanism is the combination of different wear mechanisms, it is very difficult to calculate the wear rate. In this thesis, the typical pin-on-disk tests on M2 high speed steels are performed in ambient temperature ranging from 25 to 35 ^{o}C and a relative humidity of 50±5%. Two kinds of balls: 100Cr6 and WC-Co with diameters of 6 mm are used as counterparts and the applied load kept at 5 N (or 2N) with a sliding velocity of 0.2 m/s. The friction coefficient is determined after a sliding distance of 1000 m (or 500m) and the wear tracks are measured using an optical microscope, SEM and a 3D topographical profilometer.

2.3.8 Potentiodynamic polarization

The measurement of the polarization behavior of coating/substrate system is a powerful method for determining the corrosion behavior of PVD thin film coated system. During the test, a polarization curve is a plot of the current from the working electrode surface versus the measurement of the rate of the overall process at each potential. There are in general two techniques to obtain the polarization curve: potentiostatic and potentiodynamic polarization methods. The potentiostatic polarization technique measures the polarization behavior of a working electrode by applying a series of discrete potential steps (for example, increasing or decreasing potential (50 mV) vs. open circuit potential in increments of 5 minutes) and monitoring the current response at each applied potential. However, with the widely available modern instrumentation, most anodic polarization curves are now obtained potentiodynamically. In potentiodynamic polarization, the potential is changed continuously with a constant scan rate (e.g. 100 mV/min) and the response current is measured simultaneously. From this study, characterization of a coated specimen by its current-potential relationship provides important information such as: the ability of the material to spontaneously passivate in a particular medium; the potential region over which the specimen remains passive; and the corrosion rate. In anodic polarization, the working electrode (thin film coated specimen) potential is scanned continuously in the positive direction versus open circuit potential and hence acts as an anode; in this way, the coated metal or the substrate material corrodes or forms a metal oxide, the passive coating. This method permits the easy automation of curves and real time plots of the experimental data.

The scan rate and scan range with respect to the applied potential are very important during the potentiodynamic polarization tests. In general a scan rate is selected to minimize testing time but slow enough to obtain a polarization curve at near steady-state conditions. The magnitude of the current measured at each potential has been reported as a function of the scan rate [84].

The fundamental procedure for experimentally evaluating corrosion current

density is by Tafel extrapolation. In general, a potential scan greater than ± 50 mV versus corrosion potential is required to reach potentials at which the anodic and cathodic Tafel behavior dominates and to determine whether a linear section of at least one decade of current is present. To obtain anodic and cathodic polarization curves with a single scan, the starting potential in the scan is a negative (-200 to -400 mV). However, a lager starting potential can alter the steady-state condition established at the corrosion potential and influence the measurement of the corrosion current density. In addition, the ASTM standard G5-94 recommends a potential range of 0 to 1.6 V versus corrosion potential for anodic polarization curves.

In this thesis, the corrosion behaviors of various single or multilayer coatings are evaluated by means of a radiometer PGP201 (Radiometer, Denmark) potentiostat/galvanostat interfaced to a computer. A conventional three-electrode cell setup is applied for the electrochemical tests. The saturated calomel electrodes (SCE) and the platinum wire are used as the reference and counter electrodes respectively. The specimens are sealed in a small Teflon box with leaving an area of 2.543 cm^2 (Φ = 0.9 cm) exposed to the 3.5% NaCl aqueous solution. The tests are carried out at room temperature and under open-air conditions. The specimens are the coated AISI304 stainless steels. These specimens are initially stabilized for 2 min before polarization, and then the dynamic potential scan begins from -800 to + 1200 mV with a rate of 120 mV/min (2mV/s). The analyses for these potentiodynamic measurements are performed using the VOLTA MASTER 4 software. Corrosion potential and current are determined following the program with “1st Stern-Tafel” method. After the corrosion tests, generally, the specimens are observed by SEM observations so that their mechanisms can be drawn out.

Chapter 3. Deposition and optimization of monolayer CrN coatings

3.1 Introduction

Following the successful applications of TiN coating for cutting tools and machine parts, increasing amounts of attention are devoted to chromium nitride coatings because of their excellent corrosion and wear properties [85-87]. Chromium nitride coatings produced by PVD techniques have been considered promising candidates for clean replacements of electroplated chrome. In comparison with electroplated chrome, the nitrogen doped chromium coatings offer even greater advantages of abrasive wear resistance and corrosion resistance [17, 73, 88]. On the other hand, chromium nitride coating can also be used as a substitute material for TiN coating, which is due to their high toughness and micro-hardness, superior wear resistance [89, 90], as well as excellent oxidation resistance and adhesion to steel substrates [85].

In chromium nitride binary system two stoichiometric nitride phases are very important: hexagonal Cr_2N (β-Cr_2N) and face centre cubic (FCC) CrN [66]. Generally, Cr_2N is harder and offers better corrosion resistance whereas CrN shows better abrasive wear resistance [91]. From Cr-N binary phase diagram (Fig. 3.1), one can see that the stable composition of Cr_2N strongly depends on temperature; at room temperature it varies in a very narrow range from 30.3 to 33.3 at. % N. In contrast to Cr_2N, the homogeneity range of CrN at room temperature is even narrower, only extending from 49.5 to 50 at. % N. For these reasons the pure single-phase Cr_2N and CrN are difficult to produce, especially in PVD deposition processes, the mixture phases Cr+Cr_2N or Cr_2N + CrN are generally obtained and the control of the coating microstructures and properties becomes very important. Moreover, even it is easier to deposit stoichiometric CrN in a pure N_2 atmosphere than in the mixture of Ar and N_2, the problem of a decreasing deposition rate is inevitable [35]. In addition, the

preferred orientation of the deposit coating is strongly dependant on the deposition parameters [92]. Therefore, for applications where specific properties are required, deposition parameters need to be strictly controlled. In various chromium nitride PVD deposition techniques [93, 94], DC reactive magnetron sputtering techniques are widely used in industry because of their high efficiency [34].

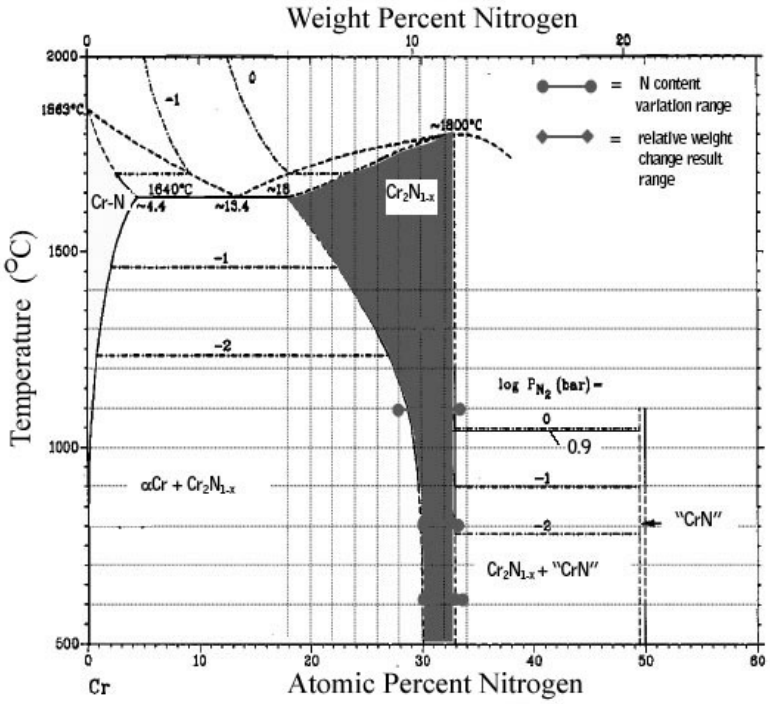

Fig. 3.1. Cr-N binary phase diagram [91].

During the deposition process of various PVD techniques, especially magnetron sputtering system, the use of low energy ion bombardment has become increasingly important in order to improve coating properties. Through affecting the nucleation and growth kinetics of films, it eventually alters the coating microstructure, texture, surface morphology and internal stress [95]. Very frequently, ion bombardments are realized by applying negative bias on the substrates. The advanced DC pulse or the RF bias is considered favorable to deposit isolate or low conductive coating because they can depress small arc discharges on substrate surface [74]. However, due to the complexity of the physico-chemical mechanisms in applying bias that many interdependent processes take place simultaneously, for instance: in the cases of

depositing nitride coating in Ar-N_2 mixed atmosphere, the fundamental process under bias effects has not been fully understood [96, 97]. It has been argued that during the deposition without chemical reaction, depending on the value of the bias voltage, several phenomena can appear, such as cleaning, densification and resputtering [74]. On the other hand, in the cases of reactive sputtering process, the reaction process to synthesis compounds on the coating surface occurs simultaneously under ion bombardment. In addition, the interactions are generally non linear [97]. Therefore, it is very interesting to determine the role of a negative bias especially RF potential applied to substrate during the film deposition as the strong coupling effects between magnetron sputtering discharge and RF capacity discharge would modify the plasma characteristics and finally affect the plasma chemistry process.

In this chapter, two important deposition parameters for CrN coatings are investigated: the nitrogen partial pressure and the RF substrate bias. The hysteresis curves and plasma optical emission spectra (OES) are used to monitor chromium nitride coating synthesis process and to optimize coating properties. It is expected to fabricate the stoichiometric Cr, Cr_2N and CrN by controlling nitrogen partial pressure. On the other hand, during the investigation of the RF bias on coating structures and properties, OES signals are recorded and analyzed in order to obtain an optimum value of the bias, under which the mobility of surface species and the chemical activity would enhance. In turn, it improves surface qualities, increases coating density and reduces the numbers of pinhole defects.

3.2 Coating preparations

In this chapter, two kinds of materials: boron-doped Si(100) wafers and AISI 304 stainless steel were used as substrate materials. Stainless steel substrates were firstly lapped, polished with diamond paste (0.1 μm); and then rinsed ultrasonically together with silicon wafer in acetone and alcohol successively. The deposition setup and the selected basic deposition parameters have been described in chapter 2. In this chapter, only one single Cr target (purity: 99.99%) was employed to produce the

nitride coatings. An Advanced Energy DC power unit (regulation of the current) was regulated at 1.5 A for Cr target during all the deposition processes. To eliminate the small arc discharge on the substrate holder and improve the quality of the deposited coatings, a RF power was applied to enhance ion bombardment. Without any special issues, the standard deposition steps are defined as follows:

1) Before sputtering, the substrates were etched (-300 V) with an argon flow rate of 10 sccm for 15 min.

2) During the last 5 minutes of etching, the target was powered to remove the contamination layer on the target surface. In this process, the target and substrate were separated by a shutter to avoid contamination.

3) After that, a pure metal (i.e. chromium) interlayer was deposited for 5 min before the compound coating synthesis started.

4) All the depositions were made at room temperature and the deposition time for chromium nitrides was fixed at 60 min.

For chromium nitrides, two series coatings were deposited. The first one focused on the influence of nitrogen atmosphere on coating properties. It was controlled by varying the introduced nitrogen flow rates while keeping the RF self-bias voltage at -100 V. The corresponding RF power was 50 W. The second one was dedicated to the effects of RF bias ion bombardment. In this investigation, the nitrogen flow rate remained at 12 sccm while RF negative bias decreased progressively from 0 to -200 V.

3.3 Influence of N_2 flow rates on structures and properties of chromium nitride coatings

3.3.1 The hysteresis effects and deposition parameter selection

The total sputtering pressure and sputtering voltage versus nitrogen flow rate curves were recorded and are presented in Fig. 3.2 at a constant argon flow rate of 10 sccm. The pressure was monitored by an accurate capacitive Baratron MKS 670

gauge. This method was usually used in reactive sputtering process for deciding the sputtering target working mode: metallic, transition or reactive [35]. The sputtering voltages from the sputtering power supply were also in-situ recorded. The curves were obtained by increasing the nitrogen flow continually from zero to a maximum of 20 sccm with an interval time of 2 min for each point. During the short interval time, the pressure in the deposition chamber can reach nearly stable, which means that the equilibrium between gas absorption (and consumption by reacted with sputtering target) and desorption can be obtained approximately.

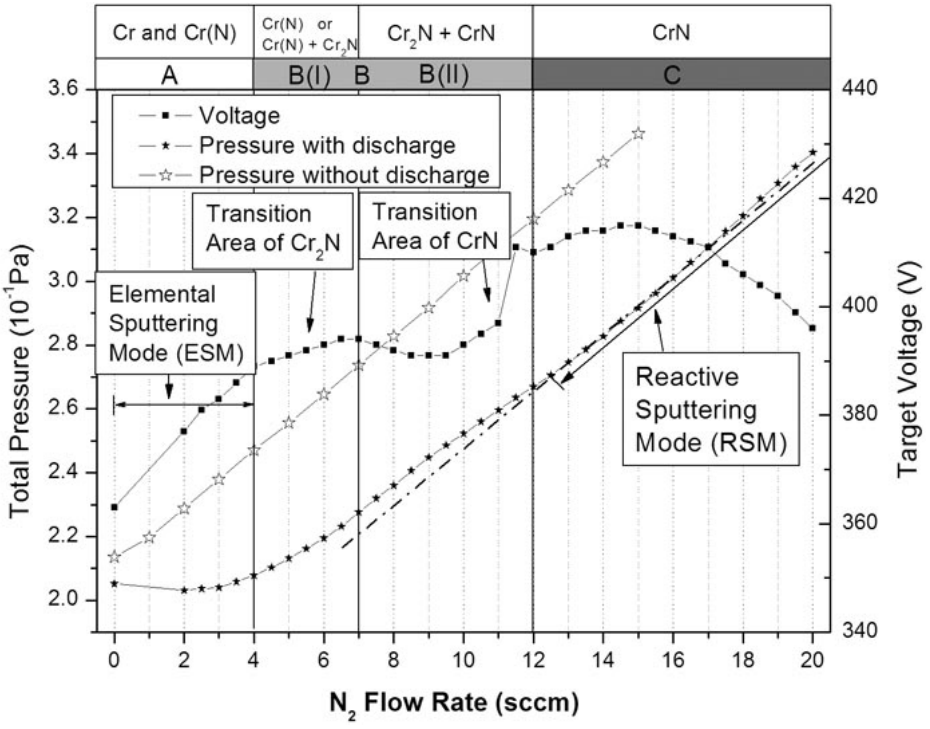

Fig. 3.2 Evolution of the total deposition pressure and sputtering voltage as a function of the introduced nitrogen flow rates.

In Fig. 3.2, the typical hysteresis (or instability) effects [33] on the total pressure versus nitrogen flow rate curve are not observed. This is due to the facts that nitrogen does not react readily with Cr as it does with other reactive elements such as Ti [98]. However, when comparing the pressure versus flow rate curve with and without discharge, it is still possible to specify the curve into three different zones with different nitrogen flow rates, which properly corresponds to three different target

working modes. As indicated in Fig. 3.2, in zone A, the target works on an elemental sputtering mode, under which all the reactive gases were gettered by the sputtered metal and the chamber wall. As a consequence, every small increase in nitrogen flow rate results in few variations of total pressure in the deposition chamber. On the other side, zone C can be thought to correspond to a reactive sputtering mode, where a further increase of nitrogen flow rate leads to a linear increase of total pressure as it does without plasma discharge. One can see the two lines have very close slopes. For Zone B, it is more complicated because the target works on a transition mode but the pressure vs. flow rate curve can not clearly indicate this transition process either from Cr to Cr_2N or from Cr_2N to CrN. However, the recorded sputtering voltage vs. nitrogen flow rate curve gives some useful information, where two different transition regions: B(I) (4-7 sccm N_2) and B(II) (10-12 sccm N_2) can be distinguished as indicated in the figure. In region B(I), the sputtering voltage increases nearly linearly with increasing nitrogen flow rate. In contrast, in region B(II), the voltage initially decreases till the nitrogen flow rate of 9~10 sccm and then increases again, particularly from 10 sccm the velocity of increase is quite high. This unstable transition process reflects the sharp change of the target surface status. These two regions possibly correspond to the transitions of the covering layer materials on the sputtering target from metal chromium, to chromium rich compound and to nitrogen dominated compound. Therefore, the experiment parameters of nitrogen flow rate are determined and listed in Table 3.1.

Table 3.1.Deposition parameters under a constant argon flow rate of 10 sccm and the main characteristics of the Cr-N coatings.

N_2 flow (sccm)	working pressure (10^{-1}Pa)	at.% Cr	at.% N	Thickness (μm)	critical load Lc_1 (N)	critical load Lc_2 (N)
0	2.05	100	0	5.5	9.8	-
2	2.03	90.2	9.8	5.2	4	17.5
4	2.08	77.9	22.1	5.0	3.7	13.7
5	2.13	73.7	26.3	4.8	4.1	14.0
6	2.20	65.9	34.1	3.8	4.3	15.0
10	2.52	54.0	46.0	3.4	2.5	16.2
12	2.67	51.5	48.5	3.1	2.6	15.1

3.3.2 Coating compositions and microstructures

The compositions of the deposited coatings as a function of nitrogen flow rate can be found in Table 3.1. The composition results measured by Electron Probe Micro-Analysis Micro (EPMA) using an EPMA-1600 electron probe (Acc.V=15KV, SHIMADU corporation) indicate that the nitrogen concentration in the coatings increases with increasing nitrogen flow rates. The coatings deposited in the zone A of Fig. 3.2 have N concentration below 10 at. %, which could be associated with the formation of Cr or Cr solid solution (Cr(N)) according to the binary diagram of this system (See Fig. 3.1). On the other hand, as predicted by the target voltage versus nitrogen flow rate curve, the region B(I) with nitrogen ranging from 4 to 7 sccm corresponds to chromium-rich coatings, which can be considered as a mixture of cubic Cr and hexagonal Cr_2N phases since here the atomic ratio of chromium to nitrogen is below 2:1. At the nitrogen flow rate of 6 sccm, the atomic ratio of Cr to N is nearly 2:1, which most possibly corresponds to Cr_2N phase. In the following region B(II) where the nitrogen flow rate is between 7 to 12 sccm, Cr and N atomic ratio continuously increases to nearly 1:1, which, however, should be attributed to the formation of Cr_2N and CrN mixtures. The coating deposited at 12 sccm forms nearly stoichiometric CrN. As the nitrogen flow rate increases into zone C, it would be expected to be the single phase CrN. The composition evolutions present good corresponding correlations with the curves presented in Fig. 3.2. It is also found that these results are in good agreements with the Cr-N binary phase diagram indicated in Fig. 3.1.

Since EPMA analysis for light element (i.e. N, O) is not very accurate, to confirm the composition results from EPMA and to investigate the element distribution along the depth direction, a GDOES depth analysis was performed. The sample deposited with the nitrogen flow rate of 5 sccm was chosen, and the obtained GDOES depth profile is presented in Fig. 3.3. The average chemical composition of this chromium nitride coating is 74.5 at. % Cr and 25.5 at. % N, which is in good agreement with the results from EPMA (73.7at. % Cr and 26.3 at. % N). It should be

noted that there is rare oxygen and carbon observed in both kinds of analyses. From the depth spectrum, there is a slight slope on both the Cr and N composition traces, indicating that the nitrogen content of the film is slightly higher next to the Cr interfacial layer than close to the surface of the coating. This would be associated to the slight variation of deposition temperature under continual ion bombardment.

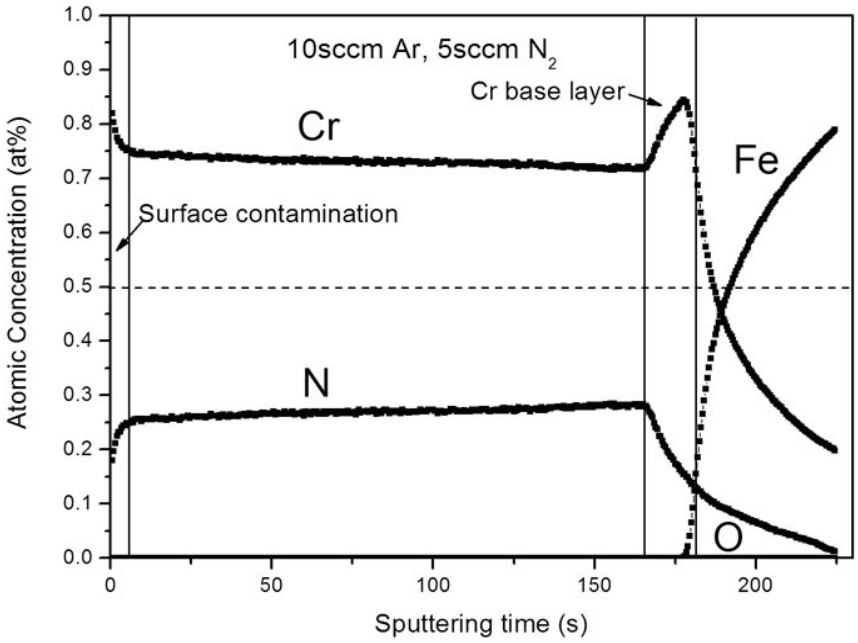

Fig. 3.3 GDOES quantitative elemental depth profile of chromium nitride coatings deposited at Ar flow rate of 10 sccm and N_2 flow of 5 sccm.

The phase evolutions of the deposited chromium nitride coatings with different nitrogen flow rates were examined by X-ray diffraction in θ-2θ mode. The obtained XRD spectra are shown in Fig. 3.4. Again, a good correspondence between the sputtering pressure, target voltage evolutions and the phase developments with respect to nitrogen flow rate can be found, therefore, the same zones A, B and C discussed on the hysteresis curve are used here. The results show an evident trend that the coating phases vary from a single bcc-Cr phase to Cr+Cr_2N (or Cr(N)), then stoichiometric Cr_2N. A further increase of the nitrogen flow rate changes the phase into mixed Cr_2N + CrN structures and finally nearly stoichiometric CrN is reached. This transition process in zone B of XRD patterns is well predicted by the sputtering voltage versus nitrogen flow rate curve from Fig. 3.2 and also confirms the composition results of

EPMA. Moreover, the results are in good agreement with the Cr-N binary diagram [66] and previous reports [99].

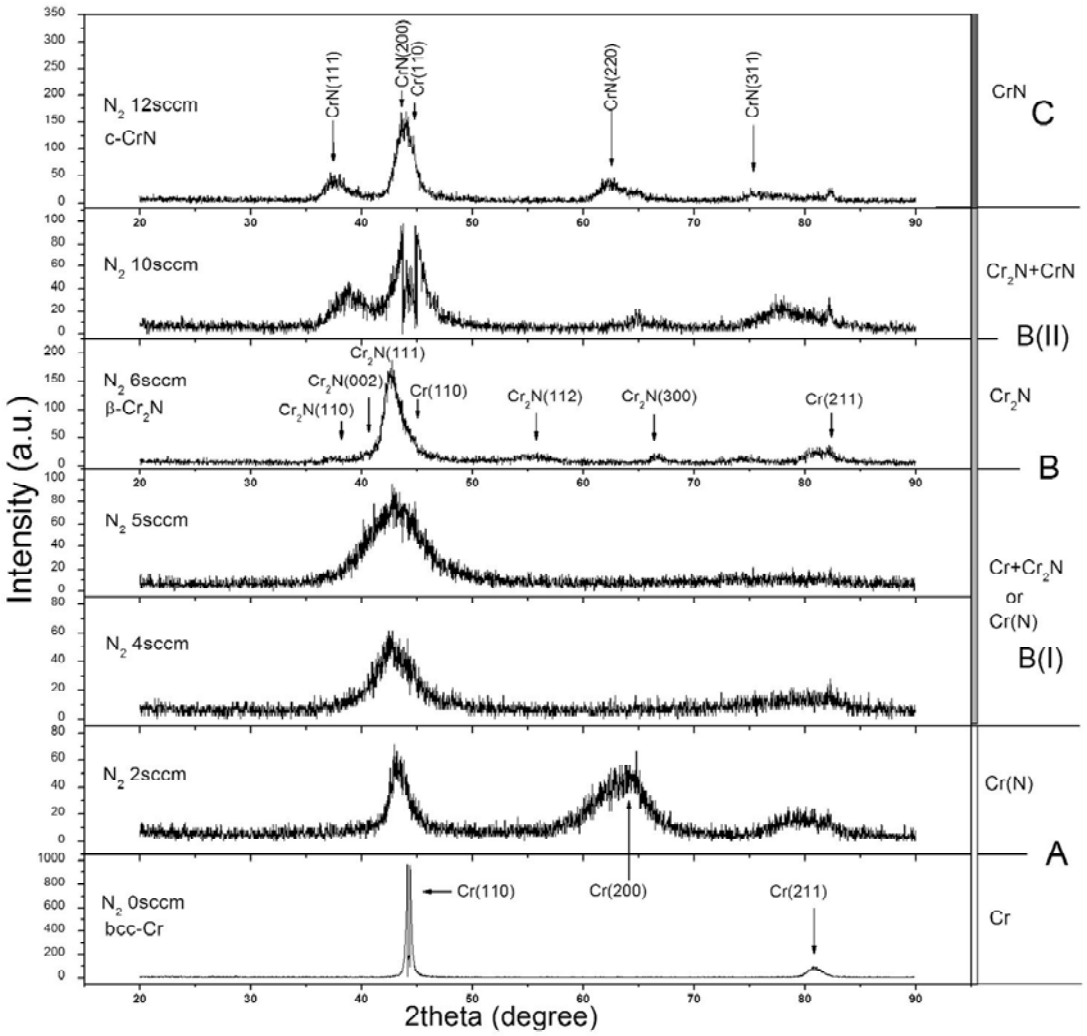

Fig. 3.4 XRD spectra of chromium nitride thin films deposited with different nitrogen flow rates.

From the XRD patterns, the bcc Cr phase with a stronger <110> texture firstly appears at a pure argon atmosphere. With the addition of a small amount of nitrogen (≦ 2 sccm), one can observe not only the broadening of the peaks due to the nitrogen incorporation into the Cr lattice, but also a preferred growth orientation transition from <110> to <200>. It is a little surprising that the halo of amorphous phase was found when nitrogen flow rates are between 2 and 6 sccm, which indicates the obtained coatings have very small grain size. When the nitrogen flow rate is 6 sccm, XRD spectra present sharp peaks and the hexagonal Cr_2N phase occurs as

expected from the composition results of EPMA. In contrast, the coating deposited at 12 sccm N_2 is FCC CrN with a lattice constant of 0.412nm, slightly smaller than that of the bulk phase, 0.414nm [JCPDS76-2494]. This CrN coating has a preferred orientation of <200>, which can be associated with the theory of the minimization of surface energy [91]. Nonetheless, the stoichiometric CrN can be readily obtained, as long as an adequate nitrogen flow is supplied. However, a decreasing trend of deposition rate with increasing nitrogen flow rate is evident from Table 3.1. Moreover, the preferred crystallographic orientation is still unclear upon further introductions of nitrogen. It should be noted that in this thesis, this is a basic result that the stoichiometric CrN can be obtained with a mixture of 10 sccm Ar and 12 sccm N_2 under a low RF bias and with a Cr target current of 1.5 A. Although a further investigation is needed in order to optimize the properties of various CrN at further increased nitrogen flow rate, the following work in the next chapters still used these deposition parameters to ensure the stoichiometric CrN because such deposition parameter configurations contribute to a high deposition rate.

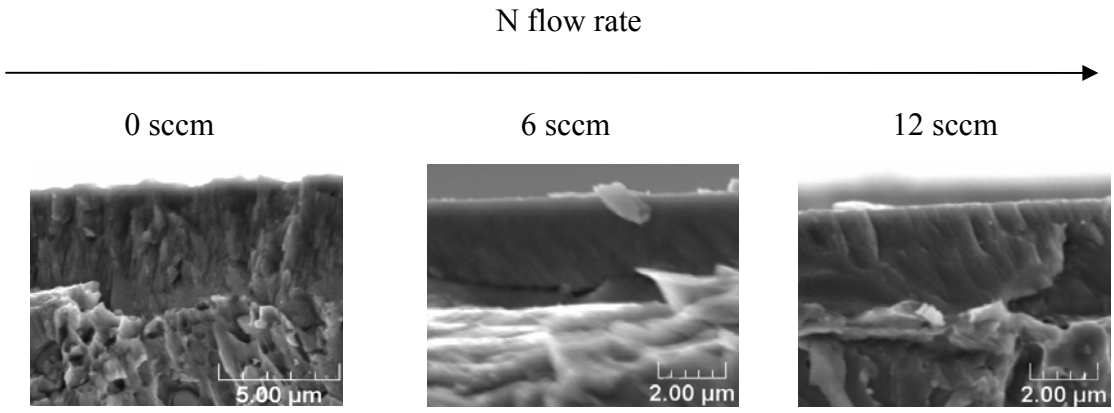

Fig. 3.5 Scanning electron micrographs of fracture cross-sections.

The cross-sectional micrographs of fractured specimens in Fig, 3.5 are obtained by cooling the coated AISI 304 stainless steel substrates to liquid nitrogen and fracturing them when the temperature is below the ductile-to-brittle transition

temperature. It can be observed that the coating thicknesses range from 3 μm to 6 μm. In comparison with the pure Cr, the chromium nitrides exhibit lower deposition rates. The columnar growth structures are clearly visible due to a low deposition temperature and low Ar pressure [100]. The pure chromium has a dense fibrous structure with (110) preferred growth orientation (Fig. 3.5a). Cr_2N phase presents an almost featureless structure corresponding to very fine pore free columnar structure (Fig. 3.5b) whereas the stoichiometric CrN phase appears to be a compact columnar structure (Fig. 3.5c) similar to the pure chromium. A similar morphology evolution has been reported in the literature [101, 102].

3.3.3 Mechanical properties

The evolutions of the nano-hardness (H) and elastic modulus (E) of the deposited coatings versus nitrogen flow rate are shown in Fig. 3.6. The measured nano-hardness and elastic modulus of chromium nitride coatings are in the range of 12 to 25 GPa and from 221 GPa to 338 GPa, respectively. The sputtered Cr coatings have the lowest hardness but the highest elastic modulus in comparison with the other chromium nitrides. The maximum hardness of approximately 25 GPa is achieved at a nitrogen flow rate of 12 sccm, corresponding to the stoichiometric CrN. The hardness of stoichiometric Cr_2N is 23.7 GPa, close to that of CrN. It is of great interest that N-containing solid solution Cr(N) formed at 2 sccm N_2 also presents a relatively high hardness of 23.3 GPa, nearly the same value as Cr_2N. This is very interesting because it provides another possibility to replace electroplated chrome directly because this coating has a high deposition rate as it was deposited under an elemental sputtering mode. A number of factors could account for the unexpected variation, including residual stresses, texture and grain growth (size and density) [66]. Here the nanocrystalline grain size and the transition of the preferred orientation from Cr(110) to Cr(200) may be the most reasonable explanations for the unexpected high hardness of the coating deposited at 2 sccm N_2. On the other hand, the very low hardness of Cr+ Cr_2N coatings can be associated with their amorphous-like structures because

amorphous phases generally present lower hardness in comparison with their crystalline phases.

A high hardness H does not necessarily correspond to a good wear resistance; the elastic modulus E also plays an important role in determining coating wear resistance. According to S.Y. Lee et al. [103], the H^3/E^2 ratio is a strong indicator of a coating resistance to plastic deformation in the elastic-plastic plate contacts. The values of H^3/E^2 of chromium coatings at various nitrogen flow rates are also presented in Fig 3.6. The value of H^3/E^2 for the pure Cr is very low, only 0.016. Conversely, in the case of chromium nitrides, the maximum value of H^3/E^2 (0.15 GPa) is achieved at the nitrogen flow rate of 12 sccm (CrN). A high H^3/E^2 with the value of 0.144 GPa is also obtained for the stoichiometric Cr_2N coating. Therefore it is expected that the stoichiometric chromium nitride coatings show better wear resistance than the non-stoichiometric coatings.

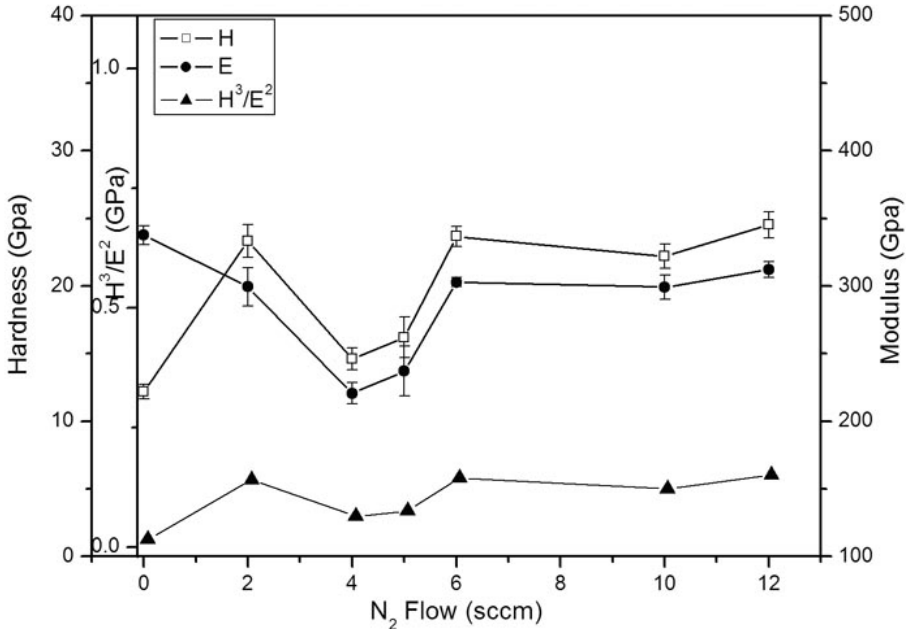

Fig. 3.6 Hardness and elastic modulus at various nitrogen flow rates.

The progressive load scratch tests were carried out to evaluate the practice adhesion between coatings and substrates in this study. The first derivatives of the friction force, the acoustic emission (AE) signal were recorded and optical microscopy observations were performed to determine the critical load. Two kinds of

critical loads are defined: the first is the cohesive failure critical load (L_{c1}), which corresponds to the start of cracking and generally reflected by a sudden change of the first derivative of the friction force or AE signal at low loads; the second one is the adhesion failure critical load (L_{c2}), where the first damage (chipping, delamination) of the coatings is visual under the optical microscope and the first derivatives of the friction force and AE signal fluctuates dramatically. However, considering the accuracy of optical observations, it is very hard to draw the real value of critical load from that. Thus, in this study, the results of the obtained critical load values were drawn from the friction force signals. The test results are listed in Table 3.1. It can be observed that the critical loads do not show any evident dependence on the nitrogen flow rates. This can be explained by the drawbacks of this test technique. The test parameters have more effects than a coating substrate system on the final results. However, one can still draw some useful information from the test results.

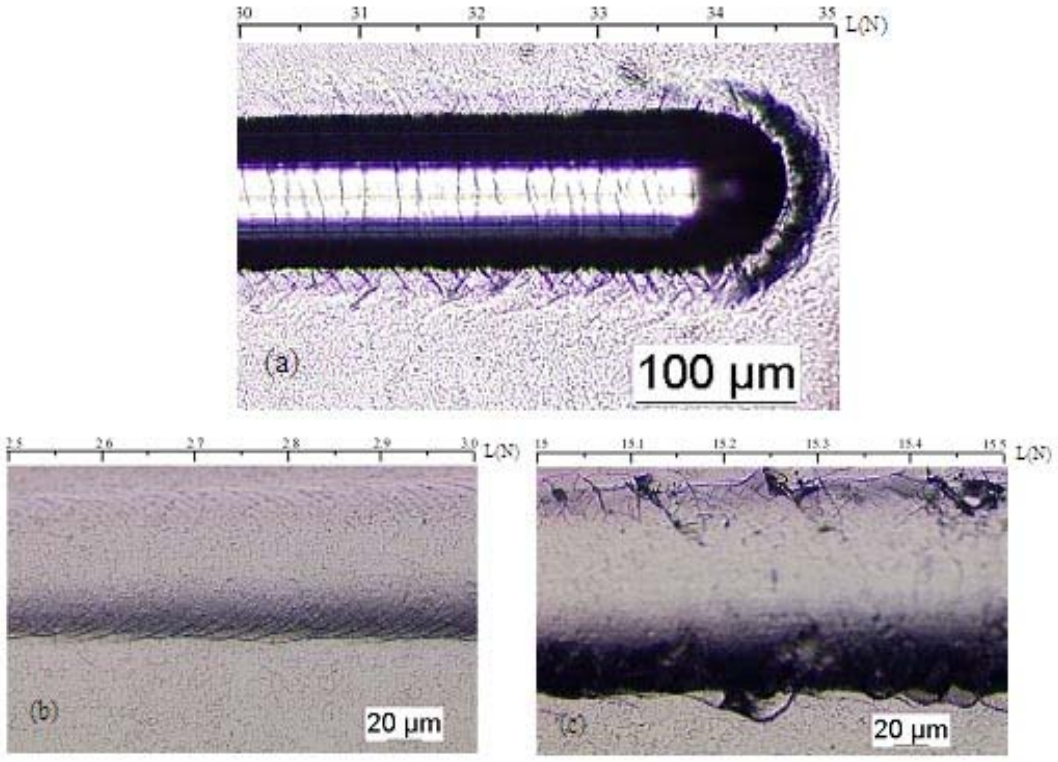

Fig. 3.7 Optical micrographs of the scratch tracks (a) Cr at the end of the track; (b) Conformal cracks for chromium nitride deposited at 12 sccm N_2 with L_{c1}=2.6 N; (c) Chipping failure for chromium nitride deposited at 12 sccm $N_2$with L_{c2}=15.1 N.

Fig. 3.7 presents the optical micrographs of the scratch tracks. For the pure Cr, there is no visible delamination although the arc tensile crack occurs at a load of nearly 10 N (Fig.3.7 a). However, for the chromium nitride coatings, the cohesive failures occur at relatively low loads in the range of 2-5 N. The failure mechanism of these coatings appears to be conformal cracking in the scratch track (Fig. 3.7b). These kinds of cracks are often associated with relatively soft substrates and hard coatings. And in our cases, they could be related to the soft stainless AISI 304 substrates. The adhesive failures of chromium nitride coatings are caused by the chipping at the edge of the scratch track as shown in Fig. 3.7c. For the chromium nitride coatings, the adhesive failure critical loads (L_{c2}) have normal values between 10 to 20 N. The Lc_2 for stoichiometric Cr_2N and CrN coatings are 15 and 15.1 N, respectively. These values seem low as compared to the adhesion properties deposited by other PVD techniques (35-40N) [94], which can be attributed to the presence of a high stress at low temperature and the soft substrate. However, it should be noted that the scratch test results strongly depend on the test setup and test environments. The comparison among different literatures can't provide any evidence to prove that the coating adhesion is better or worse. In this case, in order to improve the adhesion strength, a combination of galvanic and PVD coating maybe a good choice, as suggested by B. Navinsek et al. [104]. Some attempts should be done in the project of replacing electroplated chrome.

3.3.4 Tribological properties

The tribological properties of chromium nitride coatings were examined using a CSM pin-on-disk tribometer with 100Cr6 counterparts. The applied load was 5 N with a sliding velocity of 0.2m/s. These operations were performed in ambient temperature ranging from 25 to 35 ^{o}C and a relative humidity of 50±5%. The average friction coefficient values were calculated using the regions of friction coefficient versus distance curves where the friction coefficient reached a relatively constant value. Two typical curves of friction coefficient vs. sliding distance with

respect to Cr_2N and CrN are shown in Fig. 3.8. It can be observed that the first 200 m distance corresponds to a typical "running-in" process. In this process, the evolution of Cr_2N friction coefficient presents a progressive increase whereas for CrN, the friction coefficient decreases dramatically from the initial 0.9 to 0.5 during the sliding distance of 200 m. After that, the friction coefficient maintains a relatively constant value. Thus, the mean friction coefficient value during the rest distance was taken as the real friction coefficient for all the deposited coatings.

Fig. 3.9 presents the friction coefficients of the deposited coatings at different nitrogen flow rates. It can be seen that the friction coefficients range from 0.5 to 0.75. The pure Cr and stoichiometric CrN have relatively low friction coefficients of nearly 0.5. However, the nanocrystalline Cr(N) solid solution and stoichiometric Cr_2N coatings have the high friction coefficients of 0.73.

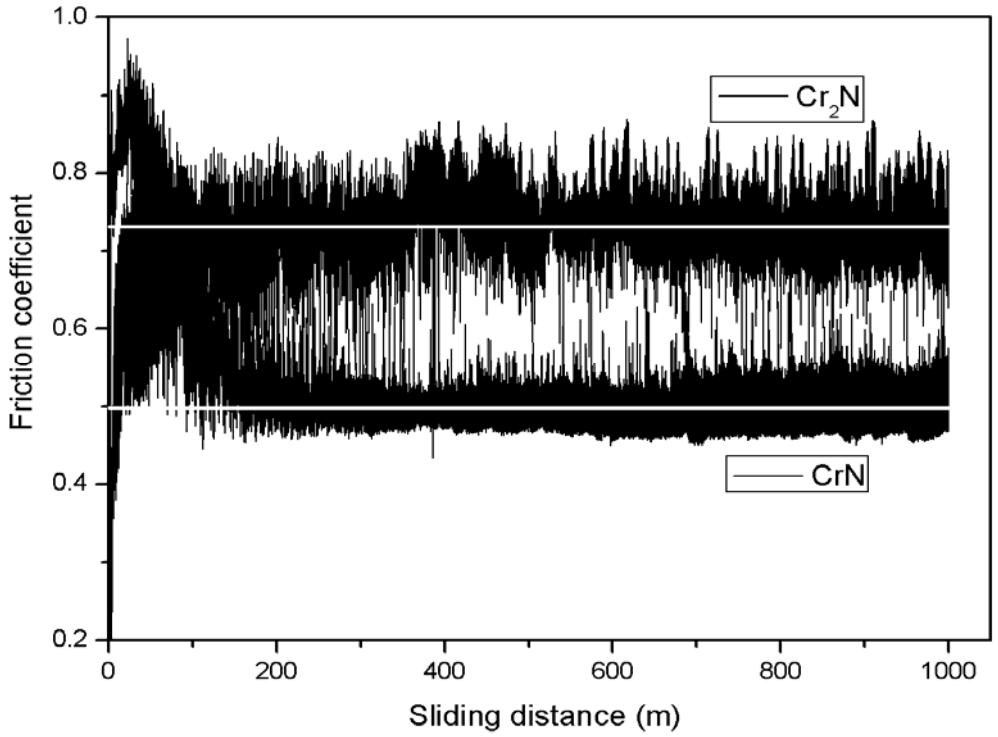

Fig. 3.8 Two typical curves of friction coefficients vs. sliding distance.

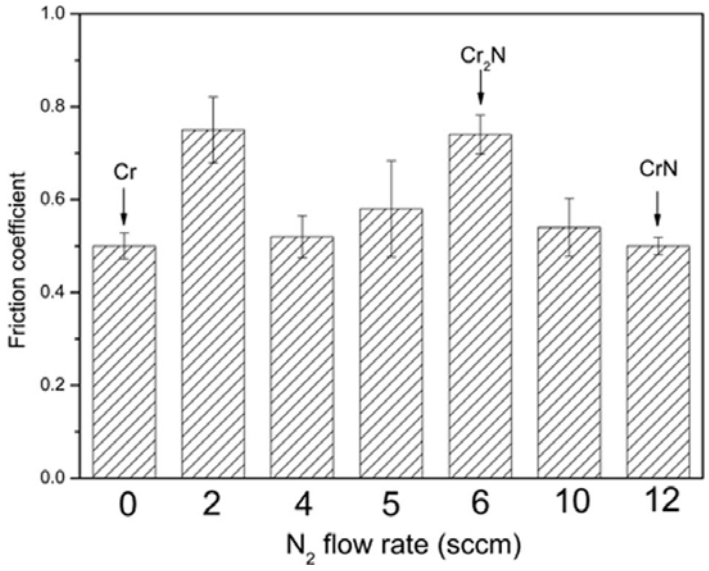

Fig. 3.9 Friction coefficients at different nitrogen flow rates.

Fig. 3.10 shows the results from optical and 3D profile observations for the sputtered Cr, Cr_2N and CrN coatings after pin-on-disk tests. In these cases, the transferred materials from the counter-ball to the disc in the wear track can be clearly seen from the 3D topographies. The sputtered Cr coating shows little damages despite of its relatively low friction coefficient of 0.53. The adhesive wear between the materials on 100Cr6 ball and the materials transferred from the counterpart may be responsible for that. After tests, the observed wear on the counter balls under the optical microscopy also supports the fact of adhesive wear (See Fig. 10d). However, for Cr_2N coating, the abrasive wear by wear debris occurs during sliding contact. As a result of combined abrasive and adhesive wears, the friction coefficients yield the characteristic of high values of approximately 0.73. In the case of CrN coating, material transfer occurs but the damage was quite weak, which can be related to the low friction coefficient in combination with high hardness and modulus in comparison with those of Cr_2N. As shown in Fig. 3.10, different wear mechanisms occur simultaneously during the sliding process, it is very difficult to calculate their wear rate and make comparisons. For this reason, no wear rate is calculated here, the directive observations from coating wear confirm that CrN has a better abrasive resistance compared to Cr_2N, as reported in other literature [91].

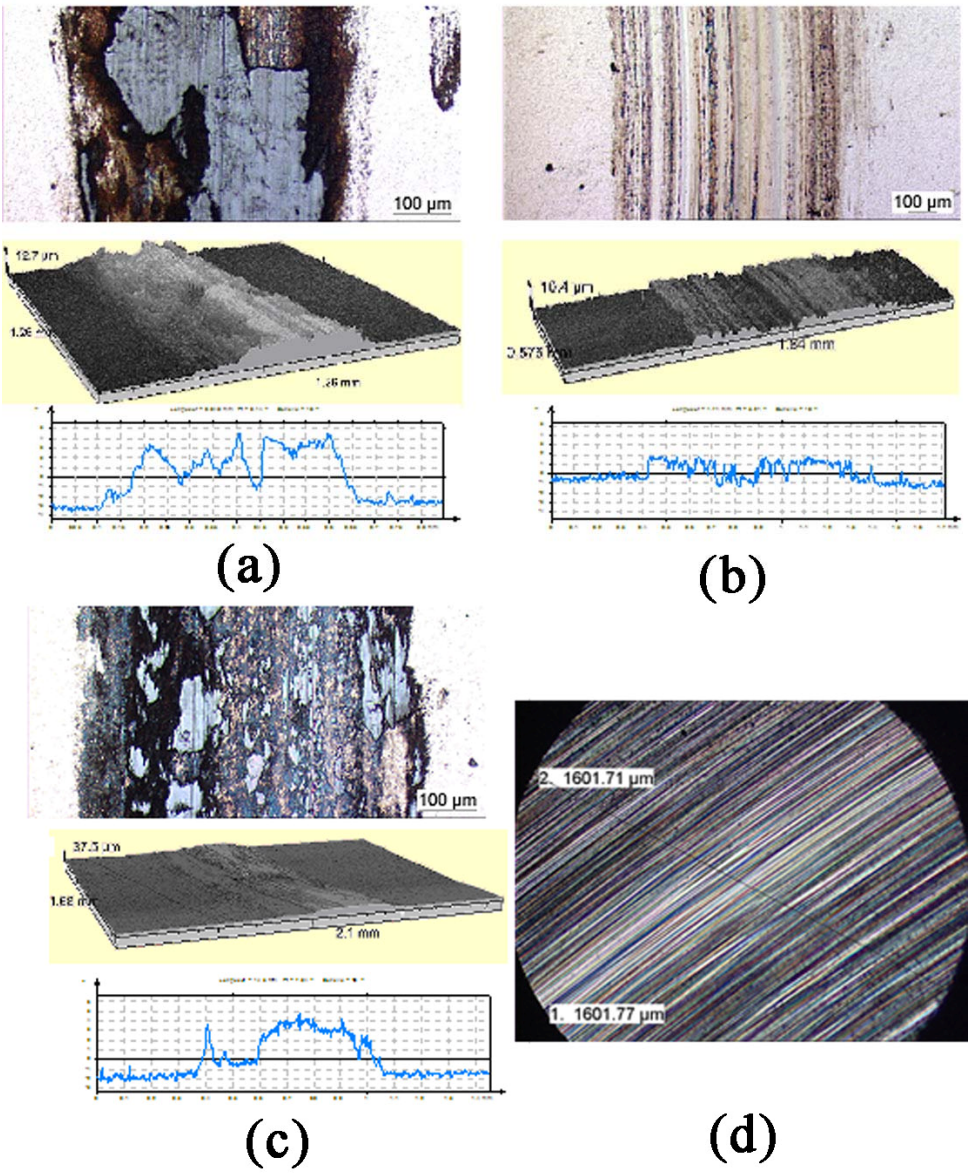

Fig. 3.10 Optical, 3D photographs and profiles of the wear track after the pin-on-disc tests (a) Cr; (b) Cr_2N; (c) CrN coatings; (d) typical ball wear scar.

3.3.5 Corrosion properties

The principle of dynamical polarization method and the test setup to evaluate coating corrosion resistance has been described in Chapter 2. The polarization curves of chromium nitride coatings for different nitrogen flow rate are presented in Fig. 3.11. In this figure, the corresponding nitrogen flow rate to deposit the chromium nitride coating was marked as N_i. For comparison, the polarization curve of the AISI 304 substrate is also plotted in the same figure. The first remark is that the coated

specimens show relative positive corrosion potentials and very low corrosion current densities in contrast to those of the substrate, indicating their strongly protective characteristics. The typical passive behaviors can be observed for all coated specimens and so does the substrate. This is due to the presence of Cr in the materials, which was oxidized during the tests. Therefore the corrosion products (chromium oxides) can stop a further corrosion as they are generally inert in the test environments.

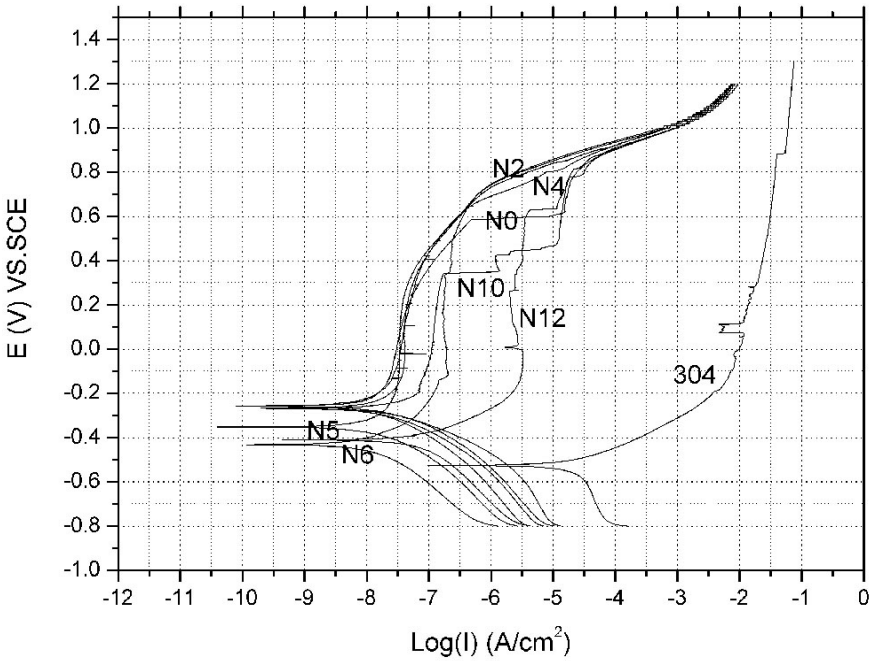

Fig. 3.11 Polarization curves for different chromium nitride coatings and AISI 304 substrates (N_i corresponds to the nitrogen flow rate; i.e. N_2: 2 sccm N_2).

The corrosion potential (E_{corr}) and corrosion current density (I_{corr}) drawn from the Tafel linear zone are presented Fig. 3.12. In all cases, I_{corr} is lower and E_{corr} shows more positive for the coated specimens when compared to the substrate. However, when comparing their E_{corr}, one can find that the non-stoichiometric coating presents more positive E_{corr}, which is due to the formation of chromium oxides in these coatings. The most positive E_{corr} is -260 mV (vs. SCE) for both the pure Cr and the amorphous-like chromium nitride coatings (a-CrN). On the contrary, the stoichiometric CrN present the most negative E_{corr} of -451 mV. E_{corr} of Cr_2N coating

has a little improvement of 30 mV to positive direction in comparison with CrN. For I_{corr}, similar results are found. A-CrN with a nitrogen flow rate of 4 sccm presents the lowest I_{corr} of one order of magnitude than the highest I_{corr} from stoichiometric CrN. This can be attributed to the homogenous composition distribution in the amorphous phase. As to pure Cr and Cr_2N, they present medium I_{corr} comparable to that of a-CrN (4 sccm N). In short, the order of corrosion resistance of the chromium nitride coatings in a 3.5 % NaCl aqueous solution is a-CrN > Cr > Cr_2N > CrN > AISI 304.

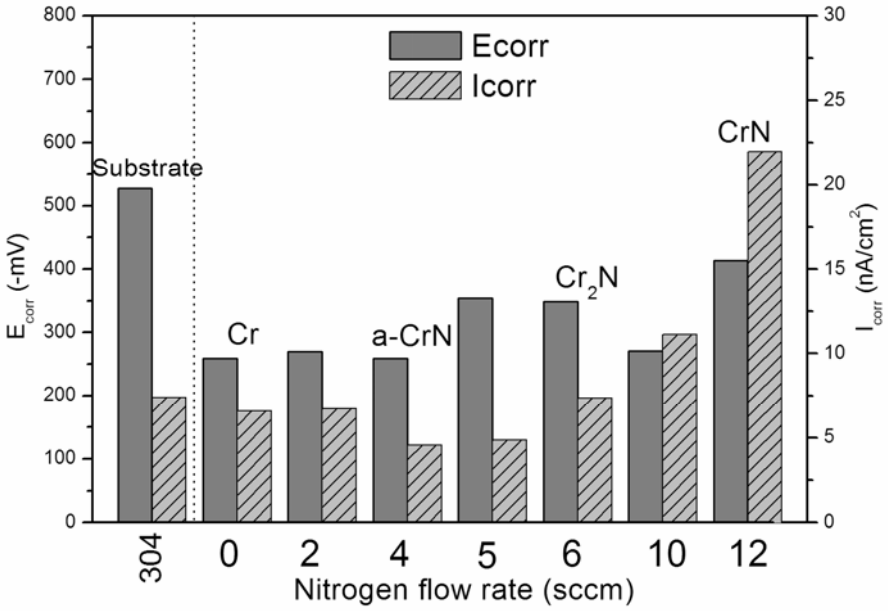

Fig. 3.12 E_{corr} and I_{corr} of chrome nitrides as a function of nitrogen flow rate.

After the tests, the coating surfaces were examined by SEM. The SEM images of the pure Cr, stoichiometric Cr_2N and CrN are shown in Fig. 3.13. From this figure, the coating surfaces were almost uncorroded, which can also be reflected by the extremely low I_{corr} in nano order. However, as shown in the figure, there are still a very small amount of parts of the surfaces that were corroded. Since the transition metal nitride coatings are generally inert to the environments, the most common corrosion behaviors are the pitting corrosions. This means that the most important corrosion part in the coated system is the substrate, which is caused by the Cl^- ion etching in and finally it formed a pathway between the corrosion solution and the substrate. Pinholes can be observed on the coating surface as shown in Fig. 3.13.

Taking into account I_{corr} of all the coated specimens, it is suggested that during the initial stages of corrosion, the pinholes are very small and most of them may become blocked by corrosion debris. Therefore, no breakdown or spalling of the coating was observed as what has been reported for the PVD coating [105]. This is possibly associated with the corrosion products filling in the hole, thus plugging the holes and blocking the passage of the electrolyte for further corrosion to occur. These small pitting corrosions are often originated from the growth defects or are due to the no density columnar structures.

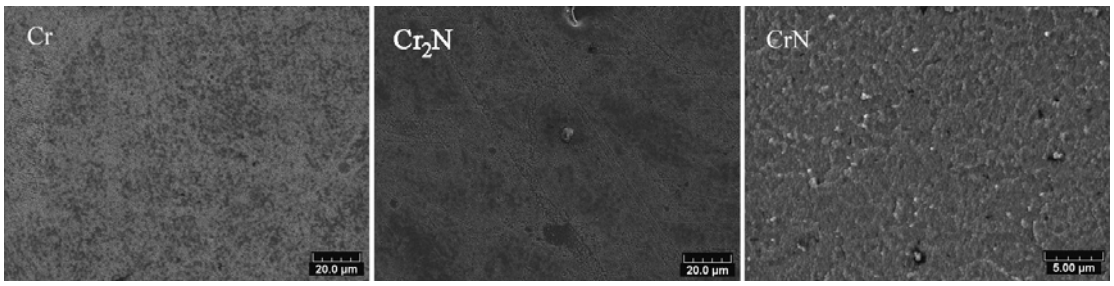

Fig. 3.13 coating surface morphologies after corrosion test.

3.4 Influence of RF bias on structures and properties of CrN coatings

3.4.1 Plasma characteristics by OES on film synthesis

In this part, an Optical Emission Spectroscopy (OES) diagnose system was used to identify plasma spectra as it yields information about the formation of ions and radicals in plasma [106]. The information is very important to understand the internal physical and chemical process of the plasma during the coating deposit. On the other hand, the information on variations of OES signals and the correlations between OES signals and the structure and properties of the deposited coating are very useful for optimizing the deposition process and for controlling the quality of deposited coatings

[95, 96, 107]. In the present work, as the substrate was polarized by RF discharge during the DC reactive magnetron sputtering process, the electric yield near substrates greatly influences the flux and energy of incident species, in turn, the coating growth process. In this study, the recorded OES signals near both target and substrate were investigated by varying RF self-bias from 0 to -200 V.

OES measurements of the plasma discharges were performed by means of a computer-controlled system, which comprises a Proper Scientific SpectraPro-500i imaging monochromator with a triple grating, the focal length of 500 mm, and a spectral resolution of 0.05 nm. The emitted light was studied at two different positions named “near-target-zone” and “near-substrate-zone”, respectively. The “near-target-zone” is the position located at the edge of the sputtering target and nearly 2 cm from the target surface. The collected spectra in this position can be considered all from the magnetron target discharge plasma. The “near-substrate-zone”, however, is at the edge of the round substrate holder and nearly 2 cm from its surface. In this position, the collected spectra yield the information of physical and chemical processes occurring on the substrate. The emission spectra were collected using a fiber optical cable fitted with a 1500 mm long, rectangular collimator, pointing perpendicularly toward the axis. All the spectra were collected with an integration time of 0.5 s per wavelength and the step of length was 0.1 nm. Generally, the zone between 300 to 550 nm was selected for analysis as this zone includes most of information about N_2 and Ar discharging.

For the obtained OES spectrum, molecular and atomic emission lines were identified by using the literatures [106, 108] and NIST Atomic Spectra Database. In Fig. 3.14, a typical OES spectrum from “near-target-zone” is shown. On the top axis, various lines are identified and the selected lines to represent specified particles such as Cr, Ar, Ar^+, N_2, and N_2^+ are marked with stars. The lines were selected following the criteria suggested by K.S. Mogensen et al. [106]: (1) the lowest possible activation energy; (2) no overlap between lines originating from different species. The selected represented lines are listed in Table 3.2. In Fig. 3.14, it can be found that N and Cr^+ emission lines are too weak to be observed, which, in the present case, can be attribute

to the low electron temperature in this conventional magnetron sputtering unit since N, Cr^+ are mainly formed by dissociative excitation and ionization [97].

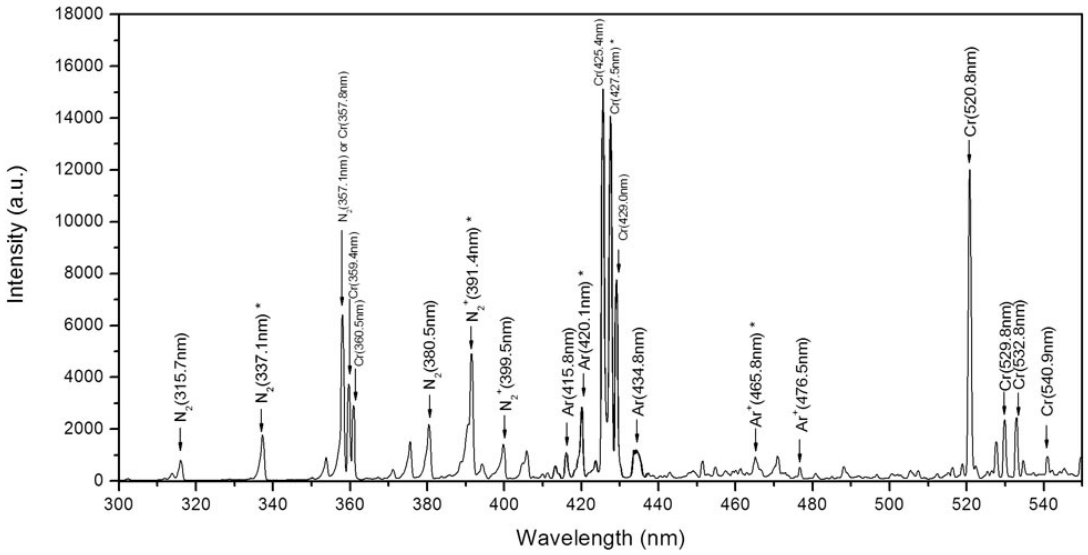

Fig. 3.14 Typical OES spectrum at "near-target-zone".

Table 3.2. Selected optical emission spectroscopy lines. The data was referenced to National Institute of Standards and Technology (NIST) atomic spectra database and Ref [9,11].

Species	Wavelength (nm)	Transition	Excitation energy (eV)
N_2	337.1	$C^3\prod_u - B^3\prod_g(0\text{-}0)$	11.1
N_2^+	391.4	$B^2\sum^+_u - X^2\sum^+_g$ (0-0)	18.7
Ar	420.1	$3s^23p^5(^2p^0_{3/2})4s - 3s^23p^5(^2p^0_{3/2})5p$	14.5
Ar^+	465.8	$3s^23p^4(^3p)4s - 3s^23p^4(^3p)4p$	19.8
Cr	427.4	$3d^5(^6s)4s\text{-}3d^5(^6s)4p$	2.8

Ion bombardment characteristics during magnetron sputtering depositions are fundamental plasma parameters and the ion flux and energy are important. In the present study, the flux of ion bombardment arriving on the growing thin films can be evaluated by the total time average discharge current density ($\bar{J}_s$) on the substrate holder. However, for the ion energy, it is a little complex as the ion species and energy distribution could not be determined simply. A simple analysis can be carried out to understand the relationship between the mean ion energy, in terms of L/λ_i ratio, and substrate bias $|U_b|$ [108], where L is the sheath thickness, and λ_i is the ion mean free path for the collisions leading to losses of ion energy in the sheath. During the

depositions, as the total pressure kept constant, the ion mean path (λ_i) can be thought unchanged. When rising $|U_b|$, the plasma sheath thickness would increase correspondly, as a result, the ion mean energy to bombard the growing thin films increased. Table 3.3 summarizes the effects of $|U_b|$ on the magnetron target discharge characteristics. The constant target current corresponds to a target current density J_{dc} = 17.7 mA/cm^2, at a nearly constant pressure of 0.27 Pa. From this table, a gradual increase flux of ions bombarding the growing thin films can be observed and two different ion flux levels are distinguished. The lower $|U_b|$ (< 100 V) corresponds to the average ion flux of 0.22 mA/cm^2 while the higher $|U_b|$ (> 100 V) has another level of 0.26 mA/cm^2. On the other hand, one can find that the mutual coupling effect between DC magnetron discharge and RF capacitive coupling discharge leads to the increase of $|U_{dc}|$. As a consequence, the power exerted on the target increased (7% roughly from 0 to -200 V bias) and the sputtered Cr flux increased with the higher $|U_b|$.

Table 3.3. Effects of RF substrate bias voltage on the discharge characteristics. The corresponding target current I = 1.5 A, J_{dc} = 17.7 mA/cm^2, and the total pressure p = 0.27 Pa.

$-U_b$ (V)	P_b (W)	$\bar{J}_s$ (mA/cm^2)	U_{dc} (V)
0	0	-	454
20	10	0.22	458
60	30	0.22	469
100	50	0.22	472
150	90	0.26	480
200	120	0.26	485

The effects of $|U_b|$ on various OES signals at “near-target-zone” are presented in Fig. 3.15. All the signals were normalized to the values at 0 V bias. In Fig. 3.15, the evolution of OES signals at “near-target-zone” with growing $|U_b|$ does not present any evident linear relationship. Three different parts in this figure can be roughly distinguished. Part I corresponds to a lower $|U_b|$ (< 20 V), where all the excited line intensities keep unchanged in comparison with those without $|U_b|$, suggesting that low RF bias applied on the substrate holder did not affect the target discharge characteristics and the two different discharge zones do not show any interactions.

This can also be identified by the very small variations of sputtering power (see Table 3.3). Part II is related to the moderate $|U_b|$ ($20 < |U_b| < 100$ V). In such part, Cr, Ar^+, N_2^+ and N_2 line intensities increase with growing $|U_b|$ whereas Ar line intensity firstly shows a little increase then slightly decreases. The increase of the selected line intensities can be associated with the growing of species energy as more power was introduced on the sputtered target. This also indicates that the coupling effects between magnetron target zone discharge and deposition zone increase. Part III was for $|U_b|$ beyond 100 V, in which the RF bias effects on Ar^+, Cr line intensities and N_2, N_2^+ and Ar line intensities are totally different. Ar^+, Cr line intensities continue to increase when the higher $|U_b|$ (> 100 V) was applied. However, the line intensities of N_2, N_2^+ and Ar present a trend of decrease under the same conditions. This phenomenon can be attributed to the well-known sputtering wind effect [109, 110], which proceeds from the heating of the gas by the energetic sputtered metal atoms and is the origin of a decrease in the gas density in front of the target. As a result, the increased power on the target reduces the nitriding kinetics on the target surface. In turn, the increase of sputtered Cr flux can be expected. The increased sputtered particles would carry away more reactive species and further reduce nitrogen density near the target. In the evolution of OES signals with growing $|U_b|$, this was shown as the increased Cr line intensity and the decrease of both N_2 and N_2^+ line intensity. From Fig. 3.15, it would be very interesting to conclude that to keep the formation of stoichiometric nitrides as the sputtering target work in a transition zone, more nitrogen are needed as the substrate bias increases.

The effects of $|U_b|$ on OES signals at “near-substrate-zone” are illustrated in Fig. 3.16. It can be found that all the considered emitted line intensities increase when increasing $|U_b|$, suggesting the growing of the species populations in the excited states. The most significant increased lines with growing $|U_b|$ are N_2^+ and Ar^+ excited states. As these two signals correspond to relatively high excitation energies (see Table 3.2), the formation of such states can be related to the power activated desorption of containing species from the surface of the growing films and electron impact dissociation of gas molecules in RF sheath [108]. It should be noted that the

intensities measured at "near-substrate-zone" are much lower than those at "near-target-zone" due to the facts that the detect zone is largely inside the dark region of the RF sheath and the supplied RF power is less than that of magnetron discharge.

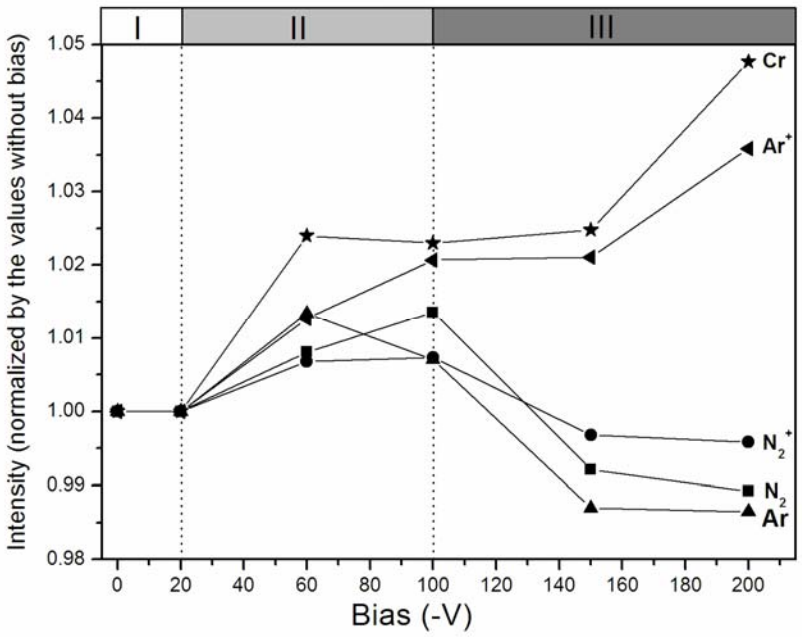

Fig. 3.15 Various OES signals as functions of the substrate bias at "near-target-zone".

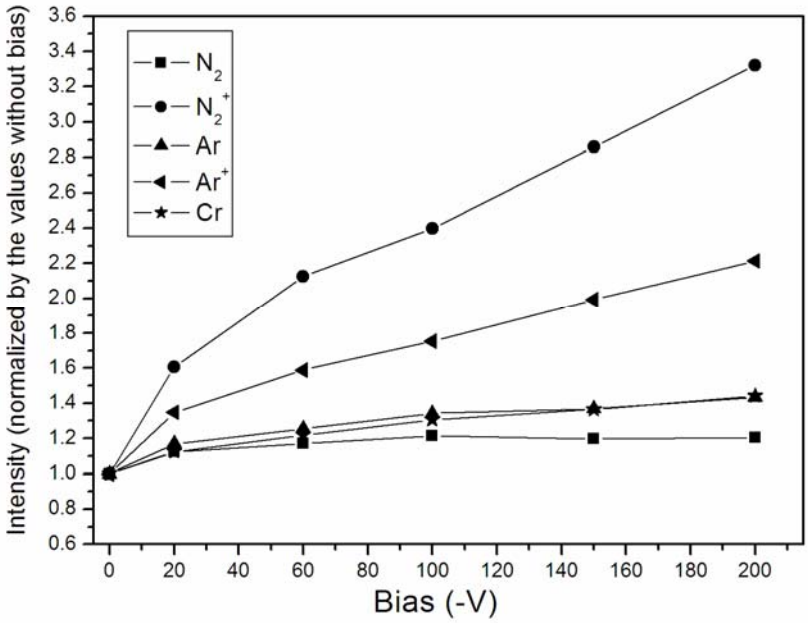

Fig. 3.16 Various OES signals as functions of the substrate bias at "near-substrate-zone".

3.4.2 Correlations between OES signals and coating compositions and structures

The results of $|U_b|$ on the coating compositions and structures are shown in Fig. 3.17 and Fig. 3.19 respectively. The evolution of composition vs. $|U_b|$ indicates that the concentrations of Cr in the coatings increase with growing $|U_b|$ whereas the simultaneous decrease of nitrogen content can be observed.

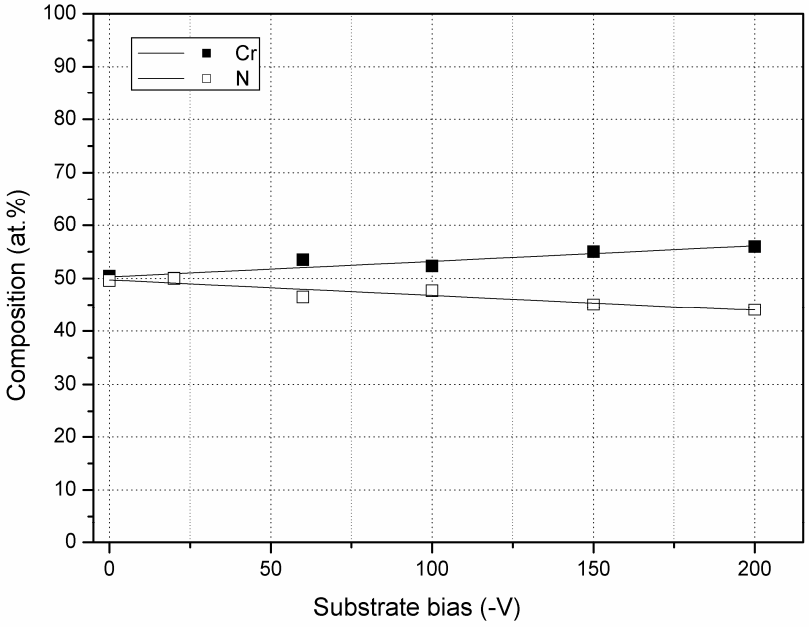

Fig. 3.17 Evolution of coating compositions vs. substrate bias $|U_b|$.

The applications of a bias on the substrate during magnetron sputtering process have often been expected to enhance ion bombardment effects. RF bias, however, additionally provides the possibilities to affect the internal reactive kinetic process during a reactive sputtering. When CrN coatings were synthesized using magnetron sputtering, it is likely that the reaction process occurred on substrate surface or target surface or both as the working atmosphere chosen initially can form stoichiometric CrN at a transition zone. Taking into account the process on target surface firstly: assuming that the nitrogen molecules gather on target surface and react with target atomics to form a thin covering layer, then electron impact dissociated Ar^+ and N_2^+ ions. These ions are accelerated to bombard target surface and eject Cr or CrN species.

As there isn't any CrN optical emission characteristics to be observed, the sputtering CrN molecules should be instantaneously dissociated and reinjected into plasma as Cr + N according to Ref [111]. However, the fact is that there is also no N emission lines found in OES spectrum. The reasonable explanations are that on the target surface, the sputtering of Cr is predominant in spite of the possibility of forming CrN layer. This is also based on the fact that nitrogen does not react readily with Cr as it does with an element such as Ti [98]. The obtained CrN coating without bias having a high deposition rate can also confirm this. Therefore, the main reaction process to form compound coatings occurs on substrate surface.

Focusing on the chemical reaction kinetics on the substrate surface, when taking into account the effect of plasma process on coating composition, two important factors should be considered: one is the arrived sputtering atomic flux and the other is related to the process of gas kinetics (absorption and desorption) on the substrate surface. The increased Cr flux arriving on substrate can be expected as a consequence of increased sputtering Cr flux from target with growing $|U_b|$, which can also be confirmed by the increased OES signal of Cr at "near-substrate-zone". On the other hand, for the process of gas molecular absorption and desorption on the substrate surface, the increased $|U_b|$ improves the positive Ar^+ ion bombarding effects, which would provoke the nitrogen gas adatoms tending to be desorbed because ion bombardment can play the same role as improving substrate temperature [74, 95]. The process can be identified by the increased signal intensities of both N_2^+ and N_2 emitted lines at "near-substrate-zone". As a result, the insufficient nitrogen absorption on the substrate surface and the increased Cr flux would form N deficient coatings. In addition, the preferential sputtering of nitrogen at enhanced ion bombardment can also contribute to this N deficiency phenomenon [108].

Many research works argued that atomic N plays an important role in the deposition of nitride coatings [108, 111]. However, in our cases, it doesn't seem to act like that. The fact that no atomic N emission characteristics were found in both "near-target-zone" and "near-substrate-zone" inferred that Cr and atomic N reaction is not dominant in the formation of CrN coatings. In contrast, the predominant reaction

probably occurs between the sputtered Cr and the absorbed nitrogen. As the emission line intensity of N_2 can be roughly thought to be proportional to the reactive nitrogen，therefore, the emission line ratio of $I(N_2)/I(Cr)$ is used to predict coating compositions. Although there are big differences between their excitation energies, it can still be expected to roughly show the evolution trends of composition vs. RF self-bias. The results are shown in Fig. 3.18. For comparison, the real composition ratio C(N)/C(Cr) is also given in the same figure. As it has been mentioned that the stoichiometric CrN can form under a condition without bias, thus $I(N_2)/I(Cr)$ ratio was normalized to 1:1 at $|U_b| = 0$ V. It can be seen that $I(N_2)/I(Cr)$ curve was very consistent with the real composition curve C(N)/C(Cr), which would be useful when using an OES system to monitor the CrN coating deposition process.

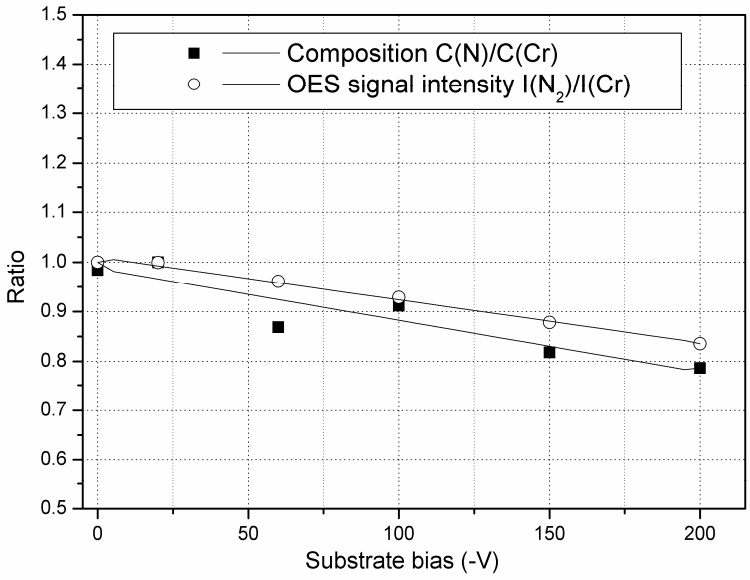

Fig. 3.18 A good agreement between OES signal intensity ratio $I(N_2)/I(Cr)$ and composition ratio C(N)/C(Cr).

The evolution of CrN structure with growing $|U_b|$ is shown in Fig. 3.19. The coating without RF bias presents a face centered cubic (FCC) stoichiometric CrN structure. The diffraction peaks such as CrN(200), (111), (220), (311) can be well indexed. When increasing $|U_b|$ to less than 20 V, the action of the bias does not show any important effects on the coating structure as predicted by the OES signals. However, when the RF bias $|U_b|$ increased to 60 V, all peak intensities decrease.

Moreover, the peak of CrN(200) indicates a splitting, which can be related to the decrement of nitrogen in the coatings. As $|U_b|$ is beyond 60 V, ion bombarding exhibits their effects on decreasing grain size, which can be concluded by the increase of FWHM (Full width at Half Maximum) at peak position of CrN(200).

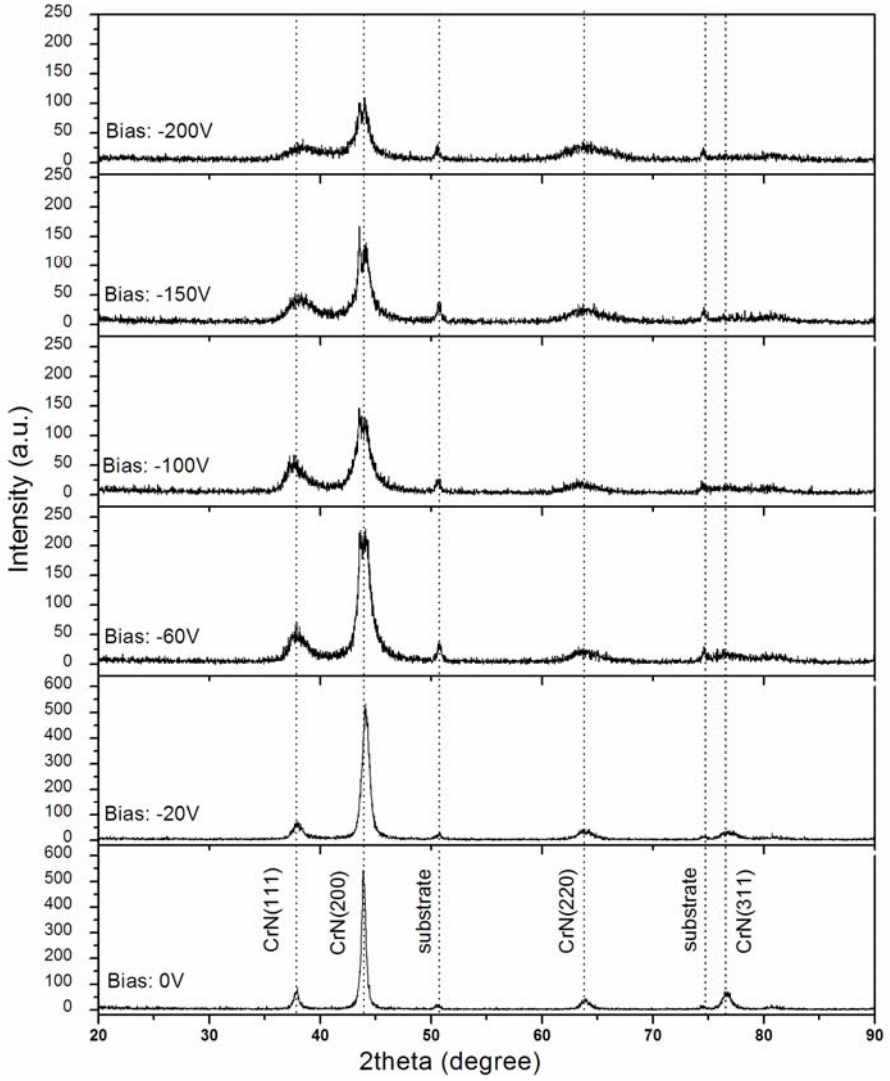

Fig. 3.19 Evolution of CrN coating structures vs. substrate bias $|U_b|$ in XRD patterns.

The other evident change observed in Fig. 3.19 is the decrease of diffraction intensity when increasing $|U_b|$. As $|U_b|$ increased to 150 V, the peak of CrN(200) splits into two peaks. However, the coating still presents CrN predominated phase. The results of structure analysis show good agreements with those of composition analysis.

3.4.3 Coating morphologies

The cross-section micrographs for all the coatings on the silicon substrates vs. different substrate biases are presented in Fig. 3.20. The columnar structures for the coating deposited at $|U_b|< 20$ V can be observed clearly. The coating thickness shows little change under this lower bias. When the coatings were deposited with $|U_b|$ between 60 to 100 V, their thicknesses decreased and the columnar structures became ambiguous, which indicates the coating microstructures become denser. The further increase of $|U_b|$ leads the coating cross-section morphologies to return to an evident columnar structure again. However, such coatings have the same thickness like that without bias, which means they have high deposition rates. This is due to the fact that the sputtered target surface covered less compound containments. From the evolution of coating morphology, it is inferred that the range of bias potential between -60 to -100 V could improve the microstructure and restrict the void-type columnar and eliminate the network of crack-like voids as reported by others [112].

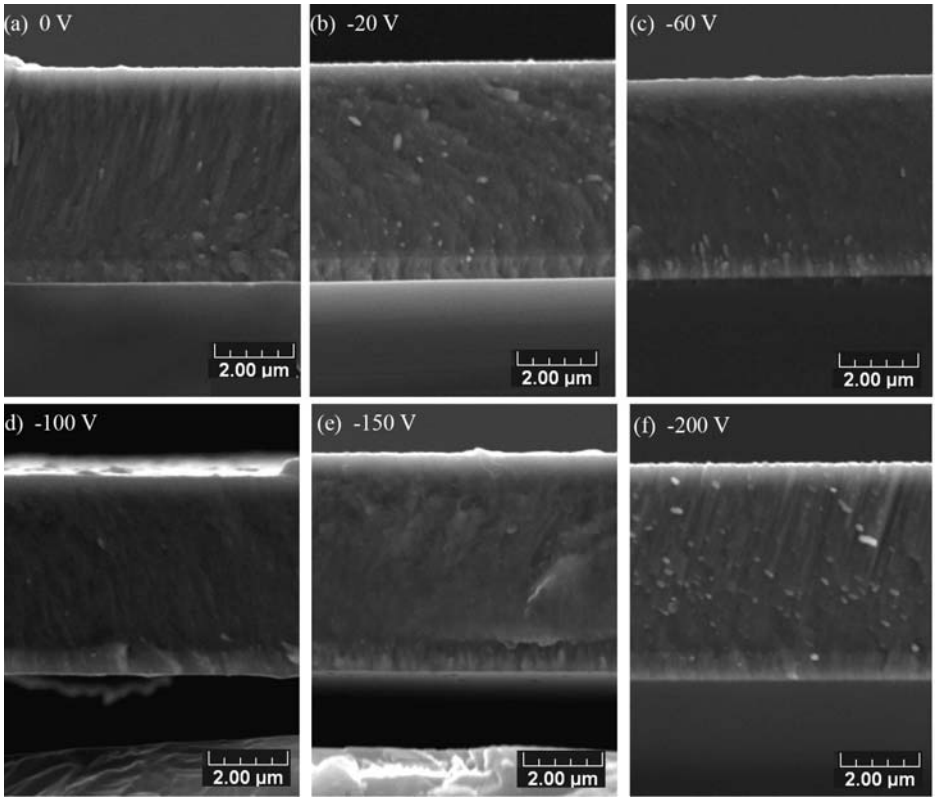

Fig. 3.20 Evolution of CrN cross-section morphology vs. substrate bias $|U_b|$.

The top-view morphologies of CrN coatings by Atomic Force Microscope (AFM: 1μm x 1μm) are given in Fig. 3.21. It is can be observed that without bias, the coating surface is composed of many different height hilltops, which array tightly and are isolated by small boundaries. With increasing $|U_b|$, the difference of height between the hilltops reduces. As $|U_b|$ increases to 200 V, the top-view image of the coating returns to that without bias and the small difference is that the hilltops become tighter and more regular. This could also be related to their high deposition rate. Correspondingly, the variations of the coating surface morphology are related to the change of surface roughness. The roughness initially increases from 5 nm to 8 nm when $|U_b|$ increase from 0 to 60V. The further increase causes the roughness to decrease to 6.5 nm at $|U_b|$ = 150 V. Finally, the coating roughness returns to a relative high value of 9.4 nm when a higher $|U_b|$ of 200 V was applied.

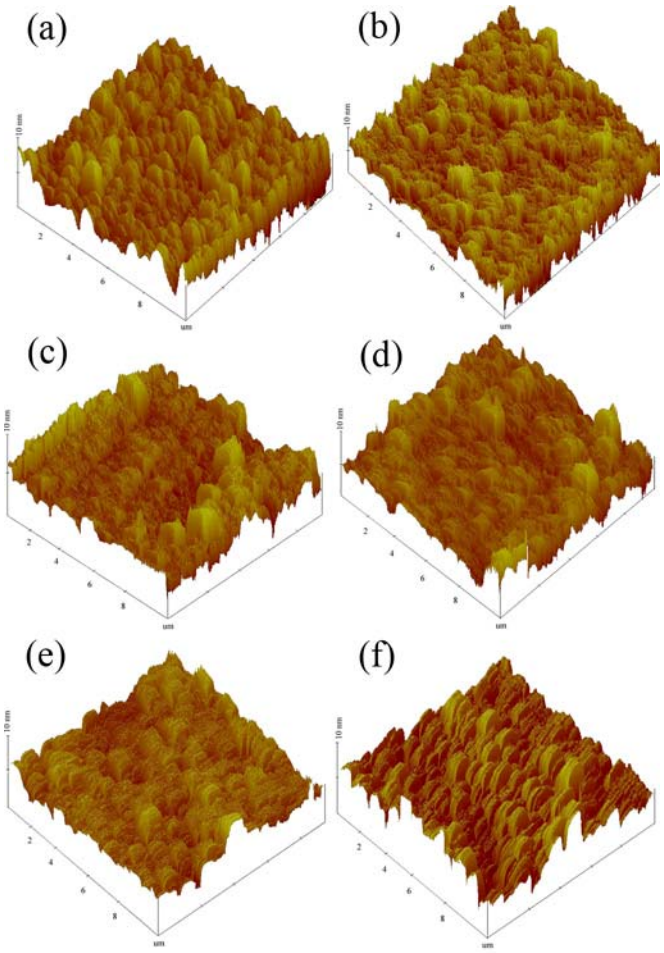

Fig. 3.21 The top-view AFM images of CrN coatings deposited at different substrate bias $|U_b|$: 0 V; (b) 20 V; (c) 60 V; (d) 100 V; (e) 150 V; (f) 200 V.

The evolutions of cross-sectional and top-view morphologies indicate that ion bombarding due to the application of RF bias has great influences on coating morphology. It is well known that the adatom surface migration plays an important role in the coating morphology. The abilities of adatom mobility are mainly determined by substrate temperature and ion bombardment energy. In our study, as no substrate heating system was used, the applied substrate bias plays a decisive role for the adatom mobility. Taking into account the coating-atom condensation process for pure metals, it is usually divided in three stages [113]. The first stage is the collision of incident atoms with the substrate surface. They transfer kinetic energy to the lattice and become loosely bonded "adatoms". These adatoms may diffuse over the surface, exchanging energy with the formed lattice and other adsorbed species in the stage two. The diffusion of these adatoms ends when they are desorbed, by evaporation or sputtering, or become trapped at low energy sites. The final stage is the readjustment of the trapped atoms within the lattice. During the three stages different physical processes are involved in the trajectory of an atom: 1) shadowing, the geometric interaction between the roughness of the growing surface and the angular direction of the arriving atoms; 2) surface diffusion, which is related to the activation energy for surface diffusion; 3) bulk diffusion, which depends on the activation energy for bulk diffusion; and 4) the desorption which is controlled by the sublimation energy.

At different temperature ranges different processes might dominate. Therefore, the structure zone model for growth is divided into ranges determined by the ratio (t) between the deposition temperature ($T_{deposit}$) and the melting temperature (T_{melt}), i.e. $t= T_{deposit}/ T_{melt}$. It is should be noted that for a reactive sputtered film the heat of formation can also be of importance in the deposition process. Nevertheless, in many cases, it is suggested that the existing models are roughly divided into three zones:

1. $T_{deposit}/ T_{melt} < 0.3$ consists of tapered crystals with domed tops, which are separated by porous boundaries: low activity or surface diffusion.
2. $0.3 < T_{deposit}/ T_{melt} < 0.5$ consists of columnar grains separated by distinct dense, inter-crystalline boundaries. The surface has a smooth appearance.
3. $T_{deposit}/ T_{melt} > 0.5$ consists of equiaxed grains controlled by bulk diffusion.

CrN has a melting temperature of 1773 K [114]. As in our case, no heating system was used; the maximum deposition temperature detected by an infrared thermometer is only about 600 K even at a high RF substrate bias of 200 V. Thus, the CrN coating should have a morphology that is comparable to that of the first zone. Indeed, from either the cross-sectional images or the top-view, it can be seen that without bias, the coating morphology presents a structure consisting of tapered crystals with domed tops (see Fig. 3.20a and Fig. 3.21a) as the surface atomic mobility is very low at room deposition temperature. When $|U_b|$ increases more than 60 V, Ar^+ ion bombarding energy increases as indicated in the OES signal, which can improve the coating microstructure, restrict the columnar structure and finally make the coating dense and smooth. This is comparable with an increase in surface diffusivity, a change to zone 2. This influence on coating morphology can be clearly seen in Fig. 3.20b, c and Fig. 21b, c, d. A little difference is that the coating seems to be denser in comparison with those without bias. When $|U_b|$ increases further (> 100V), it is surprising that the coating morphologies seem to be similar with that without bias. It is sure that at this level of ion bombardment, the increased amount of ion impinging on the growing film surface is expected with further increasing bias. However, the coating morphologies do not seem to enter into zone 3. This can be related to the changes of the flux ratio J_{Cr}/J_{n2} as discussed in the OES analysis and from the composition results.

3.4.4 Coating mechanical properties

The evolution of coating hardness (H) and elastic modulus (E) vs. substrate bias $|U_b|$ is present in Fig. 3.22. It can be seen that the hardness of coating initially increase with increasing $|U_b|$ until it reaches a maximum value of 24 GPa at $|U_b|$ = 60 V, then it decreases with further increasing $|U_b|$. This phenomenon could be associated with the changes of nitrogen in the coatings as the sub-stoichiometric nitride yields lower hardness in comparison with those of the stoichiometric nitrides. The evolution of elastic modulus shows very small changes with different $|U_b|$. However, one can still

observe a small amount of increment of modulus when the bias was between 60 and 100 V. The maximum modulus of 308 GPa is achieved at RF bias of 20 V. However, the modulus for the coating deposited with bias of 60 V has a comparable value of 301 GPa. It is suggested that the bias between 60 and 100 V is a good choice for obtaining CrN coating with both high hardness and high modulus.

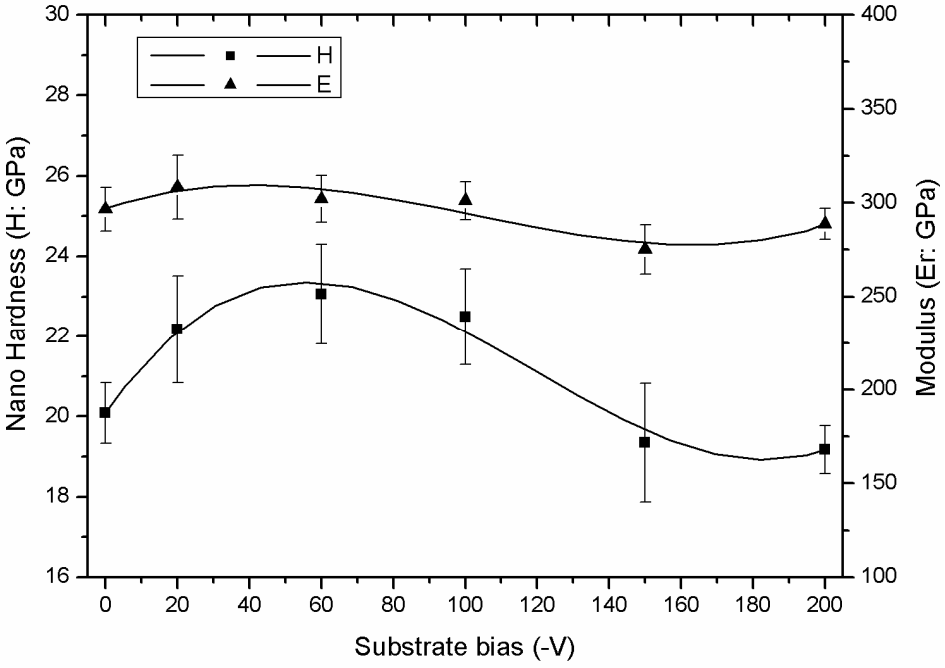

Fig. 3.22 Nano hardness and elastic modulus as functions of the substrate bias $|U_b|$.

The scratch test results are shown in Fig. 3.23. The cohesive critical loads (L_{c1}) and adhesive critical loads (L_{c2}) are defined as what has been done in the investigations of nitrogen influence on CrN. It can be seen that the chromium nitrides with substrate bias present low critical loads (L_{c1}) between 5 N and 7 N. On the contrary, the coating without bias shows a relative high L_{c1} nearly 20 N. In addition, it can also be found that the values of L_{c1} do not show too much dependence on the substrate bias. For L_{c2}, they present a similar evolution as L_{c1}, the coating without bias present L_{c2} of 22 N, much higher than the others. In fact, the value of the critical load depends not only on the interfacial adhesion between coating and substrate, but also on the thickness of the coating, substrate/coating properties such as hardness, internal stresses in the coating and the friction coefficient between coating and stylus [115]. As

presented in Fig. 3.20, the thicknesses of all the coating do not show too much difference. The coating structure and the stylus didn't change during the scratch tests, hence, the unchanged friction coefficients. On the other hand, the hardness of CrN without bias and the CrN with the highest bias have the almost same values whereas their critical loads have big differences. Therefore, the only reasonable explanation for this is the difference of internal stress due to the ion bombardment. Generally, these coatings under substrate bias have a compressive residual stress, which acts as a pre-load on the coating/substrate interface [116]. Although the presence of such stress improves coating hardness as presented in Fig. 3.20, they also reduce the practical adhesion and therefore the critical load.

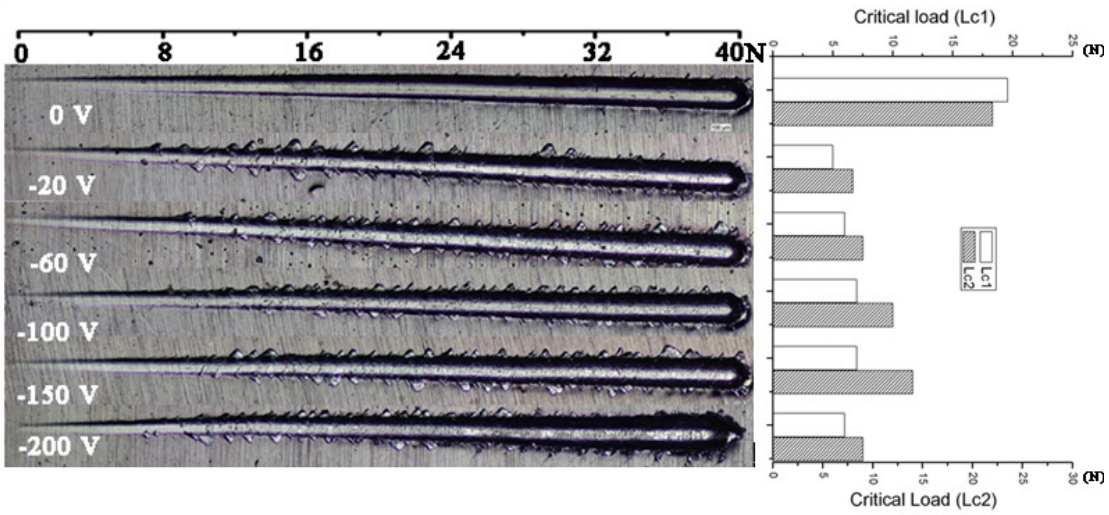

Fig. 3.23 Optical images of scratch test results of chromium nitride coatings and their critical load with different substrate bias.

3.4.5 Coating tribological properties

The tribological properties of chromium nitride coatings with different substrate biases were examined with 100Cr6 counterparts. The applied load was 2 N. The other test parameters were used as they were evaluated on the investigation of nitrogen partial influence on CrN. The evolution of friction coefficients with different substrate biases can be found in Fig. 3.24. It can be found that the friction coefficient are almost

the same level of nearly 0.7 except for the coating deposited with a bias of – 60 V, which has a relatively low friction coefficient of 0.55. This can be attributed to the high hardness of this coating.

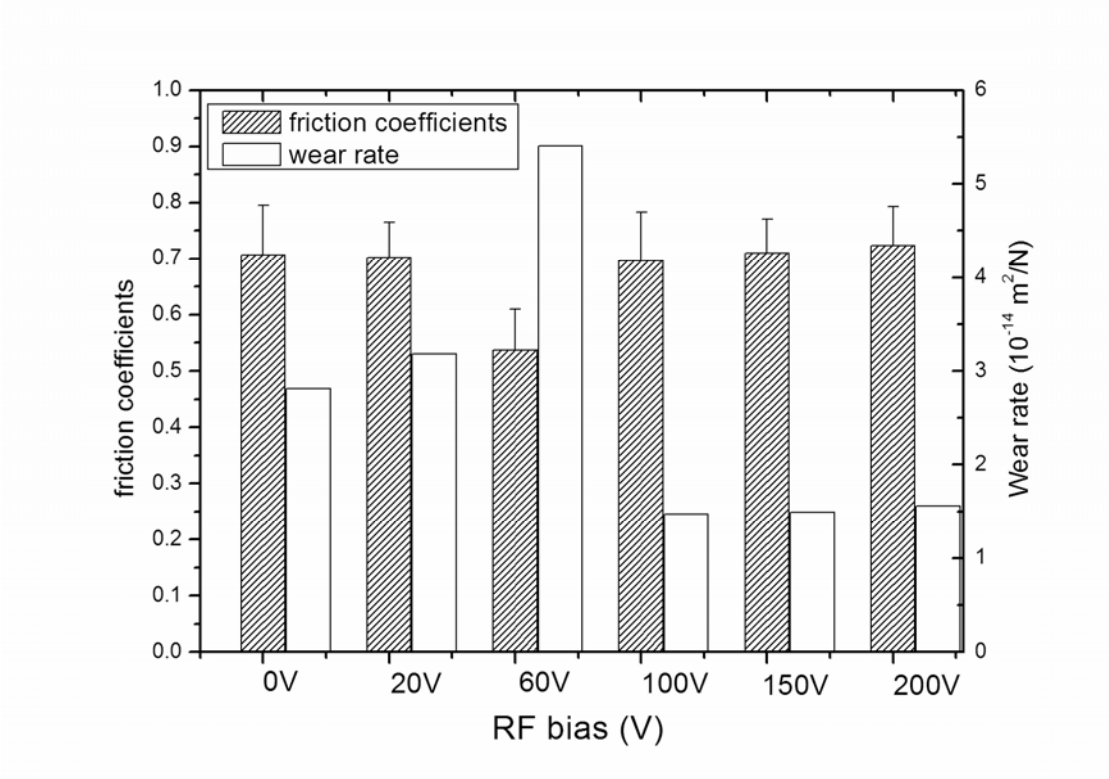

Fig. 3.24 Friction coefficients and wear rates during the sliding wear for chromium nitride coatings with different substrate biases.

Fig. 3.25 presents the wear track and the counter-ball surface morphologies under the optical observations. These images correspond to a typical chromium nitride coating with a bias of -100 V. In fact, the wear track and the ball morphologies for the other coatings show the similar photographs. From this figure, it is evident that the main failures occurs on the ball surface instead of the coating surface. This is due to the high hardness of chromium nitride coatings. Thus, the abrasive wear on the ball surface is thought to be the main wear mechanism. Hence, the wear rate can be calculated following the methods described in Chapter 2 and the results are presented in Fig. 3.23. It can be found that the wear rate has a good correlation with the hardness. The coatings with higher hardness have the higher wear rate from the ball. The maximum hardness corresponding to the coating deposited with a substrate bias of -60 V has a maximum wear rate of 5.4 x 10^{-14} m^2/N.

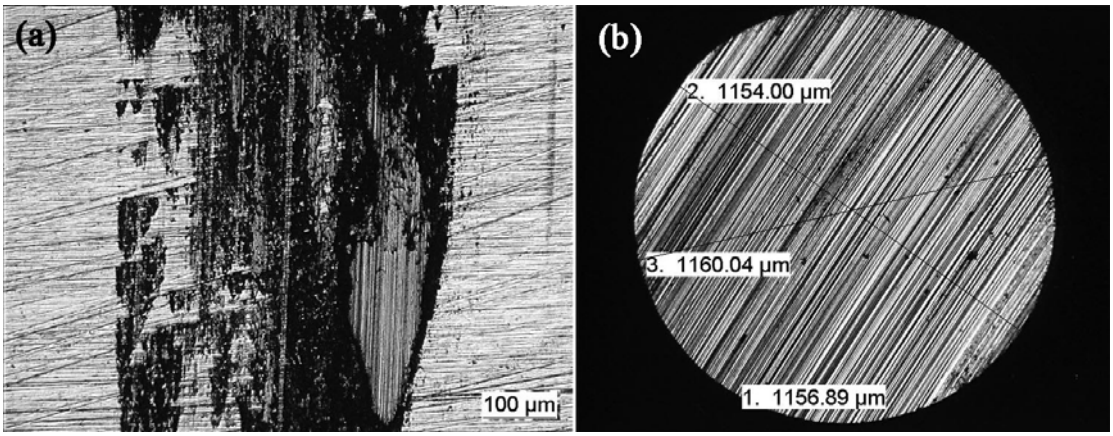

Fig. 3.25 wear tracks after the pin-on-disk tests for the coating deposited with a substrate bias of -100 V. (a) wear track on the coating; (b) wear track on the counter ball.

3.4.6 Coating corrosion properties

As described in the investigations of nitrogen partial influence on coating properties, the dynamic polarization technique was used to compare chromium nitride corrosion properties for different substrate biases. The obtained polarization curves are presented in Fig. 3.26. It can be seen that whatever the substrate bias, the polarization curves always present typical passive behaviors, which are related to the presence of Cr in the coatings. Their corrosion potential and corrosion current density as a function of substrate bias are shown in Fig. 3.27. From this figure, E_{corr} can be seen to shift to negative potential as the substrate bias increased, which is attributed to the decrease of nitrogen in the coatings. The coatings deposited below 60 V show the same level E_{corr} of nearly 330 mV whereas E_{corr} for the coatings deposited above 60 V have moved to negative direction of about 70 mV. It is suggested the stoichiometric CrN has higher chemical inertness than the non-stoichiometric coatings in the presented test medium. For I_{corr}, they show the similar trend like E_{corr} where I_{corr} increased when increasing substrate bias as the higher bias brought more defects into the coatings. However, since all I_{corr} are at the same nA/cm^2 order of magnitude, it is very difficult to determine which kind of coating has the best resistance for further corrosion when corrosion occurred.

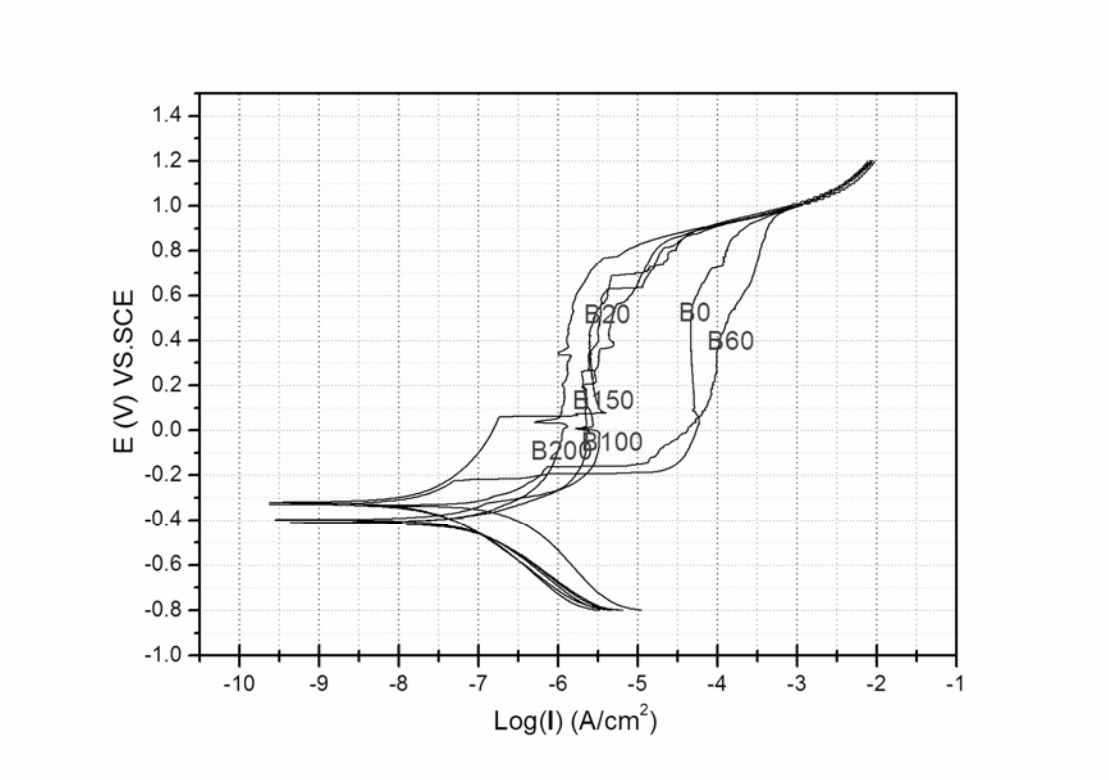

Fig. 3.26 Dynamic polarization curves for chromium nitride coatings with different substrate bias (i.e. B20: $|U_b|$=20 V).

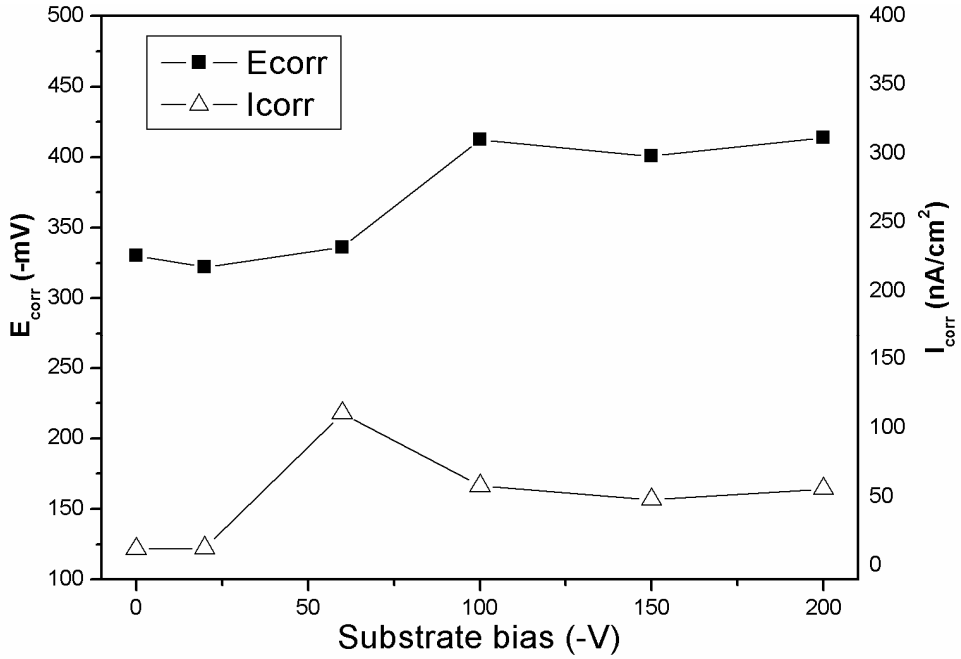

Fig. 3.27 Corrosion potential (E_{corr}) and corrosion current density (I_{corr}) as a function of substrate bias.

The SEM surface images of chromium nitrides with different substrate biases after corrosion tests are presented in Fig. 3.28. One can observe that the surfaces exhibit little corrosion, which is the reason why I_{corr} is quite low. However, there are still some pitting corrosions found on the corroded coating surfaces. As discussed before, the corrosion mechanism in these coatings is mainly from the pitting which is introduced either by the columnar structure or by the growth defects due to ion bombardments. The coating without bias has a tapered structure, which made the surface corroded as indicated in Fig. 3.28a. However, the corrosion medium can not further attack the interface between coating and substrate because the corrosion products block the pathway. In contrast, the coating deposited with bias had denser structures, which show good corrosion resistance. With increased bias, ion bombardment introduced more defects. In addition, the nitrogen content in the coatings decreases. These two reasons made their corrosion resistance decrease with the enhancing ion bombardment. The pitting numbers have a good correspondence with I_{corr}; from this figure, the more defects introduced by the RF bias bombardment, the easier corrosion occurres.

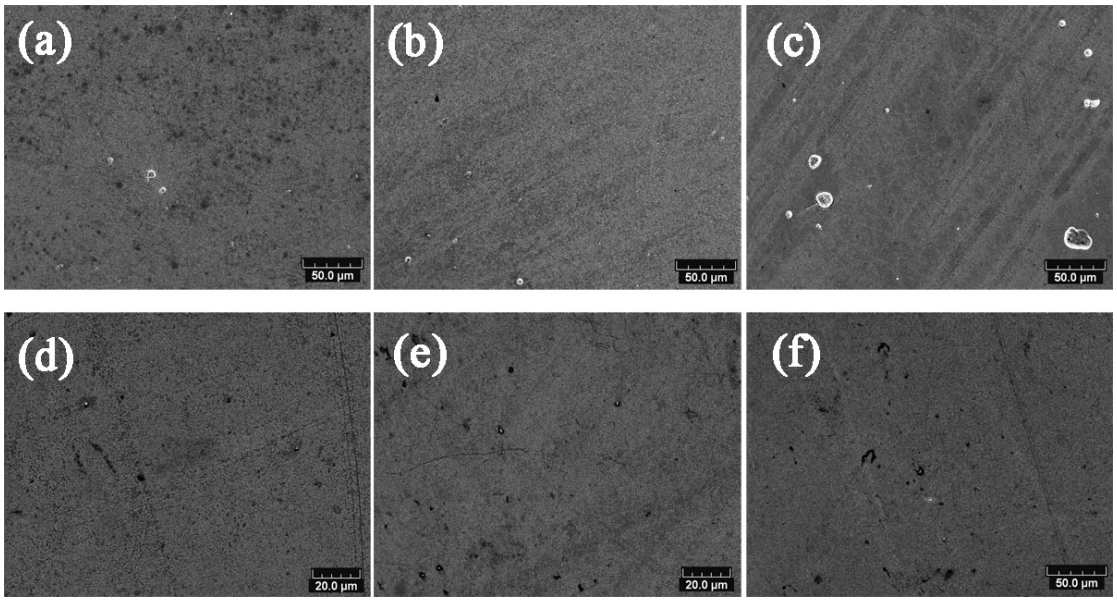

Fig. 3.28 SEM surface images of chromium nitride after dynamic polarization tests; (a) 0 V; (b) -20 V; (c) -60 V; (d) -100 V; (e) -150 V; (f) -200 V.

3.5 Summary

This chapter focuses on the synthesis and optimization of chromium nitride coatings. It is found that the hysteresis curve and target voltage vs. nitrogen flow rate curve can be well used to predict the chromium nitride phase evolution. The stoichiometric Cr_2N and CrN are synthesized with a nitrogen flow rate of 6 sccm and 12 sccm respectively. Their composition and structure evolution behaviors are in good agreement with what has been predicted from the hysteresis curves. The stoichiometric Cr_2N, CrN and the nanocrystalline Cr(N) solid solution with <200> preferred orientations present the higher hardness and modulus, so as to their better performance to wear resistance during pin-on-disk tests. However, in contrast to Cr_2N, CrN shows better abrasive wear resistance. The corrosion tests show that the non-stoichiometric chromium nitride coatings have higher corrosion resistance than the stoichiometric. The amorphous-like coatings have the best corrosion resistance despite that they present the lowest hardness. The abilities of corrosion resistance of chromium nitride coating in a 3.5 % NaCl solution are a-CrN > Cr > Cr_2N > CrN > AISI 304.

Another investigation is devoted to the influence of the RF substrate bias on coating structure and properties. OES analysis reveals that the formation of CrN mainly occurs on the substrate surface. The increased substrate bias leads to the decrease of nitrogen content in the coatings. The morphology evolution as a function of RF bias is in good agreement with OES analysis. Pin-on-disk tests show that coatings with moderate bias can combine low friction coefficient and best abrasive wear thanks to their higher hardness and modulus. In the corrosion tests, only the coating deposited with a low bias below 100 V presents good chemical inertness. However, all coatings demonstrate very low corrosion current density in nA/m^2 order. The CrN coating deposited with a RF bias of -60 V demonstrate a good combination of tribological and corrosion properties and is thought to be the optimized bias value for CrN deposition.

Chapter 4. Structure and properties of monolayer and multilayer coatings of Cr-Zr-N

4.1 Introduction

Single layer chromium nitrides (CrN) have been extensively investigated in the applications of the protective coatings due to their high hardness, good wear resistance as well as excellent corrosion and high temperature oxidation resistances [66, 85, 93, 117]. In some cases, they have been used as replacements of electroplated chrome. However, in many applications, the requirements for coated material surface can not be fulfilled by such a single coating alone. A further development to adapt some of their properties to the desired values for specific applications is to produce composite coatings, where different material properties are combined and some new desired properties could be created [39, 47, 49].

To elaborate composite coatings, an efficient method is to alloy them by adding a third element into an existing single phase coating. In most cases, their structures are characterized by multi-phase structures though some of them can also form solid solutions [118]. The additional element, however, can either be diluted in the matrix to form a new single phase (i.e. solid solution) or exist as a second phase separating in the form of nano-dimension grains (i.e. nanocomposite) [119]. The formation of nanocomposite in such a way provides a great flexibility to adjust coating structures and properties [120]. The composition variations allow a fine tuning to adjust structural parameters like lattice constant, defects, crystal phase and texture. Consequently, the various structures offer opportunities to optimize physical properties such as hardness, elasticity, oxidation behavior and corrosion stability in specific applications [39, 121].

In recent years, many research efforts have been dedicated to CrN-based ternary nitrides. The reported Cr-Ti-N [122], Cr-Al-N [123], Cr-W-N [124] coatings actually present high hardness and high thermal stability in comparison with the binary CrN.

However, although some basic correlations between the basic deposition parameters and the properties have been explored widely, it is still difficult (or impossible) to theoretically predict the influence of an alloyed element on the final performance in a specified application, especially in the case where the final properties are controlled by a nonlinear interaction of different parameters [39]. Moreover, it has been argued that even a very small amount of the third element plays a decisive role in the modification of chemical bonding, structure and morphology of the thin films [125].

In the first part of this chapter, the Zr modified CrN coatings were initially deposited. The selection of Zr is based on the facts that ZrN is much stable, easy to synthesize and has better corrosion resistance in comparison with other binary nitrides used in industry [126]. Although some research efforts have been devoted into Cr-Zr-N system [105, 119, 121, 123, 127], there are few works concerning their corrosion properties. In this study, a small amount of Zr was doped into CrN by sputtering alloy target. This alloying method has been expected to affect the lattice distortion, modify the ionic-covalent bonding degree, and change surface morphologies, therefore, the possible improvements in tribological and corrosion resistance.

Following the idea of using Zr to modify the properties of chromium nitride, another interesting viewpoint was introduced, which is to fabricate multilayer coatings (especially nanoscale multilayer) in this ternary system (Cr-Zr-N). The nanoscale multilayer structures were generally achieved by repeating layer of two different materials in nanometer dimensions deposited onto a surface. The thickness of each successive pair of layers has been known to play an important role on the multilayer properties [128]. By adjusting bilayer thickness (or modulated period: Λ) to realize a functional design, materials may be combined with different functions; and by structural variations (e.g., grain size, constitution, as well as ratio and constitution of interfaces), the obtained coating can be optimized in their properties to fulfill some specified applications [42, 129]. In the past decades, several material systems, including TiN/CrN, TiAlN/CrN, CrN/AlN and TiN/ZrN, have been developed and exhibited stronger enhancement in properties [103, 116, 129-135]. However, only a

few research activities concern the CrN/ZrN system [136]. In fact, there are many reports showing that CrN coatings exhibited excellent corrosion and wear properties and even better oxidation resistance, as well as better adhesion on tool steel when compared to TiN coatings [31, 137]. On the other side, ZrN coatings have also demonstrated comparable mechanical properties and even better corrosion resistance than TiN [84, 119]. Taking into account these two points, the idea to substitute TiN by CrN in the widely investigated TiN/ZrN system or to replace TiN by ZrN from the much concerned TiN/CrN system seems to be interesting. Therefore, in the secondary part of this chapter, CrN/ZrN multilayer coatings are designed and deposited with bilayer periods (Λ) in nanometer dimension. The investigations on their microstructural evolution with decreasing bilayer thickness and their related mechanical, tribological and corrosion properties have been performed in detail.

4.2 Coating preparations

From the results of Chapter 3, the stoichiometric CrN can be synthesized at a mixture of 10 sccm Ar and 12 sccm N_2 atmospheres. In order to compare coating structures and properties conveniently, the reactive gases were regulated at the same conditions during the deposition of Zr modified CrN coatings. The substrate bias was fixed at –150 V, which provided the possibility to decrease grain sizes. To add Zr into the CrN coating, a simple method was employed: the rounded Zr coupons (diameter: 10 mm) were placed homogeneously on the erosion track of the Cr target (See Fig. 4.1). In this way, Zr content in the deposited coatings could be controlled by varying the total numbers of coupons from 0 to 10. A thin adhesive layer of CrZr was deposited for 5 min on both silicon wafers and AISI 304 stainless steel substrates before introducing N_2. The deposition steps and deposition parameters were regulated the same way as those used for CrN coatings.

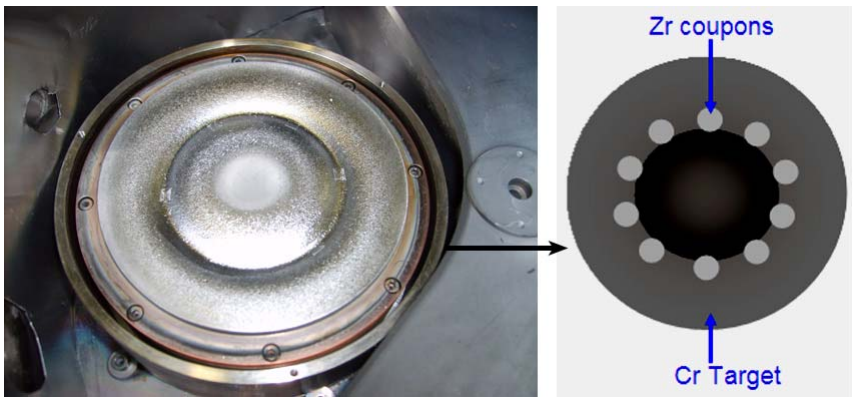

Fig. 4.1. Schema of a simple alloying method to add Zr into CrN.

During the preparation of multilayer coatings, CrN and ZrN coating were deposited as references. The depositions were carried out using the same deposition parameters and deposition steps as CrN coatings. The substrate bias was -60 V. There is a very small difference between the depositions of CrN and ZrN: the interlayer in ZrN is a pure Zr layer deposited in 2 min while in CrN the interlayer is a 5 min deposition of Cr. For the multilayer coatings, the deposition parameters of each individual layer were the same as their single layers whereas the substrate RF self-bias was adjusted to -60 V. In order to evaluate the real properties of multilayer coatings, no interlayer was applied in all the depositions of multilayer coatings. The initial deposit layer was CrN, then ZrN and CrN individual layers were deposited alternately and finally CrN was deposited as the outermost. The multilayer bilayer thickness (Λ) was controlled by turning alternately the substrate holder platform toward the target surface and exposing the samples to the Cr or Zr targets for certain times. The total deposing time for multilayer coatings was maintained for 60 min while the designed total layer number varied from 30 to 180. Therefore, the deposition times for each layer were from 20 to 120 seconds. In order to control the process conventionally, sample static exposing time to Cr and to Zr target was regulated equally. The detail design parameters for multilayers can be found in the second part of this chapter.

4.3 Zr modified CrN coatings

4.3.1 Coating compositions and structure characteristics

The obtained Zr modified CrN coatings have thickness ranging from 4 to 5 μm. Their compositions, as a function of the Zr coupon numbers are shown in Table 4.1. The results clearly indicate that Zr atomic concentration in the coatings has a nearly linear increase with increasing Zr coupons. The maximum Zr content (3.2 at. %) was achieved at a maximum coupon numbers of 10. On the other hand, the nitrogen to metal atomic ratio x = N/(Cr+Zr), increases from 0.82 to 0.96 as Zr coupons increase, indicating that nitrogen is easier to react with Zr than as it does with Cr. The GDOES typical depth profile analysis curve for the coating with 3.2 at. % Zr content is shown in Fig. 4.2. It can be observed that carbon and oxygen elements are rarely found throughout the depth of the coating. In contrast, a uniform composition distribution along the depth direction can be seen. The increases of both Cr and Zr contents are observed in the coating-substrate interface, which resulted from the CrZr adhesive layer.

Table 4.1. Element content and nitrogen to metal ratios of x=N/(Cr+Zr) in the Cr-Zr-N coatings as a function of the numbers of Zr coupons.

Zr coupons	Cr (At. %)	N (At. %)	Zr (At. %)	x=N/(Cr+Zr)
0	55.0	45.0	0	0.82
2	54.0	45.2	0.8	0.82
4	53.0	45.4	1.6	0.83
6	51.7	46.2	2.1	0.85
8	49.6	47.7	2.7	0.91
10	47.8	49.0	3.2	0.96

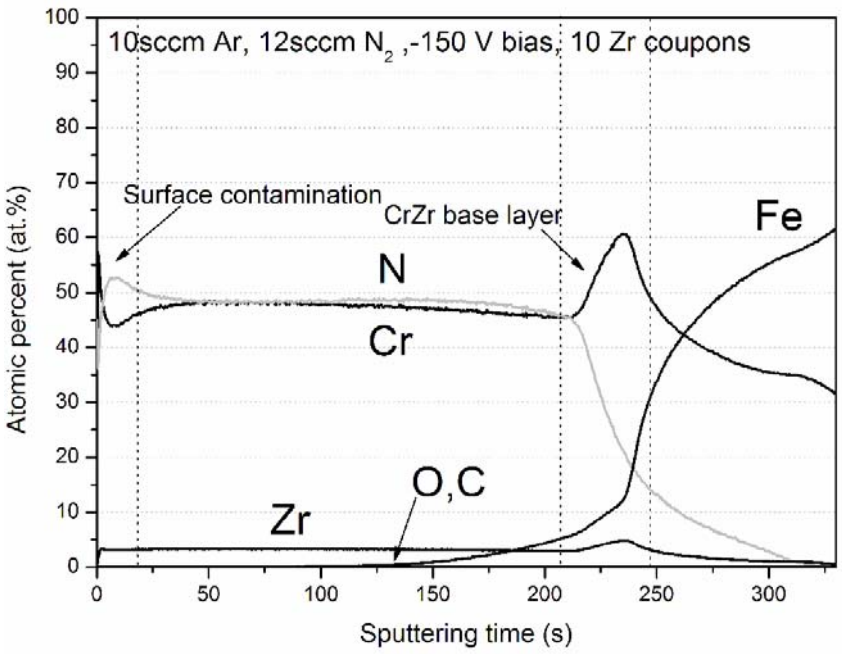

Fig. 4.2. Typical GDOES elemental depth profile of CrN(Zr) coatings deposited with Zr content of 3.2 at. %.

The evolution of the structure of CrN(Zr) coatings with various Zr contents is shown in Fig. 4.3. As expected, the coating without Zr presents a face centered cubic (FCC) lattice structure although their composition shows N deficiency (Table 4.1). The diffraction peaks of CrN(111), (200), and (220) can be clearly indexed. This coating has a <200> preferred orientation in comparison with the powder diffraction spectra (JCPDS76-2494). As indicated in the figure, some peaks from the substrates can also be observed. In order to calculate the average grain size, the diffraction peaks located near 44° were fitted to a pseudo-Voigt function. The average grain size of CrN coating subsequently evaluated from Scherrer formula is about 13 nm. This nanocrystalline grain structure can be attributed to the effects of ion bombardment. When the Zr content in the coatings increases, no diffraction lines from ZrN are identified for all the Zr modified CrN coatings. On the contrary, the shift of all CrN peaks towards lower angles can be found. The structure evolution results reveal that the small amounts of Zr in the coatings substituted the positions of Cr and formed substitute solid solutions CrN(Zr), which can be easily understood by the same lattice structure (fcc) between CrN and ZrN. The lattice parameters of the CrN(Zr) coatings,

which were deduced from the CrN(220) reflection peak, increase from 0.4135 nm to 0.4208 nm with increasing Zr contents. The lattice distortions are the results of the substitution of Cr with Zr since the atomic radius of Zr (0.161 nm) is larger than that of Cr (0.136 nm) [127]. These results are in good agreement with the reported results by other researchers [119, 127], where whatever the addition of Zr into CrN or Cr into ZrN, the shift of the diffraction peaks towards low angle with increased doping element contents were observed. From Fig. 4.3, it can also be seen that with the increase of Zr content, the CrN(Zr) coating diffraction intensities show no evident variations, which means that the small amount of Zr doped into CrN have little effects on the refinement of grain structures. Thus, the CrN(Zr) coatings might have an average grain size in nano dimension like that in CrN coating. The only evident change during structure evolutions is the peak intensity of CrN(220), which keeps almost constant as Zr content in the coatings is below 1.5 at. %, and above this point, it increases with increasing Zr contents, indicating the preferential orientation change from <200> to <220>. This is probably due to the effects of residual stress or the increase of N content.

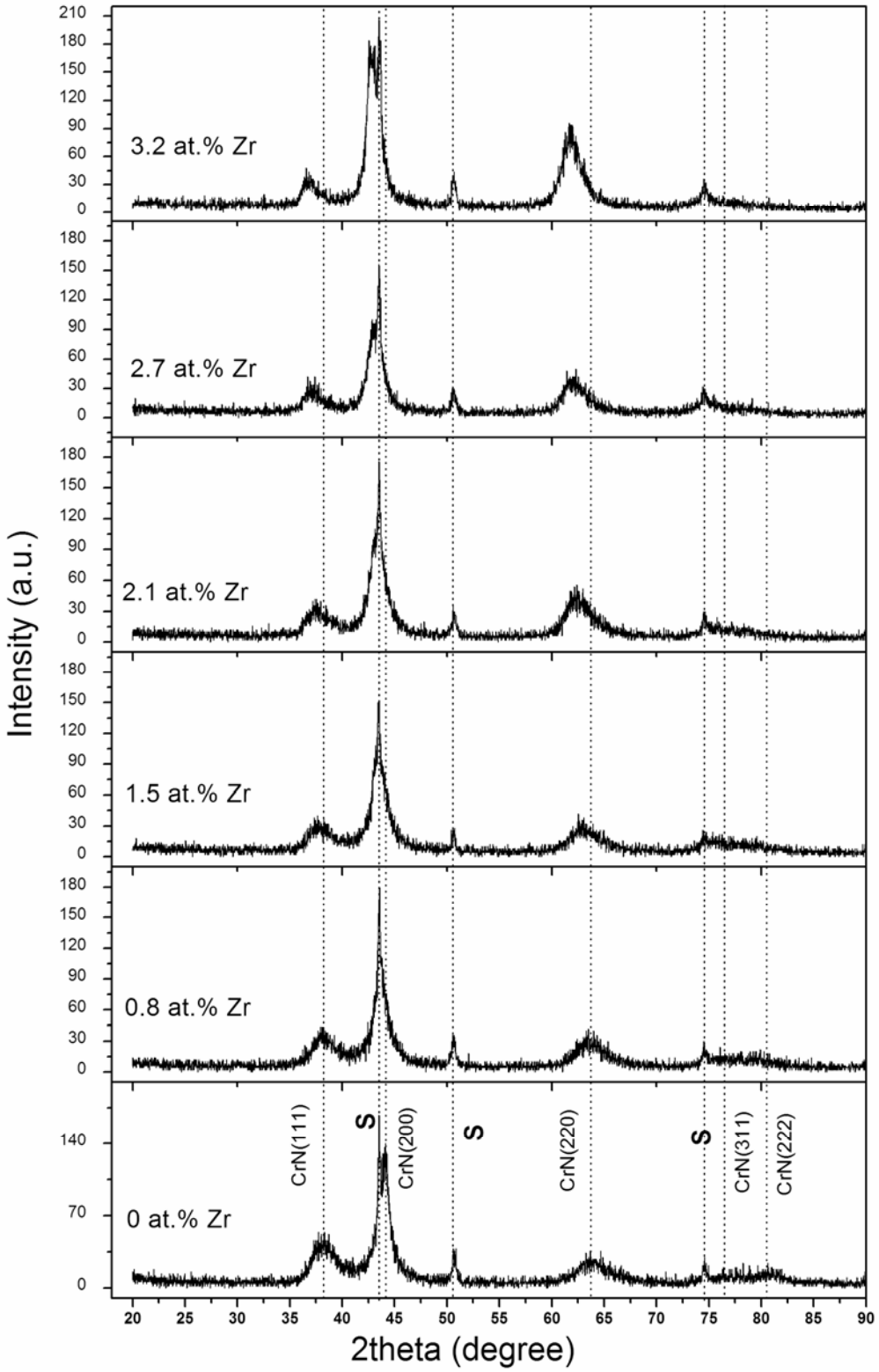

Fig. 4.3 X-ray diffraction patterns of Zr modified CrN coatings with different Zr contents (S: substrate).

Fig. 4.4 a and b present the typical fracture cross-sectional SEM from Si wafer substrates. Fine, dense columnar structures can be observed. However，in comparison with the morphology of CrN, the Zr modified CrN coating shows more granular morphology, suggesting that the addition of Zr improved the coating microstructure. These fine grained morphologies could be expected to perform better in an aggressive aqueous environment. These observations are in agreement with the results from the multi-component coatings reported in the literatures [127, 138]. On the other hand, the surface microscopy image (Fig. 4.4c) from AISI 304 substrates shows a flatter surface. However, the surface also displays macroparticles and pronounced pinholes. The macroparticles were due to the small liquid droplets that incorporated during coating growth while the pinholes were the results that the macroparticles debonding from the coatings. Similar results were obtained in a PVD TiN/TiAlN system and the detail explanations of formation such as topographies have been performed by the authors [139]. It should be noted that although these topographies are typical for ion plating and sputtering deposition process, they are still considered as drawbacks for the practical applications especially for erosion and corrosion resistance fields.

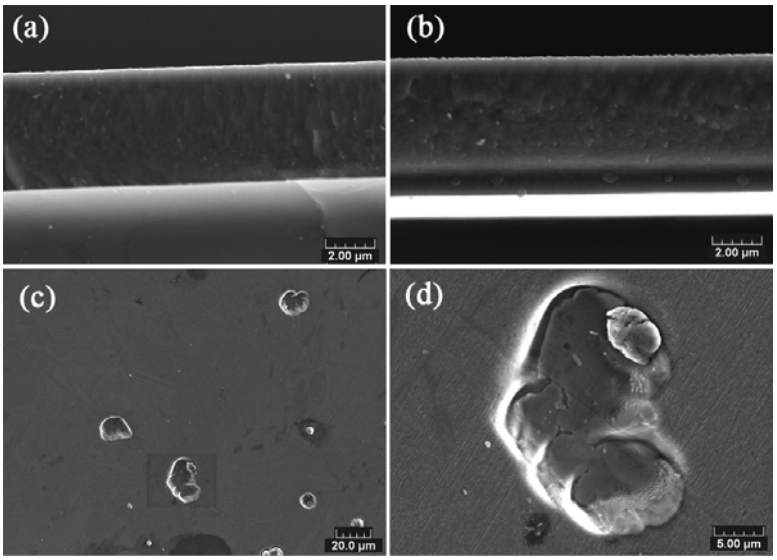

Fig. 4.4 SEM showing fracture cross-section from Si substrate and surface morphologies from AISI304 substrate (a) CrN coating; (b) CrN(Zr) coating with Zr content of 2.1 at. %; (c) Surface defects of CrN(Zr) coatings; (d) magnification image of typical defects.

4.3.2 Coating mechanical properties

Fig. 4.5 shows the nanohardness (H) and Young's modulus (E) as a function of Zr content. The values were measured by nanoindenter using a continuous stiffness mode (CSM), which enables to obtain the continuous hardness and modulus from the initial to the final indentation depth. The detailed principle and operation have been introduced in Chapter 2. The hardness and modulus of each measurement were determined at the indentation depth ranging from 100 to 300 nm. Nine indentations were performed and the final values of H and E are the mean values of these nine measurements. From Fig. 4.5, coating hardness values are between 19 and 24 GPa, which are comparable to those reported in the literature ranging from 18 to 30 GPa, depending on the growth conditions. In particular, the hardness agrees well with those reported for films under the comparable experimental conditions [121]. The evolution of H and E with increasing Zr content indicates that both H and E increase slightly until the maximum values of approximately 24 GPa and 308 GPa, respectively, at Zr content of 1.5 at.%. Further increases of Zr content result in a slight decrease in both H and Er. By comparing the hardness values of CrN and CrN(Zr) coatings, the solid solution strengthening effects can be derived. However, the lattice distortion effects on inhibiting the mobility of the dislocations are small as the increase of H is not significant. The result is different in comparison with those reported in the literature [119, 127], where significant enhancements of H were observed. This difference can be attributed to the low level Zr content in the present coatings. On the other hand, the results are similar to those reported by Lamni et al. for the Cr-Zr-N system [121], although their methods to enhance hardness are to add Cr into ZrN thin films. According to the authors, the little hardness enhancement could be attributed to the effects in terms of local bond strengthening and conduction band state occupancy.

The influence of Zr content on coating hardness is the result of complex combination of the chemical and physical properties of the film material and of the growth process. The growth process particularly has a great influence on coating morphology and stress state. The hardening of a ternary transition metal nitride is

often interpreted in terms of solid solution strengthening, decrease of the crystallite (Hall-Petch relation) and film densification. Taking into account the results of structure analysis, it can be concluded that the solid solution strengthening effects existed in the present system. However, the grain size or Hall-Petch hardening effects can be ruled out because, as deduced from XRD, the crystallite does not change significantly although they remained in nano dimensions. On the other hand, the influence of the grain shape (elongate or equiaxed) and the grain orientation on the mechanical properties is not completely understood. It is clear that hardness is in general an anisotropic property. As indicated in the cross-sectional images, the columnar microstructures are the same for all the coating, thus they would have little effects on the coating mechanical properties. Actually, the crystalline orientation transition from <200> preferred to <220> are clear when Zr content reached 1.5 at. %. This change is well consisted with the hardness evolution, which would result in the fact that both H and E decreased as Zr content is greater than 1.5 at.%.

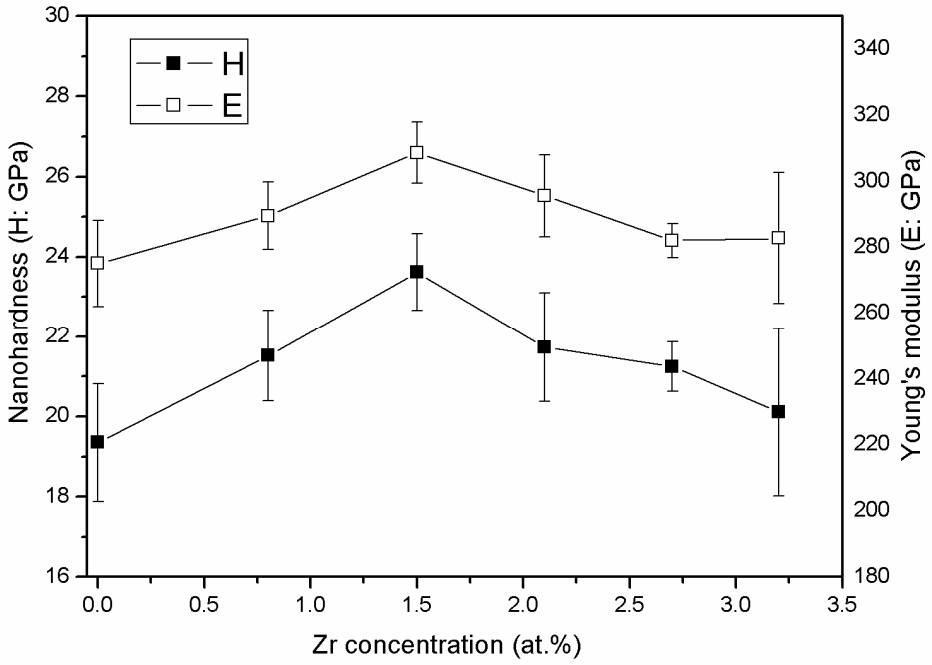

Fig. 4.5. Nanohardness (H) and Young's modulus (E) of CrN(Zr) coatings as a function of the atomic percentage of Zr in the coatings.

The scratch tests were carried out to evaluate coating/substrate adherence strength. The applied test parameters have been described in chapter 2. Two tests for one specimen were performed to verify the reproducibility. Fig. 4.6 shows typical curves of friction force, acoustic emission signal versus the applied normal load. A corresponding scratch track was also presented in the figure simultaneously. As it can be seen, in the cases of Zr modified CrN coatings, cohesive failure (L_{c1}, which is usually remarked by the start of cracking) is too difficult to be found. The adhesive failure critical load L_{c2} is defined as the starting point of chipping failure extending from the wear track. On the other hand, L_{c3} is associated with the point where the coating was completely removed. The results of such critical loads as a function of Zr content in the coatings are shown in Fig. 4.7. From this figure, all L_{c2} have relative low values between 6 to 12 N, which is due to the soft substrates. It can be noticed that L_{c2} increases with the additions of Zr into CrN coatings. However, the maximum L_{c2} is only 12 N at the maximum Zr content. In contrast to L_{c2}, L_{c3} does not show too much correlation with Zr content, which is probably due to the difference of coating thickness as shown in the cross-sectional SEM. Although the measured values of critical loads depend on many factors as discussed in chapter 3, the results indicate that adding Zr into CrN coating has positive effects to enhance the adhesion.

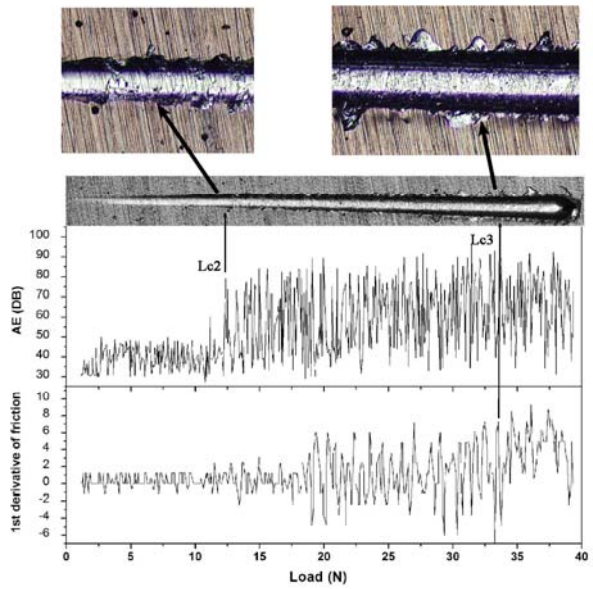

Fig. 4.6. Determining adhesive critical load (L_{c2}) and coating spalling out critical load (L_{c3}) using a combination of friction force, acoustic emission signal and optical image.

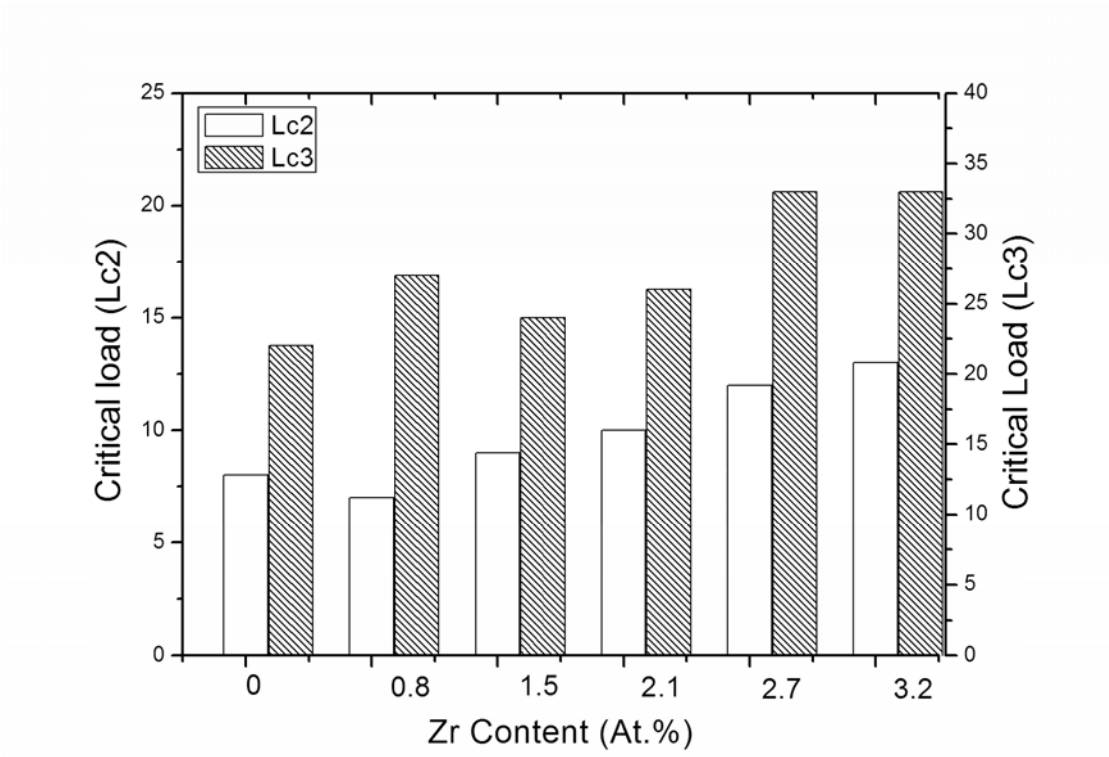

Fig. 4.7. Adhesive critical load (L_{c2}) and critical load (L_{c3}) as a function of Zr content in Zr modified CrN coatings.

4.3.3 Coating tribological properties

The tribological properties of Zr modified chromium nitride coatings with different Zr contents were examined with 100Cr6 counterparts on a pin-on-disk tribometer. The applied load was 2 N. The other test parameters were defined in Chapter 2. Fig. 4.8 shows a typical curve of friction coefficient versus sliding distance during 500 m. It can be seen that the friction coefficient of this Zr modified CrN decreases smoothly from 0.65 down to 0.55 within the first 100 m, and then remains constant around 0.5 for the rest of the test. The initial variations of friction coefficient could be associated with the "running-in" process. This is a general process for mechanical components with surface contacts before they reach steady-state operation. For this process, when one of the contacting surfaces is comparatively hard and the lubrication conditions prevent metallic transfer during running-in, wear will be principally confined to the softer surface and this exhibits a transitional topography

[140]. In the present case, the coating surface is much harder than the counter ball; as a result, the counter ball surfaces were worn continuously until they reach the steady-state. In all the cases of Zr modified CrN coatings, the steady-states were defined after the sliding distance of 100 m. Therefore, the average friction coefficients were calculated as the mean value of the rest sliding distance.

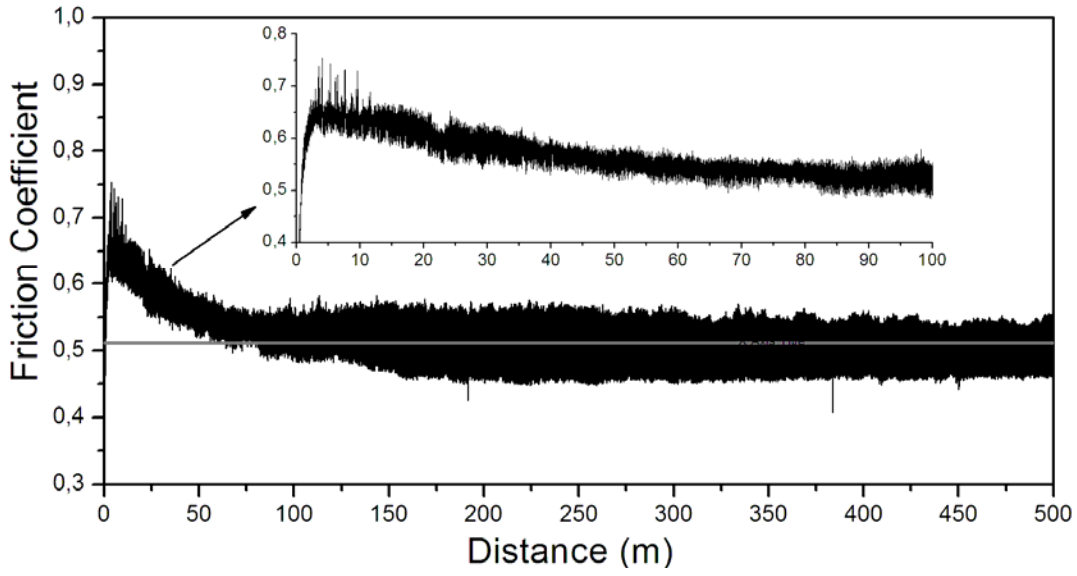

Fig. 4.8. Evolution of the friction coefficient during 500 m against a 100Cr6 ball of 6 mm in diameter and a 2 N applied load for: 1.5 at. % CrN(Zr) coating.

Fig. 4.9 presents the evolution of friction coefficients with different Zr contents in the CrN(Zr) coatings. From this figure, it can be found that the lowest friction coefficient of 0.52 corresponds to the highest hardness of 24 GPa, which has a Zr content of 1.5 at. %. For the other cases, it seems the higher the hardness is, the lower the friction coefficients are. This principle could be explained by the combination of abrasive and adhesion wear during the sliding process. As discussed above, during the tests, wear occurred principally on the counter ball surface. However, in some cases, very small amounts of coating surface were also damaged, which is due to the small abrasive particles detached from the coating. If the coating surface was not damaged, in the steady-state, the counter ball would slide on the transferred material surface. As a result, the friction coefficients present a very low value as the transferred materials

could play a role of lubricant. In contrast, if some coating particles were detached into the transferred ball materials in some surface weak areas, abrasive could occur during the sliding process. In such case, the friction coefficients would show relatively higher values as the abrasive wear contributed the resistance to the movement of the counter balls. However, in all cases, no evident abrasive wear tracks on the coating surface were found according to the coating surface images after the test. The typical coating surface morphologies are shown in Fig. 4.10. Fig. 4.10a is a typical wear track without any abrasive wear. In contrast, Fig. 4.10b shows the coating surfaces were slightly damaged.

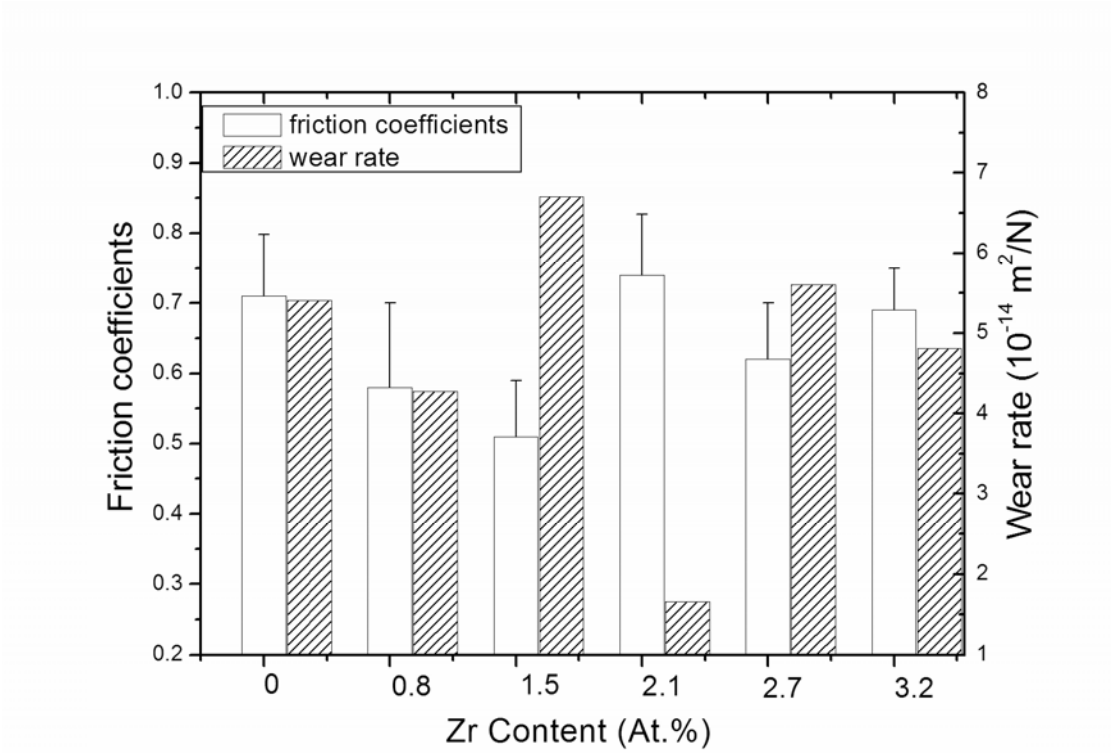

Fig. 4.9. Friction coefficients and wear rates during the sliding wear for CrN(Zr) coatings with different Zr contents.

As the abrasive wear mainly occurred on the counter ball surfaces, the wear rate can be estimated by the volume loss of the counter balls. The result is plotted in Fig. 4. 9. It can also be found the highest hard coating corresponds to the greatest ball volume loss. In the other cases, depending on the level of the abrasive wear, wear rate shows very small variations but still remains in the same order, which could be related

to their flatter surfaces with similar roughness. In conclusion, the tribological results show that these Zr modified CrN coatings have excellent abrasive wear resistance, which could be attributed to their high hardness.

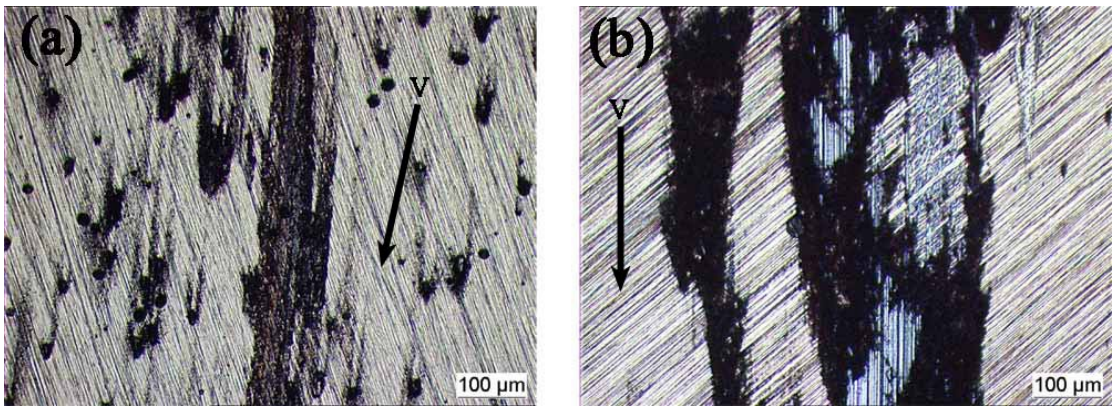

Fig. 4.10. Wear track of CrN(Zr) coatings: (a) 1.5 at.% Zr coating with complete adhesive wear, coating surface was not damaged; (b) 3.2 at.% Zr coating has a combination of abrasive and adhesive wear, a few damages of coating surface can be observed.

4.3.4 Coating corrosion properties

Fig. 4.11 shows the potentiodynamic polarization curves of Zr modified CrN coatings with different Zr contents. For comparison, the polarization behavior of the AISI304 substrate is also plotted in the same figure. The first remark is that the coated specimens show relative positive corrosion potentials and lower corrosion current densities in contrast to the substrate, indicating their stronger protective characteristics. Due to the presence of Cr in the coatings, the typical passive behaviors can be observed for all coated specimens, especially for CrN and CrN(Zr) coating with a Zr content of 2.1 at. %, which have wide and relatively stable passive stages ranging from -200 mV to +800 mV (vs. SCE). However, the passive current density of CrN(Zr) specimen is under the order of $\mu A/cm^2$, lower than that of CrN sample. For the other coated specimens, the passive current densities show the characteristics of instability. This scattering of current density in the anodic passive region can be explained by the clogging of the corrosion product in the pinholes and the breaking down of the coatings on the coated specimens [84].

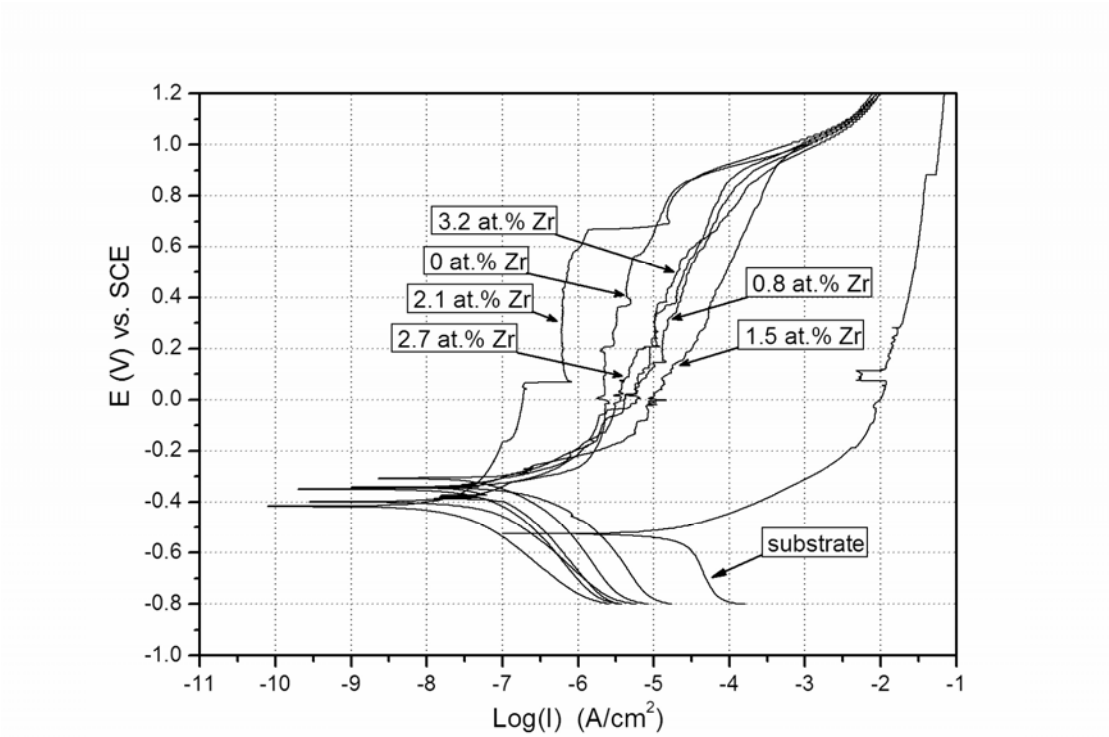

Fig. 4.11. Potentiodynamic polarization curve for CrN(Zr) coatings with different Zr contents and the substrate.

Table 4.2 summaries the corrosion potentials (E_{corr}) and corrosion current densities (I_{corr}) obtained from the polarization curves. It can be seen that the Zr modified CrN coatings (except for 2.1 at. % Zr) have higher corrosion potentials in comparison with that of CrN, which indicates that the additions of Zr improve the coating chemical inertness in an aggressive aqueous environment. The highest corrosion potential of -312 mV, corresponding to 1.5. at % Zr in the coatings, has moved approximately 90 mV to positive values when compared to CrN. Even for the CrN(Zr) coating with 2.1 at. % Zr, as discussed above, the relative lower passive current density corresponds to higher ability to suspend corrosion extension when corrosions occurred. The improvements of corrosion potential are associated with the increased nitrogen to metal atomic ratio, by which more metal atomics were bonded by N instead of being corroded by the environment medium. The better corrosion resistance of ZrN may also contribute to that [84].

Table 4.2. The corrosion current (Icorr), and corrosion potentials (Ecorr) determined from the polarization curves in a 3.5 % NaCl solution for the CrN(Zr) coatings with different Zr contents.

Zr content (at. %)	E_{corr} (mV)	I_{corr} (nA/cm^2)
substrate	-480	6431
0	-401	19
0.8	-344	74
1.5	-312	36
2.1	-420	8
2.7	-352	11
3.2	-348	20

The corrosion current density is commonly used as an important parameter to evaluate the kinetics of corrosion reactions and is normally proportional to the corrosion rate. The coated specimens present exceptionally low corrosion current densities in the nA/cm^2 scale, up to three orders of magnitude lower than the substrate. As the transition metal nitrides are generally inert to chemical attacks [141], the results reveal that the Zr modified CrN coating specimens possess excellent capabilities for preventing localized galvanic attacks between the coating and the substrate. This can be attributed to the dense compact structures as shown in Fig. 4.4. As the corrosion current density is usually influenced by many factors during tests, i.e. temperature, surface conditions, oxygen in the solution, etc, the comparison between the I_{corr} of CrN(Zr) coatings and that of pure CrN coating does not provide direct evidence that the Zr modified CrN coatings have a lower corrosion rate. However, as all of the I_{corr} are at least comparable to that of CrN, considering the results from E_{corr}, it is sure that the addition of Zr into CrN coating is effective in improving corrosion resistance. It should also be noted that both corrosion potential and current density do not show a stronger dependence on Zr content. This can be explained by the composition results where the addition of Zr into CrN coatings also leads to the changes of both Cr and N compositions. As a result, the doped Zr is not a unique factor to affect corrosion resistance. Since Cr was very sensitive to environment oxidation, the decreased Cr and increased N as well as increased Zr may play

different important roles to affect the initial sample surface states; subsequently, resulted in the no systematic variations of E_{corr} and I_{corr}.

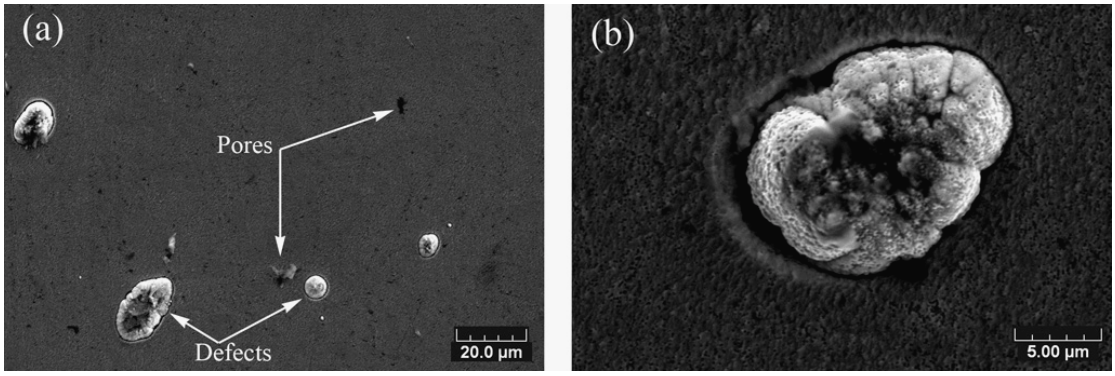

Fig. 4.12. SEM micrographs of corroded spots on Zr modified CrN coatings (a) corrosion on the points of small pores and defects, (b) magnification of corrosion on the defect point.

The electrochemical data gives the evidences that the corrosions in the coated specimens are very slight. The SEM micrographs show that the surface did not exhibit any apparent corrosion impressions after the polarization tests (Fig. 4.12a). The EDX analysis on the corroded sample surface detects the evident signal of Cr, Zr, N and O but very weak from iron, indicating that there is no evident degradation of substrate materials. However, the corrosion was clearly observed during the electrochemical tests. As the transition metal nitrides are generally immune to corrosion, the lower corrosion current density means that the corrosion can not occur on the entire sample surface but in some specific areas. The typical pitting corrosion should be responsible for that as reported in the literature [84, 105, 142]. As shown in Fig. 4.12a, for all the specimens, two structural flaws can be identified: the small pores resulted from the columnar structure and the growth defects coming from the metal liquid droplets as discussed in Fig. 4.4, both of which distributed randomly over the sample surface. There was no breakdown or spalling of the coating around these structural flaws. This can be associated with the inactive Cr based corrosion products (i.e. Cr_2O_3) in the structured defects, thus plugging the pores or defects and blocking the passage of the electrolytic for further corrosion [105]. This is the case especially for the small pores

as present in Fig. 4a. However, for the growth defects, they usually have low nitrogen content [139, 143, 144] and were weakly bonded to the coating as demonstrated by the crack at the rim and by the similar morphology between the bottom of the pinhole and the coating surface (see Fig. 4.4). According to H.W.Wang et al. [145] (see Fig. 4.13), the corrosion behaviors may start from the N deficient pinhole rim, anodic to the neighboring coating nitrides, which can be confirmed by the flocculence corrosion products collected around the rim of the pinhole as shown in Fig. 4.12b. This initial corrosion process created solution paths, which benefited to the consequent formations of various galvanic couplings. The effect of the initial defect edge corrosions are considered as the trigger of more galvanic dissolutions or pitting corrosion to the substrate as the solution contained Cl^- ion [145]. On the other hand, the accelerated corrosion processes can be blocked either by the block of corrosion products or stop when the growth defects were not through-thickness types. If the defects are large enough to cross the coating thickness, as illustrated in Fig. 4.13, the created corrosion solution paths can also reach the substrate, thus the localized galvanic corrosion of substrate occurs. The lower corrosion current densities in the present study indicate that most of the growth defects are not completely through-thickness types. Moreover, the CrZr adhesive layer may also play important roles to suppress the further corrosion process.

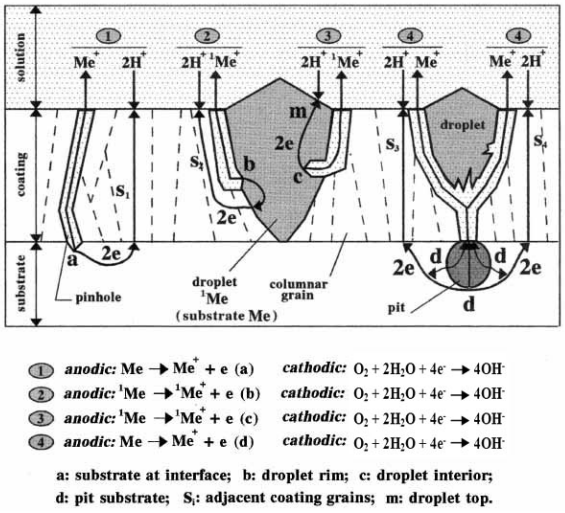

Fig. 4.13. Schematic diagram outlining the corrosion mechanisms of macroparticles and growth defects (reaction 2 and 3) and the galvanic corrosion of the substrate associated with these (reaction 4) and other defects such as droplet shrinkage pinholes (reaction 1) [145].

4.4 CrN/ZrN multilayer coatings

4.4.1 Coating microstructure characteristics

The detailed coating deposition process has been described in the part of coating preparations. The characteristics of the obtained CrN/ZrN multilayer are listed in Table 4.3. From this table, the single layer CrN and ZrN coating thicknesses during 60 min depositions are 3.5 and 1.3 μm, respectively. In contrast, the total thicknesses of multilayer CrN/ZrN coatings range from 1.9 to 2.1 μm. Hence, the bilayer thickness between 11.7 and 66.7 nm are obtained from the ratio of coating thickness vs. layers. The corresponding layer thickness ratio of CrN/ZrN in the bilayer thickness is determined from the single layer coating growth rate and nearly equals to: $t_{CrN} : t_{ZrN} = 3 : 1$.

Table 4.3. Main parameters of deposited CrN/ZrN coatings.

Coating	Exposing time	Thickness (μm)	Bilayer Period (nm)	Hardness (GPa)	Reduced elastic modulus (GPa)	H^3/E^2
CrN	-	3.5	-	22.2	303	0.12
ZrN	-	1.3	-	29.0	290	0.29
30x(CrN/ZrN)	CrN :60s/ZrN:60s	2.0	66.7	28.5	321	0.22
45x(CrN/ZrN)	CrN :40s/ZrN:40s	1.9	42.2	28.6	309	0.25
60x(CrN/ZrN)	CrN :30s/ZrN:30s	2.1	35.0	27.7	298	0.24
90x(CrN/ZrN)	CrN :20s/ZrN:20s	1.9	21.1	26.5	294	0.22
180x(CrN/ZrN)	CrN :10s/ZrN:10s	2.1	11.7	28.0	308	0.23

A low-angle ($2\theta \leqslant 15°$) XRD reflectivity pattern results from the reflection of X-rays off the interfaces between layers and it is not affected by the crystalline quality within each layer. Thus, the low-angle XRD reflectivity pattern can be used to calculate the bilayer thickness. In the present study, to verify the above calculated bilayer thickness, a low-angle XRD test was carried out using the sample with 180 layer deposition. The operation was performed in 2θ-ω geometry with a Bruker D8 discovery XRD system (CuKα λ=0.1541nm). The test result is shown in Fig. 4.14. It can be seen that two low angle diffraction peaks emerge in the figure, indicating the formation of obvious composition modulation structure in the multilayer. Therefore,

the bilayer thickness was drawn out from the modified Bragg equation [146]:

$$\sin^2\theta = \left(\frac{n\lambda}{2\Lambda}\right)^2 + 2\delta$$

where 2θ is the peak position of the n^{th} order reflection, λ is the X-ray wavelength (0.1541 nm), δ is the deviation of the average refractive index of the film, and Λ is the bilayer period. By plotting $\sin^2\theta$ vs. n^2 and fitting to a straight line with a constant slope $(\lambda/2\Lambda)^2$, the Λ could be determined. Thus, the average Λ is 12.6 nm, which is in agreement with the calculated bilayer thickness of 11.7 nm.

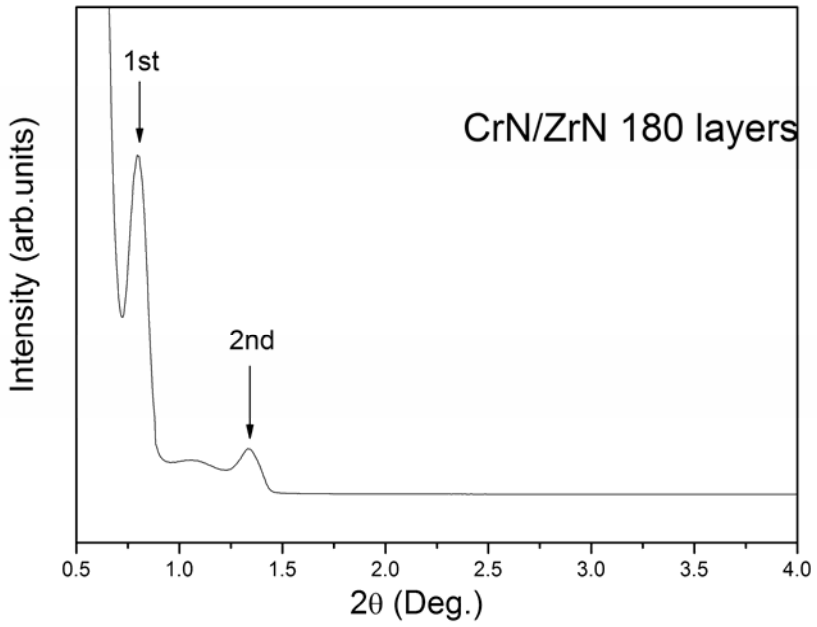

Fig. 4.14. Low angle XRD diffraction spectra of CrN/ZrN with 180 layers. The calculated bilayer thickness from the ratio of thickness vs. layer is about 11.7 nm.

Fig. 4.15 presents the X-ray spectra of CrN and ZrN single layer and CrN/ZrN multilayer coatings. As described previously, the CrN monolayer thin film presents an intense (200) peak, a medium (111) and a weak (220) peak, which are in agreement with the powder diagram (JCPDS 76-2494). On the other hand, ZrN thin film shows only one intense peak (111), indicating a stronger preferred orientation in this monolayer coating. This texture appears due to a critical level of internal stress in the coating since this orientation tends to minimize the stress [147].

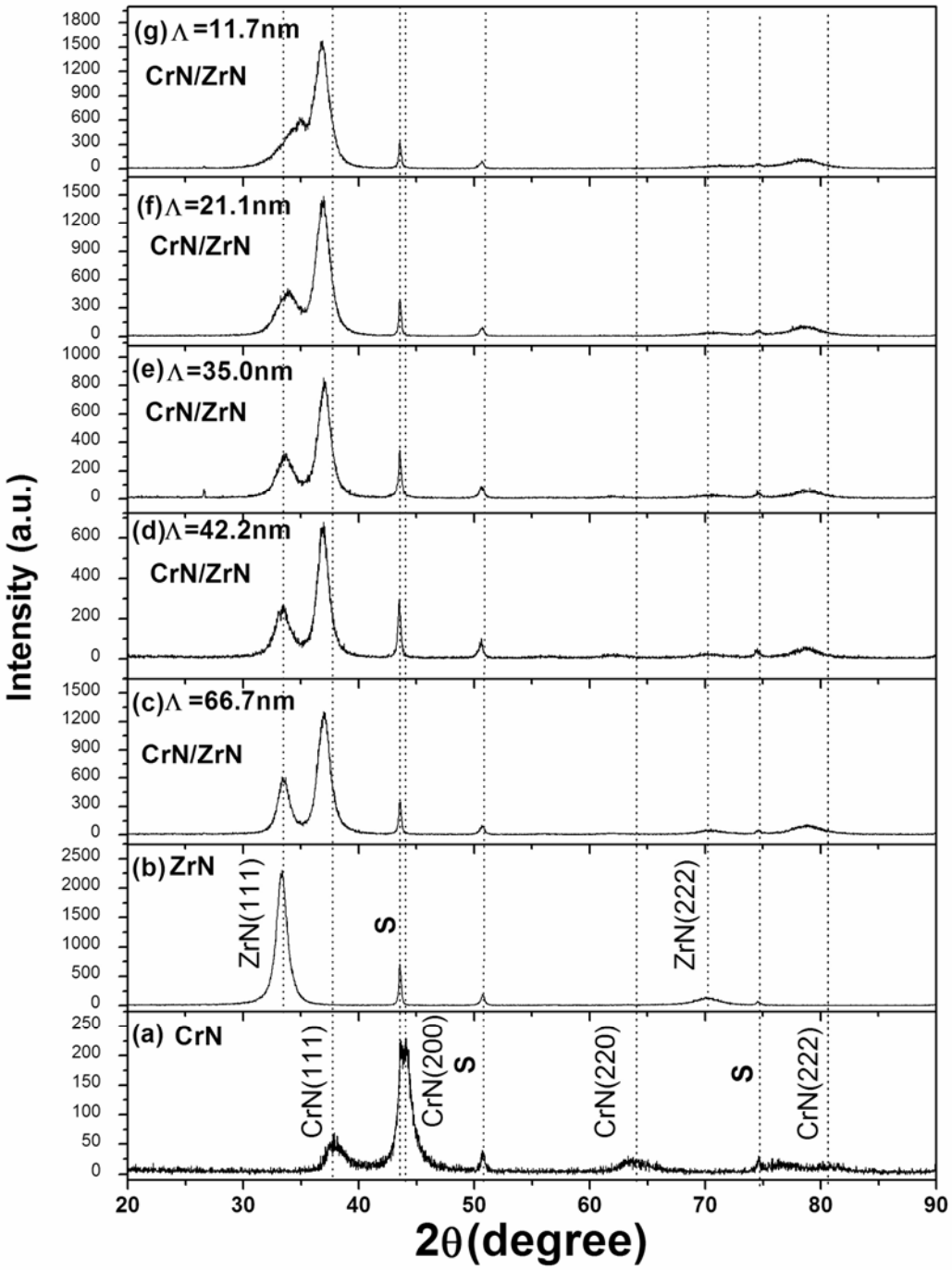

Fig. 4.15. X-ray diffraction patterns of CrN, ZrN and CrN/ZrN multilayer (S: substrate).

For CrN/ZrN multilayer coatings, only ZrN(111) and CrN(111) peaks can be observed except apart from the peaks from substrates. It is should be note that the preferred growth orientation of CrN has a great change from <200> to <111>. It could be associated with the stress at individual layer interface. This can be confirmed by the fact that the positions of CrN(111) peak in multilayer coatings show a great shift

to low angles in comparison with that in the monolayer coating. In addition, with decreasing the bilayer thickness, the peak of CrN(111) show a continuous shift to low angle. However, the peak position of ZrN(111) shows unaffected until the bilayer thickness $\Lambda > 35.0$ nm. As a smaller bilayer thickness was constituted, the position of ZrN(111) has a shift toward high angles. When the bilayer thickness decreased to 11.7 nm, the coating presents an evident CrN(111) peak while ZrN(111) peak seems to become the 1st order negative satellite peak of this peak. It probably suggests the formation of superlattice structure in such coating [134]. Hence, the bilayer thickness can also be calculated by the main Bragg and satellite peak position [148]. However, the calculated bilayer thickness is only 5.7 nm, which is half of the result obtained either by the ratio of coating thickness vs. layer number or the low angle XRD reflectivity. This indicates that the multilayer structure for such coating is not a superlattice. However, the structure evolution with decreasing bilayer thickness suggests the possibility to form superlattice structure with a lower bilayer thickness.

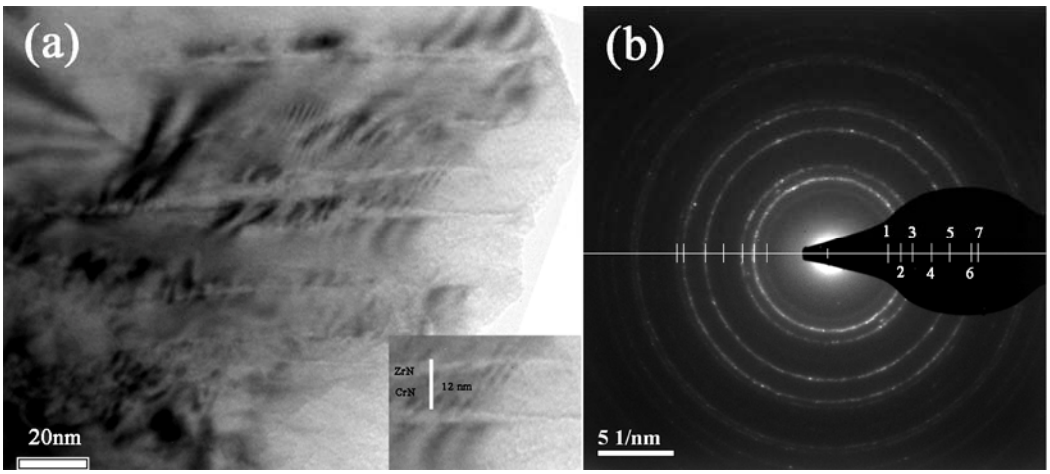

Fig. 4.16. Cross-sectional TEM bright field image and corresponding electron diffraction pattern for the CrN/ZrN multilayer with Λ=11.7 nm.

To verify the multilayer coating structures and their phases, the cross-sectional TEM for a minimum bilayer thickness coating of 11.7 nm was performed. The cross-sectional TEM bright field image and corresponding electron diffraction pattern (ED) of CrN/ZrN multilayer coating are presented in Fig. 4.16. The lamellar structure

can be identified from Fig. 4.16a. The alternate layer structure can be found in the magnified inset. The different deposited layers can be distinguished by their different deposition rates and have been marked in the inset of Fig. 4.16a. The average bilayer thickness measure from TEM observation was about 12 nm, agreeing with the estimated values. However, it is difficult to determine the layer thickness ratio due to the preparations of the TEM samples. The ED ring pattern is shown in Fig. 4.16b and the measured "d" values for different diffraction rings can be found in Table 4.4. The presence of many diffraction rings in the diffraction pattern is due to two or more structures coexisting. The diffraction rings marked 2,3,5,6 clearly show that there is a B1 NaCl type crystal structure in this multilayer coating. These rings are continuous instead of sharp spots, indicating the very small size grains distribution. As indicated in Table 4.4, such structure can be attributed to CrN although the experimental d values present a lattice mismatch of approximately 2.5% as compared to CrN phase. ZrN phase, on the other hand, can also be indexed from the different rings as indicated in Table 4.4. In comparison with CrN phase diffraction patterns, ZrN diffraction patterns present diffuse scattering, which could be associated with the presence of an amorphous phase in such multilayer. The presence of amorphous phase for ZrN coating at a high nitrogen flow rate has been observed previously [149]. Like Si_3N_4, Zr-N system can also form Zr_3N_4 structure [149]. The similarity of structure may offer an additional choice to form a new kind of amorphous layer contained multilayer structure.

Table 4.4. Interplanar distances for CrN, ZrN and the CrN/ZrN multilayer with Λ=11.7 nm.

Ring No.	Experimental d_{hkl} (Å ± 0.02 Å)	CrN a = 4.14(Å)	ZrN a =4.63 (Å)
1	2.72		2.67 (111)
2	2.45	2.39 (111)	2.31 (200)
3	2.16	2.07 (200)	
4	1.68		1.64 (220)
5	1.49	1.46 (220)	1.40 (311)
6	1.26	1.25 (311)	1.34 (222)
7	1.21	1.2 (222)	

The cross-sectional views of monolayer CrN, ZrN and multilayer CrN/ZrN coatings on silicon substrates are shown in Fig. 4.17. The images confirm the previous measured thickness results. CrN coating exhibited higher deposition rate than ZrN. The monolayer nanocrystalline CrN shows fine-grained dense columnar growth morphologies, which can be described by the Zone-T structure of Thomton's structure zone model [113]. In contrast, ZrN coating shows a dense morphology without columnar growth characteristics, which is related to their high internal stresses during deposition at a high nitrogen partial pressure. All the multilayered CrN/ZrN coatings show fine dense columnar structures. It is a little surprising that this typical growth style throughout the thickness was not disrupted even when the coatings were deposited with a large bilayer thickness of Λ = 66.7 nm. The columnar growth phenomenon of multilayer coatings have been observed in the other systems [129, 150, 151], which could be related to the layer structure waviness along the direction of coating growth. Such waviness originates from the substrate as a result of previous substrate surface treatments (i.e. polishing, ion etching).

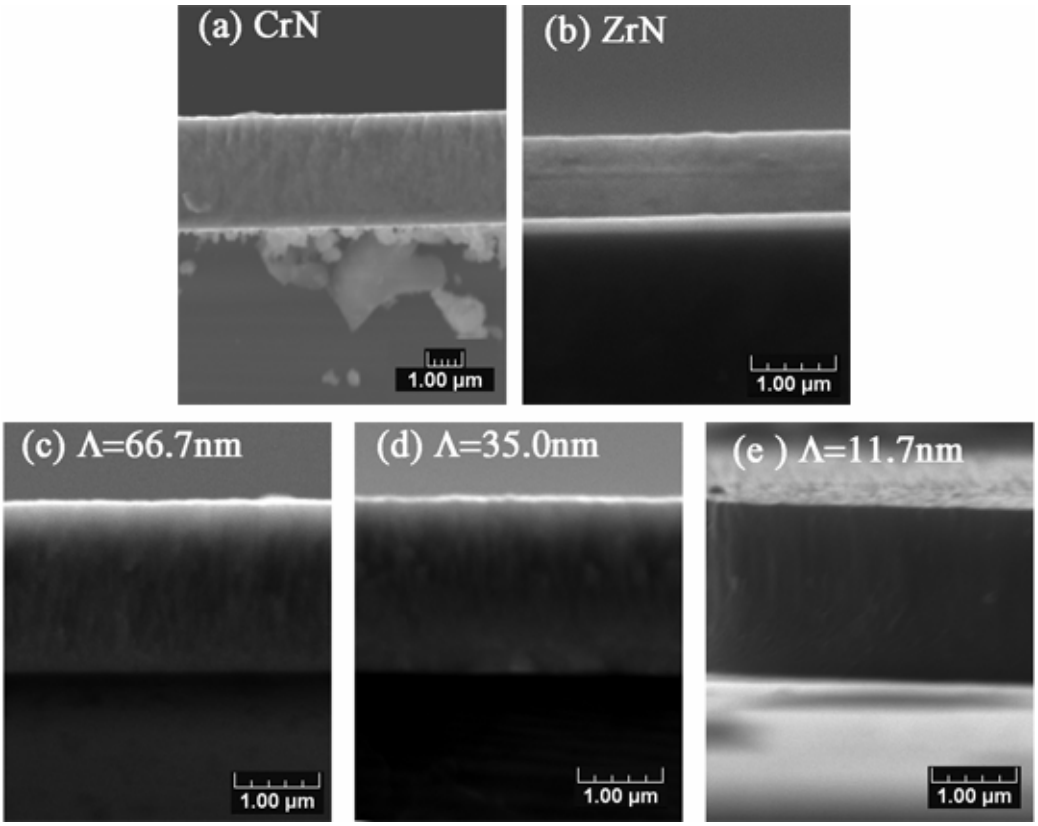

Fig. 4.17. SEM cross-sectional images on Si substrates (a) CrN; (b) ZrN; (c) CrN/ZrN Λ=66.7 nm; (d) CrN/ZrN Λ=35.0 nm; (e) CrN/ZrN Λ=11.7 nm (180 layers).

4.4.2 Coating mechanical properties

Fig. 4.18 exhibits the nanohardness (H) and elastic modulus (E) as a function of multilayer bilayer thickness. For comparison, the test results for the CrN and ZrN monolayer coatings are also involved. The nano-indentation hardness of the CrN and ZrN films are 22 and 29 GPa and E of these coatings are 303 and 290 GPa, respectively. The multilayered coatings do not show any superhardness effects even in the smallest bilayer thickness. In addition, they don't show much dependence with the bilayer thickness. The values of H for the multilayered coatings remain almost constant in spite of varying the bilayer thickness. The multilayer coatings exhibit a higher nanohardness of 29 GPa and comparable reduced elastic modulus of 250 GPa in comparison with the monolayer CrN coatings. However, these values are comparable to ZrN. Apparently, the hardness and modulus dependence on the bilayer thickness are different from either the "rule of mixture" or the Hall-Petch relation [152]. In multilayer system, the hardness enhancement mechanism is usually explained by the difference in the elastic modulus or existence of coherent interface. The former is related to Koehler theory [153], which attributed the hardness anomalies to the modulus difference. The later, however, is deduced by Gahn's coherent strain model [154], which suggests that the coherent strain in the multilayers plays a main role in the hardness anomalies. In the present study, there is little difference in elastic modulus between the constituent materials of CrN and ZrN. However, the presence of coherent stress is possible. One side, from Table 4.4, the interface lattice mismatch along (111) plane is evident. On the other side, the difference of room temperature thermal expansion coefficient of CrN (2.3×10^{-6} K^{-1} [137]) and ZrN(7.2×10^{-6} K^{-1} [155]) is enough to cause thermal stress in the interfaces. However, in the multilayer coatings, as CrN layer posses more volume fraction (t_{CrN} : $t_{ZrN} \approx 3 : 1$), it can play a role to release the various stress from the interface. As a result, CrN individual layer was forced to change their growth orientation to (111) in order to decrease the stress. The other consequence is that the alternate stress fields crossing the total multilayer thickness did not form. Therefore, no stronger

enhancement of hardness due to Cahn's coherent stress model occurs.

The evolution of E shows a similar trend to hardness. A little difference is that E has a small amount of improvements at the smallest bilayer thickness. For coating practical applications, usually the high hardness of coating is not the only factor for improve coating wear resistance; elastic modulus can also be an equally important factor [156]. A combination of hardness and elastic modulus can be used to evaluate coating plastic deformation resistance [103, 132]. The ratio of H^3/E^2 was widely used to indicate the coating resistance to plastic deformation in the types of rigid-ball on elastic/plastic plate. The results of H^3/E^2 for all the coatings can be found in Fig. 4.18. However, these results still show a similar evolution trend as H and E, which means the resistance to plastic deformation of the multilayer coatings could not present an evident improvement.

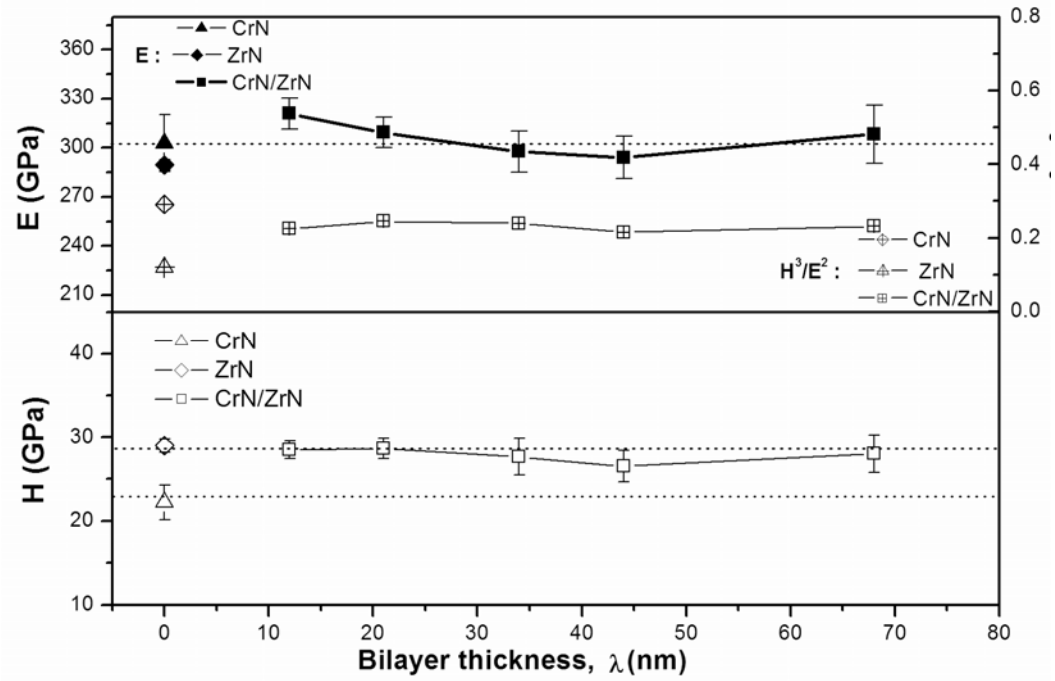

Fig. 4.18. Nanohardness (H) and Elastic Modulus (E) of CrN/ZrN multilayer coatings as a function of bilayer thickness.

Fig. 4.19 gives the cohesive critical load (L_{c1}) and adhesive critical load (L_{c2}) for monolayer and multilayer coatings. The test parameters were regulated as what has been introduced in Chapter 2 and the definitions of L_{c1} and L_{c2} are the same as those described in Chapter 3. As presented previously, CrN coating has a high L_{c2} due to its excellent toughness. However, the obtained ZrN coatings show great brittleness and their adhesive critical load L_{c2} is very low, which can be associated with the residual stress as the deposition was operated at a fully reactive mode. For multilayer coatings, almost all of them present the same L_{c1} and L_{c2} like ZrN. It seems that the multilayer structure did not benefit to enhance the adhesion. However, note that the multilayer coatings were deposited without any interlayer, their poor adhesion with substrate can be attributed to the great stress at the coating substrate interface. To improve coating/substrate adhesion, even for a multilayer structured coating, a tough metal interlayer is proposed.

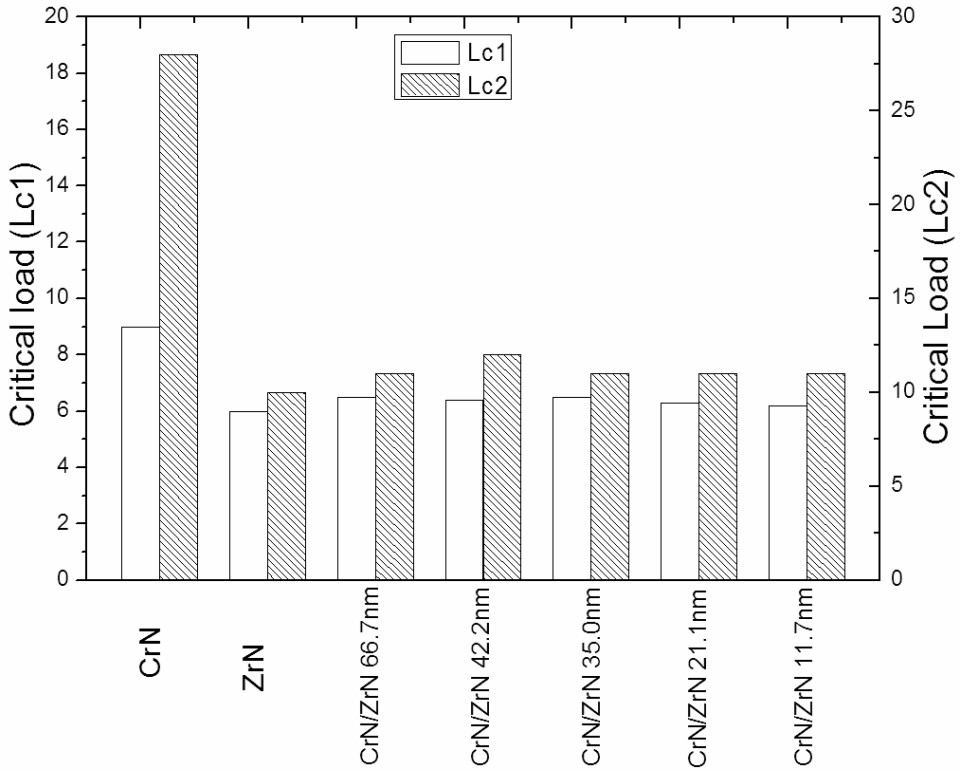

Fig. 4.19. Cohesive critical load (L_{c1}) and adhesive critical load (L_{c2}) of CrN/ZrN as a function of bilayer thickness.

4.4.3 Coating tribological properties

The tribological properties of CrN/ZrN multilayer coatings with different bilayer thicknesses were examined with WC-Co counterparts on a pin-on-disk tribometer. The applied load was 2 N. The other test conditions were defined in chapter 2. Fig. 4.20 shows the friction coefficients of CrN and ZrN monolayer coatings and typical CrN/ZrN multilayer coatings (Λ = 66.7 and 11.7 nm) as a function of operating time. It can be found that their friction behaviors can be distinguished into two stages. The first stage of the "running in" process shows a sharp increase of friction coefficients with increasing operating time, which can be attributed to the effects of surface oxide layers and the variations of contact stress. The secondary stage is linked to the rest working stage after the "running in" process. The average friction coefficients under this stage can be evaluated as the real friction coefficient values of these coatings with WC-Co counterparts. From this figure, the friction curves of CrN and the multilayer coatings with high Λ = 66.7 nm under the working stage are stable with few fluctuations. The average friction coefficients are 0.41 and 0.32, respectively. In contrast, the friction coefficient curve of ZrN indicates slow improvements with increasing operating time. On the other hand, as shown in Fig. 4.20d, the friction coefficient curves of the other multilayer coatings present an unstable characteristic during the sliding process. This typical unstable friction curve corresponds to a small Λ of 11.7 nm. It can be observed that the friction coefficient was degraded abruptly at the end of the "running-in" process. After a short period of operation time, a relative stable working situation was reached. The unstable friction coefficients with operating time have been reported in a CrN/WN multilayer system [157]. The authors attributed that to the environmental sensitive factors (i.e. humidity, temperature et al.) during the measurements. However, the periodic layer structure of the multilayers may affect the friction coefficients.

The measured friction coefficients are shown in Fig. 4. 21. For multilayer coating, the friction coefficients present an increase tendency with decreasing bilayer thickness. The lowest friction coefficient of CrN/ZrN coating with Λ = 66.7 is 0.32,

comparable to CrN while the highest friction coefficient of CrN/ZrN coating with Λ = 11.7 is 0.54, approached that of ZrN.

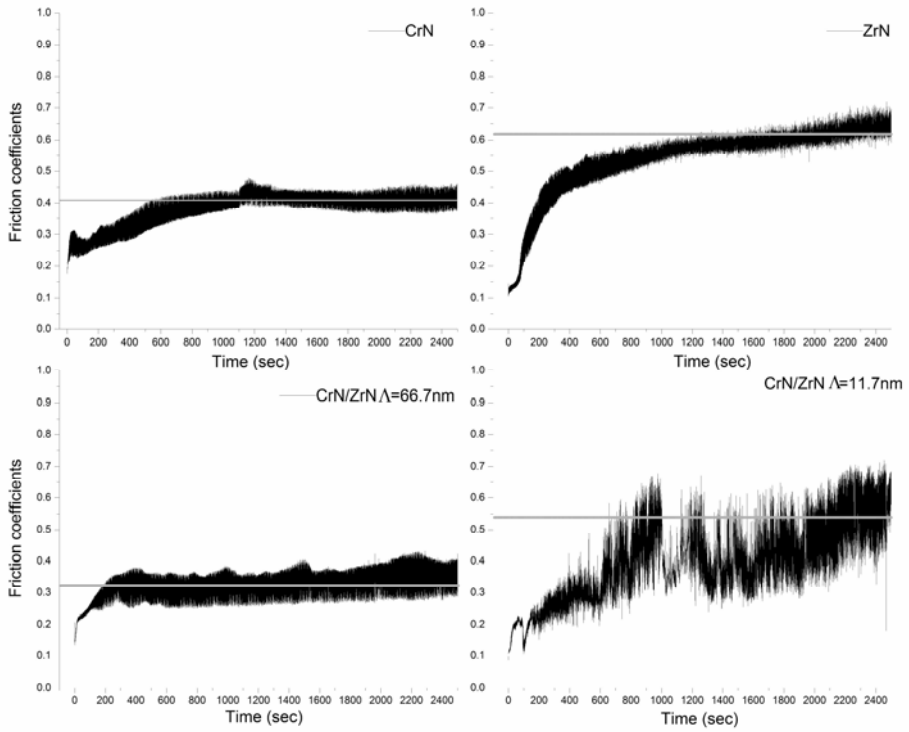

Fig. 4.20. The friction coefficients of CrN, ZrN and CrN/ZrN multilayer coatings with bilayer thickness of 66.7 nm and 11.7 nm as a function of sliding times.

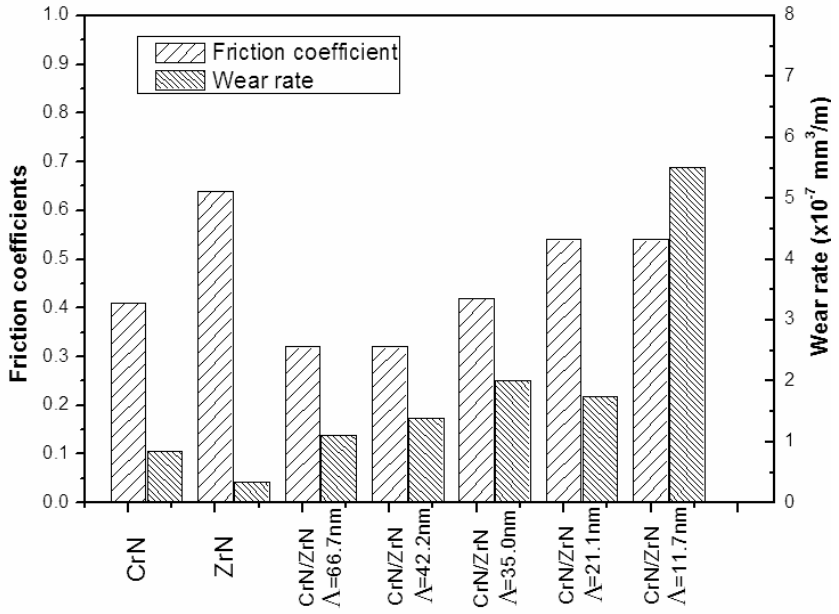

Fig. 4.21. Friction coefficients and wear rates of the as-deposited CrN/ZrN multilayer coatings.

The surfaces of both coatings and counterparts were examined after the pin-on-disk tests. It was found that the significant wear scar appeared on the counter ball surface. The typical coating surface plan views observed by SEM and 3D profile are shown in Fig, 4. 22. In Fig. 4.22a, the multilayer coating with Λ = 66.7 nm seems to be worn out on the wear tracks. However, the corresponding 3D morphology (Fig. 4. 22c) clearly shows that there is little failure occurred on the coating surface. On the contrary, a lot of accumulated materials over the wear track can be observed. These materials were identified to be from WC-Co counterpart in EDX analysis as they contain considerable amount of W element. For the other series coatings including monolayer and multilayer, the occurrence of materials transferred from the counterpart to coating surfaces were also observed. This is a well-known phenomenon in sliding system [158]. Usually, the transferred materials were compacted and adhered to coating surface. In some cases, due to the local high flash temperature as a consequence of the drying sliding, these materials can react with oxygen and formed oxides, which would affect the friction coefficients during test process. The unstable friction coefficient curve in Fig. 4.21d is the case. Fig. 4.22b and d show the morphologies for this coating. It is can be seen that the covered transferred materials are homogeneously distributed on the broader wear track in contrast to the multilayer coating of Λ = 66.7 nm, which is the reason why it has a higher friction coefficient.

The little worn surface of the coatings suggests that the dominant wear mechanism is the abrasion, where the harder coating surface plays a role to cut the softer counterpart. Hence, the simple evaluations of wear rate from the counterpart worn volume can be performed and the results are presented in Fig. 4.20. It can be found that the wear rates of multilayer coatings are higher than the constitute composition, indicating their better wear resistance in the present test conditions For the multilayer coatings, the wear rate increases when decreasing bilayer thickness. The higher wear rate indicates that the coating is more effective to resist failure caused by plastic deformation or micro-cracks in cutting applications. The CrN/ZrN multilayer coating with the lowest Λ of 11.7 nm has the highest wear rate of 5.5 x 10^{-7} mm^3/m, indicating the best wear resistance in the present test conditions.

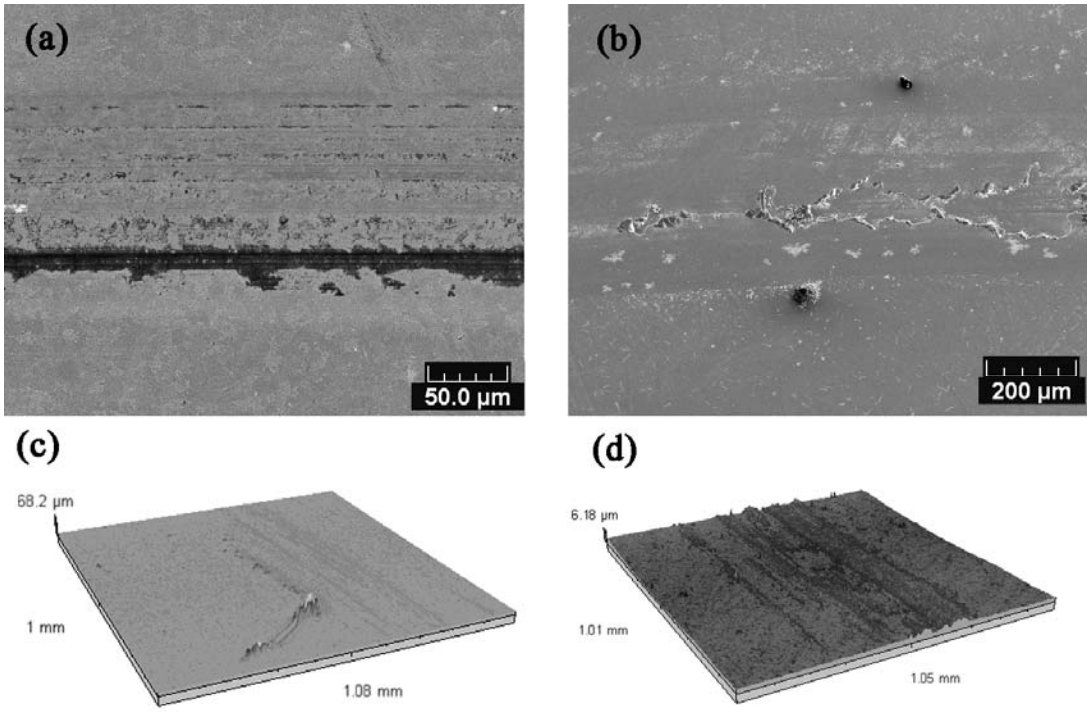

Fig. 4.22. Surface and 3D morphologies after pin-on-disk tests for CrN/ZrN multilayer coatings: (a),(c) Λ=66.7 nm ; (b),(d) Λ=11.7 nm.

4.4.4 Coating corrosion properties

The potentiodynamic polarization curves obtained for single layer CrN, single layer ZrN and multilayer CrN/ZrN coatings with various bilayer thicknesses in 3.5% NaCl solution are shown in Fig. 4.23. The test parameters were the same as what has been described in Chapter 2. Similar to the corrosion behaviors of Zr modified CrN coatings, the typical passive behaviors can be seen for all coated specimens. One should be noted that the passive current densities of multilayer specimen show improvements when compared to ZrN. This can be associated with the additions of CrN individual layer. As presented in the same figure, CrN demonstrates a smooth passive curve, suggesting a very slight pitting corrosion. It indicates that CrN has a stronger resistance to pitting corrosion. The passive current densities of the multilayer coated specimens show the characteristics of instability as well as the single layer ZrN. This scattering of the passive current density in the anodic passive region is a typical

pitting corrosion behavior. It comes from the interactions of the clogging of the corrosion product in the pinholes and the breaking down of the coatings on the coated specimens. However, the average passive current densities from the multilayer coatings still remain under the order of $\mu A/cm^2$, suggesting that the pitting corrosion is not heavy when compared to the passive behaviors of the substrate (See Fig. 4.11).

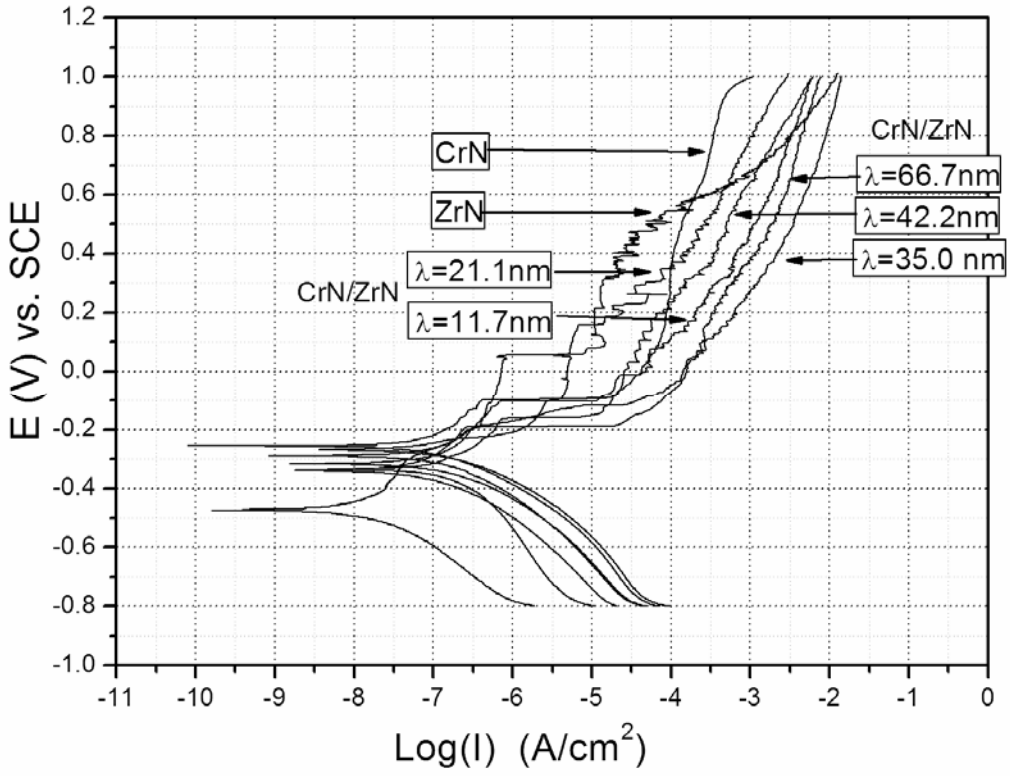

Fig. 4.23. Potentiodynamic polarization curve for CrN, ZrN and CrN/ZrN multilayer coatings with different bilayer thicknesses.

Fig. 4.24 shows the corrosion potentials (E_{corr}) and corrosion current densities (I_{corr}) obtained from the polarization curves. It can be found that the multilayer CrN/ZrN coatings have more positive corrosion potentials in comparison with both of their constituent single layers: CrN and ZrN, which indicates that the multilayer structure is an effective method to improve the coating chemical inertness in an aggressive aqueous environment. The lowest corrosion potential of -270 mV has

moved approximately 66 mV to positive values as referred to CrN and 95 mV when compared to ZrN.

For I_{corr}, it can be found that similar to the Zr modified CrN coatings, the multilayer coated specimens present exceptionally low corrosion current densities in the nA/cm^2 order, up to three orders of magnitude lower than the substrate (Table 4.2). As discussed previously, the transition metal nitrides are generally inert to chemical attack; the results reveal that the multilayer structure provides excellent capabilities for preventing localized galvanic attacks between the coating and the substrate. This can be attributed to the dense columnar structures. However, it should also be seen that compared to the dense compact structure of ZrN without any columnar characteristics, the columnar structure shows its insufficiency to resist pitting attacks. This viewpoint can be concluded from the comparison of the corrosion current densities between ZrN and the other multilayer coatings. The lowest corrosion current density is 42 nA/cm^2 for the multilayer coating with Λ =42.2 nm, which is almost one order higher in comparison with ZrN corrosion current densities of 6.4 nA/cm^2. However, note that the multilayers were deposited without any additions of interlayer, the multilayer coatings with interlayer should be expected to present better performance than they did in the present study. Actually, there are many reports indicating that the interlayer can strongerly improve coating performance in various applications [117, 159, 160]. For instance, as mentioned in Chapter 1, a Nb barrier layer in CrN/NbN system significantly improved the multilayer corrosion performance during the salt spray tests [54]. From the previous evaluations of adhesion and tribological properties of these multilayers, an interlayer is proposed strongly for these multilayers in practical applications.

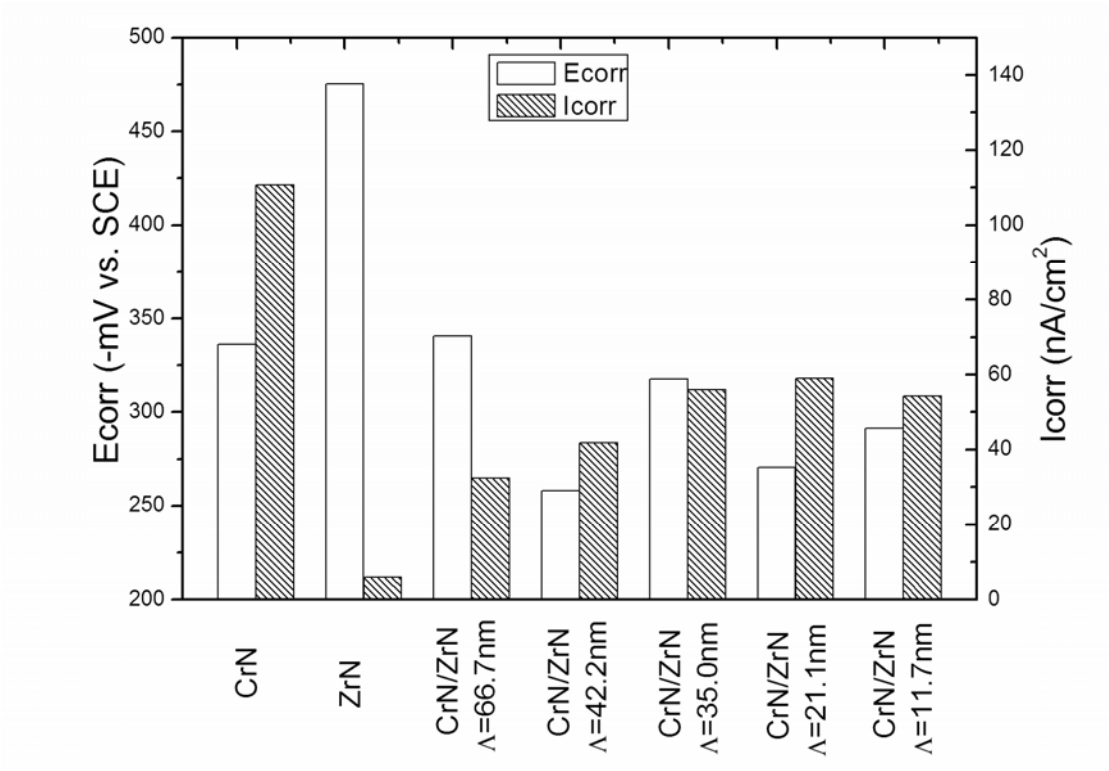

Fig. 4.24. Variations of I_{corr} and E_{corr} of single CrN, ZrN and CrN/ZrN multilayers with different bilayer thicknesses in 3.5% NaCl solution.

The electrochemical data give the evidences that the corrosions in the coated specimens are very slight. However, SEM micrographs show that the surface exhibited apparent corrosion impressions after the polarization tests. The micrographs of the corroded multilayer coatings with the bilayer thickness of 66.7 nm and 11.7 nm are shown in Fig. 4.25. The micrographs actually represent the fully open corrosion pits. This opening could be attributed to the flaking of the coating as a result of chemical attack. The corrosion at the interface of coating and substrate leads to the formation of rust and consequently increases the interface volume, which results in the flaking of the coating. When comparing the corrosion morphologies between CrN and CrN/ZrN multilayer coatings (See Chapter 3), it is clear that the corrosion behaviors of CrN/ZrN coatings are different from CrN. The open corrosion spot morphologies can be attributed to the absence of adhesion since no interlayer was applied.

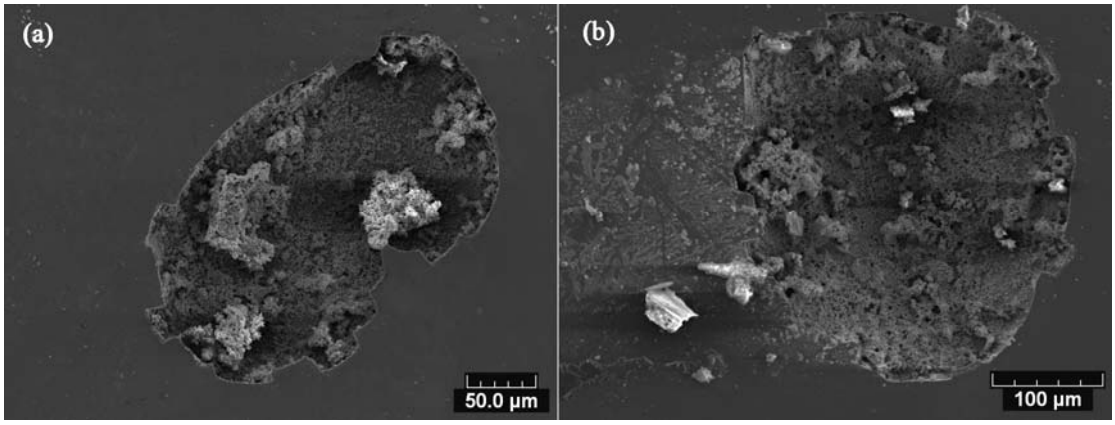

Fig. 4.25. SEM micrographs of corroded spots on CrN/ZrN multilayer coatings (a) Λ =66.7 nm ,(b) Λ =11.7 nm.

The results presented above suggested that the corrosion resistance of coatings improved with multilayer structure, though this improvement was not significant. However, the typical crevice corrosion can also be clearly seen. As discussed earlier, the good corrosion behavior of single layer coatings was due to a dense microstructure with low through-coating porosity. In order to further substantiate the positive effects of layering, the layer number should be increased so that the coatings will denser as more interfaces disrupted the pathway between the corrosion medium and the substrate. However, as indicated in the cross-sectional SEM, the columnar structure can't be eliminated through decreasing bilayer thickness (or increasing layer number). Instead, the structures became more evident when the bilayer thickness decreased. The columnar structure can be considered the main original defects, which prevents the improvements of coating corrosion resistance. An effective method to decrease this effect is to add another element to disrupt such growth characteristics, it will be studied in the next chapter. The other way to improve coating corrosion properties is to add an interlayer, with which a barrier layer between coating and substrate can sustain the corrosion of substrate. However, the results presented in the study of CrN/ZrN multilayer coatings demonstrate the positive effect of layering for improving the corrosion resistance of transition metal nitride coatings.

4.5 Summary

In this chapter, Zr modified CrN coatings with various Zr contents and nanoscale multilayer CrN/ZrN coatings with a bilayer thickness ranging from 11.7 to 66.7 nm are deposited. The detailed investigations in terms of composition, phase structure, morphology, mechanical, tribological and corrosion properties have been carried out.

For the Zr modified CrN coatings, XRD analysis reveals that the synthesized coatings form a nanocrystalline solid solution structure (CrN(Zr)), where Zr substitutes Cr in the CrN lattice. Their lattice parameters increases with increasing Zr content but the grain sizes show little effect. Cross-sectional SEM observations show that all the coatings have dense compact columnar structures. The maximum hardness value of approximately 24 GPa is obtained for the CrN(Zr) coating with Zr content of 1.5 at. %. The Zr modified CrN coatings demonstrate excellent abrasive wear resistance during the pin-on-disk tests. In the potentiodynamic polarization tests, the coated samples exhibit excellent protective characteristics to the stainless steel substrates. The additions of Zr into CrN improve coating chemical inertness. The corrosion mechanism is due to the pitting corrosions, which are mainly localized in the droplet growth defects.

For the investigations of CrN/ZrN multilayers, it is found that single layer CrN and ZrN present <200>, <111> preferred orientations, respectively. However, in the multilayer coatings, CrN individual layers change their growth orientations from <200> to <111> in order to release the stress at interfaces. With decreasing the bilayer thickness, CrN(111) peak shifts continuously to low angles. Low angle XRD confirms the multilayer modulate structures. However, from TEM observations, the multilayer coating does not form a superlattice structure instead of consisting of nanocrystalline CrN and ZrN. Columnar growths for all the multilayer coatings are observed by cross-sectional SEM. The multilayer coatings present a constant hardness of 29 GPa in spite of the variations of the bilayer thickness, which are comparable to monolayer ZrN but higher than monolayer CrN. Pin-on-disk test results show that the multilayer

coating friction coefficients and wear rates increase with decreasing the bilayer thickness. The CrN/ZrN multilayer coatings show excellent performance in tribological tests. In the electrochemical tests, the multilayers demonstrate good chemical inertness as well as very low corrosion current densities. However, the pitting corrosion phenomenon is still found on the coating surface, which is due to the columnar growth characteristics and the absence of interlayer.

Chapter 5. Influence of Si additions on microstructures and properties of CrN/ZrN coatings

5.1 Introduction

In order to further improve coating performance, the concept of composite has been introduced for designing coatings. A composite coating usually consists of two or more phases combined either with different layers (multilayer) or with a homogeneous isotropic mixture of different phases (multiphase) [39]. In this way, the coatings exhibit superior properties to their single constitutions. In the case of multiphase, a well-documented example is Ti-Si-N nanocomposite structured coating developed by S. Veprek et al [64]. This system presents actually the superhardness effect and the high hardness maintains unchanged even at a high temperature of 1000 °C. The principle behind the preparation of such kind of superhard Me-Si-N (Me: transition metal) nanocomposite is based on a strong spinodal phase segregation during depositions, which results in nanocrystalline transition metal nitride (nc-MeN) embedded into amorphous Si_3N_4 matrix (a-Si_3N_4) [64]. As a consequence, strengthening effects originating from grain size effect act three-dimensionally; the classical deformation and fracture like dislocation activity, grain boundary sliding and microcrack propagation in amorphous phase are suppressed [161]. In pursuit of such design ideas, many attempts have been undertaken, which include either substituting TiN by the other transition nitrides (i. e. Cr-Si-N [69, 70], Nb-Si-N [162], Zr-Si-N [163-165]) or synthesizing nanoscale multilayer in the similar systems, such as TiN/ Si_3N_4 [166], CrN/ Si_3N_4 [137, 167] and ZrN/ Si_3N_4 [168]. These new coating systems have shown the abilities to combine desired properties from different components as well as the creation of new properties generated by the combination of suitable materials, which opens new applications for thin film fields.

In this chapter, based on the previous works in CrN/ZrN multilayer system

(Chapter 4), the attempts to add Si element either into CrN individual layer or into ZrN individual layer have been done. The obtained coatings are expected to have a nanocomposite/nanocrystalline multilayer structure, which can combine the advantages of both nanocomposite and multilayer structure so that the coating properties could be enhanced. However, as shown in this chapter, the additions of Si into these individual layers result in great changes in the structure and properties of multilayer coatings. The nanocomposite structures for the single layer coatings are actually obtained by adding Si into the binary transition nitrides. However, once the thickness of the nanocomposite coatings decreases into nano-scale and the single layer becomes a individual layer of multilayer coatings, the structures of these individual layers change significantly from nanocomposite structure to amorphous-like phase. Moreover, such changes even affect the structures of their pairs. Consequently, two kinds of multilayer coatings: nc-CrSiN/a-ZrN and nc-CrN/a-ZrSiN (nc-: nanocrystalline; a-: amorphous) are finally produced. In this chapter, the evolutions of their structures and properties with different bilayer thicknesses (modulate period: Λ) are still the main study objects.

5.2 Coating preparations

From the previous work in Chapter 3, the stoichiometric CrN can be synthesized at a mixture of 10 sccm Ar and 12 sccm N_2. The corresponding Cr target current is 1.5 A. In order to compare the evolution of coating structure and property conveniently, in this chapter, for the depositions of both CrSiN/ZrN and CrN/ZrSiN multilayer coatings, the target current and the reactive gases are still regulated at the same conditions as the deposition of CrN/ZrN multilayer coatings. The substrate bias was the optimized value of –60 V. It is assumed that this level bias has little effect on coating composition and provides an optimized ion bombardment on coating microstructures. To add Si into the individual layer, the simple method as described in Chapter 4 for the deposition of CrZrN coatings was employed: the square Si coupons (10 mm x 10 mm) were placed homogeneously on the erosion track (approximately

177 cm^2) of Cr (or Zr) target.

In this chapter, CrN, ZrN, CrSiN and ZrSiN monolayer coatings were deposited as references. Boron-doped Si (100) wafers, AISI 304 ($HV_{0.1}$ = 180) stainless steels and M2 high speed steel (without heating treatment $HV_{0.1}$ = 230) were used as substrates. The steel substrates were firstly lapped and polished; then they were cleaned in acetone, placed in an ultrasonic bath for degreasing. Afterward they were rinsed in ethanol before depositions. The depositions of these single layer coatings followed the standard deposition steps as described in Chapter 3. The deposition parameters are simply described as follows: the substrate to target distance was 80 mm. The system was evacuated to a based pressure below 5.0 x 10^{-4} Pa prior to deposition. Afterward, the substrates were cleaned by argon ion etching for 15 min, with a RF substrate bias of -300 V. The target was powered on a current regulation of 1.5 A. After a thin adhesive layer of Cr (or CrSi, ZrSi) was deposited at 10 sccm Ar, 12 sccm N_2 was introduced to synthesize the compound coatings. The working pressure was about 0.3 Pa. The deposition times were 60 min for CrN, ZrN CrSiN and ZrSiN single layer coatings.

For the depositions of multilayer coatings, as described in the preparation of CrN/ZrN multilayer coatings, the layer structures were controlled by turning the substrate holder platform and exposing the samples alternately to the sputtering targets. The thickness of each bilayer was determined by the exposure time and the deposition rate of each individual layer. In order to control the multilayer structure conveniently, the deposition parameters of the individual layer remained the same as their single layer depositions so that their deposition rates can be roughly estimated from their single layer depositions. The exposure time was regulated equally for the individual layer. The total deposition time for all the multilayer coatings was 60 min. The further information of multilayer structure characteristics can be found in the next sections.

5.3 CrSiN/ZrN multilayer coatings

5.3.1 Coating structure characteristics

Monolithic CrSiN and ZrN were firstly deposited to provide the basic results for the further deposition of multilayer coatings. GDOES depth profiles showed that CrSiN coating contained 2.8 at. % Si. XRD patterns of single layer CrSiN, ZrN are shown in Fig. 5.1. It can be seen that for the ZrN thin film, only one intensive peak (111) can be observed, indicating that this coating has a stronger <111> texture. In contrast, for CrSiN coating, the broaden CrN(111), (220) peaks can be indexed, suggesting the presented CrN crystals have very small grain sizes. CrN(200) peak located at nearly 44° can also be identified from the magnified inset. However, no peaks from Si_3N_4 phase are observed. According to the previous works in Cr-Si-N system [69], for a coating with Si content in such a level, the structure is nanocomposite where CrN nanocrystalline was embedded into Si_3N_4 amorphous matrix. Accordingly, the single layer ZrN coating has a nanocrystalline structure with <111> texture while the single layer CrSiN coating presents a nanocomposite structure.

Afterward, five types of CrSiN/ZrN with layer numbers from 30 to 180 were prepared and the designed structure characters are summarized in Table 5.1. Typically, the initial deposit layer was CrSiN, then ZrN and CrSiN were deposited alternately and finally CrSiN was the outermost. No interlayer was applied.

Table 5.1. Main parameters of deposited CrSiN/ZrN coatings.

Coating	Exposure time	Thickness (μm)	Bilayer Period (nm)	Hardness (GPa)	Elastic modulus (GPa)
CrSiN	-	3.1	-	27.1	325
ZrN	-	1.3	-	29.0	290
30x(CrN/ZrN)	CrSiN :60s/ZrN:60s	2.6	86.9	18.2	248
45x(CrN/ZrN)	CrSiN :40s/ZrN:40s	2.5	54.7	17.4	236
60x(CrN/ZrN)	CrSiN :30s/ZrN:30s	2.7	44.4	17.3	232
90x(CrN/ZrN)	CrSiN :20s/ZrN:20s	2.4	27.2	16.9	227
180x(CrN/ZrN)	CrSiN :10s/ZrN:10s	2.4	13.4	17.3	215

As indicated in Table 5.1, the multilayer CrSiN/ZrN coatings have a total thickness from 2.4 to 2.7 μm. The bilayer thickness Λ between 13.4 and 86.9 nm was calculated from the ratio of thickness vs. layers. The corresponding individual layer thickness ratios of CrSiN/ZrN in the bilayer thickness were estimated from the single layer coating deposition rate and approximately equals to: $t_{CrSiN} : t_{ZrN} \approx 3.2 : 1$.

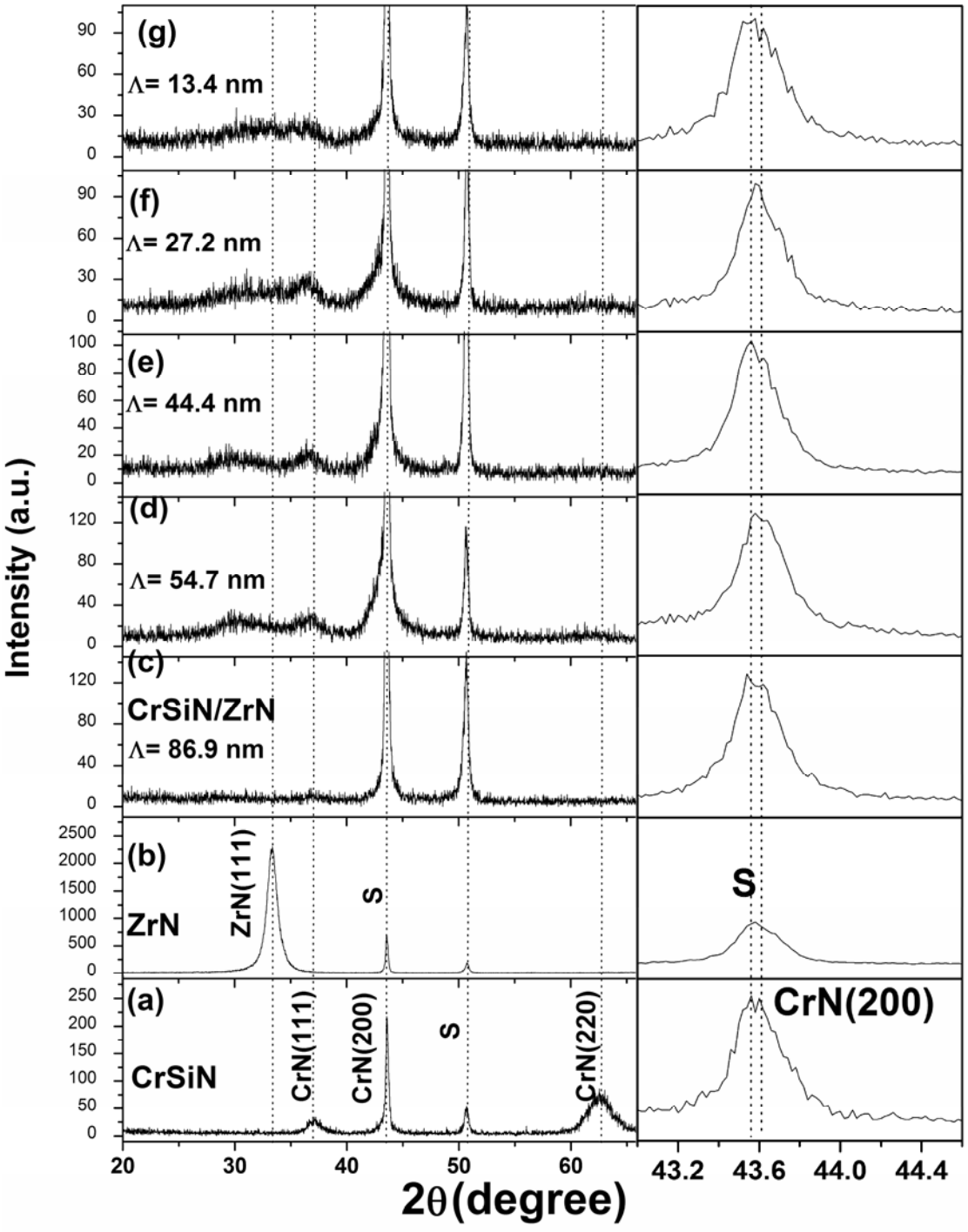

Fig. 5.1. X-ray diffraction patterns of CrSiN, ZrN and CrSiN/ZrN multilayers.

The evolution of multilayer coating structure with different bilayer thicknesses is also shown in Fig. 5.1. It is of interest that in the multilayer coatings, the phase structures of CrSiN and ZrN are different from their single layers. In the XRD patterns of the multilayer coatings, apart from the very stronger steel substrate diffraction peaks, only CrN(111) and CrN(200) (see the magnified inset) can be dimly identified. CrN(111) peak even presents an amorphous-like halo shape. This means that CrSiN individual layer consisted of nanocrystalline grains. In contrast CrSiN, no peaks from ZrN can be indexed. On the contrary, near the position of ZrN(111), an amorphous halo can be found, which means that the ZrN individual layer has an amorphous structure. The structure difference between multilayers and their single layers can be understood by the Barna-Adamik structure zone model (SZM) [169]. This model predicts a transition from columnar to globular microstructure when the content of additives increases. In the present work, the additions of Si into CrN decreased their grain sizes, which resulted in the random orientation of the nucleation during the initial CrSiN growth. As a consequence, the microstructure varied at an increased thickness, which leads to the difference of microstructures between the single layer CrSiN coating with a thickness of 3.1 μm and CrSiN individual layers in nano-dimension. The formation of the amorphous phase for ZrN coating in nano-dimension is similar to CrSiN. In addition, the nucleation of zirconium nitride occurred at the supported amorphous CrSiN layer may also contribute to that.

TEM was used to complement the structural characterizations of the multilayer coatings. The cross-sectional TEM image and corresponding electron diffraction pattern (ED) for a 180 x CrSiN/ZrN multilayer with the smallest bilayer thickness of 13.4 nm are shown in Fig. 5.2. The bright field TEM micrograph (Fig. 5.2a) indicates a layered structure. In this figure, one can roughly estimate the average bilayer thickness value of about 13 nm, which is in agreement with the calculated bilayer thickness from the ratio of coating thickness vs. layer numbers. However, due to the preparation of TEM samples, CrSiN and ZrN individual layer can not be distinguished from this figure. The ED ring patterns confirm the nanocrystalline and

amorphous phase in this thin film. As shown in Fig. 5.2b, there is a B1 NaCl nanocrystalline lattice structure in this multilayer. According to a comparison of their d values, this B1 nanocrystalline can be attributed to CrN. No other crystal phase can be identified from the ED pattern. On the contrary, the inside diffraction fringes exhibit a continuous diffusion pattern, indicating the presence of amorphous phases. Such amorphous phases could be assigned to the combinations of ZrN and Si_3N_4 amorphous phases as taking into account the XRD analysis results.

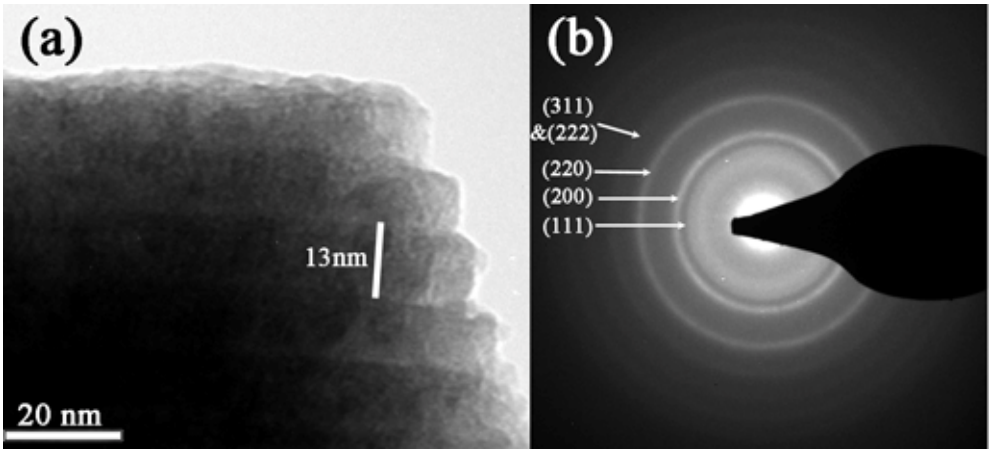

Fig. 5.2. Cross-sectional TEM images for CrSiN/ZrN coating with bilayer thickness of 13.4 nm. (a) bright field image; (b) electron diffraction image.

Fig. 5.3 shows the cross-sectional SEM photographs of various single and multilayer CrSiN/ZrN coatings on silicon substrates for (a) CrSiN; (b) Λ = 86.9 nm; (c) Λ = 44.4 nm; (d) Λ = 13.4 nm. The dense columnar growth microstructure can be clearly seen for CrSiN single coating, which corresponds to zone I in the basic structure zone model (SZM) [113]. On the other hand, for the multilayer coatings, the coatings with the biggest bilayer thickness Λ of 86.9 nm can be seen to have a layered structure with periodicity and continuity. However, for the other presented multilayers, the layer structure is unclear and only the featureless morphologies can be observed.

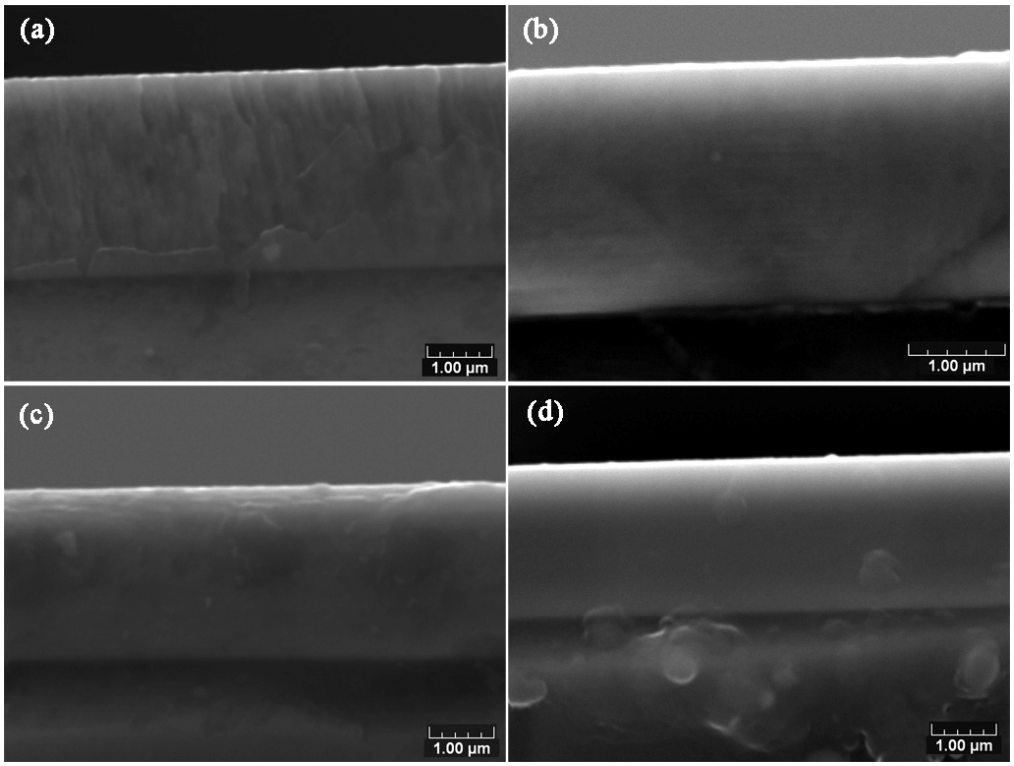

Fig. 5.3. SEM cross-sectional images on Si substrates (a) CrSiN; (b) CrSiN/ZrN Λ=86.9 nm; (c) CrSiN/ZrN Λ=44.4 nm; (e) CrSiN/ZrN Λ=13.4 nm.

5.3.2 CrSiN/ZrN mechanical properties

The nanohardness (H) and elastic modulus (E) of single coatings and multilayers with different bilayer thicknesses are presented in Fig. 5.4. The dot lines indicate the values from the monolithic coatings. The hardness of CrSiN and ZrN single layers are 29 GPa and 27.1 GPa, respectively. The hardness of nanocomposite CrSiN coating is higher than CrN (H = 24.5 GPa) coating deposited in the same conditions [170]. However, in comparison with the hardness of the single layers, the hardness of the multilayers reduces. The maximum hardness is only 18.2 GPa for the CrSiN/ZrN coating with Λ = 86.9 nm, lowering 9 GPa in contrast to CrSiN and 11 GPa when compared to ZrN. With reducing bilayer thickness, the multilayer coating hardness shows a slighter decrease. When Λ decreases down to 13.4 nm, the hardness is 17.3 GPa. The soft phenomenon for the nanocrystalline/amorphous multilayer coatings can be simply attributed to the formation of amorphous structure. As the amorphous phase

is generally softer than its crystal phase, it is not surprising that they present a lower hardness in the multilayers. The similar phenomenon of hardness decrease has been reported in SiC/B_4C amorphous multilayer system [171]. The authors attributed the decreased hardness to the absence of alternate stress field as the difference in elastic properties for the two constitutions is significant in their cases. In this work, it seems that this explanation is suitable when comparing the reduced elastic modulus of the two single layers. However, noting the decrease of the grain size from the nanocrystalline to the amorphous phase, the Hall-Petch relation may be an important factor responsible for the decrease of hardness in the multilayers. The evolution of E as a function of the bilayer thickness shows a similar tendency to that of hardness. The maximum elastic modulus is 248 GPa, corresponding to CrSiN/ZrN multilayer with the largest bilayer thickness of 86.9 nm.

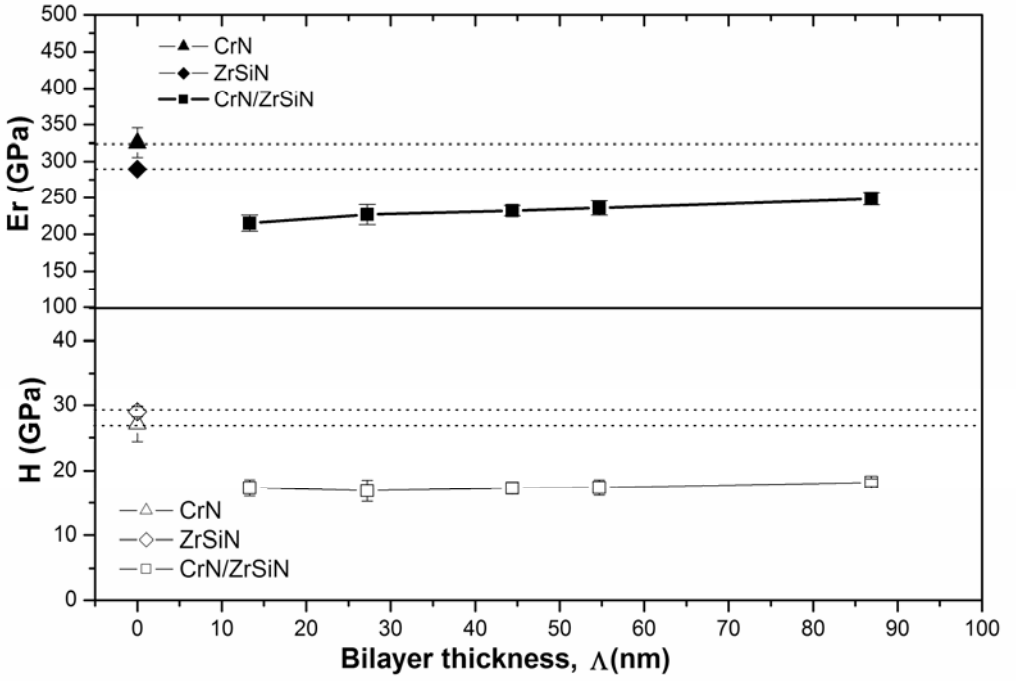

Fig. 5.4. Nanohardness (H) and Elastic Modulus (E) of CrSiN/ZrN multilayer coatings as a function of bilayer thickness.

Scratch tests for the coatings on M2 high speed steel ($HV_{0.1}$=230) substrates were carried out to evaluate the coating cohesion and adhesion. The test technique and parameters have been described in Chapter 2. The definitions of critical loads L_{c1} (cohesive failure), L_{c2} (adhesive failure) are the same as what was described in Chapter 3. The test results for the single layer CrSiN, ZrN and various multilayer CrSiN/ZrN coatings are presented in Fig. 5.5. It can be seen that the variations of L_{c1} and L_{c2} for all the coatings are not significant. Even with a continuous decrease of the bilayer thickness, both L_{c1} and L_{c2} do not show too much dependence on Λ. L_{c1} is about 6 N and L_{c2} is about 12 N for all the coatings. These values are comparable with those in the previous deposited CrN and CrZrN coatings. From the test results, it seems that the soft substrates play the most important effect on the final results of scratch tests.

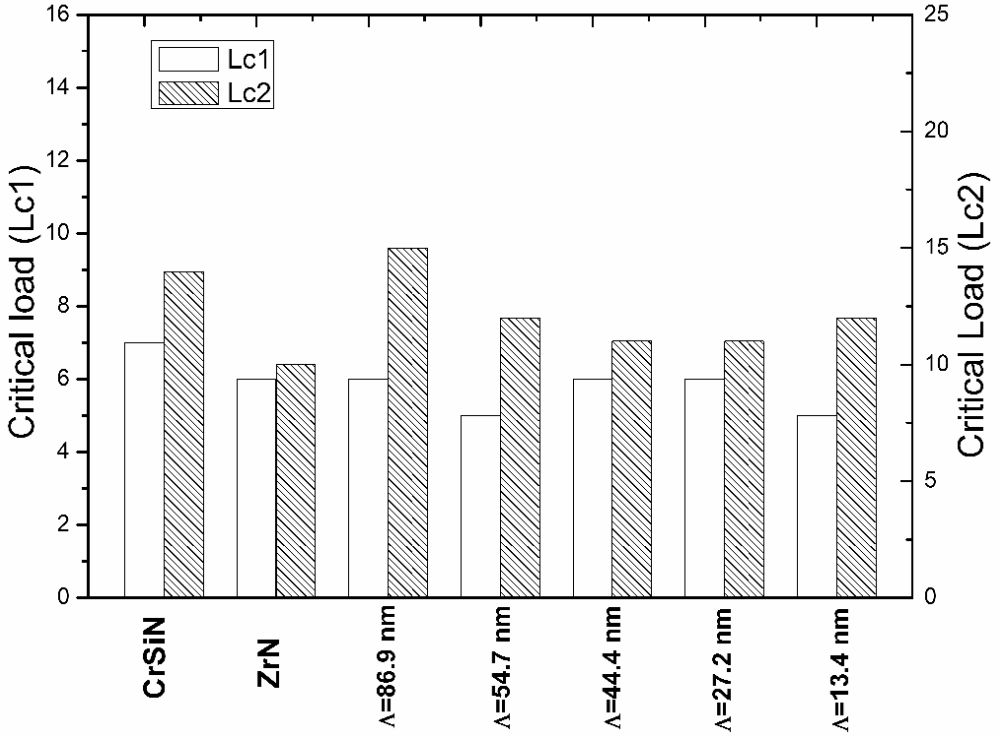

Fig. 5.5. Cohesive critical load (L_{c1}) and adhesive critical load (L_{c2}) as a function of CrSiN/ZrN multilayer coating bilayer thickness.

5.3.3 CrSiN/ZrN tribological properties

Pin-on-disk tests were used to simulate the tribological contact, where WC-Co balls exemplified the hard materials encountered in machining operations. Fig. 5.6 gives the friction coefficients of single and multilayer coatings as a function of operating time. It is shown that for all coatings, the friction curve presents a sharp increase during the initial "running-in" process, which can be attributed to the variations of contact stress. For CrSiN coating, a steady state is reached after the "running-in" process (Fig. 5.6a). The average friction coefficient of CrSiN from this steady state is 0.44 ± 0.04. In contrast to CrSiN, the friction curve of ZrN shows a slow improvement with increasing operating times even after the "running-in" process (Fig. 5.6b). The average friction coefficient of ZrN is 0.59 ± 0.05. In contrast to the friction curves of the single layers, the friction curves of the multilayers show some characteristics of discontinuance as indicated in Fig. 5c, d. The friction coefficient was degraded abruptly at some special points. After a short period of operation time, a relative stable working situation was reached again. Additionally, the distance intervals of the discontinuous friction curve are various. As the discontinuous characteristics only occurred in the multilayer friction curves, the breakdown point of the friction curve may be related to the layer failure at some locale zones. The average friction coefficients of the multilayers are evaluated from the friction curve after the "running-in" process.

Fig. 5.7 shows the average friction coefficients as a function of the bilayer thickness. For the multilayer coatings, the average friction coefficients present a slighter increased tendency with decreasing multilayer bilayer thicknesses. The lowest friction coefficient of CrSiN/ZrN coating with $\Lambda = 86.9$ is 0.68 ± 0.03, which is in a similar range when compared to the ZrN reference coatings. The highest friction coefficient of CrSiN/ZrN coating with $\Lambda = 13.4$ is 0.82, higher than both of the referenced ZrN and CrSiN coatings.

The wear tracks on both the coating surfaces and the counterpart surfaces were examined after the pin-on-disk tests. It was found that the significant wear scar

appeared on the counter ball surface whereas the coating surfaces showed little wear. Fig. 5.8 shows the typical 3D morphologies of wear scars on the coating surfaces and the corresponding counter ball surface optical morphologies of CrSiN/ZrN coating with Λ = 86.9, 13.4 nm after a sliding distance of 500 m. As it can be seen, over the wear tracks of the coating surfaces, there are a lot of accumulated materials, which were identified to be from the WC-Co counterparts in EDX analysis since they contained considerable amount of W element. On the other hand, comparing the widths of the wear tracks, it can be found that the coating with a larger bilayer thickness of 86.9 nm exhibits a narrower wear track than that of the coating with a smaller bilayer thickness of 13.4 nm. Correspondingly, a larger wear circular scar can be found on the counter ball surface, which is against the CrSiN/ZrN multilayers with Λ = 13.4 nm during the test.

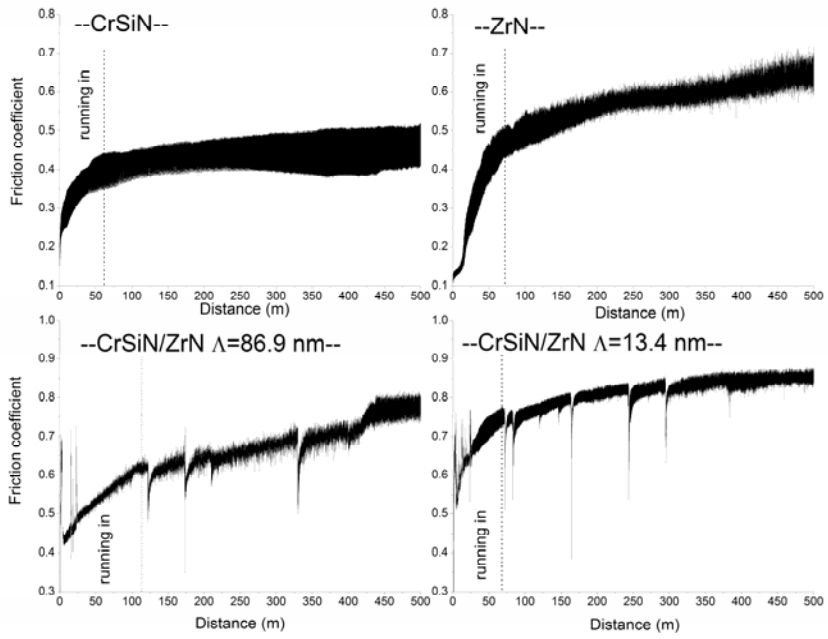

Fig. 5.6. The friction coefficients of CrSiN, ZrN and CrSiN/ZrN multilayer coatings with bilayer thickness of 86.9 nm and 13.4 nm as a function of sliding distance.

The counterpart wear rates, which were evaluated from the loss volume of the counter balls, are typically 12 up to 20 x 10^{-7} $mm^3N^{-1}m^{-1}$ as shown in Fig. 5.7. These values are at least one order of magnitude higher than those for the single coatings.

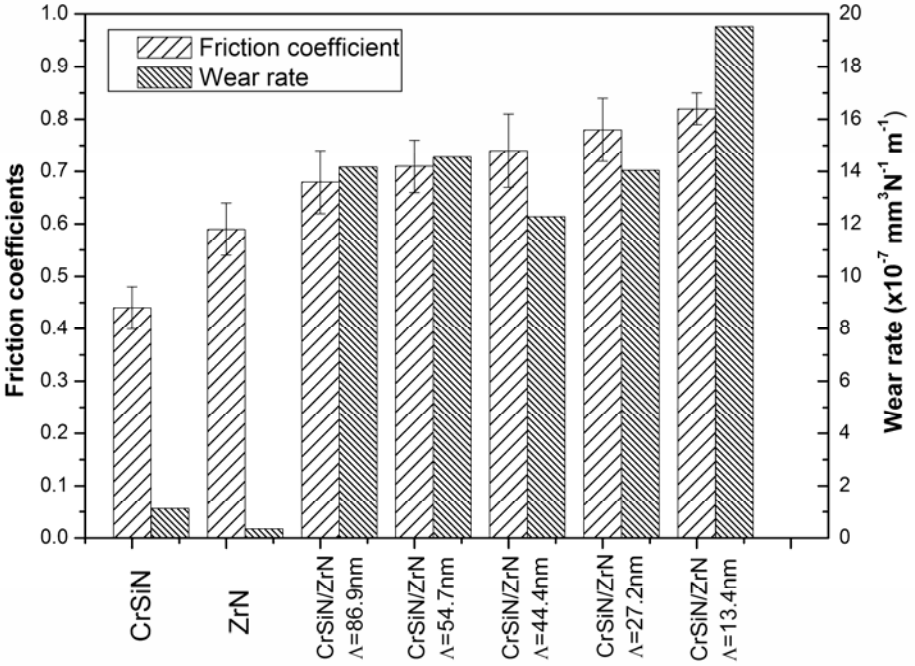

Fig. 5.7. Friction coefficients and wear rates of as-deposited coatings.

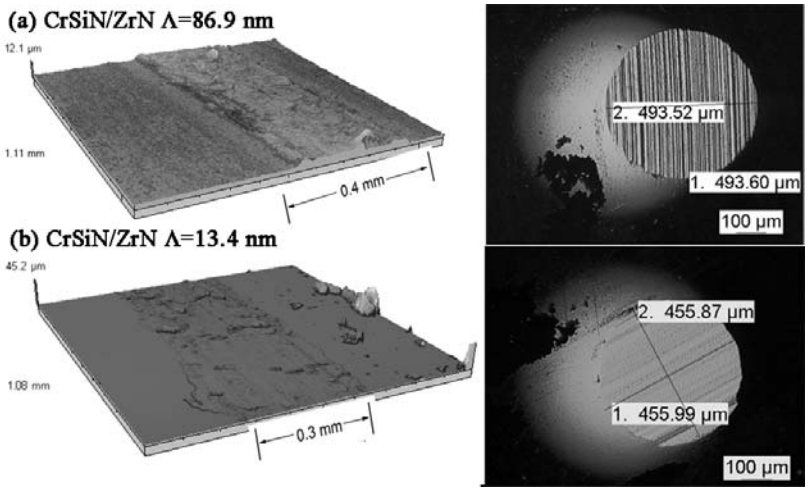

Fig. 5.8. Coating surface 3D morphologies and counter ball optical images after pin-on-disk tests for CrSiN/ZrN multilayer coatings: (a) Λ=86.9 nm; (b) Λ=13.4 nm

The counter ball has a hardness of $HV_{0.1}$ = 1500, which is lower than those of single layer and multilayer coatings in this study. Similar to the soft counterpart sliding on the hard coatings such as TiN/CrN [133, 158], the counter balls undergo predominantly adhesive wear, where the metal transfer layer is formed on the coatings surface as indicated in Fig. 5.8. The further wear and friction is solely determined by

the metal-metal contact. This is the case for the single layer CrSiN and ZrN coatings. However, for the multilayers, it is argued that the locale failure of the surface individual layer occurred under the cyclic stress. The detached small and hard particles from the coating surface may play a role of "third body" in the sliding process, which leads to a sudden change of friction coefficient. After a short sliding, these particles were ejected out from the wear track or submerged in the transferred materials from the counter balls. This can be helpful to explain the friction curve discontinuous characteristics.

5.3.4 CrSiN/ZrN coating corrosion properties

The potentiodynamic polarization curves obtained for the single layer CrSiN, and the multilayer CrSiN/ZrN coatings in 3.5% NaCl solution are shown in Fig. 5.9. In order to compare the corrosion resistance of multilayer coatings with those of their single layers, the polarization curve of ZrN is also involved. It can be seen that similar to the corrosion behaviors of Cr-Zr-N system, the passive behaviors can be seen for all coated specimens. Depending on the samples, the passive current densities between 10^{-3} A/cm^2 to 10^{-5} A/cm^2 can be found. The difference can be associated with the surface conditions before corrosion tests. However, the characteristics of instability for the passive current densities can also be observed. As what has been explained in Cr-Zr-N system, this instability suggests the typical pitting corrosion for PVD coatings.

Fig. 5.10 exhibits the corrosion potentials (E_{corr}) and corrosion current densities (I_{corr}) calculated from the polarization curves. It can be seen that the multilayer CrSiN/ZrN coatings have more positive corrosion potentials in comparison with both of their constituent single layers: CrSiN and ZrN, which indicates the positive effects of multilayer structure for improving the coating internal chemical inertness in an aggressive aqueous environment. The lowest corrosion potential of -221 mV for CrSiN/ZrN with Λ = 44.4 nm has moved approximately 162 mV to positive values as referred to CrSiN and 250 mV when compared to ZrN.

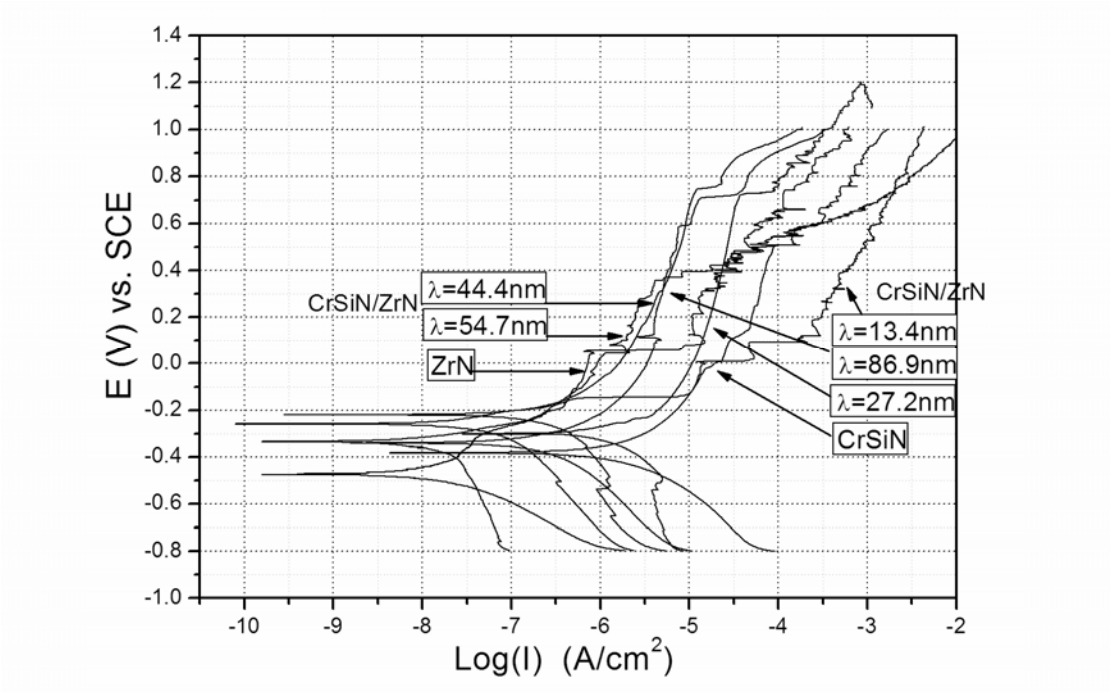

Fig. 5.9. Potentiodynamic polarization curve for CrSiN, ZrN and CrSiN/ZrN multilayer coatings with different bilayer thicknesses.

I_{corr} presents exceptionally low values like the other CrN based coatings. The multilayer coated specimens have corrosion current densities at the nA/cm^2 order, much lower than that from the substrate (Table 4.2). The lowest corrosion current densities is 5 nA/cm^2 for the multilayer coating with Λ =27.2 nm, which means the excellent protective characteristics to the stainless steel substrates. As discussed previously, the transition metal nitrides are generally inert to chemical attacks so that the capabilities of such coatings to resist corrosion are related to their defects (i.e. porosity, macroparticles) and the density of microstructure. The low corrosion current densities reveal that the multilayer structure can provide excellent capabilities to prevent localized galvanic attacks between the coating and the substrate. However, in comparison with the dense compact structure of ZrN without any columnar characteristics (See SEM micrograph), apart from the multilayer coating with Λ =52.7 nm, the featureless morphology for multilayer coatings still shows its insufficiency to resist pitting attack. It should be noted that the multilayers were deposited without any interlayer. As indicated in the CrN/NbN system [52], a thin interlayer may

dramatically improve coating corrosion resistance. The multilayer coatings with interlayer would be expected to have even better performance than they did in the present study.

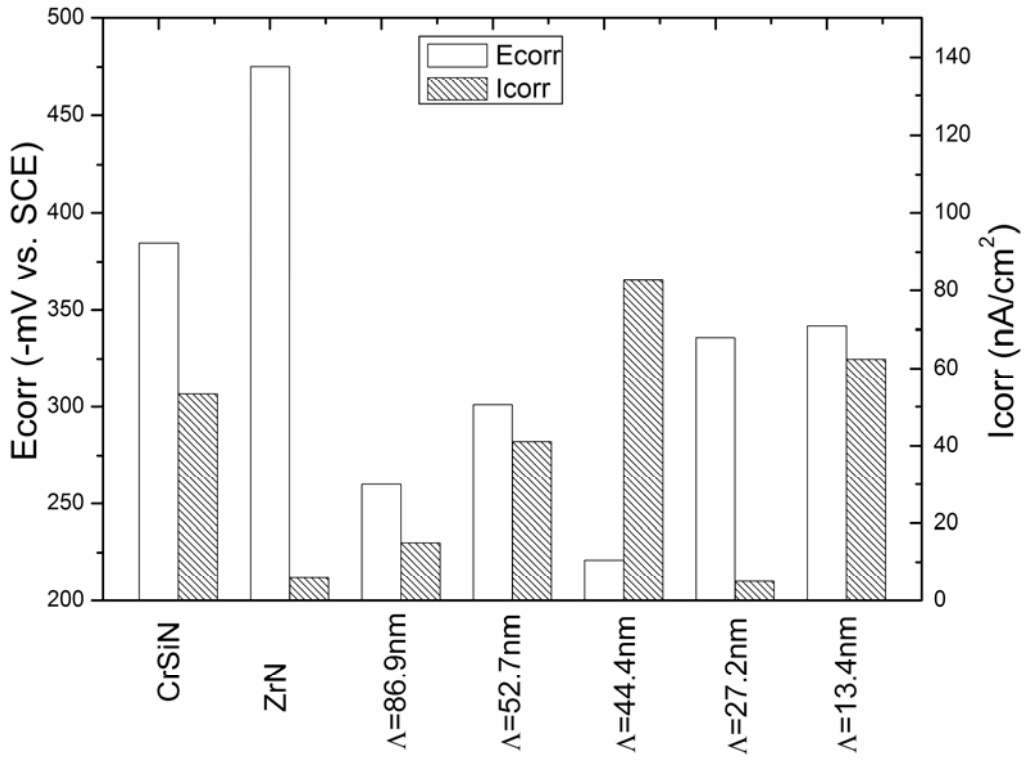

Fig. 5.10. Variations of I_{corr} and E_{corr} of single CrSiN, ZrN and CrSiN/ZrN multilayers with different bilayer thickness in 3.5% NaCl solution.

The electrochemical data indicate that the corrosions in the coated specimens are very slight according to their exceptional low I_{corr}. However, the optical observations after the polarization tests showed that the surface exhibited corrosion impressions in some special locations and in some cases these corrosion spots are evident. The SEM surface micrographs of CrSiN and multilayer coatings with Λ =13.4 nm after the electrochemical tests are shown in Fig. 5.11. From this figure, the fully open corrosion pits are observed. This phenomenon could be attributed to the flaking of the coating as a result of chemical attack as described in CrN/ZrN multilayer coatings.

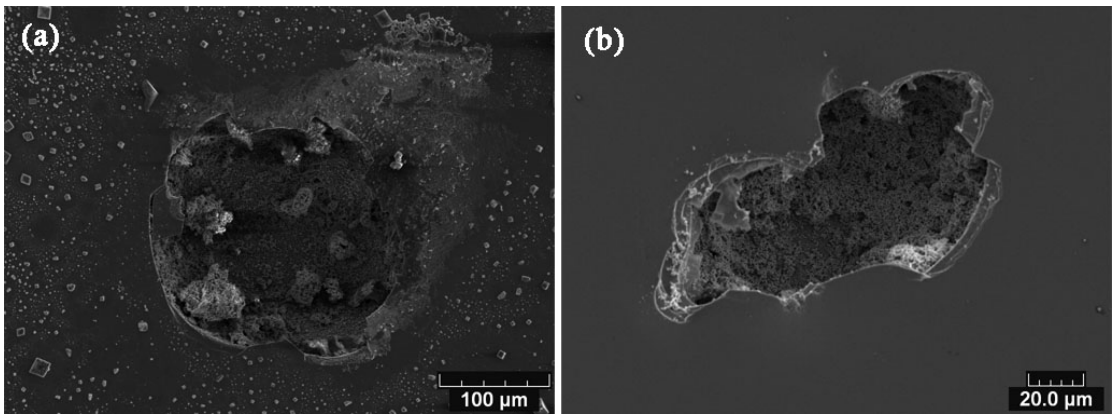

Fig. 5.11. SEM micrographs of corroded spots after corrosion test (a) CrSiN single layer; (b) CrSiN/ZrN with Λ =13.4 nm.

5.4 CrN/ZrSiN multilayer coatings

5.4.1 Structures of ZrSiN and CrN/ZrSiN multilayer coatings

Fig.5.12 presents the X-ray diffraction patterns of CrN and ZrSiN single layer coatings. The single layer CrN thin film can be well indexed as a face centered cubic (FCC) phase as described in Chapter 3. The single layer ZrSiN (4.0 at. % Si) thin film, however, exhibits a stronger <111> preferred orientation as only an relatively intensive ZrN(111) peak and a weak ZrN(222) peak was found. The absence of peaks from the Si_3N_4 phase in the XRD spectra suggests that the added Si either substituted Zr in ZrN lattice or formed a Si_xN_y amorphous phase. However, note that the peaks of ZrN have a general shift nearly 1° towards low angle in comparison with the powder diffraction spectra, which indicates the presence of lattice expansion. Because the atomic radius of Si (0.1177 nm) is smaller than Zr (0.162 nm) [172], the substitution of Zr atomic by Si atomic in the ZrN lattice would lead to a reduction of the lattice constant. Therefore, the absence of peaks from the Si_3N_4 phase cannot be the sequence of the replacement of Zr by Si in ZrN lattice. The formation of Si_xN_y amorphous phase in this ZrSiN thin film seems more reasonable. Moreover, the shift of all ZrN diffraction peaks to low angle indicates the compressive stress in the coating. The formation of nanocomposite in ZrSiN coating are in good agreement

with earlier reports for ZrSiN system [165, 172, 173], where the addition of silicon into ZrN was highly effective for grain refinements.

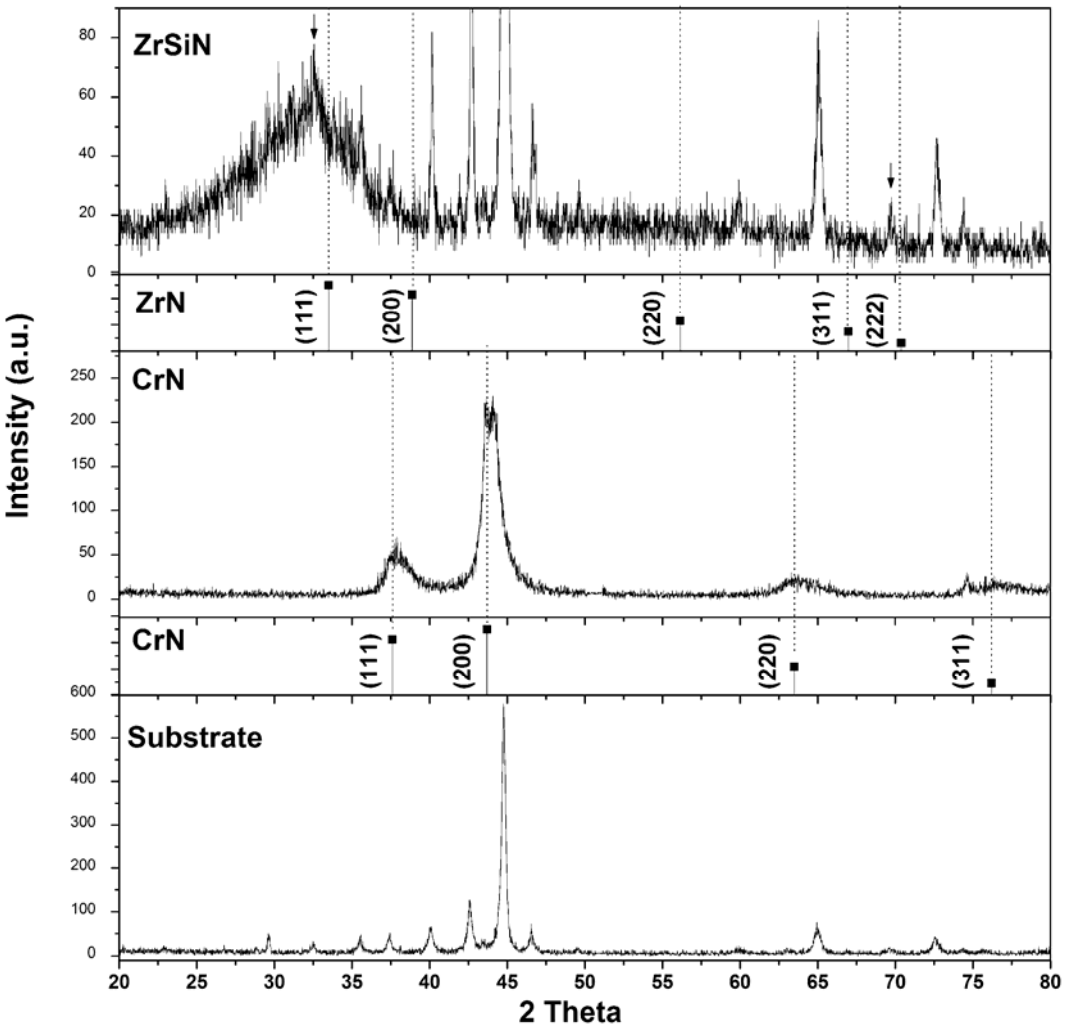

Fig. 5.12. X-ray diffraction patterns of single layer CrN and ZrSiN coatings.

The further characteristics of ZrSiN nanocomposite thin film by FTIR spectral measurements can be found in Fig. 5.13. It has been argued that the formation of amorphous phase is due to the interaction between Zr and Si [173]. However, the presence of Si-N bonds was clearly confirmed from this figure. The absorption spectra of ZrSiN film exhibits a broad absorption band between 800 and 1050 cm^{-1}. The deconvolution of this band gives three Gaussian peaks centered at 800, 840 and 930 cm^{-1}, as shown by dotted lines at the bottom of Fig. 5.13. The mode at 840 cm^{-1} is attributed to asymmetric stretching vibrations of NSi_3 groups; the mode at 800 cm^{-1} is

attributed to the Si-N bond vibration in the SiN_n configuration and the high frequency mode at 930 cm^{-1} may be correlated with the NSi_3 groups as planar configurations [174]. By comparing their integrated intensities, it is clear that nitrogen atoms are predominantly incorporated into the NSi_3 groups in the Si_xN_y amorphous phase.

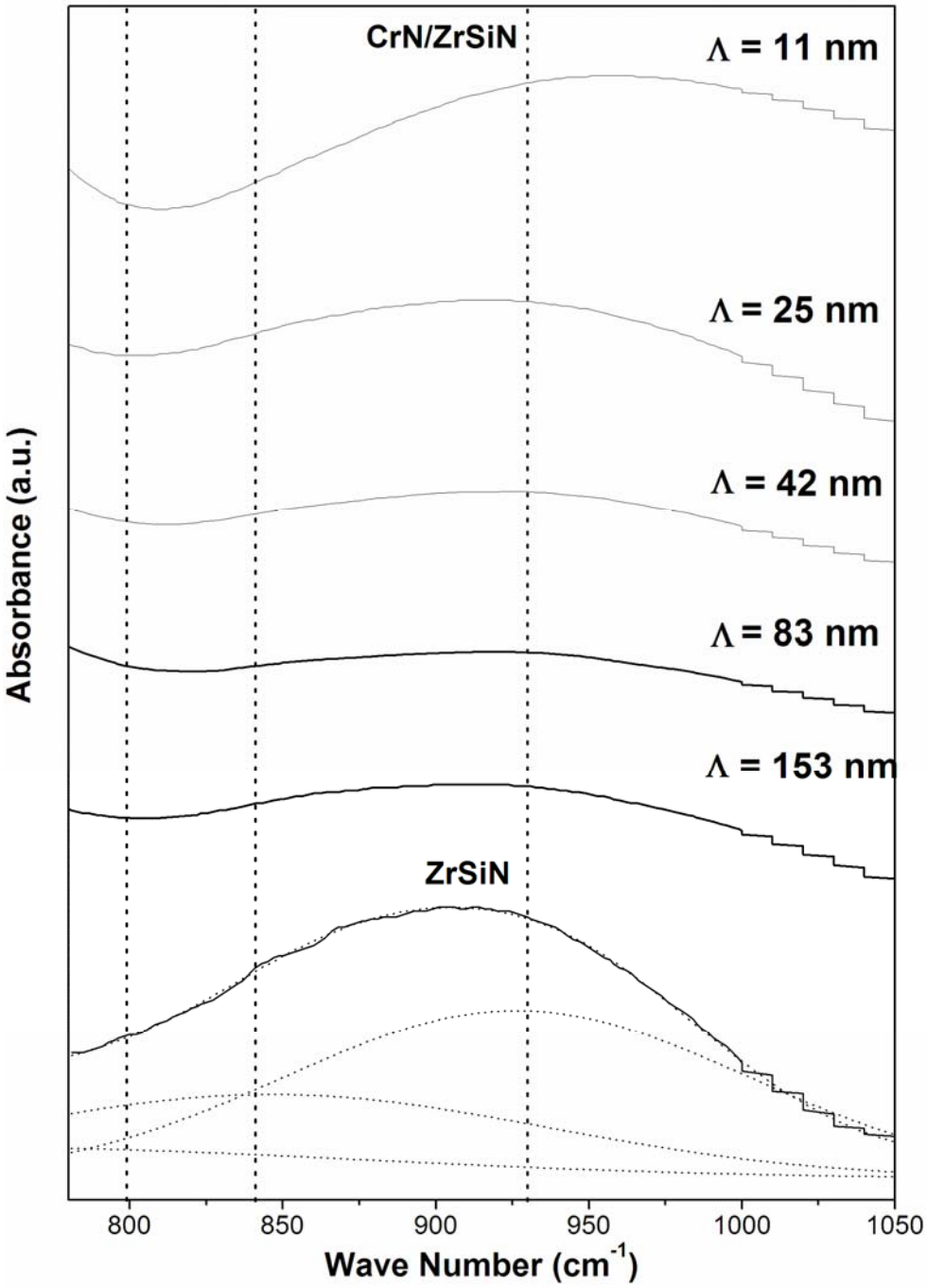

Fig. 5.13. FTIR absorption spectra for different bilayer thickness CrN/ZrSiN coatings.

For multilayer CrN/ZrSiN coatings, the total thickness ranged from 2.0 to 2.5 μm. The bilayer thickness Λ between 11 and 153 nm can be estimated from the ratio of thickness vs. layers (Table 5.2). The corresponding individual layer thickness ratios of CrN/ZrSiN in the bilayer thickness were determined from the single layer coating deposition rate and approximately equals to: $t_{CrN} : t_{ZrSiN} = 3.3 : 1$.

Table 5.2. Main parameters of deposited coatings

Coating	Exposing time	Thickness (μm)	Λ (nm)	H (GPa)	E (GPa)	W_p (mN*nm)
CrN	-	3.2	-	22.8	309	8130
ZrSIN	-	1.6	-	25.4	307	6073
15x(CrN/ZrSiN)	CrN :120s/ZrSiN:120s	2.3	153	30.7	351	10478
30x(CrN/ZrSiN)	CrN :60s/ZrSiN:60s	2.5	83	30.4	342	9508
60x(CrN/ZrSiN)	CrN :30s/ZrSiN:30s	2.5	42	29.3	330	9729
90x(CrN/ZrSiN)	CrN :20s/ZrSiN:20s	2.3	25	30.5	338	9146
180x(CrN/ZrSiN)	CrN :10s/ZrSiN:10s	2.0	11	28.0	325	8684

The evolution of multilayer coating structures with different bilayer thicknesses is shown in Fig. 5.14. The peaks from CrN can be identified from XRD patterns. These broaden and low intensity peaks suggest that their grain sizes are very small. Considering the nano-dimensional bilayer thickness, CrN individual layer should consist of nanocrystalline. However, in contrast to the nanocomposite ZrSiN single layer, no diffraction peaks from ZrN can be identified for all the multilayer coatings, which suggests that the grain sizes of ZrSiN individual layer have been refined through the multilayer structure; probably the presence of ZrSiN in the multilayer coatings is an amorphous structure. With decreasing bilayer thickness down to 11 nm, CrN diffraction peak intensities and positions don't show any evident variations. However, when the bilayer thickness decreased to 11 nm, the peaks of CrN are almost submerged into the background, which indicates the smaller grain size in this coating in comparison with the other multilayers.

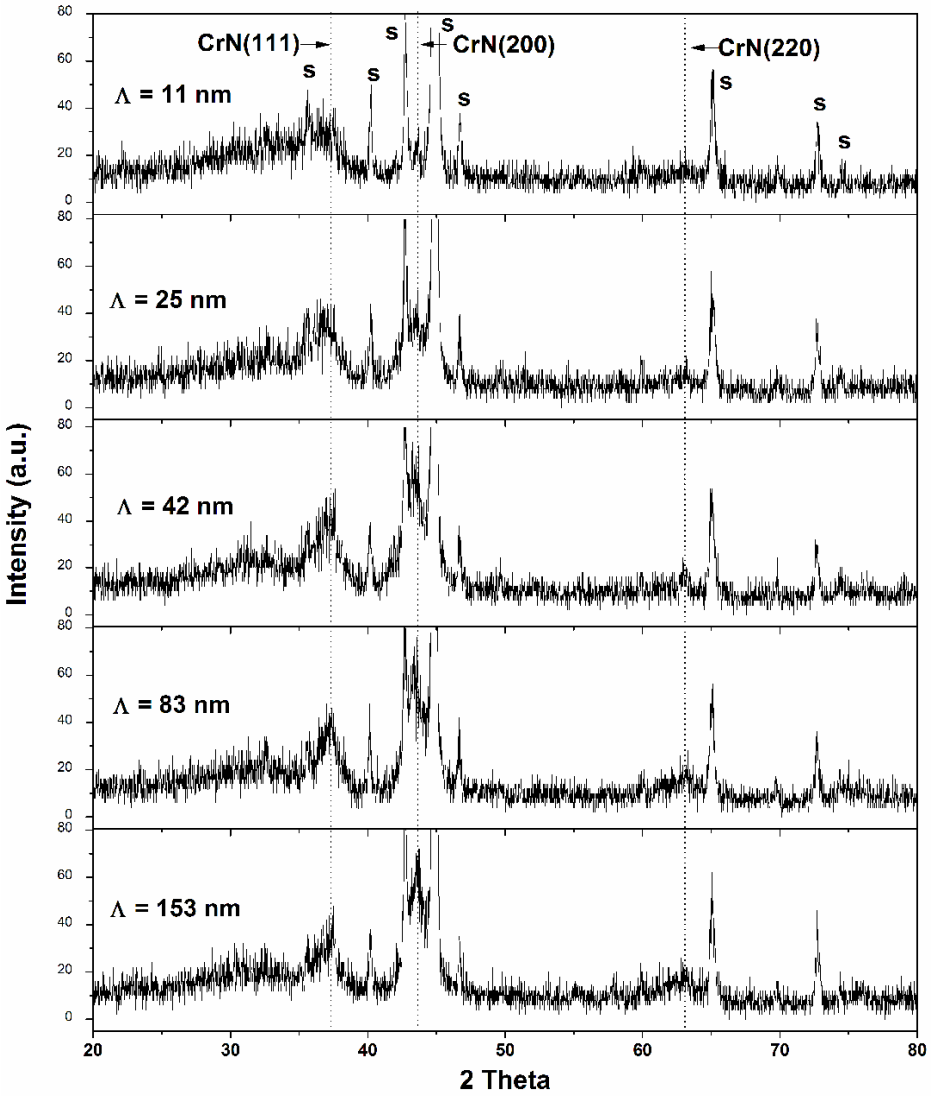

Fig. 5.14. X-ray diffraction patterns of multilayer CrN/ZrSiN coatings with bilayer thickness from 11- 153 nm.

The FTIR absorption spectra of multilayer coatings are shown in Fig. 5.13. In contrast to the spectra of the ZrSiN thin films, the shapes of the existed Si_xN_y absorption band in multilayer coatings clearly vary. This band is unclear when the bilayer thickness is above 42 nm, which can be related to the addition of CrN constituent. However, this band becomes evident under a further decrease bilayer thickness. It is possible to deduce that the band shifts toward higher wave number with decreasing bilayer thicknesses when contrasting the band shapes of CrN/ZrSiN with the highest Λ = 153 nm and the lowest Λ =11 nm, where a fairly remarkable change can be observed. The shift to a higher wave number corresponds to an increase

of NSi_3 planar configurations, which indicates the increased formation of β-Si_3N_4 configurations in the multilayer coatings with decreasing bilayer thickness [174].

The cross-sectional TEM images and corresponding electron diffraction pattern (ED) for CrN/ZrSiN coating with a bilayer thickness of 11 nm are shown in Fig. 5.15. The bright field TEM image (Fig. 5.15a) shows a well defined multilayer structure. CrN and ZrSiN layers alternating along growth direction are shown as the bright and dark interval fringes. The ED ring pattern (Fig. 5.15b) shows that there is a B1 NaCl lattice structure in this multilayer. The outside diffraction fringes have "d" values of 2.4 Å, 2.1 Å, 1.5 Å, and 1.2 Å, which do well coincide with the face center cubic (FCC) CrN structure in JCPDS card (76-2494). The homogenous continuous fringes suggest the very small grain size, which is consistent with XRD analysis. In addition, the inside diffraction fringes show a continuous diffusion pattern, indicating the existence of the amorphous-like phase. This phase can be assigned to ZrSiN amorphous phase as identified in XRD patterns and FTIR spectra. Fig. 5-15c shows the dark field image as selecting the highlight diffraction rings d = 2.4 Å and 2.1 Å. From this figure, it can be derived that the bright layer is ZrSiN while the dark layer is attributed to CrN. The distinguished individual layers can also be confirmed by the different single layer coating deposition rates. In Fig. 5.15c, the measured average bilayer thickness is about 11.3 nm and the thickness ratio $t_{CrN} : t_{ZrSiN} \approx 3.5 : 1$, which are in agreement with the results from coating thickness and layer numbers.

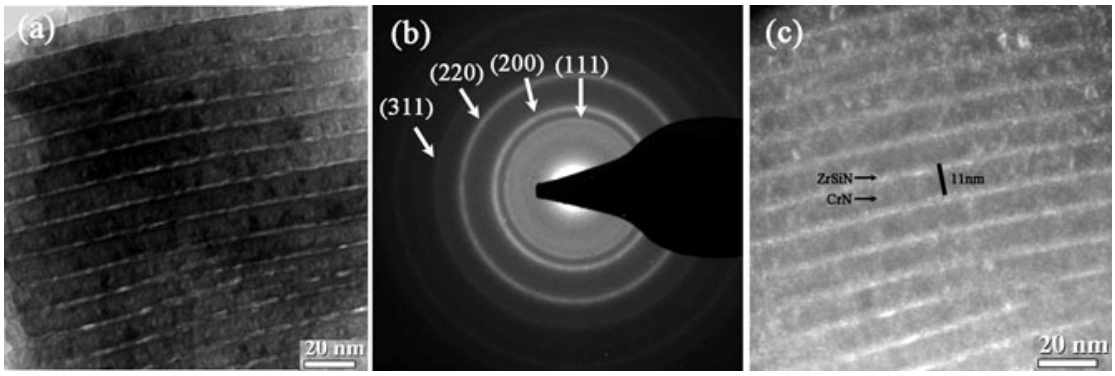

Fig. 5.15. Cross-sectional TEM images for CrN/ZrSiN coating with bilayer thickness of 11 nm. (a) bright field image; (b) electron diffraction; (c)dark field image.

The cross-sectional view of single CrN, ZrSiN and multilayered CrN/ZrSiN coatings are shown in Fig. 5.16. The cross-sectional images confirm the previous measured thickness results. The single layer nanocrystalline CrN exhibits fine-grained dense columnar growth morphology, which can be described by the Zone-T structure of Thomton's structure zone model [113]. In contrast, the nanocomposite ZrSiN shows nearly featureless morphology. On the other hand, for the multilayered CrN/ZrSiN coatings with a larger bilayer thickness above 42 nm, the ZrSiN amorphous layer disrupted the columnar growth of CrN and the layer structure can be dimly seen. The further decrease of bilayer thickness resulted in the layer structure ambiguous and the featureless morphology can be seen.

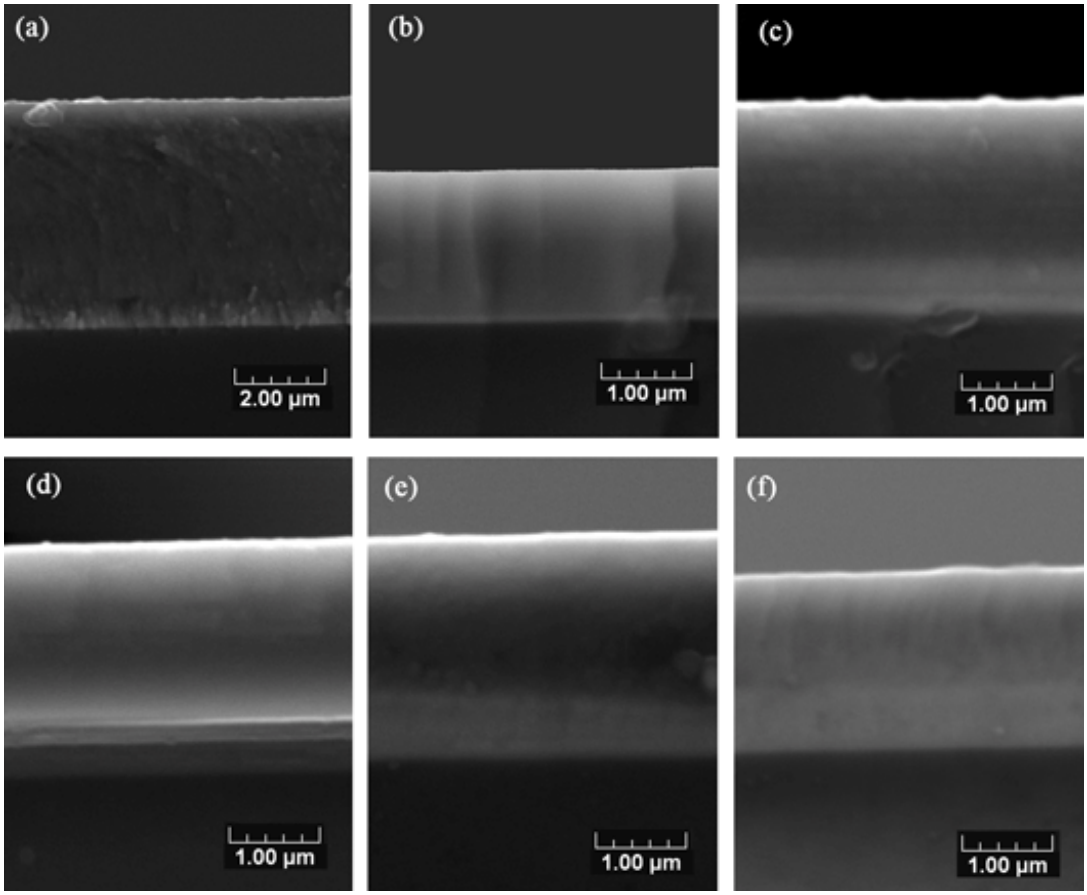

Fig. 5.16. SEM cross-sectional images of as-deposited coatings: (a) CrN; (b) ZrSiN; (c) CrN/ZrSiN, Λ=153 nm; (d) CrN/ZrSiN, Λ=83 nm; (e) CrN/ZrSiN, Λ=42 nm; (f) CrN/ZrSiN, Λ=11 nm.

5.4.2 Mechanical properties of CrN/ZrSiN coatings

Coating hardness (H) and elastic modulus (E) were measured by nanoindentation tests in continuous stiffness measurement (CSM) mode. In such CSM mode, the intrinsic hardness of thin film, not including the substrate effect, could be generally obtained from a plateau region of hardness vs. displacement curve. Fig. 5.17 shows the evaluated process. As can be seen, depending on the film thickness, the start points and ranges of the plateau regions are different. However, the selected nanoindentation depth was still limited to 1/10 of the coating thickness. The average value from the plateau region was the result of one measurement. Nine indentations were made in each sample and the final results are the mean of these nine measurements. The elastic modulus was determined using the same method.

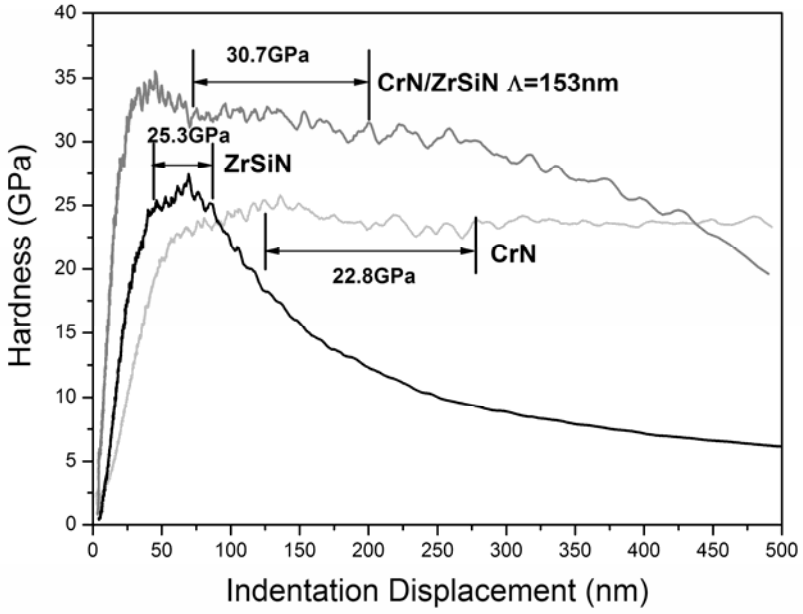

Fig. 5.17. Hardness as a function of displacement of indentation.

Fig. 5.18 shows the obtained nano-hardness (H) and elastic modulus (E) as a function of multilayer bilayer thickness. For comparison, the test results for CrN and ZrSiN single layer films are also involved. H of CrN and ZrSiN films are 22.8 and 25.3 GPa and E of these coatings are 309 and 307 GPa, respectively. In contrast, the multilayered coatings exhibit higher hardness and modulus, which significantly

exceed that of expected from the "rule of mixture". However, no superhardness effect was found in this work. The maximum hardness of 30.7 GPa was achieved at the largest Λ of 153 nm. In addition, the multilayered coatings do not show too much dependence on their bilayer thicknesses. Apart from the multilayer with Λ =11 nm, the other multilayer coatings exhibit almost a constant hardness of nearly 30 GPa. The hardness of the multilayer with the lowest Λ of 11 nm is 28 GPa, a slight decrease in comparison with the other multilayers but still higher than both single layer coatings. The evolution of elastic modulus shows a similar tendency as well as hardness. The maximum E of multilayer is 351 GPa for the largest Λ of 153 nm.

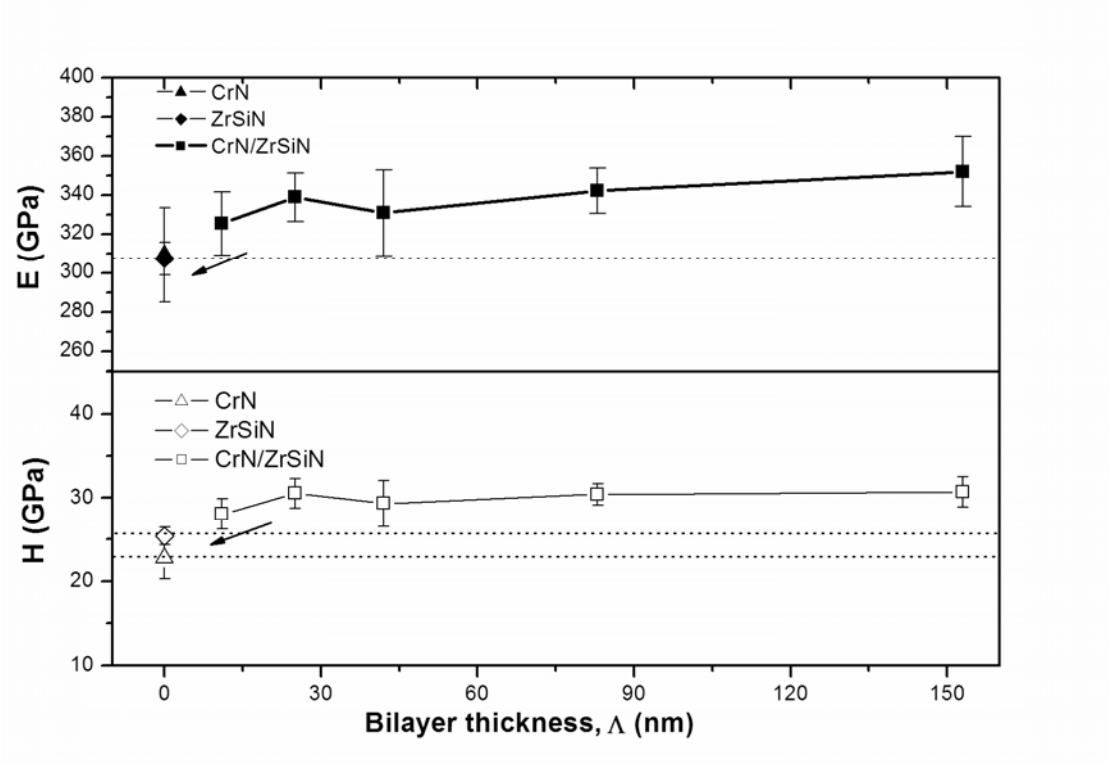

Fig. 5.18. Nano-indentation Hardness (H) and Elastic Modulus (E) of CrN/ZrSiN multilayer coatings as a function of bilayer thickness.

During the nanoindentation tests, the load-displacement curves were recorded simultaneously. Fig. 5.19 shows the typical nanoindentation load-displacement curves for CrN, ZrSiN and CrN/ZrSiN with Λ = 153 nm. As shown by the shadow zone, the plastic deformation work W_p to a definite depth (500 nm) is defined as the integrated area by the loading and unloading curves. It can be used to assess coating resistance to

plastic deformation or to wear [175]. In this study, each W_p was calculated from the indentation curve that presented the most approximate hardness value to the average hardness. The results are listed in Table 5.2. As all the samples were indented to the same depth of 500 nm, the larger plastic deformation work W_p means that it is more difficult to reach the same plastic deformation effects. As a result, the larger W_p corresponds to the better resistance to plastic deformation. From Table 1, single layer CrN exhibits higher resistance to plastic deformation than ZrSiN, thanks to its larger W_p. This result could be associated with the high toughness of CrN. On the other hand, W_p of the multilayer coatings exhibit larger values than both of the single layers. Such a result reveals that the multilayer coatings have better resistance to plastic deformation than the single layers, which probably suggests their higher toughness.

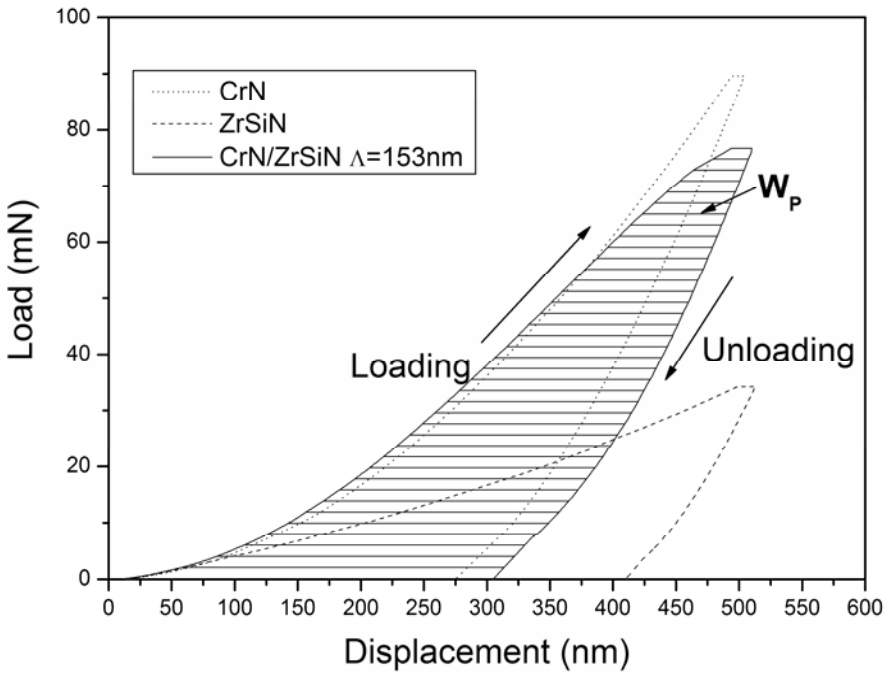

Fig. 5.19. Typical load-displacement curve of CrN, ZrSiN and CrN/ZrSiN multilayer coatings.

However, it is very difficult to determine the coating toughness by means of a quality method. The routine method to estimate coating toughness as suggested by Zhang et. al. [45, 176] has a great measurement error because it is very difficult to determine the crack length. Moreover, the other methods to determine coating

toughness are generally correlated with a series of assumptions and are in association with some special techniques [46]. A discussion of how to determine a coating toughness is beyond the topic of this thesis. In this study, we performed a direct comparison in toughness by use of a Vickers indenter at a 10 N (1kg) load for all the coatings on 304 stainless steel substrates. This method is based on the experimental fact that the low toughness materials are prone to either fragmentation or debonding [177]. Fig. 5.20 shows the typical SEM indentation micrographs of CrN, ZrSiN and CrN/ZrSiN multilayer coating with Λ = 153 nm. It can be seen that under such a high load, CrN and CrN/ZrSiN multilayer coating present only the typical "picture-frame" crack patterns, which are characterized by the diffuse circle-like cracks from the indentation center. ZrSiN coating; however, in addition to the "picture-frame" crack morphology, numerous radial cracks crossing the "picture-frame" cracks can also be seen. These radial distribution cracks are very similar to the crack morphology of the brittle materials (i.e. glass), which suggests that the coating is easier to be fractured. The multilayer coatings show similar crack morphology to CrN, which suggest that they have the same response to the high load. As CrN coating are usually considered as a high toughness coating, it is likely that the CrN/ZrSiN multilayers also present good toughness.

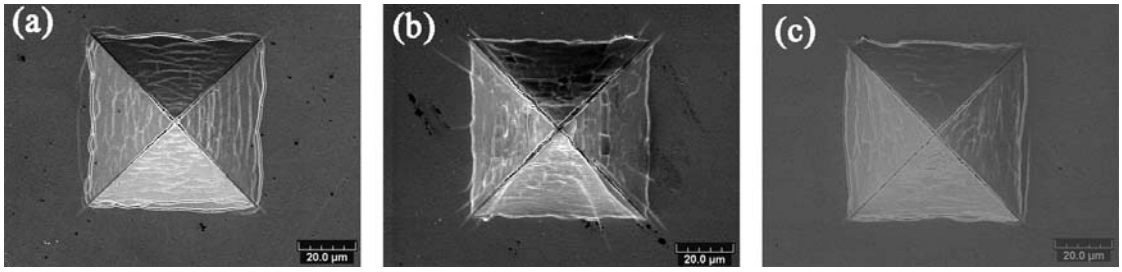

Fig. 5.20. SEM micrographs at a high load of 10 N Vickers indentation for (a) CrN; (b) ZrSiN; (c) CrN/ZrSiN Λ = 153 nm.

Nano-structured composite coatings or multilayer structured coatings can exhibit mechanical properties differing significantly from those of their single layer components. The enhancement mechanism of their mechanical properties is generally

associated with the dislocation entrapment with high interface density. In this study, the synthesis of nanocrystalline/amorphous multilayer coating has been expected to improve coating mechanical properties as the amorphous-like layer can play an important role to hamper the dislocation movement at the interface. The results from mechanical property evaluations show that the multilayer coatings actually have enhanced hardness and modulus in comparison with the single layer coatings. However, the expected stronger enhancements or superhardness effects were not found. On the contrary, the decrease of hardness was observed when varying the bilayer thickness down to 11 nm. To understand this, one should firstly consider the measured method for the complicated multilayer hardness characteristics. In this work, as described above, the method to evaluate coating nanohardness is based on CSM mode, which enables to measure the continuous hardness of coatings from initial to final indentation depth [103]. The hardness values were evaluated from different measure zones and the coating thickness depth range was defined to minimize the soft substrate effects. Comparing the maximum bilayer thickness and the mean depth range for hardness evaluations, the top layer shallow effects can be neglected [178]. The measured hardness can be thought to represent the coating intrinsic hardness. Therefore, the variations of multilayer hardness should be related to the variations of their structures and morphologies.

In crystalline materials, the hardening effects may be attributed to several mechanisms that can contribute in a complicated way, such as grain boundary hardening, the ability to withstand the growth of micro-crack and the movement of dislocations [167]. In the cases of multilayers, to explain the superhardness effects, these mechanisms were embodied into three main theories including the dislocation blocking by layer interfaces, the strain effects at the layer interfaces and the classical Hall-Petch strengthening. The absence of superhardness effects in this work may be related to the dissatisfactions of the common requirements of these theories on coating microstructure and interface nature.

The dislocation blocking mechanism at the layer interfaces by the different elastic modulus was proposed by Koehler [153]. In the present work, apparently, the

modulus difference for CrN and ZrSiN is too small to cause any superhardness effects. However, the enhancements of hardness have been clearly observed. Therefore, several other reasons related to the multilayer structures could be proposed to explain that. The first one is Gahn's coherent strain model [154], in which the coherent strain in the multilayers plays a major role in the hardness anomalies. As ZrSiN coating presents an amorphous phase in multilayer, the stress caused by the lattice mismatch in the interface could not form. Moreover, the thermal stress caused by the mismatch of thermal expansion coefficients is not expected as referring to the similar system CrN/Si_3N_4 [137]. Thus, the typical origins to form alternate stress fields can be excluded. In fact, the phenomenon that the absence of superhardness effects is due to the short of alternative stress fields have been reported in the nc-CrN/a-Si_3N_4 and Cr/Cr_3C_2 multilayer system [137, 179]. However, in this work, the presence of compressive stress in ZrSiN individual layer is possible as indicated by the single layer coating. This stress can strengthen the adjacent CrN individual layer. As a result, the enhanced harnesses can be expected. On the other hand, as the tough CrN layer possesses more volume fraction ($t_{CrN} : t_{ZrSiN} \approx 3.5 : 1$) than ZrSiN in the multilayers, They can play a role to release the stresses from the interface. Thus, the effects of such strengthening are limited; consequently, coating hardness has been improved by a multilayer method but not reached to superhardness level.

Considering the exceptional slight decrease of hardness for multilayer with bilayer thickness $\Lambda = 11$ nm, such result can be related to the changes of its structure and morphology. The amorphous-like CrN from XRD, the improved NSi_3 planar configurations from FTIR and the featureless morphology made it different from the other multilayers. However, in any case, the enhancement of hardness has still been achieved in comparison with the single layer coatings. Moreover, the increase of the toughness has been confirmed, which is due to the stress relaxation and the reduction of crack propagation by crack dissipation at the nanocrystalline/amorphous interface [171].

Fig. 5.21 gives the cohesive critical load (L_{c1}) and adhesive critical load (L_{c2}) for monolayer CrSiN, ZrN and CrSiN/ZrN multilayer coatings on AISI M2 high speed steel substrates. The test parameters were regulated as what has been introduced in Chapter 2. As presented previously, CrN coating has a higher L_{c2}, which is attributed to their excellent toughness. ZrSiN coating presents a lower L_{c1} and L_{c2}. For multilayer coatings, almost all of them present the similar L_{c1} and L_{c2}, which are comparable to those of ZrSiN. Like in the CrN/ZrN system, it seems that the multilayer structure does not provide enhanced adhesion. Again, it confirms that the main factors to affect the coating adhesion are coating thickness and the hardness of substrates. Therefore, a tough metal interlayer is proposed to enhance the adhesion of coatings.

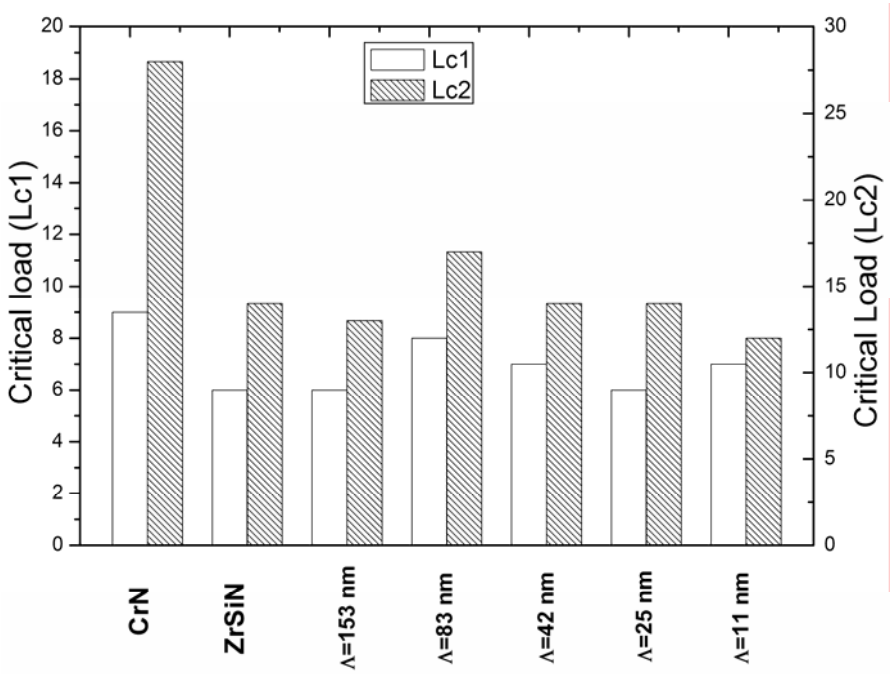

Fig. 5.21. Cohesive critical load (L_{c1}) and adhesive critical load (L_{c2}) as a function of CrN/ZrSiN bilayer thickness.

5.4.3 CrN/ZrSiN tribological properties

The tribological properties of CrN/ZrSiN multilayer coatings with different bilayer thicknesses were examined with WC-Co counterparts on a pin-on-disk tribometer. The applied load was 2 N. The other test conditions have been defined in

Chapter 2. The friction coefficient curves of CrN/ZrSiN multilayer coatings show similar unstable behaviors to CrSiN/ZrN coatings (See Fig. 5.6b). Therefore, the friction coefficients for CrN/ZrSiN were defined as the average friction coefficient for all the sliding distance. The evolution of friction coefficient vs. bilayer thickness was plotted in Fig 5.22. From this figure, the friction coefficients of multilayer exhibit a slight increase from 0.54 to 0.78 when decreasing the bilayer thickness from 153 nm to 83 nm. The low friction coefficient is nearly the same as CrN single layer coatings. As this coating has a bigger bilayer thickness, it seems that the outermost CrN layers play the role as what they do in the single layer coating during all the sliding process. When further decreasing the bilayer thickness from 83 nm to 11 nm, the friction coefficients remain a high value of 0.76 and then slightly decreased to 0.59. The wear mechanism, however, is still the same as indicated previously: the local failure of multilayer coating individual layers resulted in the increase of the friction coefficients. The lower friction coefficient for CrN/ZrSiN with Λ =11 nm may be attributed to the mixture wear of CrN and ZrSiN individual layers with the counter ball when comparing the friction coefficients of CrN, ZrSiN and the other multilayer coatings. The phenomenon that local failures of the multilayer coating occurred during a sliding process can be confirmed by the observations of the surfaces of both coatings and counterparts after the tribological tests. It shows that the wear occurred mainly on the counter balls but in some cases, a slight failure impression on the coating surface can also be observed. Thus the lost volumes from the counter ball can be used to calculate the wear rates. The results are presented in Fig. 5.22. It can be found that the wear rates do not show too much dependence on the bilayer thickness. All the wear rates have the same order of 10^{-7} mm^3/m in spite of varying the bilayer thickness. It can be related to the non-difference on hardness for these coatings. Anyhow, these multilayer coatings indicate their excellent abrasive wear resistance in the present test conditions.

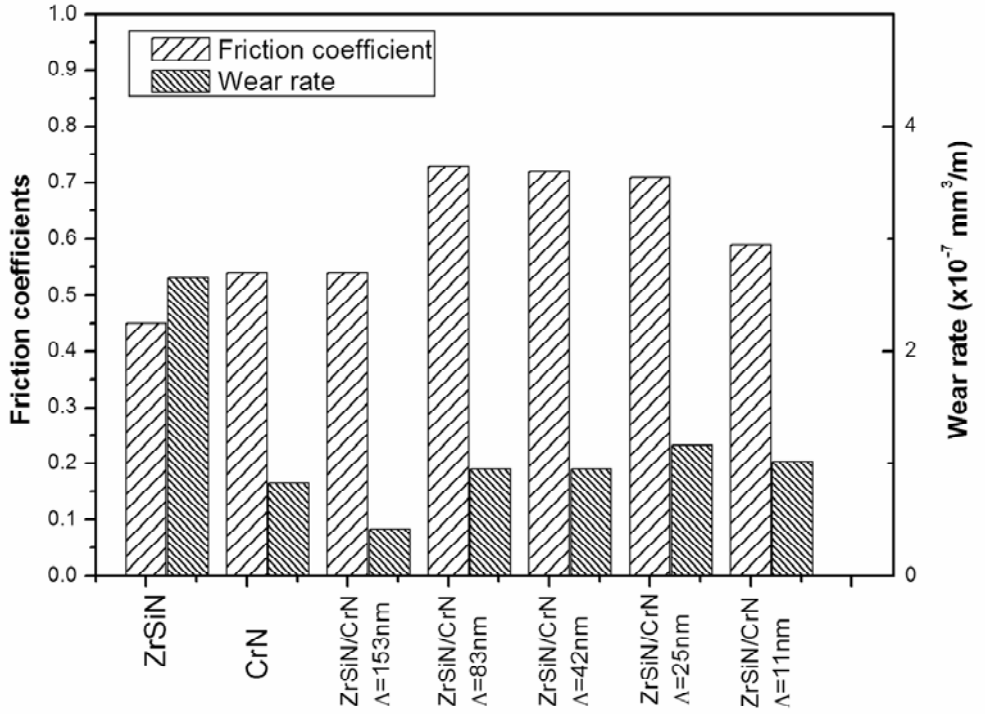

Fig. 5.22. Friction coefficients and wear rates of as-deposited CrN/ZrSiN multilayer coatings.

5.4.4 CrN/ZrSiN corrosion properties

The potentiodynamic polarization curves obtained for single layer CrN, single layer ZrSiN and multilayer CrN/ZrSiN coatings with various bilayer thicknesses in 3.5% NaCl solution are shown in Fig. 5.23. As it can be seen, similar to all the Cr contained coatings, the typical passive behaviors can be seen for all coated specimens.

Fig. 5.24 presents the corrosion potentials (E_{corr}) and corrosion current densities (I_{corr}) calculated from the polarization curves. It can be found that multilayer CrN/ZrSiN coatings with big bilayer thicknesses have almost the same E_{corr} as CrN. However, when the bilayer thickness decreases, E_{corr} shifts to positive direction rapidly. The highest E_{corr} of -145 mV corresponds to CrN/ZrSiN with Λ =43 nm, which has moved approximately 191 mV to positive values as referred to CrN and 78 mV when compared to ZrSiN. The results indicate a more noble behavior of the multilayer coatings.

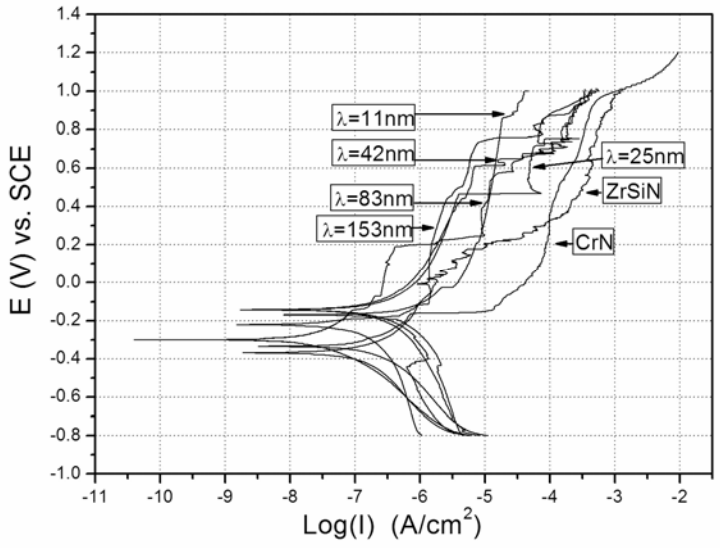

Fig. 5.23. Potentiodynamic polarization curve for CrN, ZrSiN and CrN/ZrSiN multilayer coatings with different bilayer thicknesses.

For I_{corr}, the multilayer coated specimens present low corrosion current densities in the nA/cm^2 order. As the transition metal nitrides are generally inert to chemical attacks, the results reveal that the multilayer structure provides excellent capabilities to prevent localized galvanic attacks between the coating and the substrate. Through comparing I_{corr}, it can be found that ZrSiN single layer thin film presents exceptionally low I_{corr} of 5.2 nA/cm^2, which is lower than the single CrN and most of the multilayer coatings. Only the CrN/ZrSiN multilayer coating with Λ =83 nm presents a comparable I_{corr} of 9.1 nA/cm^2. These results indicate that the coating abilities to suspend corrosion strongly depend on the coating surface properties. However, taking into account the results from E_{corr}, it is still can be derived that the layer structure provides a positive effect for improving the corrosion resistance of transition metal nitride coating.

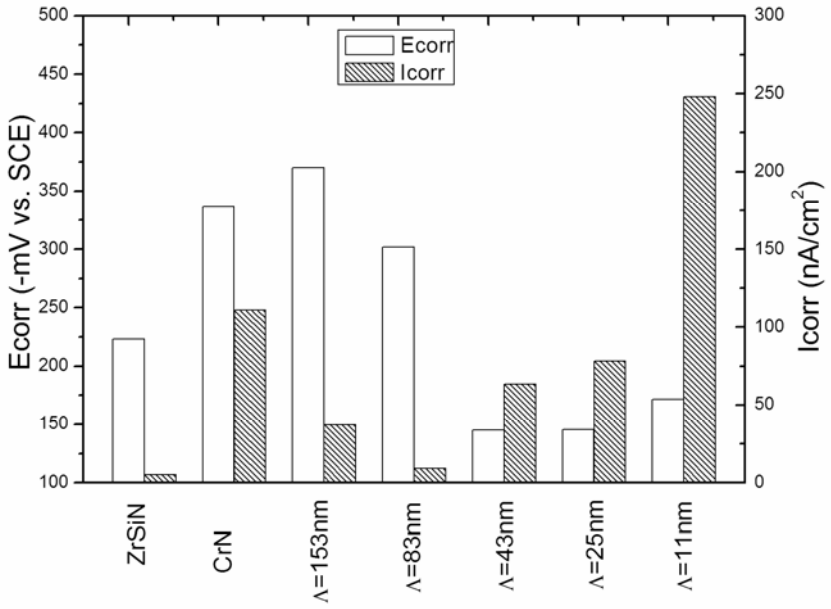

Fig. 5.24. Variations of Icorr and Ecorr of single CrN, ZrSiN and CrN/ZrSiN multilayers with different bilayer thickness in 3.5% NaCl solution.

The electrochemical data provides an evident fact that the corrosions in the coated specimens are very slight as reflected by their low I_{corr}. However, the optical observations after the polarization tests show that the surface actually exhibited corrosion impressions in some special positions especially for the single layer coatings. The typical SEM surface micrographs of ZrSiN and multilayer coatings with Λ =11 nm after the electrochemical tests are shown in Fig. 5.25. From this figure, the fully open corrosion pit for ZrSiN surface can be seen clearly. It could be attributed to the flaking of the coating as a result of chemical attack. For CrN/ZrSiN multilayer coatings, it is interesting that even it presented a relatively high corrosion current density as shown in Fig. 5. 24, the SEM micrograph clearly showed that there is no evident pitting corrosion throughout the coating thickness. This can be attributed to the blocking effects of corrosion products for the Cr contained coatings. In comparison with the behaviors of CrN/ZrN multilayer coatings, the positive effects of Si addition into ZrN to prevent pitting corrosion is obvious. And when comparing the behaviors of CrSiN/ZrN and CrN/ZrSiN, it is surprising that this positive effect for inhabiting pitting corrosion only occurred when Si was added into ZrN individual layer. It seems that the nc-CrN/a-ZrSiN multilayer present better corrosion resistance

than the nc-CrSiN/a-ZrN multilayer coatings. However, taking into account their microstructure and the excellent anti-pitting corrosion behaviors for CrN (Chapter 3), it can be concluded that in order to improve coating resistance on pitting corrosion, the Cr contained individual layer is preferred. In addition, from the corrosion behaviors of CrN/ZrN multilayer, the columnar structure should be reduced in the multilayer so that the pitting corrosion pathway can be blocked at the interface by the formation of Cr corrosion products.

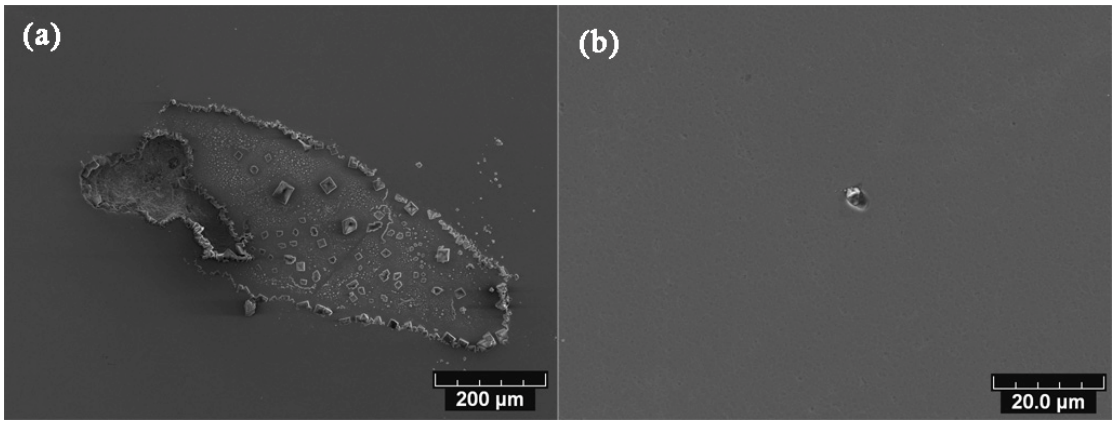

Fig. 5.25. SEM micrographs of corroded spots on CrN/ZrSiN multilayer coatings (a) ZrSiN; (b) CrN/ZrSiN Λ =11 nm.

5.5 Summary

In this chapter, the effect of Si on CrSiN/ZrN and CrN/ZrSiN multilayer coatings has been studied. The key point for these systems is the evolution of multilayer structure and properties as a function of the bilayer thickness.

For CrSiN/ZrN multilayer coatings with a bilayer thickness (Λ) from 13.4 nm to 86.9 nm, XRD analysis reveals that the synthesized coatings form a nanocrystalline/amorphous structure, where CrSiN individual layer is nanocrystalline and ZrN is amorphous. TEM observations confirm the designed layered structure and their phase compositions. Cross-sectional SEM show that the multilayer coatings with a higher Λ exhibit layered structure. With decreasing Λ, the layered structure becomes unclear and the featureless morphologies can be observed. Nanoindentation tests

show that the multilayer coatings present the reduced hardness and elastic modulus in comparison with their single layers. The maximum value of approximately 18 GPa is found for the CrSiN/ZrN coating with Λ = 86.9 nm. The tribological tests reveal that the CrSiN/ZrN coating friction coefficients exhibit a slight increase when decreasing the bilayer thickness. In the potentiodynamic polarization test, the coated multilayer samples exhibit improved corrosion potentials when compared to their single layers. However, the pitting corrosion can not be inhibited by the addition of Si into CrN individual layers.

In the investigation of CrN/ZrSiN multilayers, it is found that the single layer ZrSiN is a nanocomposite structure. The multilayer coatings with bilayer thickness from 11 nm to 153 nm form a nanocrystalline/amorphous structure (nc-CrN/a-ZrSiN). TEM analysis confirms the period layered structure and their phase compositions. Cross-sectional SEM shows that columnar growths are disrupted by ZrSiN amorphous layer for CrN/ZrSiN coatings with a larger bilayer thickness up to 42 nm. A further decrease of the bilayer thickness results in the featureless morphology. The multilayer coatings present almost a constant hardness of 30 GPa in spite of the variation of their bilayer thickness, which is higher than the monolayer ZrSiN and CrN. Moreover, the multilayer structure show a good combination of high hardness from ZrSiN and excellent toughness from CrN. Pin-on-disk tests show that the friction coefficients of multilayer coatings have a slight increase when compared to their single layers. In the electrochemical tests, the multilayers demonstrate good chemical inertness and very low corrosion current densities. The highest E_{corr} of -145 mV corresponds to CrN/ZrSiN with Λ =43 nm. The additions of Si into ZrN individual layer improve the multilayer chemical inertness. Furthermore, the method that Si is added into ZrN individual layer has been found to be an efficient way to inhibit pitting corrosion.

Conclusion and perspectives

Conclusion

This research focuses on the synthesis and characterization of CrN based multilayer coatings for the replacement of electroplated chrome. Because of the diversity of the electroplated Cr applications, in this thesis, the aim is to find the reliable coating systems based on the magnetron technology so that the coating performance can be optimized to satisfy the replacement of Cr on industry scale. The depositions are accomplished by a conventional magnetron sputtering system. Coating structures is determined by various techniques such as GDOES, XRD, SEM, TEM. Mechanical, tribological and corrosion properties are characterized using nanoindentation, scratch test, pin-on-disk and dynamic polarization.

The investigations of CrN depositions concern the influence of the nitrogen flow rate and the RF substrate bias on coating structure and properties. It has been demonstrated that the hysteresis curve and target voltage vs. nitrogen flow rate curve can be well used to predict the phase evolution of chromium nitride deposition. The stoichiometric Cr_2N and CrN have been fabricated with the nitrogen flow rate of 6 sccm and 12 sccm respectively. The stoichiometric Cr_2N, CrN and the nanocrystalline Cr(N) solid solution with a <200> preferred orientation present a higher hardness and elastic modulus than the others so as to their better performance to wear resistance during pin-on-disk tests. However, in contrast to Cr_2N, CrN shows better abrasive wear resistance. The abilities of corrosion resistance of the chromium nitride coating in a 3.5 % NaCl solution are a-CrN > Cr > Cr_2N > CrN > AISI 304.

The optical emission spectroscopy (OES) analysis for various RF biases reveals that the increased substrate bias leads the nitrogen content to reduce in the coatings, thus the evolution of structure from stoichiometric to N deficiency CrN. The CrN coating deposited with RF bias of -60 V demonstrates a good combination of

tribological and corrosion properties. Therefore, RF bias of -60 V is considered to be an optimized value for CrN deposition.

In Cr-Zr-N ternary system, Zr modified CrN coatings with various Zr contents and nanoscale multilayer CrN/ZrN coatings with bilayer thickness ranging from 11.7 to 66.7 nm are deposited. The Zr modified CrN coatings form a nanocrystalline solid solution structure, where Zr substitutes Cr in CrN lattice. The maximum hardness value of approximately 24 GPa is found corresponding to a CrN(Zr) coating with Zr content of 1.5 at. %. In the tribological tests, the Zr modified CrN coatings show excellent abrasive wear resistance. They exhibit excellent protective characteristics to the stainless steel substrates. The addition of Zr into CrN improves coating chemical inertness.

In the investigation of CrN/ZrN multilayers, it is found that CrN individual layers are forced to change their growth preferred orientations from <200> to <111> in order to release stress at interfaces. Low angle XRD and TEM are used to identify the multilayer modulated structures. The multilayer coating consist of nanocrystalline CrN and ZrN. They present a constant hardness of 29 GPa in spite of the variations of the bilayer thickness. Pin-on-disk test results show that the multilayer coating friction coefficients and wear rates from the loose counter ball volume increase with decreasing the bilayer thickness. The multilayers demonstrate good chemical inertness as well as very low corrosion current densities. However, due to the columnar growth characteristics, the pitting corrosion can still be found on the coating surface.

A further effort to add Si into CrN/ZrN multilayer has been made. The deposited CrSiN/ZrN multilayer coatings with a bilayer thickness (Λ) from 13.4 nm to 86.9 nm form a nanocrystalline/amorphous structure, where CrSiN individual layer is nanocrystalline and ZrN is amorphous. SEM and TEM observations confirm the designed layered structure and their phase compositions. Nanoindentation tests show that the multilayer coatings present a lower hardness and modulus in comparison with those from their single layers. The maximum value of approximately 18 GPa is found

for the CrSiN/ZrN coating with Λ = 86.9 nm. The tribological tests reveal that the CrSiN/ZrN coatings exhibit a slight increase when decreasing the bilayer thickness. Moreover, the coated CrSiN/ZrN multilayer samples exhibit improved corrosion potentials when compared to their single layers. However, the pitting corrosion can still be found in these multilayers.

The CrN/ZrSiN multilayers with a bilayer thickness from 11 nm to 153 nm form a nanocrystalline/amorphous structure although the single layer ZrSiN is nanocomposite. SEM and TEM analyses are used to identify the period layer structure and their phase compositions. The multilayer coatings presented almost constant hardness of 30 GPa, which are comparable to monolayer ZrSiN but higher than monolayer CrN. The multilayer structure shows a good combination of high hardness from ZrSiN and excellent toughness from CrN. Pin-on-disk test results show that the friction coefficients of multilayer coatings have a slight increase when compared to their single layers. In the electrochemical tests, the multilayers demonstrate good chemical inertness and very low corrosion current densities. The highest corrosion potential of -145 mV is obtained for CrN/ZrSiN with Λ =43 nm. The addition of Si into ZrN individual layer has been identified to be an efficient way to inhibit pitting corrosion in such a system.

Perspective

This work shows that the Cr based multilayer coatings possess the abilities to satisfy the replacement of electroplated Cr in various conditions. The controllable structure of these multilayers makes them suitable to versatile applications. However, for the industrial replacement of electroplated chrome by this technology, there is still a long way. Furthermore, in this thesis, there still remain a few questions and the author considers these as suggestions for future works.

1. The Cr(N) solid solutions with a very low nitrogen flow rate present an impressive hardness and elastic modulus. Additionally, in the present test conditions,

they also show excellent corrosion resistance. These make them very interesting to be the replacement of electroplated Cr because the original intention to replace electroplated Cr is to deposit pure Cr directly by sputtering techniques. The drawback of the sputtered Cr is the low hardness. However, in this thesis, it seems that using a small amount of nitrogen incorporated into Cr can significantly improve the hardness of pure Cr. Moreover, the deposited Cr(N) solid solution has a higher deposition rate in comparison with CrN, which makes it very attractive for the applications on industrial scale. Analyzing the hardness enhancement mechanisms and testing their performances in the practical applications are of interest for the replacements of electroplated chrome.

2. The amorphous Cr(N) at a low nitrogen flow rate is an unexpected result as the other amorphous transition nitrides are usually obtained at a very high nitrogen partial. Especially, these coatings presented an impressive corrosion resistance in spite of their low hardness. A further synthesis of multilayers based on this kind of coating may provide the possibility to combine an excellent corrosion resistance and the attractive properties from the other multilayer pairs.

3. Cr-Zr-N ternary multiple phase coatings have presented an enhanced hardness and corrosion resistance. Unfortunately, due to the limitation of the method to add Zr into CrN, the concentration of Zr in the coatings is very low. The attempt to synthesize Cr-Zr-N coatings with a high Zr content can be considered the further works for this system. In addition, as indicated in the CrN/ZrSiN multilayer system, the addition of Si can strongly inhibit the pitting corrosion, thus a quaternary system Cr-Zr-Si-N probably presents a further enhancement of the coating property.

4. The Zr-Si-N coating has formed a nanocomposite structure. However, the expected superhardness effect is not found. In this thesis, the detailed investigations for this system have not been carried out. For this system, the superhardness effects have been reported in literatures. To take advantages from nanocomposite and multilayer structures, the studies in Zr-Si-N system are also of interest.

5. In the evolution of CrN/ZrN structure as a function of bilayer thickness, it is clear that there is a trend to form a superlattice. Although it is not the case finally

identified by TEM, the further decrease of bilayer thickness is still expected to clearly reveal the evolution from the nanoscale multilayers to superlattice structure. However, to fabricate these coatings with a lower bilayer thickness, the multilayer deposition method should be changed. A rotating substrate holder system is proposed. However, for a rotating substrate, the deposition rates, the compositions, even phase structures, may change. Consequently, the detailed investigations in the corresponded single layer deposition are needed. In addition, the investigation on the multilayer interface by HRTEM may provide the direct evidence for the principle of the superlattice formation. And the enhanced properties due to the superlattice are also expected.

6. In this thesis, the scratch test results for all the deposited coatings are not superior to those reported for PVD coatings in literatures, which usually have very high critical loads (L_{c2}) overe than 50 N. Although the comparison for different coating systems and different test setups is not a good idea, the results indicated that in spite of our efforts, the coating adhesion does not show too much improvement. The reason is probably attributed to the test parameters during scratch tests, the tip shape as well as the substrate types. Therefore, a detailed investigation on these factors is necessary. Moreover, to evaluate coating adhesion, the attempts of using a new test method (i.e. nano-scratch test) may provide the possibility to compare the results universally. Anyhow, efforts to enhance coating adhesion are needed.

Reference

[1] B. Navinsek, P. Panjan, and I. Milosev, "*PVD coatings as an environmentally clean alternative to electroplating and electroless processes",* Surf Coat Tech. 116-119(1999) 476-487.

[2] P.C. Wynn and C.V. Bishop, "*Replacing hexavalent chromium",* T I Met Finish. 79(2001) 27-30.

[3] M. El-Sharif, "*Replacing hexavalent chromium in electroplating",* T I Met Finish. 75(1997) 143-146.

[4] E. Groshart, "*Finishing in the green : Chromium plating replacements",* Metal Finishing. 95(1997) 70-72.

[5] K.O. Legg, M. Graham, P. Chang, F. Rastagar, A. Gonzales, and B. Sartwell, "*The replacement of electroplating",* Surf Coat Tech. 81(1996) 99-105.

[6] K.L. Bruce D. Sartwell, Philip E. Bretz., "*Status of HCAT/JG-PP Program on Replacement of Hard Chrome Plating With HVOF Thermal Spray Coatings on Landing Gear",* Proceedings of AESF Aerospace Plating and Metal Finishing Forum. (2000) 131-139.

[7] K. Stevens, "*Hard Chrome Plating-A Clean Bill of Health",* Trans.IMF. 75(1997) B33-B34.

[8] K.O. Legg, "*Overview of Chromium and Cadmium Alternative Technologies",* Surface Modification Technologies XV. (2002).

[9] B.A. Graves, "*What to do about hard chromium",* Products Finishing (Cincinnati). 69(2005) 56-59.

[10] J. Gaul, "*WEEE/RoHS - A historical look",* SMT Surface Mount Technology Magazine. 19(2005) 20.

[11] K.L. Charles Pellerin, Christian richter, "*SERDP/ESTCp Metal finishing Workshop Summary Report",* SERDP/ESTCp Metal finishing Workshop Summary Report. (2006).

[12] M. Bielawski, "*Hard chromium plating alternative technologies",* Canadian Aeronautics and Space Journal. 46(2000) 140-149.

[13] M. Pye, "*Alternatives to decorative hexavalent chrome electrodeposits",* T I Met Finish. 79(2001) 83-84.

[14] G.E. Shahin. *Electrodeposited Alloys as a Alternative for Decorative Hexavalent Chromium*. 2000. Chicago, IL, United States: American Electroplaters and Surface Finishers Soc. Inc., Orlando, FL 328203-3075, United States.

[15] G. Editorial. and B.D. Sartwell., "*Thermal Spray Coatings Replace Hard Chrome Plating on Aircraft Components",* The AMPTIAC Newsletter,. 3(1999) 1-16.

[16] S. M. and R. Unger., "*Thermal Spray Coating Replace Hard CHromium",* Adv Mater Process. 152(1997) 19-21.

[17] G.J. Van der Kolk, W. Fleischer, M. Eerden, and T. Hurmans, "*PVD coating as alternative to electroplated chromium",* Galvanotechnik. 92(2001) 3058-3066.

[18] A. Bagdonas, "*Magnetron Sputtering as a Certain Perspective Alternative to the Electrochemical Technologies",* Environmental research, engineering and management,. 2(2003) 55-60.

[19] J.H. Wu, B.S. Phillips, W. Jiang, J.H. Sanders, J.S. Zabinski, and A.P. Malshe,

"*Bio-inspired surface engineering and tribology of MoS2 overcoated cBN-TiN composite coating",* Wear. 261(2006) 592-599.

[20] J.I. Onate, M. Brizuela, J.L. Viviente, A. Garcia-Luis, I. Braceras, D. Gonzalez, and I. Garmendia, "*MoSX lubricant coatings produced by PVD technologies",* T I Met Finish. 85(2007) 75-81.

[21] C.W. Moura e Silva, J.R.T. Branco, and A. Cavaleiro, "*Characterization of magnetron co-sputtered W-doped C-based films",* Thin Solid Films. 515(2006) 1063-1068.

[22] M. Ikeyama, S. Nakao, Y. Miyagawa, and S. Miyagawa, "*Effects of Si content in DLC films on their friction and wear properties",* Surf Coat Tech. 191(2005) 38-42.

[23] Y. Xiang, W. Cheng-biao, L. Yang, Y. De-yang, and F. Zhi-qiang, "*Cr-doped DLC films in three mid-frequency dual-magnetron power modes",* Surf Coat Tech. 200(2006) 6765-6769.

[24] A. Erdemir and C. Donnet, "*Tribology of diamond-like carbon films: Recent progress and future prospects",* Journal of Physics D: Applied Physics. 39(2006) 311-327.

[25] E. Bozyazi, M. Urgen, and A.F. Cakir, "*Comparison of reciprocating wear behaviour of electrolytic hard chrome and arc-PVD CrN coatings",* Wear. 256(2004) 832-839.

[26] A. Hurkmans, D.B. Lewis, and W.D. Munz, "*Magnetron sputtered CrN coatings as alternative to electroplated hard chromium",* Surface Engineering. 19(2003) 205-210.

[27] T. Hurkmans, J. Kubinski, T. Trinh, W. Fleischer, and G.J. van der Kolk, "*Perspective for replacement of hard chrome by PVD",* Proceedings, Annual Technical Conference - Society of Vacuum Coaters. (1999) 364-367.

[28] G.J. Van Der Kolk, T. Hurkmans, C. Strondl, and W. Fleischer, "*Perspective for replacement of hard chrome by PVD",* Vide: Science, Technique et Applications. 1 (4)(2000) 38-47.

[29] A. Matthews, A. Leyland, and P. stevesnson, "*Widening the market for advanced PVD coatings",* J Mater Process Tech. 56(1996) 757-764.

[30] A.F. Jankowski, "*Metallic multilayers at the nanoscale",* Nanostruct Mater. 6(1995) 179-190.

[31] B. Navinsek, P. Panjan, and I. Milosev, "*Industrial applications of CrN (PVD) coatings, deposited at high and low temperatures",* Surf Coat Tech. 97(1997) 182-191.

[32] B. Window, "*Issues in magnetron sputtering of hard coatings",* Surf Coat Tech. 81(1996) 92-98.

[33] S. Berg and T. Nyberg, "*Fundamental understanding and modeling of reactive sputtering processes",* Thin Solid Films. 476(2005) 215-230.

[34] W.D. Sproul, D.J. Christie, and D.C. Carter, "*Control of reactive sputtering processes",* Thin Solid Films. 491(2005) 1-17.

[35] J. Musil, P. Baroch, J. Vlcek, K.H. Nam, and J.G. Han, "*Reactive magnetron sputtering of thin films: Present status and trends",* Thin Solid Films. 475(2005) 208-218.

[36] R.D. Arnell and P.J. Kelly, "*Recent advances in magnetron sputtering",* Surf Coat Tech. 112(1999) 170-176.

[37] P.J. Kelly and R.D. Arnell, "*Magnetron sputtering: A review of recent developments and applications",* Vacuum. 56(2000) 159-172.

[38] I. Safi, "*Recent aspects concerning DC reactive magnetron sputtering of thin films: a review",* Surf Coat Tech. 127(2000) 203-219.

[39] R. Hauert and J. Patscheider, "*From alloying to nanocomposites - Improved performance of hard coatings",* Adv Eng Mater. 2(2000) 247-259.

[40] J.R. Coleman, "*Take control with CNC",* Manuf Eng. 104(1990) 35-40.

[41] C. Subramanian and K.N. Strafford, "*Review of multicomponent and multilayer coatings for tribological applications",* Wear. 165(1993) 85-95.

[42] H. Holleck and V. Schier, "*Multilayer PVD coatings for wear protection",* Surf Coat Tech. 76-77(1995) 328-336.

[43] A.A. Voevodin, J.S. Zabinski, and C. Muratore, "*Recent advances in hard, tough, and low friction nanocomposite coatings",* Tsinghua Science and Technology. 10(2005) 665-679.

[44] P.C. Yashar and W.D. Sproul, "*Nanometer scale multilayered hard coatings",* Vacuum. 55(1999) 179-190.

[45] S. Zhang, D. Sun, Y. Fu, and H. Du, "*Toughening of hard nanostructural thin films: A critical review",* Surf Coat Tech. 198(2005) 2-8.

[46] J. Chen and S.J. Bull, "*Assessment of the toughness of thin coatings using nanoindentation under displacement control",* Thin Solid Films. 494(2006) 1-7.

[47] P.E. Hovsepian and W.D. Munz, "*Recent progress in large-scale production of nanoscale multilayer/superlattice hard coatings",* Vacuum. 69(2003) 27-36.

[48] P.H. Mayrhofer, C. Mitterer, L. Hultman, and H. Clemens, "*Microstructural design of hard coatings",* Prog Mater Sci. 51(2006) 1032-1114.

[49] S. Zhang, D. Sun, Y. Fu, and H. Du, "*Recent advances of superhard nanocomposite coatings: A review",* Surf Coat Tech. 167(2003) 113-119.

[50] P.E. Hovsepian, Y.N. Kok, A.P. Ehiasarian, A. Erdemir, J.G. Wen, and I. Petrov. *Structure and tribological behaviour of nanoscale multilayer C/Cr coatings deposited by the combined steered cathodic arc/unbalanced magnetron sputtering technique*. 2004. San Diego, CA, United States: Elsevier.

[51] P.E. Hovsepian, D.B. Lewis, C. Constable, Q. Luo, Y.N. Kok, and W.D. Munz, "*Combined steered cathodic arc/unbalanced magnetron grown C/Cr nanoscale multilayer coatings for tribological applications",* Surf Coat Tech. 174-175(2003) 762-769.

[52] P.E. Hovsepian, D.B. Lewis, Q. Luo, and A. Farinotti, "*Corrosion resistance of CrN/NbN superlattice coatings grown by various physical vapour deposition techniques",* Thin Solid Films. 488(2005) 1-8.

[53] P.E. Hovsepian, D.B. Lewis, and W.D. Munz, "*Recent progress in large scale manufacturing of multilayer/superlattice hard coatings",* Surf Coat Tech. 133-134(2000) 166-175.

[54] P.E. Hovsepian, D.B. Lewis, W.D. Munz, S.B. Lyon, and M. Tomlinson, "*Combined cathodic arc/unbalanced magnetron grown CrN/NbN superlattice coatings for corrosion resistant applications",* Surf Coat Tech. 120-121(1999) 535-541.

[55] P.E. Hovsepian, Q. Luo, G. Robinson, M. Pittman, M. Howarth, D. Doerwald, R. Tietema, W.M. Sim, A. Deeming, and T. Zeus, "*TiAlN/VN superlattice structured PVD coatings: A new alternative in machining of aluminium alloys for aerospace and automotive components",* Surf Coat Tech. 201(2006) 265-272.

[56] P.E. Hovsepian, W.D. Munz, A. Medlock, and G. Gregory, "*Combined cathodic arc/unbalanced magnetron grown CrN/NbN superlattice coatings for applications in the cutlery industry",* Surf Coat Tech. 133-134(2000) 508-516.

[57] P.E. Hovsepian, C. Reinhard, and A.P. Ehiasarian, "*CrAlYN/CrN superlattice coatings deposited by the combined high power impulse magnetron sputtering/unbalanced magnetron sputtering technique",* Surf Coat Tech. 201(2006) 4105-4110.

[58] L.A. Donohue, I.J. Smith, W.D. Munz, I. Petrov, and J.E. Greene, "*Microstructure and oxidation-resistance of Ti1-x-y-zAlxCryYzN layers grown by combined steered-arc/unbalanced-magnetron-sputter deposition",* Surf Coat Tech. 94-95(1997) 226-231.

[59] Y. Purandare, M.M. Stack, and P. Hovsepian, "*A study of the erosion-corrosion of PVD CrN/NbN superlattice coatings in aqueous slurries",* Wear. 259(2005) 256-262.

[60] W.D. Munz, D.B. Lewis, P.E. Hovsepian, C. Schonjahn, A. Ehiasarian, and I.J. Smith, "*Industrial scale manufactured superlattice hard PVD coatings",* Surface Engineering. 17(2001) 15-27.

[61] A. Leyland and A. Matthews, "*Design criteria for wear-resistant nanostructured and glassy-metal coatings",* Surf Coat Tech. 177-178(2004) 317-324.

[62] A. Erdemir, "*Review of engineered tribological interfaces for improved boundary lubrication",* Tribol Int. 38(2005) 249-256.

[63] M.P. Brady, P.F. Tortorelli, K.L. More, E.A. Payzant, B.L. Armstrong, H.T. Lin, M.J. Lance, F. Huang, and M.L. Weaver, "*Coating and near-surface modification design strategies for protective and functional surfaces",* Materials and Corrosion. 56(2005) 748-755.

[64] S. Veprek, "*Superhard nanocomposites: design concept, properties, present and future industrial applications",* Eur. Phys. J. Appl. Phys. 28(2004) 313-317.

[65] A. Erdemir, "*Design criteria for superlubricity in carbon films and related microstructures",* Tribol Int. 37(2004) 577-583.

[66] G. Bertrand, C. Savall, and C. Meunier, "*Properties of reactively RF magnetron-sputtered chromium nitride coatings",* Surf Coat Tech. 96(1997) 323-329.

[67] G. Bertrand, H. Mahdjoub, and C. Meunier, "*Study of the corrosion behaviour and protective quality of sputtered chromium nitride coatings",* Surf Coat Tech. 126(2000) 199-209.

[68] C. Meunier, S. Vives, and G. Bertrand, "*X-ray diffractometry analysis of r.f.-magnetron-sputtered chromium/chromium nitride coatings",* Surf Coat Tech. 107(1998) 149-158.

[69] D. Mercs, N. Bonasso, S. Naamane, J.-M. Bordes, and C. Coddet, "*Mechanical and tribological properties of Cr-N and Cr-SI-N coatings reactively sputter deposited",* Surf Coat Tech. 200(2005) 403-407.

[70] A. Thobor-Keck, F. Lapostolle, A.S. Dehlinger, D. Pilloud, J.F. Pierson, and C. Coddet, "*Influence of silicon addition on the oxidation resistance of CrN coatings",* Surf Coat Tech. 200(2005) 264-268.

[71] J. Musil, "*Low-pressure magnetron sputtering",* Vacuum. 50(1998) 363-372.

[72] J. Lintymer, N. Martin, J.M. Chappe, P. Delobelle, and J. Takadoum, "*Nanoindentation of chromium zigzag thin films sputter deposited",* Surf Coat Tech. 200(2005) 269-272.

[73] J.J. Olaya, G. Wei, S.E. Rodil, S. Muhl, and B. Bhushan, "*Influence of the ion-atom flux ratio on the mechanical properties of chromium nitride thin films",* Vacuum. 81(2007) 610-618.

[74] A. Thobor and C. Rousselot, "*Ion bombardment: A means to improve the properties of*

TiN/AlN multilayered coatings", Surf Coat Tech. 174-175(2003) 1264-1270.

[75] B.-Y. Shew, J.-L. Huang, and D.-F. Lii, "*Effects of r.f. bias and nitrogen flow rates on the reactive sputtering of TiAlN films",* Thin Solid Films. 293(1997) 212-219.

[76] J. Michler, M. Aeberhard, D. Velten, S. Winter, R. Payling, and J. Breme. *Depth profiling by GDOES: Application of hydrogen and d.c. bias voltage corrections to the analysis of thin oxide films*. 2004. San Diego, CA, United States: Elsevier.

[77] R. Payling, T. Nelis, M. Aeberhard, J. Michler, and P. Seris, "*Layer model approach to background correction in r.f.-GDOES",* Surf Interface Anal. 36(2004) 1384-1391.

[78] K. Shimizu, G.M. Brown, H. Habazaki, K. Kobayashi, P. Skeldon, G.E. Thompson, and G.C. Wood, "*Impurity distributions in barrier anodic films on aluminum: A GDOES depth profiling study",* Electrochim Acta. 44(1999) 2297-2306.

[79] X. Li and B. Bhushan, "*A review of nanoindentation continuous stiffness measurement technique and its applications",* Mater Charact. 48(2002) 11-36.

[80] D.L. Joslin and W.C. Oliver, "*New method for analyzing data from continuos depth-sensing microindentation tests",* J Mater Res. 5(1990) 123-126.

[81] W.C. Oliver and G.M. Pharr, "*Measurement of hardness and elastic modulus by instrumented indentation: Advances in understanding and refinements to methodology",* J Mater Res. 19(2004) 3-20.

[82] N.M. Jennett, G.M. Pharr, and C.J. McHargue, "*Instrumented indentation testing in materials research and development",* Philosophical Magazine. 86(2006) 5153-5154.

[83] N.X. Randall, G. Favaro, and C.H. Frankel, "*The effect of intrinsic parameters on the critical load as measured with the scratch test method",* Surf Coat Tech. 137(2001) 146-151.

[84] W.-J. Chou, G.-P. Yu, and J.-H. Huang, "*Corrosion resistance of ZrN films on AISI 304 stainless steel substrate",* Surf Coat Tech. 167(2003) 59-67.

[85] J. Xu, H. Umehara, and I. Kojima, "*Effect of deposition parameters on composition, structures, density and topography of CrN films deposited by r.f. magnetron sputtering",* Appl Surf Sci. 201(2002) 208-218.

[86] J.J. Olaya, S.E. Rodil, S. Muhl, and E. Sanchez, "*Comparative study of chromium nitride coatings deposited by unbalanced and balanced magnetron sputtering",* Thin Solid Films. 474(2005) 119-126.

[87] S. Inoue, F. Okada, and K. Koterazawa, "*CrN films deposited by rf reactive sputtering using a plasma emission monitoring control",* Vacuum. 66(2002) 227-231.

[88] A. Hurkmans, D.B. Lewis, and W.D. Munz, "*Magnetron sputtered CrNx coatings as alternative to electroplated hard chromium",* Surface Engineering. 19(2003) 205-210.

[89] A. Tricoteaux, P.Y. Jouan, J.D. Guerin, J. Martinez, and A. Djouadi, "*Fretting wear properties of CrN and Cr2N coatings",* Surf Coat Tech. 174-175(2003) 440-443.

[90] M. Oden, J. Almer, G. Hakansson, and M. Olsson, "*Microstructure-property relationships in arc-evaporated Cr-N coatings",* Thin Solid Films. 377-378(2000) 407-412.

[91] Z.B. Zhao, Z.U. Rek, S.M. Yalisove, and J.C. Bilello, "*Phase formation and structure of magnetron sputtered chromium nitride films: In-situ and ex-situ studies",* Surf Coat Tech. 185(2004) 329-339.

[92] S. Han, J.H. Lin, G.H. Wang, and H.C. Shih, "*The effect of preferred orientation on the mechanical properties of chromium nitride coatings deposited on SKD11 by unbalanced*

magnetron sputtering", Mater Lett. 57(2003) 1202-1209.

[93] S.K. Pradhan, C. Nouveau, A. Vasin, and M.A. Djouadi, "*Deposition of CrN coatings by PVD methods for mechanical application",* Surf Coat Tech. 200(2005) 141-145.

[94] G.G. Fuentes, R. Rodriguez, J.C. Avelar-Batista, J. Housden, F. Montala, L.J. Carreras, A.B. Cristobal, J.J. Damborenea, and T.J. Tate, "*Recent advances in the chromium nitride PVD process for forming and machining surface protection",* J Mater Process Tech. 167(2005) 415-421.

[95] N. Martin, D. Baretti, C. Rousselot, and J.-Y. Rauch, "*Effect of bias power on some properties of titanium and titanium oxide films prepared by r.f. magnetron sputtering",* Surf Coat Tech. 107(1998) 172-182.

[96] F. Debal, J. Bretagne, A. Ricard, M. Jumet, M. Wautelet, J.P. Dauchot, and M. Hecq, "*Optical emission of magnetron discharges as a function of the composition of argon-nitrogen gas mixtures",* Surf Coat Tech. 98(1998) 1387-1394.

[97] F. Debal, J. Bretagne, M. Jumet, M. Wautelet, J.P. Dauchot, and M. Hecq, "*Analysis of DC magnetron discharges in Ar-N2 gas mixtures. Comparison of a collisional-radiative model with optical emission spectroscopy",* Plasma Sources Science and Technology. 7(1998) 219-229.

[98] H.A. Jehn, J.-H. Kim, and S. Hofmann, "*Composition and properties of transition metal nitride thin films (ZrNx, NbNx, MoNx)",* Surf Coat Tech. 36(1988) 715-727.

[99] Z. Han, J. Tian, Q. Lai, X. Yu, and G. Li, "*Effect of N2 partial pressure on the microstructure and mechanical properties of magnetron sputtered CrNx films",* Surf Coat Tech. 162(2002) 189-193.

[100] K.H. Nam, Y.M. Jung, and J.G. Han, "*A comparative study of microstructure and mechanical properties for CrNx films with various deposition rates by magnetron sputtering",* Surf Coat Tech. 142-144(2001) 1012-1016.

[101] C. Rebholz, H. Ziegele, A. Leyland, and A. Matthews, "*Structure, mechanical and tribological properties of nitrogen-containing chromium coatings prepared by reactive magnetron sputtering",* Surf Coat Tech. 115(1999) 222-229.

[102] T. Hurkmans, D.B. Lewis, J.S. Brooks, and W.D. Munz, "*Chromium nitride coatings grown by unbalanced magnetron (UBM) and combined arc/unbalanced magnetron (ABS) deposition techniques",* Surf Coat Tech. 86-87(1996) 192-199.

[103] S.Y. Lee, G.S. Kim, and J.H. Hahn, "*Effect of the Cr content on the mechanical properties of nanostructured TiN/CrN coatings",* Surf Coat Tech. 177-178(2004) 426-433.

[104] B. Navinsek, J. Krusic, and P. Panjan, "*Hard coatings on soft metallic substrates",* Surf Coat Tech. 98(1998) 809-815.

[105] K.P. Purushotham, L.P. Ward, N. Brack, P.J. Pigram, P. Evans, H. Noorman, and R.R. Manory, "*Corrosion behavior of Zr modified CrN coatings using metal vapor vacuum arc ion implantation",* Journal of Vacuum Science and Technology A: Vacuum, Surfaces and Films. 25(2007) 110-116.

[106] K.S. Mogensen, S.S. Eskildsen, C. Mathiasen, and J. Bottiger, "*Optical emission spectroscopy on pulsed-DC plasmas used for TiN depositions",* Surf Coat Tech. 102(1998) 41-49.

[107] A. Brudnik, A. Czapla, and E. Kusior, "*AlN thin films prepared by optical emission spectroscopy-controlled reactive sputtering",* Thin Solid Films. 478(2005) 67-71.

[108] J. Vlcek, K. Rusnak, V. Hajek, and L. Martinu, "*Reactive magnetron sputtering of CNx films: Ion bombardment effects and process characterization using optical emission spectroscopy",* J Appl Phys. 86(1999) 3646-3654.

[109] F. Sanchette, T. Czerwiec, A. Billard, and C. Frantz, "*Sputtering of Al-Cr and Al-Ti composite targets in pure Ar and in reactive Ar-N2 plasmas",* Surf Coat Tech. 96(1997) 184-190.

[110] V.V. Serikov, S. Kawamoto, and K. Nanbu, "*Particle-in-cell plus direct simulation Monte Carlo (PIC-DSMC) approach for self-consistent plasma-gas simulations",* Ieee T Plasma Sci. 27(1999) 1389-1398.

[111] F. Debal, J. Bretagne, J.P. Dauchot, M. Hecq, and M. Wautelet, "*On the role of plasma-surface interactions in dc magnetron discharges in Ar-N2 gas mixtures",* Plasma Sources Science and Technology. 10(2001) 30-37.

[112] H.-W. Zhang and S.Q. Yang, "*Properties of thin films of magnetic materials produced from DC magnetron sputtering; the effects of substrate bias and the partial pressure of reactive gases",* Vacuum. 46(1995) 661-666.

[113] J.A. Thornton, "*INFLUENCE OF APPARATUS GEOMETRY AND DEPOSITION CONDITIONS ON THE STRUCTURE AND TOPOGRAPHY OF THICK SPUTTERED COATINGS",* J Vac Sci Technol A. 11(1974) 666-670.

[114] E.Bauer, "*CrN meting point",* Appl Surf Sci. 11(1982) 479.

[115] H. Ziegele, C. Rebholz, A.A. Voevodin, A. Leyland, S.L. Rohde, and A. Matthews, "*Studies of the tribological and mechanical properties of laminated CrC-SiC coatings produced by r.f. and d.c. sputtering",* Tribol Int. 30(1997) 845-856.

[116] M. Nordin, M. Larsson, and S. Hogmark, "*Mechanical and tribological properties of multilayered PVD TiN/CrN, TiN/MoN, TiN/NbN and TiN/TaN coatings on cemented carbide",* Surf Coat Tech. 106(1998) 234-241.

[117] S. Han, J.H. Lin, S.H. Tsai, S.C. Chung, D.Y. Wang, F.H. Lu, and H.C. Shih, "*Corrosion and tribological studies of chromium nitride coated on steel with an interlayer of electroplated chromium",* Surf Coat Tech. 133-134(2000) 460-465.

[118] S.M. Aouadi, K.C. Wong, K.A.R. Mitchell, F. Namavar, E. Tobin, D.M. Mihut, and S.L. Rohde, "*Characterization of titanium chromium nitride nanocomposite protective coatings",* Appl Surf Sci. 229(2004) 387-394.

[119] S.M. Aouadi, T. Maeruf, R.D. Twesten, D.M. Mihut, and S.L. Rohde, "*Physical and mechanical properties of chromium zirconium nitride thin films",* Surf Coat Tech. 200(2006) 3411-3417.

[120] M. Fenker, M. Balzer, H.A. Jehn, H. Kappl, J.J. Lee, K.H. Lee, and H.S. Park, "*Improvement of the corrosion resistance of hard wear resistant coatings by intermediate plasma etching or multilayered structure",* Surf Coat Tech. 150(2002) 101-106.

[121] R. Lamni, R. Sanjins, M. Parlinska-Wojtan, A. Karimi, and F. Lvy, "*Microstructure and nanohardness properties of Zr-Al-N and Zr-Cr-N thin films",* Journal of Vacuum Science and Technology A: Vacuum, Surfaces and Films. 23(2005) 593-598.

[122] H. Hasegawa, A. Kimura, and T. Suzuki, "*Microhardness and structural analysis of (Ti,Al)N, (Ti,Cr)N, (Ti,Zr)N and (Ti,V)N films",* Journal of Vacuum Science and Technology, Part A: Vacuum, Surfaces and Films. 18(2000) 1038-1040.

[123] H. Hasegawa, M. Kawate, and T. Suzuki, "*Effects of Al contents on microstructures of*

Cr1-XAlXN and Zr1-XAlXN films synthesized by cathodic arc method", Surf Coat Tech. 200(2005) 2409-2413.

[124] P. Hones, R. Sanjines, and F. Levy, "*Sputter deposited chromium nitride based ternary compounds for hard coatings",* Thin Solid Films. 332(1998) 240-246.

[125] C.S. Sandu, R. Sanjines, M. Benkahoul, F. Medjani, and F. Levy, "*Formation of composite ternary nitride thin films by magnetron sputtering co-deposition",* Surf Coat Tech. 201(2006) 4083-4089.

[126] C.-S. Chen, C.-P. Liu, C.Y.A. Tsao, and H.-G. Yang, "*Study of mechanical properties of PVD ZrN films, deposited under positive and negative substrate bias conditions",* Scripta Mater. 51(2004) 715-719.

[127] G. Kim, B. Kim, S. Lee, and J. Hahn, "*Structure and mechanical properties of Cr-Zr-N films synthesized by closed field unbalanced magnetron sputtering with vertical magnetron sources",* Surf Coat Tech. 200(2005) 1669-1675.

[128] J. Romero, J. Esteve, and A. Lousa, "*Period dependence of hardness and microstructure on nanometric Cr/CrN multilayers",* Surf Coat Tech. 188-189(2004) 338-343.

[129] S. Ulrich, C. Ziebert, M. Stuber, E. Nold, H. Holleck, M. Goken, E. Schweitzer, and P. Schloossmacher, "*Correlation between constitution, properties and machining performance of TiN/ZrN multilayers",* Surf Coat Tech. 188-189(2004) 331-337.

[130] M. Nordin, M. Larsson, and S. Hogmark, "*Mechanical and tribological properties of multilayered PVD TiN/CrN",* Wear. 232(1999) 221-225.

[131] Y.-Y. Chang, D.-Y. Wang, and C.-Y. Hung, "*Structural and mechanical properties of nanolayered TiAlN/CrN coatings synthesized by a cathodic arc deposition process",* Surf Coat Tech. 200(2005) 1702-1708.

[132] G.S. Kim, S.Y. Lee, J.H. Hahn, and S.Y. Lee, "*Synthesis of CrN/AlN superlattice coatings using closed-field unbalanced magnetron sputtering process",* Surf Coat Tech. 171(2003) 91-95.

[133] Y.M. Zhou, R. Asaki, K. Higashi, W.H. Soe, and R. Yamamoto, "*Sliding wear behavior of polycrystalline TiN/CrN multilayers against an alumina ball",* Surf Coat Tech. 130(2000) 9-14.

[134] A. Rizzo, M.A. Signore, M. Penza, M.A. Tagliente, F. De Riccardis, and E. Serra, "*RF sputtering deposition of alternate TiN/ZrN multilayer hard coatings",* Thin Solid Films. 515(2006) 500-504.

[135] C.J. Tavares, L. Rebouta, E.J. Alves, B. Almeida, J. Bessa e Sousa, M.F. da Silva, and J.C. Soares, "*Interfacial roughness of multilayered TiN/ZrN coatings",* Nuclear Instruments & Methods in Physics Research, Section B: Beam Interactions with Materials and Atoms. 136-138(1998) 278-282.

[136] D.J. Li, F. Liu, M.X. Wang, J.J. Zhang, and Q.X. Liu, "*Structural and mechanical properties of multilayered gradient CrN/ZrN coatings",* Thin Solid Films. 506-507(2006) 202-206.

[137] J. Xu, K. Hattori, Y. Seino, and I. Kojima, "*Microstructure and properties of CrN/Si3N4 nano-structured multilayer films",* Thin Solid Films. 414(2002) 239-245.

[138] J. Musil. and J. Vlcek., "*Magnetron sputtering of hard nanocomposite coatings and their properties",* Surf Coat Tech. 142-144(2001) 557.

[139] N.J.M. Carvalho, E. Zoestbergen, B.J. Kooi, and J.T.M. De Hosson, "*Stress analysis and*

microstructure of PVD monolayer TiN and multilayer TiN/(Ti,Al)N coatings", Thin Solid Films. 429(2003) 179-189.

[140] Y.-R. Jeng, Z.-W. Lin, and S.-H. Shyu, "*Changes of surface topography during running-in process",* Journal of Tribology. 126(2004) 620-625.

[141] H.C. Barshilia, N. Selvakumar, B. Deepthi, and K.S. Rajam, "*A comparative study of reactive direct current magnetron sputtered CrAlN and CrN coatings",* Surf Coat Tech. 201(2006) 2193-2201.

[142] L. Kwang Hee, C. Park, Y. Yoon, L. Jung Joong, and H.A. Jehn, "*Corrosion behaviours of CrNx and (Ti1-xCrx)N coatings produced by ion plating",* Journal of Vacuum Science and Technology, Part A: Vacuum, Surfaces and Films. 19(2001) 2504-2513.

[143] D.B. Lewis, S.J. Creasey, C. Wustefeld, A.P. Ehiasarian, and P.E. Hovsepian, "*The role of the growth defects on the corrosion resistance of CrN/NbN superlattice coatings deposited at low temperatures",* Thin Solid Films. 503(2006) 143-148.

[144] H.W. Wang, M.M. Stack, P. Hovsepian, and W.D. Munz, "*Macroparticle induced corrosion for arc bond sputtering CrN/NbN superlattice coatings",* J Mater Sci Lett. 20(2001) 1995-1997.

[145] H.W. Wang, M.M. Stack, S.B. Lyon, P. Hovsepian, and W.D. Munz, "*Corrosion behaviour of macroparticle defects in arc bond-sputtered CrN/NbN superlattice coatings",* Surf Coat Tech. 126(2000) 279-287.

[146] L. Wang, X. Nie, M.J. Lukitsch, J.C. Jiang, and Y.T. Cheng, "*Effect of tribological media on tribological properties of multilayer Cr(N)/C(DLC) coatings",* Surf Coat Tech. 201(2006) 4341-4347.

[147] C. Mendibide, P. Steyer, J. Fontaine, and P. Goudeau, "*Improvement of the tribological behaviour of PVD nanostratified TiN/CrN coatings - An explanation",* Surf Coat Tech. 201(2006) 4119-4124.

[148] E.E. Fullerton, I.K. Schuller, H. Vanderstraeten, and Y. Bruynseraede, "*Structural refinement of superlattices from x-ray diffraction",* Phys Rev B. 45(1992) 9292.

[149] Z. Zhiguo, L. Tianwei, X. Jun, D. Xinlu, and D. Chuang, "*N-rich Zr-N films deposited by unbalanced magnetron sputtering enhanced with a highly reactive MW-ECR plasma",* Surf Coat Tech. 200(2006) 4918-4922.

[150] S.-K. Tien and J.-G. Duh, "*Effect of heat treatment on mechanical properties and microstructure of CrN/AlN multilayer coatings",* Thin Solid Films. 494(2006) 173-178.

[151] M. Nordin and F. Ericson, "*Growth characteristics of multilayered physical vapour deposited TiN/TaNx on high speed steel substrate",* Thin Solid Films. 385(2001) 174-181.

[152] R.L. Zong, S.P. Wen, F. Zeng, Y. Gao, X.W. Li, B. He, and F. Pan, "*Microstructure and mechanical properties of polycrystalline-Ag/amorphous-CoZrNb multilayers",* Surf Coat Tech. 201(2007) 7932-7938.

[153] J.S. Koehler, "*Attempt to Design a Strong Solid",* Phys Rev B. 2(1970) 547.

[154] J.W. Gahn, "*Hardening by spinodal decomposition",* Acta Metall. 11(1963) 1275-1282.

[155] M. Takano, S. Tagami, K. Minato, T. Kozaki, and S. Sato, "*Lattice thermal expansions of (Dy, Zr)N solid solutions",* J Alloy Compd. 439(2007) 215-220.

[156] A. Leyland and A. Matthews, "*On the significance of the H/E ratio in wear control: A nanocomposite coating approach to optimized tribological behaviour",* Wear. 246(2000) 1-11.

[157] Y.-Z. Tsai and J.-G. Duh, "*Tribological behavior of CrN/WN multilayer coatings grown by ion-beam assisted deposition",* Surf Coat Tech. 201(2006) 4266-4272.

[158] Q. Yang and L.R. Zhao, "*Dry sliding wear of magnetron sputtered TiN/CrN superlattice coatings",* Surf Coat Tech. 173(2003) 58-66.

[159] H.C. Barshilia, M.S. Prakash, A. Poojari, and K.S. Rajam, "*Corrosion behavior of nanolayered TiN/NbN multilayer coatings prepared by reactive direct current magnetron sputtering process",* Thin Solid Films. 460(2004) 133-142.

[160] C. Liu, A. Leyland, Q. Bi, and A. Matthews, "*Corrosion resistance of multi-layered plasma-assisted physical vapour deposition TiN and CrN coatings",* Surf Coat Tech. 141(2001) 164-173.

[161] A. Akbari, J.P. Riviere, C. Templier, and E. Le Bourhis, "*Structural and mechanical properties of IBAD deposited nanocomposite Ti-Ni-N coatings",* Surf Coat Tech. 200(2006) 6298-6302.

[162] C.S. Sandu, M. Benkahoul, R. Sanjines, and F. Levy, "*Model for the evolution of Nb-Si-N thin films as a function of Si content relating the nanostructure to electrical and mechanical properties",* Surf Coat Tech. 201(2006) 2897-2903.

[163] C.S. Sandu, F. Medjani, R. Sanjines, A. Karimi, and F. Levy, "*Structure, morphology and electrical properties of sputtered Zr-Si-N thin films: From solid solution to nanocomposite",* Surf Coat Tech. 201(2006) 4219-4223.

[164] A. Winkelmann, J.M. Cairney, M.J. Hoffman, P.J. Martin, and A. Bendavid, "*Zr-Si-N films fabricated using hybrid cathodic arc and chemical vapour deposition: Structure vs. properties",* Surf Coat Tech. 200(2006) 4213-4219.

[165] H. Zhang, T.W. Guo, Z.X. Song, X.J. Wang, and K.W. Xu, "*The effect of ZrSiN diffusion barrier on the bonding strength of titanium porcelain",* Surf Coat Tech. 201(2007) 5637-5640.

[166] L. Yu, S. Dong, J. Xu, and I. Kojima, "*Microstructure and hardening mechanisms in a-Si3N4/nc-TiN nanostructured multilayers",* Thin Solid Films. 516(2008) 1864-1870.

[167] E. Martinez, R. Sanjines, A. Karimi, J. Esteve, and F. Levy, "*Mechanical properties of nanocomposite and multilayered Cr-Si-N sputtered thin films",* Surf Coat Tech. 180-181(2004) 570-574.

[168] Y. Dong, W. Zhao, J. Yue, and G. Li, "*Crystallization of Si3N4 layers and its influences on the microstructure and mechanical properties of ZrN/Si3N 4 nanomultilayers",* Appl Phys Lett. 89(2006) 121916.

[169] P.B. Barna and M. Adamik, "*Fundamental structure forming phenomena of polycrystalline films and the structure zone models",* Thin Solid Films. 317(1998) 27-33.

[170] Z.G. Zhang, O. Rapaud, N. Bonasso, D. Mercs, C. Dong, and C. Coddet, "*Control of microstructures and properties of dc magnetron sputtering deposited chromium nitride films",* Vacuum. 82(2007) 501-509.

[171] M. Lattemann and S. Ulrich, "*Investigation of structure and mechanical properties of magnetron sputtered monolayer and multilayer coatings in the ternary system Si-B-C",* Surf Coat Tech. 201(2007) 5564-5569.

[172] T. Mae, M. Nose, M. Zhou, T. Nagae, and K. Shimamura, "*The effects of Si addition on the structure and mechanical properties of ZrN thin films deposited by an r.f. reactive sputtering method",* Surf Coat Tech. 142-144(2001) 954-958.

[173] M. Nose, M. Zhou, T. Nagae, T. Mae, M. Yokota, and S. Saji, "*Properties of Zr-Si-N coatings prepared by RF reactive sputtering",* Surf Coat Tech. 132(2000) 163-168.

[174] Y.C. Liu, K. Furukawa, D.W. Gao, H. Nakashima, K. Uchino, and K. Muraoka, "*In-situ infrared reflective absorption spectroscopy characterization of SiN films deposited using sputtering-type ECR microwave plasma",* Appl Surf Sci. 121-122(1997) 233-236.

[175] Y. Zhou, R. Asaki, W.-H. Soe, R. Yamamoto, R. Chen, and A. Iwabuchi, "*Hardness anomaly, plastic deformation work and fretting wear properties of polycrystalline TiN/CrN multilayers",* Wear. 236(1999) 159-164.

[176] S. Zhang, D. Sun, Y. Fu, Y.T. Pei, and J.T.M. De Hosson, "*Ni-toughened nc-TiN/a-SiNx nanocomposite thin films",* Surf Coat Tech. 200(2005) 1530-1534.

[177] A.M.K. J.R. Tuck, "*The influence of coating cracking and delamination on the hardness of coated system",* proceedings of 13th Euro Conf on Fracture. Sep 2000,San Sebastian, Spain(2000).

[178] Y. Sakamaoto, M. Nose, T. Mae, E. Honbo, M. Zhou, and K. Nogi, "*Structure and properties of Cr-B, Cr-B-N and multilayer Cr-B/Cr-B-N thin films prepared by r.f.-sputtering",* Surf Coat Tech. 174-175(2003) 444-449.

[179] J. Romero, A. Lousa, E. Martinez, and J. Esteve, "*Nanometric chromium/chromium carbide multilayers for tribological applications",* Surf Coat Tech. 163-164(2003) 392-397.